Surface dynamics of solids upon high-intensity laser irradiation investigated by grazing incidence X-ray scattering

DISSERTATION
zur Erlangung des Grades eines Doktors
der Naturwissenschaften

vorgelegt von
M.Sc. Lisa Randolph
geb. am 17.10.1992 in Siegen

eingereicht bei der Naturwissenschaftlich-Technischen Fakultät
der Universität Siegen
Siegen 2020

Betreuer und erster Gutachter
Prof. Dr. Christian Gutt
Universität Siegen

Zweiter Gutachter
Dr. habil. Ulf Zastrau
European XFEL GmbH

Tag der mündlichen Prüfung
06.11.2020

Contents

Abstract

The excitation of solids by ultrafast, intense lasers creates high-density plasmas relevant for astrophysics, inertial confinement fusion, various practical applications including laser processing, realization of compact sources of coherent XUV to X-ray radiation and bright particles including ions. Obviously, a comprehensive understanding of laser coupling and subsequent energy transport into dense-plasma is of key importance. Up to now, the current lack of appropriate methods observing complex density dynamics with sufficient spatial resolution prevented us from a quantitative understanding of the underlying physics and benchmarking existing models. This thesis demonstrates for the first time the feasibility of single pulse grazing incidence X-ray diffuse scattering experiments from laser excited condensed matter employing single XFEL pulse of 7 fs pulse duration. The experiments, performed at the Japanese FEL facility SACLA, reveal the ultrafast evolution of the electron density in the vicinity of the surface. We deduce the dynamics of the density and surface profiles on ultrafast time scales.

The retrieved density information infers the electronic heat conduction velocity and surface ablation dynamics caused by electrostatic ablation or electron-ion collisions. As the dynamics of the multilayer sample is caused by particle penetration and pressure balance between adjacent layers, our new tool will play a central role in benchmarking various models including particle collisions and the equation of states.

The results can be anticipated to be useful for various applications that rely on transient dynamics of high-density states: material processing, isochoric heating, laser dynamic compression and relativistic laser matter interaction. Our new technique will play an important role towards long-awaited quantitative benchmark of various models that have been suffered from lack of precise experimental data.

Additionally, grazing-incidence X-ray scattering provides also information on lateral and vertical correlation and roughness properties at the surface upon laser excitation. With this surface roughness and ripples changing upon laser excitation, surface plasma instability dynamics and spatial homogeneity of shock wave with sub-μm resolution can be investigated.

Bringing together X-ray scattering techniques and high energy density science opens a complete new field in understanding the fundamental processes in laser-plasma interaction.

Zusammenfassung

Die Anregung von Festkörpern durch ultraschnelle, intensive Laser erzeugt hochdichte Plasmen, die für die Astrophysik, die Fusion unter Trägheitseinschluss, verschiedene praktische Anwendungen einschließlich Laserbearbeitung, die Realisierung kompakter Quellen für kohärente XUV- bis Röntgenstrahlung und für helle Teilchen einschließlich Ionen relevant sind. Es liegt auf der Hand, dass ein umfassendes Verständnis der Laserkopplung und des anschließenden Energietransports in dichte Plasmen von zentraler Bedeutung ist. Bislang hinderte uns der derzeitige Mangel an geeigneten Methoden zur Beobachtung der komplexen Dichtedynamik mit ausreichender räumlicher Auflösung daran, die zugrundeliegende Physik quantitativ zu verstehen und bestehende Modelle zu vergleichen. Diese Arbeit zeigt zum ersten Mal die Durchführbarkeit von Röntgendiffusionsstreuexperimenten an laserangeregter kondensierter Materie unter streifendem Einzelimpuls-Einfall mit einem XFEL-Puls von 7 fs Pulsdauer. Die Experimente zeigen die ultraschnelle Entwicklung der Elektronendichte in der Nähe der Oberfläche. Wir leiten die Dynamik der Dichte- und Oberflächenprofile auf ultraschnellen Zeitskalen ab.

Die gewonnene Dichteinformation lässt auf die elektronische Wärmeleitgeschwindigkeit und die Dynamik des Oberflächenabtrags durch elektrostatische Ablation oder Elektron-Ionen-Kollisionen schließen. Da die Dynamik der Vielschichtprobe durch die Teilcheneindringung und den Druckausgleich zwischen benachbarten Schichten verursacht wird, wird unser neues Werkzeug eine zentrale Rolle beim Benchmarking verschiedener Modelle einschließlich Teilchenkollisionen und der Zustandsgleichung spielen.

Es ist zu erwarten, dass die Ergebnisse für verschiedene Anwendungen nützlich sein werden, die auf der transienten Dynamik von Zuständen hoher Dichte beruhen: Materialbearbeitung, isochore Erwärmung, dynamische Laserkompression und relativistische Laser-Materie-Wechselwirkung. Unsere neue Technik wird eine wichtige Rolle beim lang erwarteten quantitativen Benchmark verschiedener Modelle spielen, die unter dem Mangel an präzisen experimentellen Daten gelitten haben.

Zusätzlich liefert die Röntgenstreuung unter streifendem Einfall auch Informationen über laterale und vertikale Korrelation und Rauheitseigenschaften an der Oberfläche bei Laseranregung. Mit dieser Änderung der Oberflächenrauheit und der Welligkeit bei Laseranregung können die Dynamik der Instabilität des Oberflächenplasmas und die räumliche Homogenität der Schockwelle mit einer Auflösung von sub-μm untersucht werden.

Die Zusammenführung von Röntgenstreuungstechniken und der Wissenschaft der Hochenergiedichte eröffnet ein völlig neues Feld für das Verständnis der grundlegenden Prozesse bei der Laser-Plasma-Wechselwirkung.

Chapter 1

Introduction

The interaction of high-intensity lasers with solids creates high-density, warm-to-hot temperature plasmas involving a wide range of non-linear physics phenomena [1]. Such plasmas are not only of great relevance to astrophysics [2] and inertial confinement fusion, but also hold promise for the generation of bright, coherent light sources [3] and for bright particle beams including ions [4] by efficiently depositing laser energy into plasmas. In general, laser coupling into plasmas occurs either in the under-critical density part of the expanding plasma-vacuum interface, where the laser wave can propagate, or within the skin depth of the overcritical plasma, where the laser wave is evanescent. The so-called critical density n_c is located at the position of the density profile where the local electron plasma frequency equals the laser frequency, which is about 1% of the solid density for optical frequencies. It is known that a sub-μm scale density profile at the surface strongly influences the laser-plasma coupling [5]. To obtain a complete picture of the laser-plasma coupling and the subsequent energy transport into the bulk, it is therefore crucial to extract the dynamically changing over-critical plasma profile with nanometer resolution. In the framework of this thesis, we visualize surface plasmas employing X-ray Free-Electron Lasers providing the required nm scale surface sensitivity on ultrafast time scales.
Although the surface morphology is of great importance in laser-matter interactions, in this thesis we will focus on short-pulse (40 fs) laser-solid interactions well above the material damage threshold. At laser intensities of $10^{14}\,\mathrm{W/cm^2}$ and above, surface ionization occurs on time scales of a few fs following the laser essentially interacts with a solid density plasma. The laser energy is first absorbed by electrons whose oscillatory energy is converted into random thermal energy by collisions with ions. Therefore, the collision frequency between electrons and ions is the crucial physical quantity for laser absorption, electron-ion energy transfer and electronic heat conduction. Assuming that the laser pulse duration is shorter than the electron-ion equilibration time scale ($\geq$ ps), electronic and ionic subsystems need to be considered separately. Furthermore, the local temperature gradient tends to be steeper than the electron mean free path with the electron motion

becoming non-local causing a breakdown of the classical Spitzer-Härm heat conduction treatment. In general, a proper treatment of electron-ion binary collisions and thermal conductivity under strongly non-equilibrium conditions is one of the long-standing challenges in the plasma community. This thesis will provide new benchmarks for theory and simulations.

Surfaces of laser excited matter are also of considerable practical relevance, such as solid density plasmas with sharp density gradients (compared to the incoming laser wavelength) used as highly-reflective optical mirrors. Such plasma-based mirrors have attracted interest for temporal cleaning of laser pulses [6] and tight focusing [7] in very compact and efficient manner since plasma optics can withstand laser intensities far above the material damage threshold. Therefore, the next-generation ultra-high-intensity laser facilities are proposed to heavily rely on the usage of plasma optics [8]. All these functionalities require the collective plasma thermal motion to be negligible compared to the laser wavelength. In-situ visualization of the surface with sub-μm resolution is important to evaluate the ultimate focus quality behind the plasma optics, which is prone to degrade due to roughness introduced by the plasma expansion. Plasma optics enters into a non-linear regime at higher laser intensities above $10^{17}\,\mathrm{W/cm^2}$ by exciting collective plasma waves allowing the generation of higher-order harmonics (HHG) in the XUV to soft X-ray regime [3]. Above the electron relativistic intensity ($> 10^{18}\,\mathrm{W/cm^2}$) surface electron trajectories become strongly anharmonic, leading to a strong non-linear response of the reflected light fields due to the relativistic Doppler upshift. This relativistically oscillating plasma mirror is a potential future attosecond coherent light source providing photon energies up to the X-ray domain. At those high intensities the strong plasma thermal pressure and the radiation pressure push the plasma surface inwards and outwards simultaneously. This highly non-linear and complex surface plasma dynamics has been so far only studied via characterizing the generated high frequency radiation [9] and detailed insights rely strongly on simulations.

While surface-sensitive optical probing techniques, such as a frequency domain interferometry (FDI) [10,11] are powerful tools to identify the position and velocity of the expanding critical density surface, they do not provide information about density profiles inside the solid. This is due to the critical density of $\sim 10^{21}\,\mathrm{cm^{-3}}$ at the optical wavelength being about > 100 times smaller than the solid density. It is only very recently, that the solid density expansion upon intense laser irradiation can be investigated with nanometer spatial resolution by small-angle X-ray scattering (SAXS) at X-ray Free-Electron Lasers (XFEL) [12–15].

This thesis demonstrates extending the SAXS technique to grazing-incidence X-ray diffuse scattering (XDS) [16] using ultrashort XFEL pulses to obtain nm spatial in-plane and in-depth resolution from solid-density plasma surfaces. In principle, also X-ray reflectometry (XRR) provides high resolution information on surfaces and interfaces in layered

systems [17,18], however, XRR is not single shot compatible because of its requirement of scanning both incident and exit angle simultaneously. Measuring the non-specular, diffuse scattering pattern around the specular signal of an intense X-ray beam provides not only single shot compatible data but also to access different X-ray penetration depths from a few nm up to microns. This is due to the fact that the imaginary component of the momentum transfer normal to the surface Q_z varies considerably when either incident or exit wave approach the critical angle of total external reflection [17]. Note that, using a ML sample was the key to fully exploit the ability of this X-ray technique to access the depth-resolved data. Two pioneering XDS experiments have been performed in this thesis at the Japanese XFEL facility SACLA.

Here, we demonstrate the feasibility of single shot XDS which allows for the first time the visualization of transient surface density profiles with nanometer depth resolution. Using ML samples we measured the ultrafast plasma density evolution via the recorded diffuse scattering patterns and determined the speed of density perturbation propagating into the bulk, the speed of the surface ablation and intermixing of layers via thermal expansion.

This thesis is structured as follows: in Chapter 2 we introduce the theory of X-ray diffraction. In Chapter 3, we give a brief overview about the fundamentals of plasma dynamics. Experimental details are presented in Chapter 4. In Chapter 5 we present the experimental data and show a detailed analysis and explanation of the data leading to the major findings and interpret them in the framework of plasma physics in Chapter 6. Finally, in Chapter 7 we summarize the results and give an outlook on future studies.

Chapter 2

Theory of X-ray diffraction

In this chapter, we present the theoretical concepts of X-ray diffraction phenomena. In section 2.1, we describe the basic principles of X-ray reflection on single interfaces and extend it to multilayer samples in section 2.2. As multilayer samples do not have flat interfaces but a small roughness, we investigate the specular reflection from rough multilayer systems in section 2.3. These rough interfaces can be described mathematically as shown in section 2.4. These rough multilayer samples do not only contribute to the specular scattering but also have a non-specular scattering signal. This is described in the distorted wave born approximation explained in section 2.5. In section 2.6, we demonstrate the concept of the X-ray diffuse scattering technique we used in our experiment and illustrate some examples in section 2.7. In section 2.8, we explain how we can extract further information about the interface structure from the out-of-plane scattering signal.

2.1 Basic principles of X-ray reflection

The propagation of an electromagnetic wave

$$\boldsymbol{E}(\boldsymbol{r}) = \boldsymbol{E_0} \cdot \exp\left(i\boldsymbol{k}\boldsymbol{r}\right) \tag{2.1.1}$$

through a material with the index of refraction $n(\boldsymbol{r})$ is described by the Helmholtz equation

$$\Delta\boldsymbol{E}(\boldsymbol{r}) + k^2 n^2(\boldsymbol{r})\,\boldsymbol{E}(\boldsymbol{r}) = 0 \tag{2.1.2}$$

with the absolute value of the wavevector $k = \frac{2\pi}{\lambda}$ and the X-ray wavelength λ [19].
The index of refraction for an arrangement of N atoms per unit volume is defined as

$$n^2(\boldsymbol{r}) = 1 + N\frac{e^2}{\epsilon_0 m}\sum_{j=1}^{N}\frac{f_j}{\omega_j^2 - \omega^2 - 2i\omega\eta_j}, \tag{2.1.3}$$

with atoms being harmonic oscillators with resonance frequency ω_j. e denotes the electric

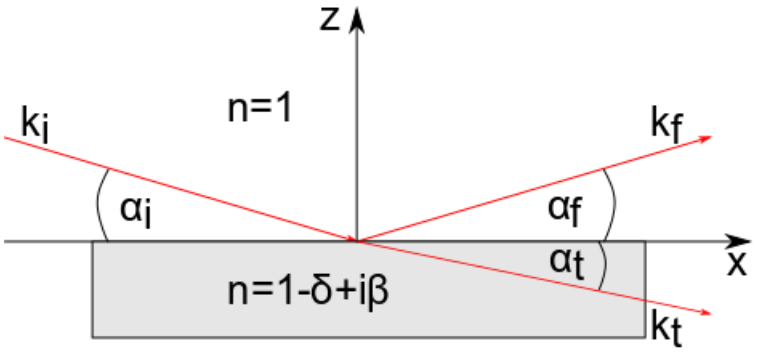

Figure 2.1: Basic principle of X-ray reflection. An incident beam with wavevector $\boldsymbol{k_i}$ impinges on a sample at an angle α_i. One part of the beam gets reflected on the surface with $\alpha_f = \alpha_i$ and exits the sample with wavevector $\boldsymbol{k_f}$. The other part is transmitted at an angle α_t and propagates into the material with $\boldsymbol{k_t}$. For X-rays, the index of refraction in material is slightly smaller than 1, thus $\alpha_t < \alpha_i$ facilitating surface sensitivity.

charge, m is the electron mass and ω describes the frequency of the incoming electromagnetic wave. n_j expresses the damping factors and f_j are the forced oscillation strengths of the electrons of each single atom. In general, f_j are complex numbers defined via

$$f_j = f_j^0 + f_j'(E) + i f_j''(E) \tag{2.1.4}$$

with $f_j'(E)$ the energy dependent dispersion correction and $f_j''(E)$ the absorption correction. If the X-ray frequency ω is larger than ω_j, Eq. (2.1.3) can be written as

$$n(\boldsymbol{r}) = 1 - \delta(\boldsymbol{r}) + i\beta(\boldsymbol{r}) \tag{2.1.5}$$

with the dispersion $\delta(\boldsymbol{r})$

$$\delta(\boldsymbol{r}) = \frac{\lambda^2}{2\pi} r_e \, \rho(\boldsymbol{r}) \sum_{j=1}^{N} \frac{f_j^0 + f_j'(E)}{Z} \tag{2.1.6}$$

and the absorption $\beta(\boldsymbol{r})$

$$\beta(\boldsymbol{r}) = \frac{\lambda^2}{2\pi} r_e \, \rho(\boldsymbol{r}) \sum_{j=1}^{N} \frac{f_j''(E)}{Z} = \frac{\lambda}{4\pi} \mu(\boldsymbol{r}), \tag{2.1.7}$$

with $r_e = 2.8 \cdot 10^{-15}$ m the classical electron radius, Z the total number of electrons, $\rho(\boldsymbol{r})$ the electron density and $\mu(\boldsymbol{r})$ the linear absorption coefficient. If the medium is homogeneous and far from absorption edges, the refractive index simplifies to

$$n = 1 - \frac{\lambda^2}{2\pi} r_e \rho + i \frac{\lambda}{4\pi} \mu. \tag{2.1.8}$$

Since the dispersion coefficient $\delta(\boldsymbol{r})$ is always positive, for X-rays the real part of $n(\boldsymbol{r})$ needs to be slightly smaller than one (Fig. 2.1). That implies that below a certain grazing incidence angle, called critical angle α_c, total external reflection is possible. Snell's law connects the incidence angle α_i to the refracted angle α_t

$$\cos\alpha_i = (1-\delta)\cos\alpha_t. \tag{2.1.9}$$

For $\alpha_t = 0$ and $\delta \ll 1$ the critical angle α_c can be approximated with

$$\alpha_c \approx \sqrt{2\delta} = \lambda\sqrt{\frac{r_e\rho}{\pi}}. \tag{2.1.10}$$

For X-rays, the critical angle has values on the order of several tenths of a degree, e.g. for silicon the critical angle is $\alpha_c = 0.224°$ (with $\lambda = 1.55\,\text{Å}$) [20]. For $\alpha_i < \alpha_c$ the electric field of the X-ray wave is decaying exponentially, called evanescent wave, and travels parallel to the sample surface as shown in Fig. 2.2. The penetration depth for $\alpha_i \to 0$ is given by

$$\Lambda_0 = \frac{1}{\sqrt{4\pi r_e\rho}} \tag{2.1.11}$$

and thus independent of the X-ray wavelength λ [19]. In practice, the penetration depth below the critical angle is on the order of 50 Å following that for grazing-incidence angles the scattering signal mainly arises from the surface. Fig. 2.3 displays the penetration depth as a function of α_i/α_c for different ratios of β/δ showing that for $\alpha_i < \alpha_c$ the penetration depth is equal for a ratios at about 60 Å and increases rapidly for angles larger than the critical angle.

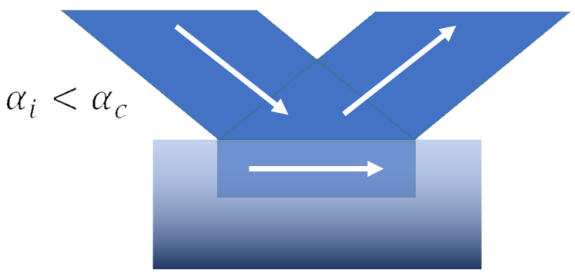

Figure 2.2: Illustration of evanescent waves occuring at an angle $\alpha_i < \alpha_c$ (adapted from [21]).

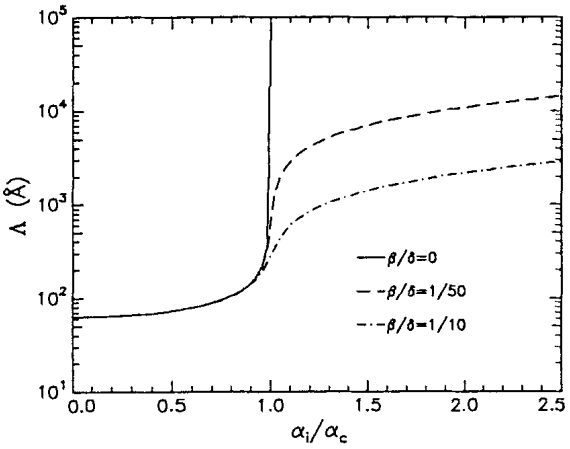

Figure 2.3: Penetration depth Λ into silicon as a function of the ratio α_i/α_c with wavelength $\lambda = 1.54\,\text{Å}$ for various ratios of absorption β and dispersion factor δ (taken from [19]).

In order to calculate the reflection and transmission amplitude of a layer, one applies the Fresnel coefficients

$$r_{j,j+1} = \frac{k_{z,j} - k_{z,j+1}}{k_{z,j} + k_{z,j+1}} \qquad \text{and} \qquad t_{j,j+1} = \frac{2k_{z,j}}{k_{z,j} + k_{z,j+1}}, \tag{2.1.12}$$

with $k_{z,j} = k\sqrt{(n_j^2 - \cos^2 \alpha_i)}$.
Fig. 2.4 displays an example of the Fresnel reflectivity R_F with fixed value of β and varying δ as a function of the ratio between incident angle and critical angle α_i/α_c. It is obvious that the absorption β is only important in the range of the critical angle. For incident angles larger than the critical angle the reflectivity coefficient R_F decreases rapidly. Fig. 2.5 shows the Fresnel transmission T_F as a function of α_i/α_c. For $\alpha_i = \alpha_c$ we recognize a sharp maximum which occurs due to interference effects of reflected and transmitted waves. For angles larger than the critical angle α_c the transmission approaches 1 meaning that absorption plays a minor role for $\alpha_i \gg \alpha_c$ and the waves can penetrate the medium almost unhindered.

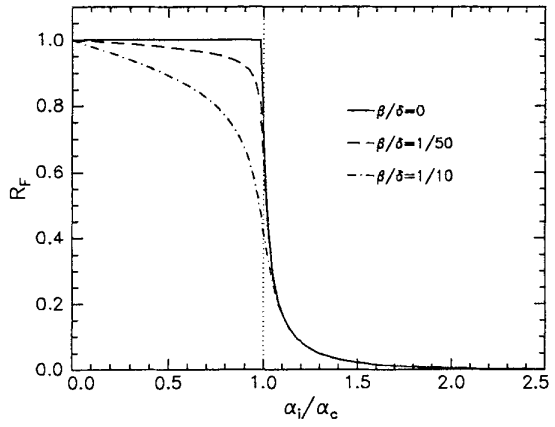

Figure 2.4: Fresnel reflectivity R_F as a function of $\frac{\alpha_i}{\alpha_c}$ for different ratios of $\frac{\beta}{\delta}$ (taken from [19]).

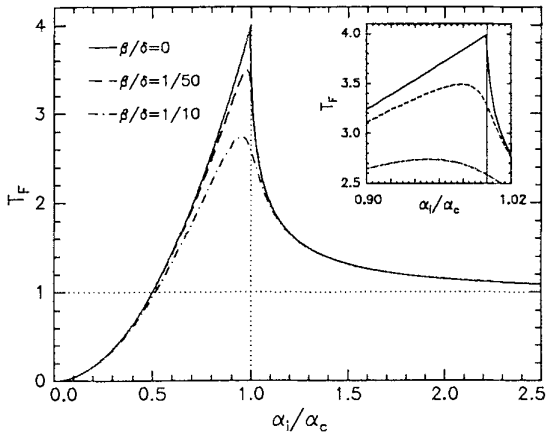

Figure 2.5: Fresnel transmission T_F as a function of $\frac{\alpha_i}{\alpha_c}$ for different ratios of $\frac{\beta}{\delta}$ (taken from [19]).

2.2 Specular reflection from multilayer systems

In this thesis, samples with multiple layers are investigated. We assume that the scattering originates from $N+1$ layers with N sharp interfaces at the positions $z_j \neq 0$ (see Fig. 2.6). Layer 1 is the vacuum with interface at $z_1 = 0$. The layer $N+1$ represents the semi-infinite substrate. Each layer has a refractive index $n_j = 1 - \delta_j + i\beta_j$ and a thickness of $d_j = z_{j-1} - z_j$. T_j denotes the wavevector amplitude of the transmitted wave while R_j represents this value for the reflected wave. The incoming wave impinges on the surface at grazing angle α_i.

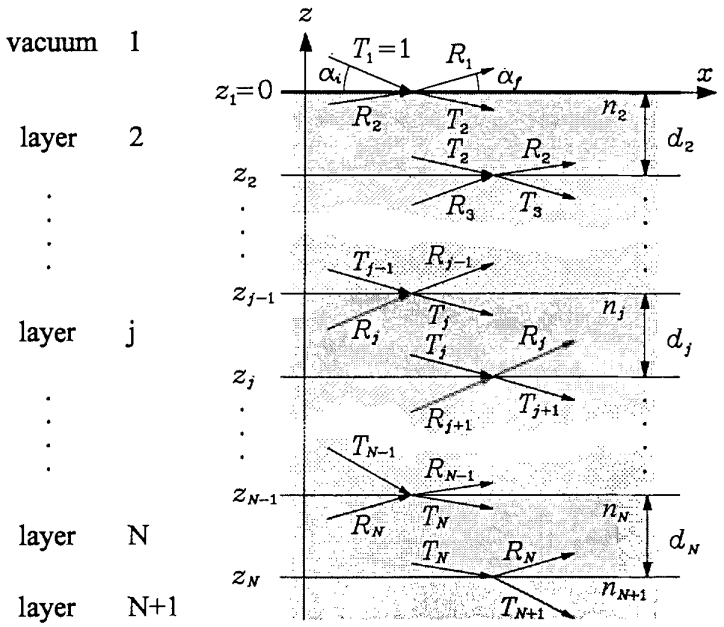

Figure 2.6: Multilayer System of N+1 layers with thickness d_N and N corresponding interfaces. Every interface has a reflection R_N and transmission T_N contribution. Here, the intensity is normalized to $T_1 = 1$ (Fig. taken from [19]).

Each interface j needs to be linked to interface $j+1$ in order to calculate the reflected amplitude after N interfaces. In 1954, Parratt formulated the first approach for a recursive formalism [22] in which X_j describes the ratio of R_j and T_j [19]

$$X_j = \frac{R_j}{T_j} = \exp\left(-2ik_{z,j}z_j\right) \frac{r_{j,j+1} + X_{j+1}\exp\left(2ik_{z,j+1}z_j\right)}{1 + r_{j,j+1}X_{j+1}\exp\left(2ik_{z,j+1}z_j\right)} \tag{2.2.1}$$

with $r_{j,j+1}$ the Fresnel coefficient. Since the thickness of the substrate is much larger than the penetration depth of the X-rays, there will be no reflection from the substrate, thus $R_{N+1} = X_{N+1} = 0$. The specular reflected intensity R after N iterations is

$$R = |X_1|^2 = |R_1|^2. \tag{2.2.2}$$

With R_1 and $T_1 = 1$ the amplitudes for R_j and T_j inside all layers can be calculated recursively via

$$R_{j+1} = \frac{1}{t_{j+1,j}} \left\{ T_j r_{j+1,j} \exp\left[-i\left(k_{z,j+1} + k_{z,j}\right) z_j\right] + R_j \exp\left[-i\left(k_{z,j+1} - k_{z,j}\right) z_j\right] \right\} \quad (2.2.3)$$

$$T_{j+1} = \frac{1}{t_{j+1,j}} \left\{ T_j \exp\left[i\left(k_{z,j+1} - k_{z,j}\right) z_j\right] + R_j r_{j+1,j} \exp\left[i\left(k_{z,j+1} + k_{z,j}\right) z_j\right] \right\} \quad (2.2.4)$$

with the Fresnel transmission coefficient $t_{j+1,j} = 1 + r_{j+1,j}$ of the j$^{\text{th}}$ interface.

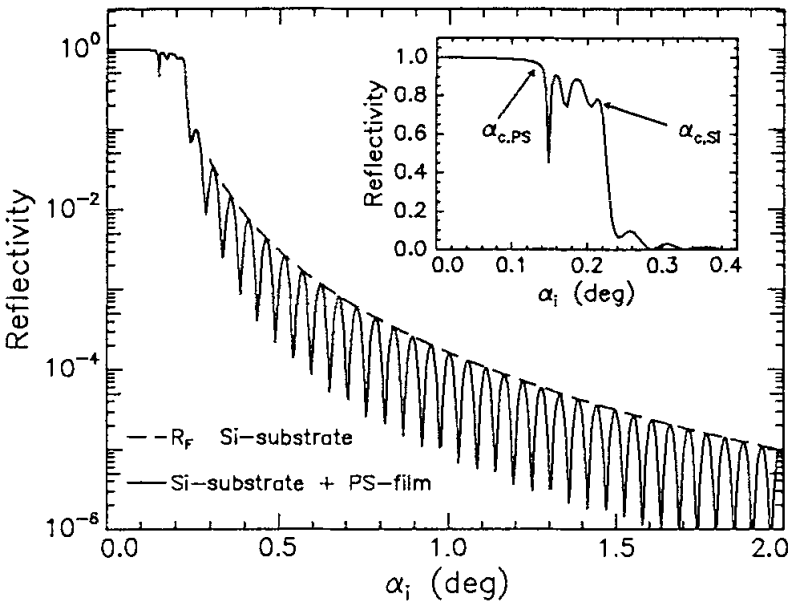

Figure 2.7: Reflectivity signal as a function of α_i measured with an X-ray wavelength $\lambda = 1.54\,\text{Å}$. The solid line shows the reflectivity of a Silicon substrate and a polystyrene (PS) film with $d = 800\,\text{Å}$ on top while the dashed line displays the signal from silicon substrate only (taken from [19]).

In Fig. 2.7 an example of a calculated reflectivity of a polystyrene (PS) film with $d = 800\,\text{Å}$ on a silicon substrate is shown. The X-ray wavelength was set to $\lambda = 1.54\,\text{Å}$ with $\delta_{\text{Si}} = 7.56 \cdot 10^{-6}$, $\beta_{\text{Si}} = 1.89 \cdot 10^{-7}$, $\delta_{\text{PS}} = 3.5 \cdot 10^{-6}$ and $\beta_{\text{PS}} = 1.75 \cdot 10^{-8}$. For small angles $\alpha_i < 0.3°$ we notice the critical angles of the corresponding materials. For larger incident angles $\alpha_i > \alpha_c$ the intensity decays several orders of magnitude following $(\alpha_c/2\alpha_i)^4$. The small oscillations are called Kiessig fringes and occur due to interference effects of the reflected waves at the different interfaces. From the period ΔQ_z of these Kiessig fringes one can obtain the multilayer thickness by

$$d = \frac{2\pi}{\Delta Q_z} \approx \frac{\lambda}{2\Delta\alpha_i} \quad (2.2.5)$$

with $Q_z = 2k \sin\alpha_i$.

2.3 Specular reflection from rough multilayer systems

Up to now we assumed that the interfaces are perfectly flat, while in practice the surfaces are rough. For a rough surface the index of refraction n_j is replaced by a continuous variation $n_j(x, y, z)$ (see Fig. 2.8). We are only interested in the specular reflectivity, therefore the wavevector transfer $\boldsymbol{Q} = \boldsymbol{k_f} - \boldsymbol{k_i}$ has only a z component. The one-dimensional refractive index profiles are then calculated as lateral averages [19]

$$n_j(z) = \int\int n_j(x, y, z)\,\mathrm{d}y\,\mathrm{d}x. \tag{2.3.1}$$

We assume that a rough interface consists of different smooth interfaces with certain z coordinates and weighted by a probability density $P_j(z)$ with its mean value

$$\mu_j = \int z P_j(z)\mathrm{d}z, \tag{2.3.2}$$

the root-mean-square (rms) roughness

$$\sigma_j^2 = \int (z - \mu_j)^2 P_j(z)\,\mathrm{d}z \tag{2.3.3}$$

and the function $f_j(k)$ given by

$$f_j(k) = \exp(ik\mu_j) \int \exp(-ikz) P_j(z)\,\mathrm{d}z. \tag{2.3.4}$$

With this Eq. (2.2.3) and (2.2.4) can be rewritten as

$$R_{j+1} = \frac{1}{\tilde{t}_{j+1,j}} \left\{ T_j \tilde{r}_{j+1,j} \exp\left[-i\left(k_{z,j+1} + k_{z,j}\right) z_j\right] + R_j \exp\left[-i\left(k_{z,j+1} - k_{z,j}\right) z_j\right] \right\} \tag{2.3.5}$$

$$T_{j+1} = \frac{1}{f_t \tilde{t}_{j+1,j}} \left\{ T_j \exp\left[i\left(k_{z,j+1} - k_{z,j}\right) z_j\right] + R_j f_r \tilde{r}_{j+1,j} \exp\left[i\left(k_{z,j+1} + k_{z,j}\right) z_j\right] \right\}. \tag{2.3.6}$$

The Fresnel coefficients are now modified to

$$\tilde{r}_{j+1,j} = \frac{f_j(k_{z,j+1} + k_{z,j})}{f_j(k_{z,j+1} - k_{z,j})}\, r_{j+1,j} \qquad \text{and} \qquad \tilde{t}_{j+1,j} = \frac{1}{f_j(k_{z,j+1} - k_{z,j})}\, t_{j+1,j} \tag{2.3.7}$$

with

$$f_r = \frac{f_j(k_{z,j+1} - k_{z,j})}{f_j(-k_{z,j+1} + k_{z,j})} \cdot \frac{f_j(-k_{z,j+1} - k_{z,j})}{f_j(k_{z,j+1} + k_{z,j})} \tag{2.3.8}$$

$$f_t = \frac{f_j(k_{z,j+1} - k_{z,j})}{f_j(-k_{z,j+1} + k_{z,j})}. \tag{2.3.9}$$

If the arguments are real, then $|f_r|$ and $|f_t| = 1$. In general, the $k_{z,j}$ terms have a large imaginary contribution in the range of the critical angle where absorption is important. However, in the X-ray regime the components f_r and f_t can indeed be approximated with 1.

We assume a continuous refractive index profile between layer j and $j+1$

$$n_j(z) = \frac{n_j + n_{j+1}}{2} - \frac{n_j - n_{j+1}}{2} \operatorname{erf}\left(\frac{z - z_j}{\sqrt{2}\sigma_j}\right) \tag{2.3.10}$$

and a Gaussian probability density ($\mu_j = 0$)

$$P_j(z) = \frac{1}{\sqrt{2\pi}\sigma_j} \exp\left(-\frac{z^2}{2\sigma_j^2}\right). \tag{2.3.11}$$

As a result, the Fresnel coefficients can be written as

$$\tilde{r}_{j,j+1} = r_{j,j+1} \exp\left(-2k_{z,j}k_{z,j+1}\sigma_j^2\right) \tag{2.3.12}$$

$$\tilde{t}_{j,j+1} = t_{j,j+1} \exp\left(\left(k_{z,j} - k_{z,j+1}\right)^2 \frac{\sigma_j^2}{2}\right). \tag{2.3.13}$$

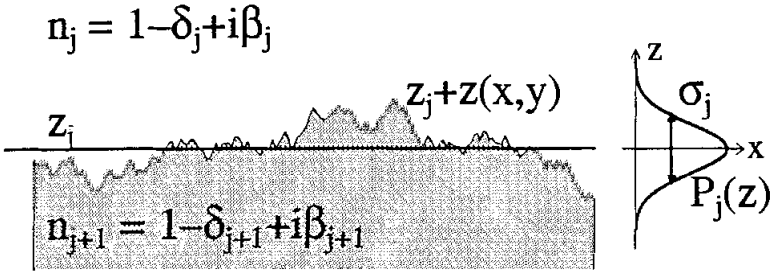

Figure 2.8: Rough surface with a mean value z_j and fluctuations of $z(x, y)$. The probability distribution $P_j(z)$ is displayed on the right (taken from [19]).

2.4 Mathematical description of rough interfaces

So far we concentrated on the specular signal only. However, the layers are not perfectly flat but contain a small roughness that gives rise to the lateral structure of the interfaces. These surfaces can be statistically described by the height-height correlation function $C_j(\boldsymbol{R})$ [23]

$$C_j(\boldsymbol{R}) = \langle \phi_j(\boldsymbol{r})\, \phi_j(\boldsymbol{r}+\boldsymbol{R}) \rangle_r \tag{2.4.1}$$

where j represents the j^{th} interface at position $z_j(\boldsymbol{R}) = z_j + \phi_j(\boldsymbol{R})$. Here $\boldsymbol{R} = (x, y)^T$ and $\boldsymbol{r}$ denote vectors in the surface and $\langle\rangle_r$ stands for the average over the (x, y) plane. $\phi_j(\boldsymbol{R})$ describes the height fluctuation of interface j at lateral position $\boldsymbol{R}$ with a mean value of $\langle \phi_j(\boldsymbol{r}) \rangle_r = 0$ and roughness of $\sigma_j = \sqrt{C_j(0)}$.
The most common correlation function $C_j(\boldsymbol{R})$ for solid states is the correlation function of a self-affine fractal surface given by

$$C_j(\boldsymbol{R}) = \sigma_j^2 \exp\left[-\left(\frac{\boldsymbol{R}}{\xi_j} \right)^{2h_j} \right], \tag{2.4.2}$$

where ξ denotes the correlation length. If $R < \xi_j$, the surface appears self-affine rough and for $R > \xi_j$ the surface appears smooth. h_j is the hurst parameter of the corresponding interface with values between 0 and 1. For small values of h_j the interfaces are extremely jagged while numbers close to 1 describe smooth changing interfaces. Fig. 2.9 and 2.10 display possible real-space structures for different hurst parameters and lateral correlation lengths. Fig. 2.9 shows various interfaces for a fixed lateral correlation length of $\xi = 1000\,\text{Å}$ and changing hurst parameter h. For $h = 0.8$ the interface looks rather smooth while for $h = 0.2$ we recognize a much more jagged surface. Fig. 2.10 illustrates various interfaces for a fixed hurst parameter $h = 0.8$ and varying lateral correlation lengths from $\xi = 25\,\text{Å}$ to $\xi = 500\,\text{Å}$. We notice that a smaller correlation length indicates a frequently changing surface that appears rough compared to a large correlation length.

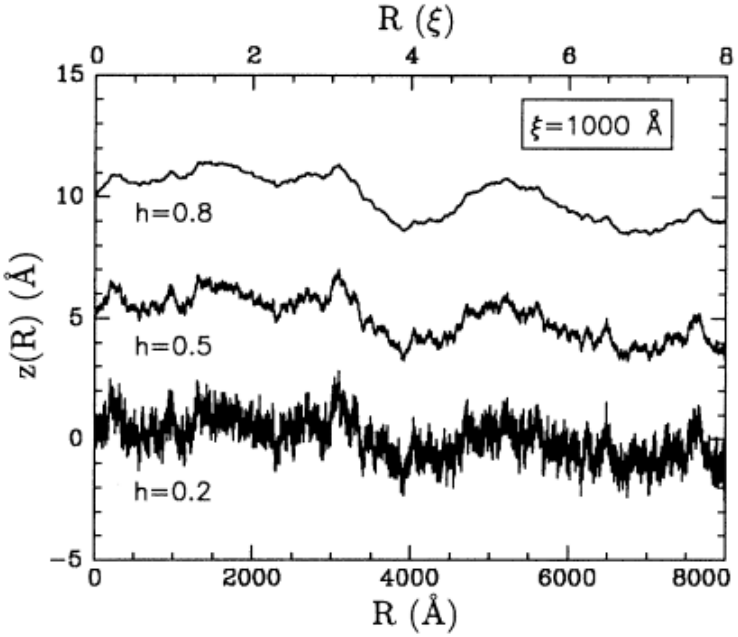

Figure 2.9: Interfaces with different hurst parameters h for a fixed lateral correlation length $\xi = 1000\,\text{Å}$. For $h = 0.8$ the profile along the interface is rather smooth while for $h = 0.2$ the interfaces is jagged (taken from [23]).

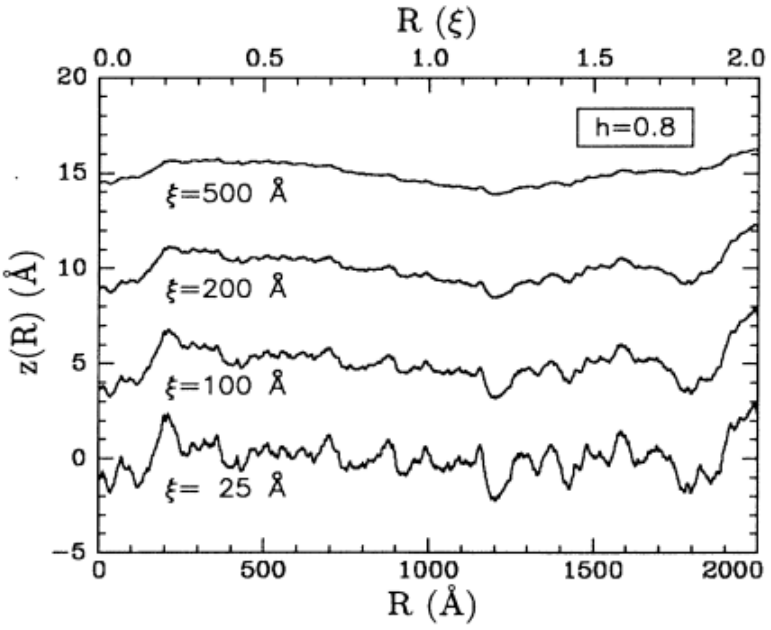

Figure 2.10: Interfaces with different lateral correlation lengths ξ for a fixed hurst parameter $h = 0.8$. A lateral correlation length $\xi = 500\,\text{Å}$ corresponds to a rather flat surface where the interface begins to look rough after 500 Å. A lateral correlation length of $\xi = 25\,\text{Å}$ implies a rather frequent changing interface (taken from [23]).

With more than one layer present the cross correlation functions

$$C_{jk}(\boldsymbol{R}) = \langle \phi_j(\boldsymbol{r})\, \phi_k(\boldsymbol{r}+\boldsymbol{R}) \rangle_r \tag{2.4.3}$$

have to be taken into account. The correlations of the roughness between the layers j and k at the positions z_j and z_k can be written as

$$C_{jk}(\boldsymbol{R}) = \frac{1}{2}\left[\frac{\sigma_k}{\sigma_j} C_j(\boldsymbol{R}) + \frac{\sigma_j}{\sigma_k} C_k(\boldsymbol{R})\right] \exp\left(-\frac{|z_j - z_k|}{\xi_{\perp,jk}}\right), \tag{2.4.4}$$

where $\xi_{\perp,jk}$ denotes the vertical correlation length meaning the distance until the correlations between j and k decay by a factor of $1/e$. If $\xi_{\perp,jk}$ is much larger than the layer thickness, the layers are perfectly correlated while $\xi_{\perp,jk} = 0$ describes completely uncorrelated interfaces [23]. Fig. 2.11 illustrates the cross correlation length (ξ_{jk}) and lateral correlation length (ξ_j, ξ_k) of two correlated interfaces while Fig. 2.12 displays these values with a small cross correlation between the interfaces.

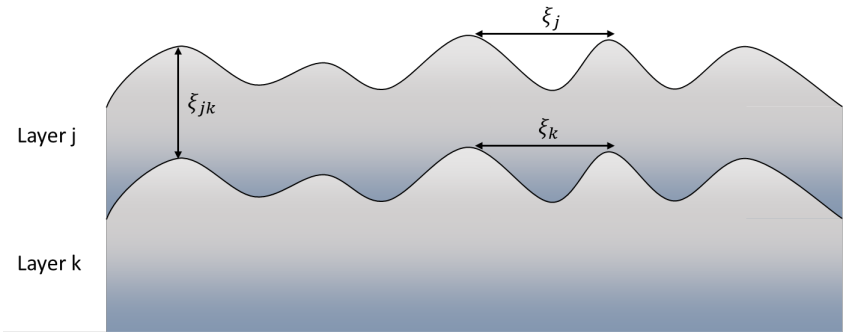

Figure 2.11: Highly correlated interfaces with cross correlation length ξ_{jk} and lateral correlation lengths ξ_j and ξ_k for layer j and k.

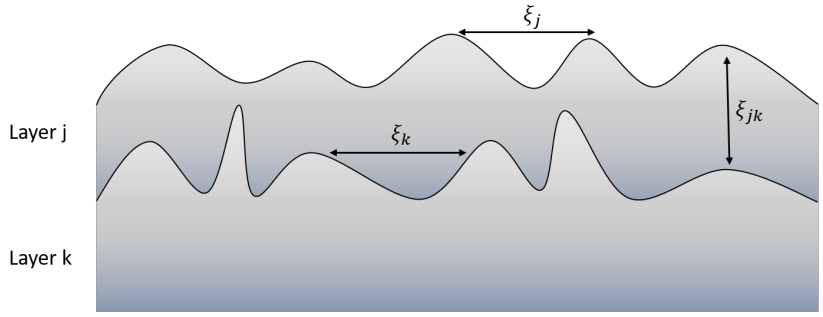

Figure 2.12: Weakly correlated interfaces with cross correlation length ξ_{jk} and lateral correlation lengths ξ_j and ξ_k for layer j and k.

2.5 Distorted Wave Born Approximation

Investigating interfaces of multilayers with X-ray reflectivity is a powerful technique to obtain electron densities, thicknesses and roughnesses of individual layers. However, more detailed information about the interface structure such as the in-plane correlation in a rough interface can be accessed by the analysis of the nonspecular scattering signal. The theoretical description of this nonspecular reflection is based on the distorted wave born approximation (DWBA). We write the wave equation as [17]

$$(\Delta + k^2)\,|\Psi\rangle = V(\boldsymbol{r})\,|\Psi\rangle \tag{2.5.1}$$

with the scattering potential $V(\boldsymbol{r})$

$$V(\boldsymbol{r}) = k^2\left[1 - n^2(\boldsymbol{r})\right]. \tag{2.5.2}$$

$k = \frac{2\pi}{\lambda}$ is the absolute value of the wavevector and $n(\boldsymbol{r})$ is the index of refraction [17]. The scattering potential can be expressed within the perturbation theory with $V^{(0)}(\boldsymbol{r})$ the potential of the undisturbed (flat) system and $V^{(1)}(\boldsymbol{r})$ the small perturbation because of the interface roughness:

$$V(\boldsymbol{r}) = V^{(0)}(\boldsymbol{r}) + V^{(1)}(\boldsymbol{r}). \tag{2.5.3}$$

Within the DWBA the averaged differential cross section from a random system is written as

$$\frac{\mathrm{d}\sigma}{\mathrm{d}\Omega} = \frac{\langle|V_{if}^{(0)} + V_{if}^{(1)}|^2\rangle}{16\pi^2}. \tag{2.5.4}$$

$V_{if}^{(0)} = \langle\Psi_f|V^{(0)}|\phi_i\rangle$ is the transition matrix element of the unperturbed system while $V_{if}^{(1)} = \langle\Psi_f|V^{(1)}|\Psi_i\rangle$ represents its perturbation. This small perturbation causes the probability of a transition from state $|\Psi_i\rangle$ to $|\Psi_f\rangle$ with $\boldsymbol{k_i} \neq \boldsymbol{k_f}$ (see Eq. (2.5.6) and (2.5.7)) meaning that only the roughness generates the nonspecular scattering contribution [17]. The incident state is a plane wave

$$|\phi_i\rangle = \exp(i\boldsymbol{k_i}\boldsymbol{r}) \tag{2.5.5}$$

and

$$|\Psi_i\rangle = T_i(z)\,\exp\left[i\boldsymbol{k_i}(z)\boldsymbol{r}\right] + R_i(z)\,\exp\left[i\boldsymbol{k_i'}(z)\boldsymbol{r}\right] \tag{2.5.6}$$

$$|\tilde{\Psi}_f\rangle = T_f^*(z)\exp\left[i\boldsymbol{k_f^*}(z)\boldsymbol{r}\right] + R_f^*(z)\exp\left[i\boldsymbol{k_f'^*}(z)\boldsymbol{r}\right] \tag{2.5.7}$$

are two independent eigenstates of the unperturbed system. $R_{i,f}$ and $T_{i,f}$ denote the complex amplitudes of the reflected and transmitted beams for the states i and f and $\boldsymbol{k_{i,f}}$ their wavevectors.
The differential cross section from Eq. (2.5.4) can be split into the specular and the diffuse part

$$\frac{\mathrm{d}\sigma}{\mathrm{d}\Omega} = \left(\frac{\mathrm{d}\sigma}{\mathrm{d}\Omega}\right)_{\mathrm{spec}} + \left(\frac{\mathrm{d}\sigma}{\mathrm{d}\Omega}\right)_{\mathrm{diff}} \tag{2.5.8}$$

with

$$\left(\frac{\mathrm{d}\sigma}{\mathrm{d}\Omega}\right)_{\mathrm{spec}} = \frac{|V_{if}^{(0)} + \langle V_{if}^{(1)}\rangle|^2}{16\pi^2} \tag{2.5.9}$$

$$\left(\frac{\mathrm{d}\sigma}{\mathrm{d}\Omega}\right)_{\mathrm{diff}} = \frac{\langle|V_{if}^{(1)}|^2\rangle - |\langle V_{if}^{(1)}\rangle|^2}{16\pi^2}. \tag{2.5.10}$$

The matrix elements for the diffuse scattering can be calculated with the help of DWBA to [23]

$$\begin{aligned}\left(\frac{\mathrm{d}\sigma}{\mathrm{d}\Omega}\right)_{\mathrm{diff}} = \frac{\mathcal{G}k_1^2}{16\pi^2} \sum_{j,k=1}^{N} \left(n_j^2 - n_{j+1}^2\right)\left(n_k^2 - n_{k+1}^2\right)^* \mathcal{C}_{jk}(Q_r) \\ \cdot \sum_{m,n=0}^{3} \tilde{G}_j^m \, \tilde{G}_k^{n*} \exp\left[-\frac{1}{2}\left[(Q_{z,j}^m \sigma_j)^2 + (Q_{z,k}^{n*}\sigma_k)^2\right]\right].\end{aligned} \tag{2.5.11}$$

$\mathcal{G}$ denotes the irradiated area of the sample and $\boldsymbol{Q_j^m} = (\boldsymbol{Q_r}, Q_{z,j}^m)^T$ the momentum transfer within each layer. $\mathcal{C}_{jk}(Q_r)$ represents the Fourier transform of the cross-correlation function of the interfaces. The values $\tilde{G}_j^m = G_j^m \exp\left(-iQ_{z,j}^m z_j\right)$ can have four different expressions due to analytic continuations of the wavefunctions at the interfaces. However, only the solutions given in Table 2.1 fulfill Eq. (2.5.11) because only these two are invariant against an exchange of $\boldsymbol{k_i}$ and $\boldsymbol{k_f}$. Solution I leads to the results from [17] and [24].

Solution I		Solution II	
$G_j^0 = T_{i,j+1}\, T_{f,j+1}$	$\boldsymbol{Q_j^0 = k_{i,j+1} + k_{f,j+1}}$	$G_j^0 = T_{i,j}\, T_{f,j}$	$\boldsymbol{Q_j^0 = k_{i,j} + k_{f,j}}$
$G_j^1 = T_{i,j+1}\, R_{f,j+1}$	$\boldsymbol{Q_j^1 = k_{i,j+1} - k_{f,j+1}}$	$G_j^1 = T_{i,j}\, R_{f,j}$	$\boldsymbol{Q_j^1 = k_{i,j} - k_{f,j}}$
$G_j^2 = R_{i,j+1}\, T_{f,j+1}$	$\boldsymbol{Q_j^2 = -Q_j^1}$	$G_j^2 = R_{i,j}\, T_{f,j}$	$\boldsymbol{Q_j^2 = -Q_j^1}$
$G_j^3 = R_{i,j+1}\, R_{f,j+1}$	$\boldsymbol{Q_j^3 = -Q_j^0}$	$G_j^3 = R_{i,j}\, R_{f,j}$	$\boldsymbol{Q_j^3 = -Q_j^0}$

Table 2.1: Two possible solutions for G_j^m and their corresponding wavevectors Q_j^m. Solution I was selected in [17] and [24] (taken from [23]).

Eq. (2.5.11) can be written as [19]

$$I_{\text{diff}}(\boldsymbol{Q}) = \frac{\mathcal{G}k_1^2}{8\pi^2} \sum_{j,k=1}^{N} \left(n_j^2 - n_{j+1}^2\right) \left(n_k^2 - n_{k+1}^2\right)^* \cdot \sum_{m,n=0}^{3} \tilde{G}_j^m \tilde{G}_k^{n*} \exp\left[-\frac{1}{2}\left[\left(Q_{z,j}^m\, \sigma_j\right)^2 + \left(Q_{z,k}^{n*}\, \sigma_k\right)^2\right]\right] S_{jk}^{mn}(\boldsymbol{Q}) \tag{2.5.12}$$

with the scattering function $S_{jk}^{mn}(\boldsymbol{Q})$

$$S_{jk}^{mn}(\boldsymbol{Q}) = \frac{1}{Q_{z,j}^m\, Q_{z,k}^{n*}} \int \left(\exp\left(Q_{z,j}^m\, Q_{z,k}^{n*} C_{jk}(\boldsymbol{R})\right) - 1\right) \exp\left(-i\boldsymbol{Q}_\parallel \boldsymbol{R}\right)\, \mathrm{d}\boldsymbol{R}. \tag{2.5.13}$$

$\boldsymbol{Q}_\parallel = (0,0)$ denotes the wavevector transfer for the specular reflection. For small $\boldsymbol{Q}$ we can apply a Taylor expansion to the exponential in Eq. (2.5.13) and obtain

$$S_{jk}^{mn}(\boldsymbol{Q}) = \frac{1}{Q_{z,j}^m\, Q_{z,k}^{n*}} \int \left(Q_{z,j}^m\, Q_{z,k}^{n*} C_{jk}(\boldsymbol{R})\right) \exp\left(-i\boldsymbol{Q}_\parallel \boldsymbol{R}\right)\, \mathrm{d}\boldsymbol{R}. \tag{2.5.14}$$

For the diffuse scattering the intensity of a single layer can be described by [24]

$$I_{\text{diff}} \propto \left|t_i(\alpha_i)\right|^2 S(\boldsymbol{Q_t}) \left|t_f(\alpha_f)\right|^2 \tag{2.5.15}$$

with the Fresnel transmission coefficients $t_i(\alpha_i)$ and $t_f(\alpha_f)$

$$t_i(\alpha_i) = \frac{2k_{i,z}}{k_{i,z} + k_{t,z;i}}, \qquad t_f(\alpha_f) = \frac{2k_{f,z}}{k_{f,z} + k_{t,z;f}}. \tag{2.5.16}$$

2.6 Grazing-incidence X-ray diffuse scattering

Grazing-incidence X-ray diffuse scattering (XDS) is a method to investigate thin films using that the incident beam is totally external reflected from the substrate resulting in a small-angle scattering of the refracted beam by a thin layer [25]. The method of XDS yields information about internal structures of thin films in addition to top surface structures of films and substrates [26].

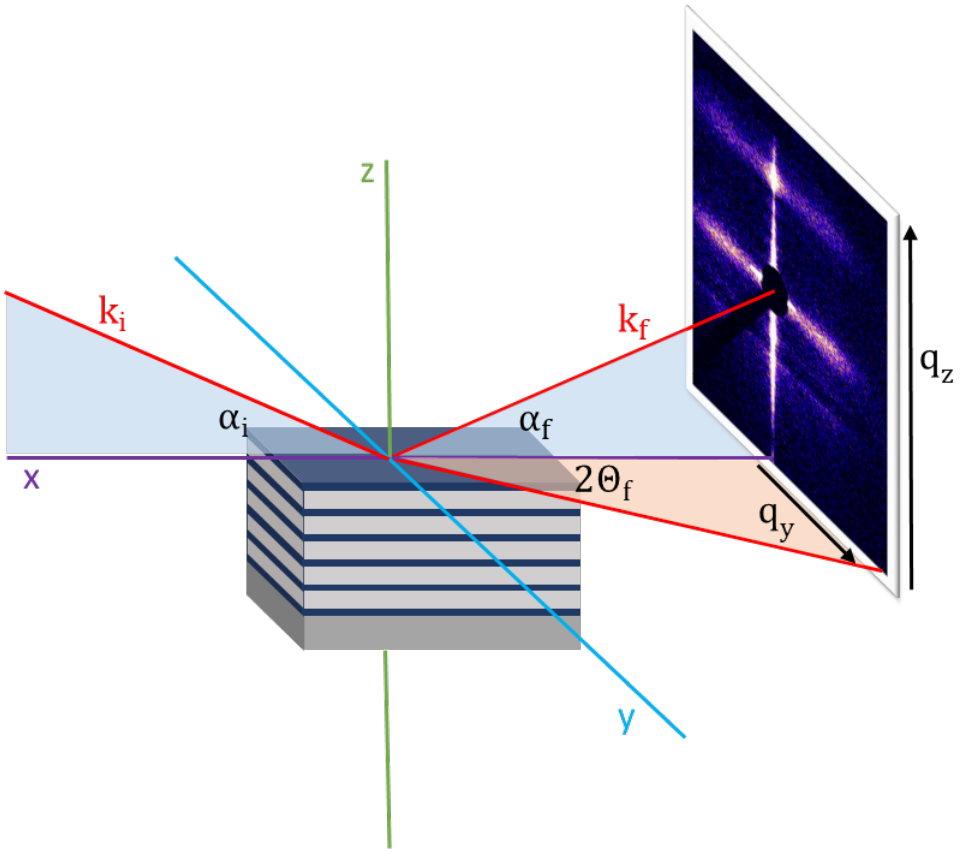

Figure 2.13: Basic principle of XDS. An incident beam impinges on a sample at angle α_i and is reflected from the surface. Due to small roughness effects we see not only the specular reflected beam but a signal that covers the full 2D range $(\alpha_f, 2\theta_f)$ (adapted from [26]).

Fig. 2.13 displays the geometry of XDS. A monochromatic X-ray beam with wavevector $\boldsymbol{k_i}$ impinges on a sample at very small angle α_i along the x-direction. The X-ray beam is scattered in $\boldsymbol{k_f}$ direction with $\boldsymbol{k_f}$ depending on $2\theta_f$ and α_f. The wavevector transfer $\boldsymbol{Q}$ is defined as the difference between incident and exit wavevector

$$\boldsymbol{Q} = \boldsymbol{k_f} - \boldsymbol{k_i}. \tag{2.6.1}$$

For the XDS geometry the scattering vector $\boldsymbol{Q}$ can be written as

$$\boldsymbol{Q} = \frac{2\pi}{\lambda} \begin{pmatrix} \cos(\alpha_f)\cos(2\theta_f) - \cos(\alpha_i) \\ \cos(\alpha_f)\sin(2\theta_f) \\ \sin(\alpha_f) + \sin(\alpha_i) \end{pmatrix}. \tag{2.6.2}$$

An 2D XDS example pattern (see Fig. 2.14) can be simulated with the program BornAgain [78] using a 20 nm thick Ta layer on a silicon substrate with a fixed cross correlation length of $\xi_{cc} = 200\,\text{nm}$, a hurst parameter of $h = 0.3$, rms roughness of $\sigma = 0.6\,\text{nm}$ and a lateral correlation length of $\xi_L = 30\,\text{nm}$. The detector area was chosen to be equal to the experimental setup.

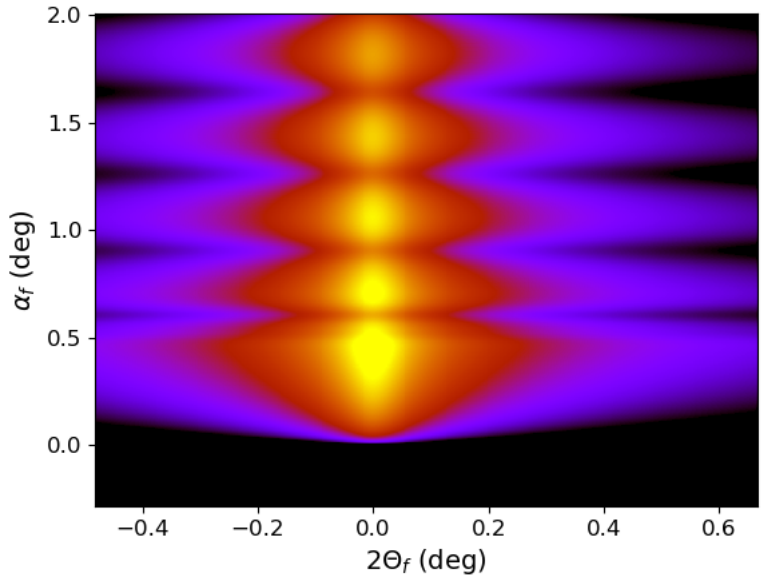

Figure 2.14: 2D XDS pattern for a 20 nm Ta layer on Si substrate with a cross correlation length $\xi_{cc} = 200\,\text{nm}$, lateral correlation length $\xi_L = 30\,\text{nm}$, rms roughness $\sigma = 0.6\,\text{nm}$ and hurst parameter $h = 0.3$ simulated with BornAgain.

2.7 Examples of scattering intensities

In the following we show examples of the influence of lateral correlation length ξ_L, hurst parameter h and cross correlation length ξ_{cc} on X-ray scattering profiles. For this purpose we performed calculations using BornAgain with a 20 nm thick Ta layer on a silicon substrate with a fixed cross correlation length of $\xi_{cc} = 200\,\text{nm}$, a hurst parameter of $h = 0.3$ and a rms roughness of $\sigma = 0.6\,\text{nm}$.
In a first step we vary the lateral correlation length ξ_L from 5 nm to 50 nm (Fig. 2.15, 2.16) and recognize that the increase of lateral correlations implies an intensity increase in the Q_z and the Q_y direction. Additionally, the intensity decay in the Q_y direction starts at smaller Q_y values for increasing the lateral correlation length, e.g. for $\xi_L = 5\,\text{nm}$ we find the decrease starting at $Q_y = 5 \times 10^{-2}\,\text{nm}^{-1}$ while for $\xi_L = 50\,\text{nm}$ the decay starts at $Q_y = 4 \times 10^{-3}\,\text{nm}^{-1}$.

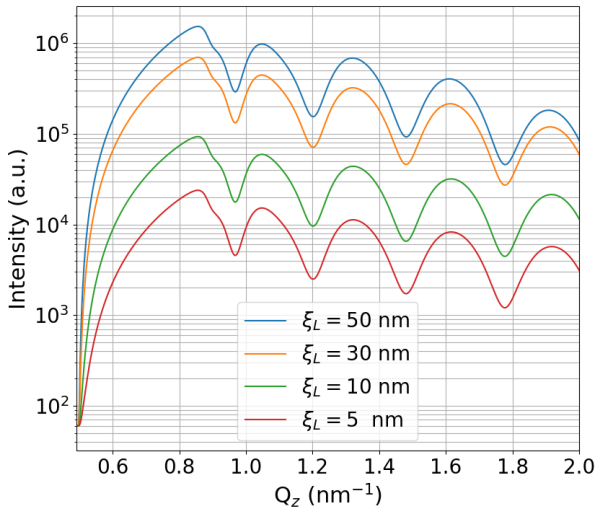

Figure 2.15: Off-specular signal in Q_z direction for a 20 nm Ta layer on Si substrate with a fixed cross correlation length $\xi_{cc} = 200\,\text{nm}$, a hurst parameter $h = 0.3$, rms roughness $\sigma = 0.6\,\text{nm}$ and varying lateral correlation ξ_L.

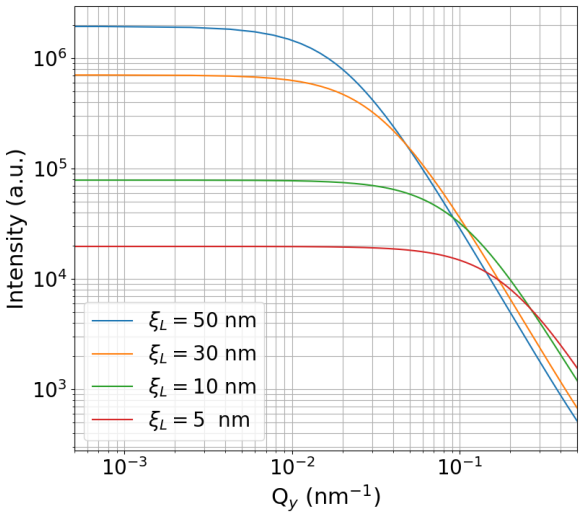

Figure 2.16: Off-specular signal in Q_y direction for a 20 nm Ta layer on Si substrate with a fixed cross correlation length $\xi_{cc} = 200\,\text{nm}$, a hurst parameter $h = 0.3$, rms roughness $\sigma = 0.6\,\text{nm}$ and varying lateral correlation ξ_L.

As a second example we fix the lateral correlation length ξ_L to 30 nm and vary the hurst parameter h from 0.1 to 1 as illustrated in Fig. 2.17 and 2.18. We find that an increasing hurst parameter results in an increased intensity in both Q directions. In the Q_y direction we also see a difference in the decay meaning that an increasing hurst parameter h results in a stronger decaying intensity for $Q_y > 0.03\,\text{nm}^{-1}$.

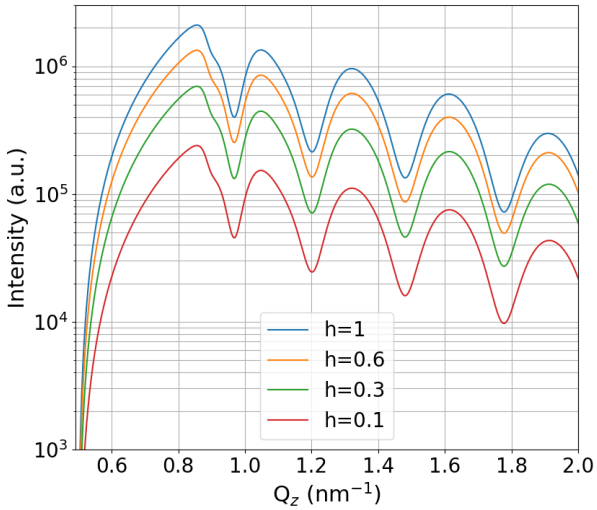

Figure 2.17: Off-specular signal in Q_z direction for a 20 nm Ta layer on Si substrate with a fixed cross correlation length $\xi_{cc} = 200\,\text{nm}$, a lateral correlation length $\xi_L = 30\,\text{nm}$, rms roughness $\sigma = 0.6\,\text{nm}$ and varying hurst parameter h.

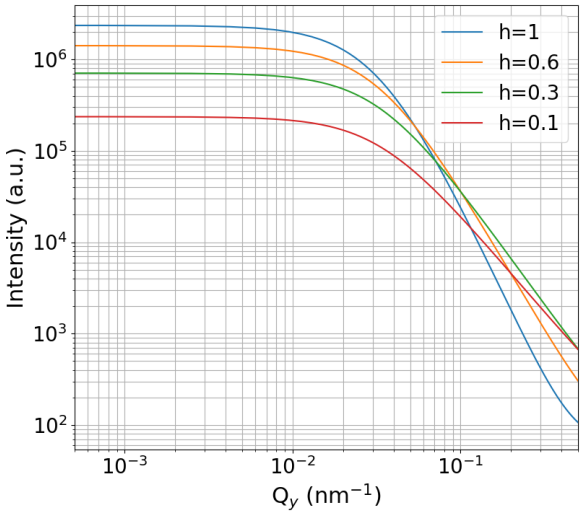

Figure 2.18: Off-specular signal in Q_y direction for a 20 nm Ta layer on Si substrate with a fixed cross correlation length $\xi_{cc} = 200\,\text{nm}$, a lateral correlation length $\xi_L = 30\,\text{nm}$, rms roughness $\sigma = 0.6\,\text{nm}$ and varying hurst parameter h.

Finally. we vary the cross correlation length ξ_{cc} from $\xi_{cc} = 200\,\text{nm}$ to $\xi_{cc} = 5\,\text{nm}$ (Fig. 2.19, 2.20) and find a significant change in the Q_z direction. If the cross correlation length gets smaller than the sample thickness, the Kiessig fringes start to vanish until we cannot recognize any structure in the scattering signal anymore. Note that the Yoneda peak intensity at $Q_z = 0.87\,\text{nm}^{-1}$ is not affected by the decreasing cross correlation length as it is attributed to the density from the surface only. In the Q_y direction the change of cross correlation lengths has just a minor effect.
Summarizing these effects we identify that the change of the lateral correlation length ξ_L defines the position of the shoulder in the Q_y direction while the hurst parameter h changes the slope of the decay in Q_y direction. The cross correlation length has an important effect on the signal in Q_z direction. We only see the scattering features, if the cross correlation length is as large as the sample.

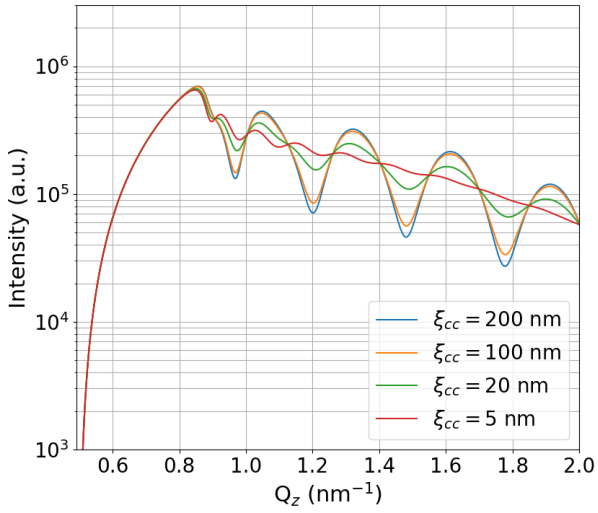

Figure 2.19: Off-specular signal in Q_z direction for a 20 nm Ta layer on Si substrate with a fixed lateral correlation length $\xi_L = 30$ nm, rms roughness $\sigma = 0.6$ nm, hurst parameter $h = 0.3$ and varying cross correlation length ξ_{cc}.

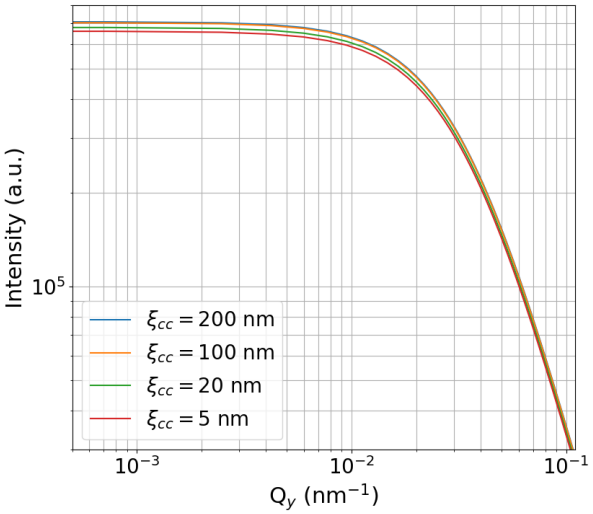

Figure 2.20: Off-specular signal in Q_y direction for a 20 nm Ta layer on Si substrate with a fixed lateral correlation length $\xi_L = 30$ nm, rms roughness $\sigma = 0.6$ nm, hurst parameter $h = 0.3$ and varying cross correlation length ξ_{cc}.

2.8 Out-of-plane scattering

The diffuse scattering function for self-affine surfaces is given by [24]

$$S_{\text{diff}}(Q) = \frac{2\pi}{Q_z^2} \exp(-Q_z^2\sigma^2) \int_0^\infty \mathrm{d}R \; RF(Q_z, R) J_0(Q_r R) \tag{2.8.1}$$

with

$$F(Q_z, R) = \exp(Q_z^2\sigma^2 \exp(-(R/\xi_L)^{2h})) - 1. \tag{2.8.2}$$

Since $Q_y \gg Q_x$ we can simplify $Q_r = \sqrt{Q_x^2 + Q_y^2}$ to $Q_r \approx Q_y$ and result in

$$S_{\text{diff}}(Q) = \frac{2\pi}{Q_z^2} \exp(-Q_z^2\sigma^2) \int_0^\infty \mathrm{d}R \; RF(Q_z, R) J_0(Q_y R). \tag{2.8.3}$$

In Fig. 2.21 we show the diffuse scattering function S_{diff} as a function of Q_y for different Q_z values and a fixed lateral correlation length $\xi_L = 8\,\text{nm}$, hurst parameter $h = 0.8$ and rms roughness $\sigma = 0.6\,\text{nm}$. The scattering functions of the four different Q_z values differ only in intensity but have same shapes.

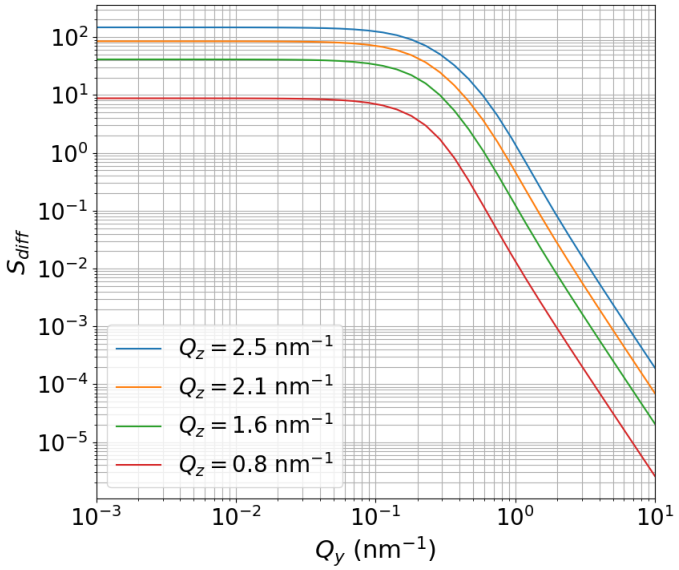

Figure 2.21: Diffuse scattering function S_{diff} as a function of Q_y with varying Q_z and fixed $\sigma = 0.6\,\text{nm}$, $\xi = 8\,\text{nm}$ and $h = 0.8$.

For small Q_y values the scattering function remains constant and then starts to decay starting from $Q_y = 3 \times 10^{-1}\,\mathrm{nm}^{-1}$ following a power law of (numerical evaluation of Eq. (2.8.2) and (2.8.3))

$$S_{\mathrm{diff}} \sim \frac{1}{Q_y^m}. \tag{2.8.4}$$

The exponent m is then a function of

$$m \sim -\log_{10}(S_{\mathrm{diff}} \cdot Q_y) \tag{2.8.5}$$

and depends on the Q_z value, the rms roughness σ, the lateral correlation length ξ_L and the hurst parameter h. Fig. 2.22 illustrates the exponent m as a function of the hurst parameter h for different Q_z values and fixed lateral correlation length $\xi_L = 8\,\mathrm{nm}$ and rms roughness $\sigma = 0.6\,\mathrm{nm}$. We note that the exponent m decreases for increasing hurst parameter h. A decreasing Q_z value corresponds to the smaller slope of the exponent. For a hurst parameter $h \approx 0.7$ the exponent is equal for all Q_z values.
Using a larger roughness of $\sigma = 1.5\,\mathrm{nm}$ (Fig. 2.23) we notice that m is increasing, e.g. from -1.8 to -1.0 for $Q_z = 2.1\,\mathrm{nm}^{-1}$. The increased roughness of 1.5 nm implies that the exponents m indicate a larger variation, e.g. for $h = 0.4$ the exponent is varying between $m = -0.7$ and $m = -1.9$.

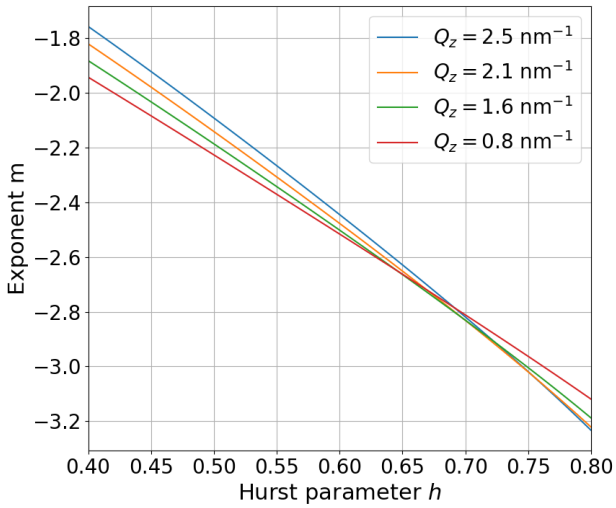

Figure 2.22: Exponent m as a function of the hurst parameter h for different Q_z values and a fixed lateral correlation length $\xi = 8\,\mathrm{nm}$, rms roughness $\sigma = 0.6\,\mathrm{nm}$ for a single interface.

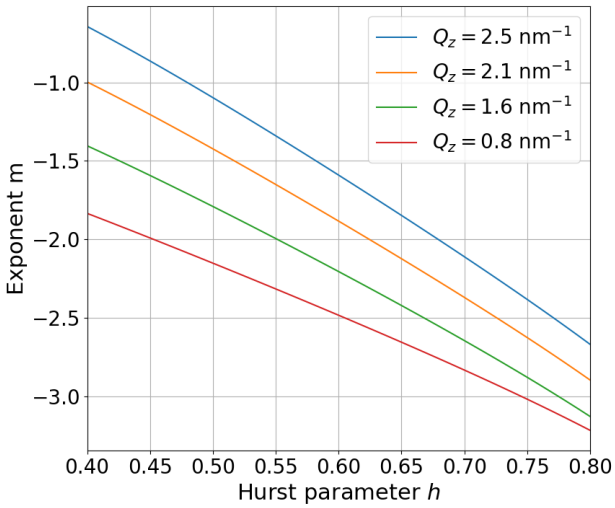

Figure 2.23: Exponent m as a function of the hurst parameter h for different Q_z values and a fixed lateral correlation length $\xi = 8\,\mathrm{nm}$, rms roughness $\sigma = 1.5\,\mathrm{nm}$ for a single interface.

Chapter 3

Theory of plasma dynamics

This thesis primarily focuses on the analysis of X-ray scattering data. However, for reasons of completeness the fundamental effects of plasma dynamics will be explained in this chapter. In section 3.1, we shortly describe the basic equations of motion of an electron in an electromagnetic plane wave. In section 3.2, we show the most important phenomena of laser matter interaction in overdense plasmas.

3.1 Motion of an electron in an electromagnetic plane wave

Plasma is one of the four states of matter and consists of a gas of ions and free electrons. In our X-ray diffuse scattering experiment, we are sensitive to dispersion profile directly connected to the electron density. The motion of a single electron travelling through an electromagnetic field $\boldsymbol{E}$ and $\boldsymbol{B}$ is experiencing the Lorentz force [1]

$$\frac{\mathrm{d}\boldsymbol{p}}{\mathrm{d}t} = -e\left(\boldsymbol{E} + \frac{1}{c}\boldsymbol{v} \times \boldsymbol{B}\right) \tag{3.1.1}$$

with momentum $\boldsymbol{p} = \gamma m \boldsymbol{v}$ and the relativistic factor $\gamma = \sqrt{1 + \frac{p^2}{m^2 c^2}}$. By determining the dot product we yield the energy equation

$$\frac{\mathrm{d}}{\mathrm{d}t}\left(\gamma m c^2\right) = -e\left(\boldsymbol{v} \cdot \boldsymbol{E}\right). \tag{3.1.2}$$

An elliptically polarized plane wave $\boldsymbol{A}(\omega, \boldsymbol{k})$ that travels into the positive x-direction is described by

$$\boldsymbol{A} = \begin{pmatrix} 0 \\ \delta a_0 \cos\phi \\ \sqrt{1-\delta^2}\, a_0 \sin\phi \end{pmatrix} \tag{3.1.3}$$

with the phase $\phi = \omega t - kx$, the normalized amplitude a_0 and the polarization parameter $\delta = \{\pm 1, 0\}$ for linear polarization and $\delta = \pm 1/\sqrt{2}$ for circular polarization. In the following we use the normalizations

$$\begin{aligned} t &\to \omega t \\ x &\to kx \\ \boldsymbol{v} &\to \frac{\boldsymbol{v}}{c} \\ \boldsymbol{p} &\to \frac{\boldsymbol{p}}{mc} \\ \boldsymbol{A} &\to \frac{e\boldsymbol{A}}{mc^2}. \end{aligned} \tag{3.1.4}$$

With $\boldsymbol{E} = -\frac{\partial \boldsymbol{A}}{\partial t}$ and $\boldsymbol{B} = \boldsymbol{\nabla} \times \boldsymbol{A}$ the perpendicular part of the momentum $\boldsymbol{p}_\perp$ in Eq. (3.1.1) can be written as

$$\frac{\mathrm{d}\boldsymbol{p}_\perp}{\mathrm{d}t} = \frac{\mathrm{d}\boldsymbol{A}}{\mathrm{d}t} + v_x \frac{\mathrm{d}\boldsymbol{A}}{\mathrm{d}x}. \tag{3.1.5}$$

Integration yields

$$\boldsymbol{p}_\perp - \boldsymbol{A} = \boldsymbol{p}_{\perp \boldsymbol{0}} \tag{3.1.6}$$

with the initial perpendicular momentum of the electrons $\boldsymbol{p}_{\perp \boldsymbol{0}}$. Taking the longitudinal components of Eq. (3.1.1) and (3.1.2) into account we get

$$\frac{\mathrm{d}p_x}{\mathrm{d}t} - \frac{\mathrm{d}\gamma}{\mathrm{d}t} = -v_y \left(\frac{\partial A_y}{\partial t} + \frac{\partial A_y}{\partial x} \right) - v_z \left(\frac{\partial A_z}{\partial t} + \frac{\partial A_z}{\partial x} \right). \tag{3.1.7}$$

Integration results in

$$\gamma - p_x = \alpha \tag{3.1.8}$$

where α is a constant of motion which has to be determined. With $\gamma^2 - p_x^2 - p_\perp^2 = 1$ and assuming $\boldsymbol{p}_\perp = 0$, we obtain a connection between longitudinal and perpendicular momenta

$$p_x = \frac{1 - \alpha^2 + p_\perp^2}{2\alpha}. \tag{3.1.9}$$

This is the general solution for the motion of free electrons in the presence of an electromagnetic field [27]. To determine α we integrate Eq. (3.1.6) and (3.1.9). With

$$\frac{\mathrm{d}\phi}{\mathrm{d}t} = \frac{\partial \phi}{\partial t} + \frac{p_x}{\gamma} \frac{\partial \phi}{\partial x} = \frac{\alpha}{\gamma} \tag{3.1.10}$$

one obtains

$$\boldsymbol{p} = \gamma \frac{\mathrm{d}\boldsymbol{r}}{\mathrm{d}t} = \gamma \frac{\mathrm{d}\phi}{\mathrm{d}t} \frac{\mathrm{d}\boldsymbol{r}}{\mathrm{d}\phi} = \alpha \frac{\mathrm{d}\boldsymbol{r}}{\mathrm{d}\phi}. \tag{3.1.11}$$

With Eq. (3.1.11) we can determine the electron orbits, e.g. in laboratory frame or in average rest frame as illustrated in Fig. 3.1.

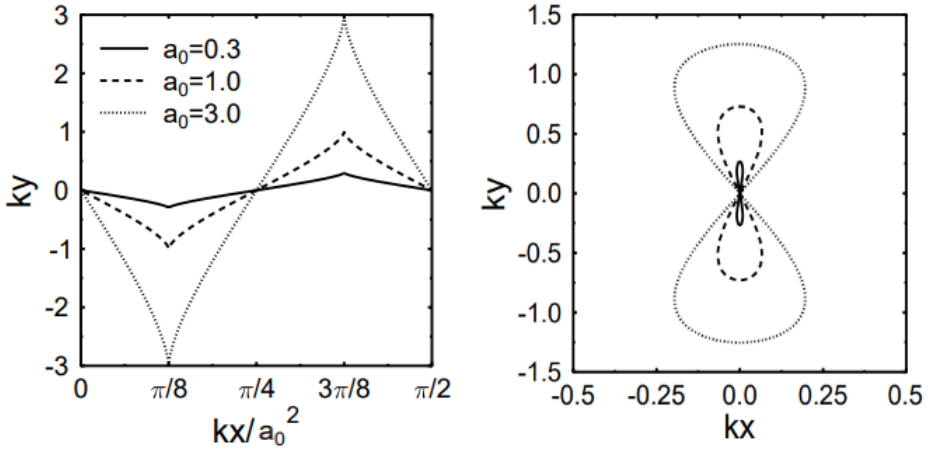

Figure 3.1: left: Electron orbits in a linearly polarized plane wave in laboratory frame for different normalized amplitudes a_0. right: Electron orbits in a linearly polarized plane wave in average rest frame for different relative laser pump strengths a_0 (taken from [1]).

3.2 Interaction with solids: overdense plasmas

In practice we do not investigate single electrons but more complex systems as metals which require a more complex description since several phenomena (described in this section) contribute depending on the laser intensity that can vary over seven orders of magnitude. Additionally, the physics of classical laser-plasmas are no longer valid for short-pulse interactions. In this section, we will briefly discuss the most important effects of short-pulse laser interactions in overdense plasmas.

3.2.1 Ionization

Field ionization due to laser excitation creates a surface plasma with a density n_{free} that is much larger than the critical density n_c which is the density where the plasma becomes opaque for electromagnetic waves with frequency ω. This relation can be described by

$$\omega^2 = \frac{4\pi e^2 n_c}{m} \tag{3.2.1}$$

with e the electron charge and m the electron mass. For the experiments described in this thesis this implies a critical density of $n_c \approx 8.8 \times 10^{20}\,\mathrm{cm}^{-3}$. The free electron density produced due to laser excitation is expressed as

$$n_{\mathrm{free}} = Z^* n_i = \frac{Z^* N_A\,\rho}{A} \tag{3.2.2}$$

where Z^* denotes the effective ion charge, N_A the Avogadro number, ρ the density and A the atomic number. Here, the free electron density is on the order of $10^{23}\,\mathrm{cm}^{-3}$.
For high density plasmas a local thermal equilibrium (LTE) is achieved, thus the ionization states can be treated as a statistical process. The relative ion populations can be calculated with the help of the Saha-Boltzmann equation [28]

$$\frac{n_{\mathrm{free}} n_{Z+1}}{n_Z} = \frac{g_{Z+1}}{g_Z}\frac{2m^3}{h^3}\left(\frac{2\pi T_e}{m}\right)^{\frac{3}{2}} \exp\left(-\frac{\Delta E_Z}{T_e}\right) \tag{3.2.3}$$

with the ion densities n_Z, n_{Z+1} belonging to the respective ionization states Z and $Z+1$. g_Z and g_{Z+1} denote the according statistical weights and ΔE_Z represents the energy difference between these states. Eq. (3.2.3) is only valid for

$$\sum_Z n_Z = n_0, \qquad \sum_Z Z n_Z = n_{\mathrm{free}}, \tag{3.2.4}$$

which provides the relative proportions of ions and the net electron density as a function of temperature. However, due to short pulse laser irradiation optically thin plasmas are produced that cover a range of several orders of magnitude in density and temperature. This situation is called non-LTE and needs to be solved with time-dependent atomic rate equations to find the charge distribution according to

$$\frac{\mathrm{d}n_Z}{\mathrm{d}t} = n_{\mathrm{free}} n_{Z-1} S(Z-1) - n_{\mathrm{free}} n_Z \left[S(Z) + \alpha(Z)\right] + n_{\mathrm{free}} n_{Z+1}\alpha(Z+1). \tag{3.2.5}$$

$S(Z)$ denotes the ionization rate and $\alpha(Z)$ the recombination rate as a function of the ion charge state Z, respectively. $\alpha(Z)$ generally has different contributions as radiative, 3-body collisional and dielectric recombination. For high Z elements this equation becomes quite difficult and is not analytically solvable anymore, also because $S(Z)$ or $\alpha(Z)$ often unknown. In practice, approximation models with a reduced number of equations are used such as [29–31].

3.2.2 Collisional absorption

Because of the short pulse duration an underdense region is formed at the surface by ablation with an ablation velocity

$$c_s = \sqrt{\frac{Z^* k_B T_e}{m_i}} \tag{3.2.6}$$

on the order of the sound velocity. Here, k_B denotes the Boltzmann constant, T_e is the electron temperature and m_i the ion mass. For an isothermal expansion of the plasma [32] the density profile will decrease exponentially with a length scale of

$$L = c_s \tau_L \approx 3 \left(\frac{T_e}{\mathrm{keV}}\right)^{1/2} \left(\frac{Z^*}{A}\right) \tau_{fs} \text{ Å} \tag{3.2.7}$$

with τ_L the laser pulse duration. Assuming a 40 fs Ti:sapphire laser heats the target to 20 eV with $A = 181$ and $Z^* = 2$ results in a length scale of $L \approx 1.2$ Å meaning that the prepulse created by amplified spontaneous emission is so small so that the surface remains unperturbed until the main pulse arrives at the sample [1]. The main laser pulse impinges on the plasma surface behaving as a mirror-like wall. The electromagnetic field is forming a standing wave in front of the target while an evanescent wave penetrates the overdense plasma region up to a skin depth l_s of

$$l_s = \frac{c}{\omega_p}, \tag{3.2.8}$$

that is on the order of several nanometers.
To calculate the absorption coefficient for arbitrarily shaped density profiles the Helmholtz equations for electromagnetic wave propagation in an inhomogeneous plasma need to be solved

$$\frac{\partial^2 E_z}{\partial x^2} + k^2(\epsilon(x) - \sin^2\theta) E_z = 0 \tag{3.2.9}$$

where

$$\epsilon(x) = n^2(x) = 1 - \frac{n_0(x)/n_c}{1 + i\frac{\nu_{ei}}{\omega}} \tag{3.2.10}$$

is the dielectric constant of the medium. ν_{ei} represents the electron-ion collision frequency [32,33]. It is important that the wave modes are transverse only following that there is no coupling between s-polarized EM waves and electrostatic modes.

In a next step we consider a p-polarized wave $\boldsymbol{E_1} = (E_x, E_y, 0)$ with $\boldsymbol{\nabla} \cdot \boldsymbol{E_1} \neq 0$ (see Fig. 3.2) meaning that a component of the laser field points in the same direction as the density gradient implying that there occur driven plasma waves along the light path. With this assumption we obtain the Helmholtz equation for the magnetic field B

$$\frac{\partial^2 B_z}{\partial x^2} - \frac{1}{\epsilon}\frac{\partial \epsilon}{\partial x}\frac{\partial B_z}{\partial x} + k^2(\epsilon - \sin^2\theta)B_z = 0. \tag{3.2.11}$$

For lasers with pulse durations in the femtosecond regime it is $kL \ll 1$ implying that no analytical solution of Eq. (3.2.11) is possible. However, numerical solutions are presented e.g. in [35–38].

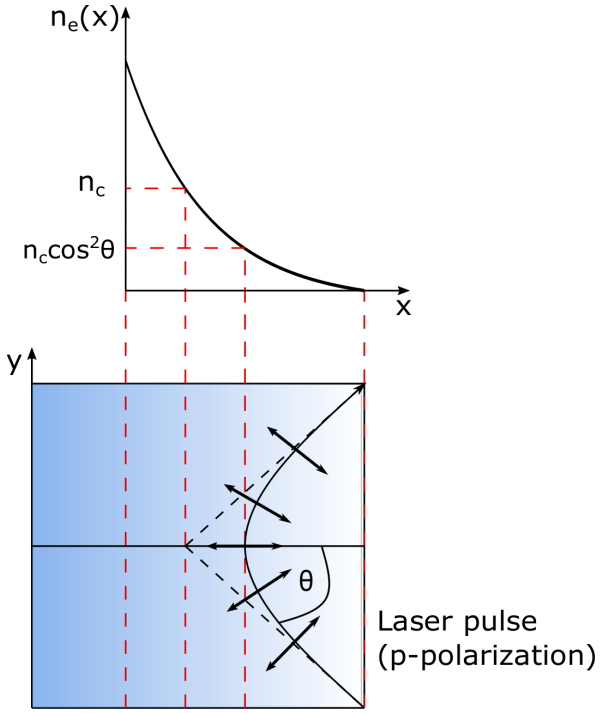

Figure 3.2: Schematic of an incident plane wave on a plasma surface for p-polarized light (adapted from [34]).

Normal skin effect

For $L \to 0$ the sample surface has a sharp density step so that the formalism of Fresnel absorption of metals can be applied. Considering s-polarized light we start from Eq. (3.2.9) and define the density using a Heaviside step function $\Theta(x)$

$$n_0(x) = n_0\Theta(x). \tag{3.2.12}$$

Here, we neglect collisions such that Eq. (3.2.10) simplifies to

$$\epsilon(x) = 1 - \frac{\omega_p^2}{\omega^2}\Theta(x). \tag{3.2.13}$$

For $x < 0$ (vacuum) the Helmholtz equation can be solved to

$$E_z = 2E_0 \sin\left(kx\cos\theta + \phi\right) \tag{3.2.14}$$

with the wavevector $k = \frac{\omega}{c}$, the amplitude of the laser field E_0 and the phase factor ϕ determined via

$$\tan\phi = -l_s \frac{\omega}{c}\cos\theta. \tag{3.2.15}$$

In the overdense region, the evanescent field is decaying exponentially

$$E_z = E(0)\exp\left(-\frac{x}{l_s}\right) \tag{3.2.16}$$

with the skin depth l_s (see Eq. (3.2.8)) and $E(0)$

$$E(0) = 2E_0 \frac{\omega}{\omega_p}\cos\Theta. \tag{3.2.17}$$

An example for an s-polarized wave impinging on a steep density gradient is illustrated in Fig. 3.3.

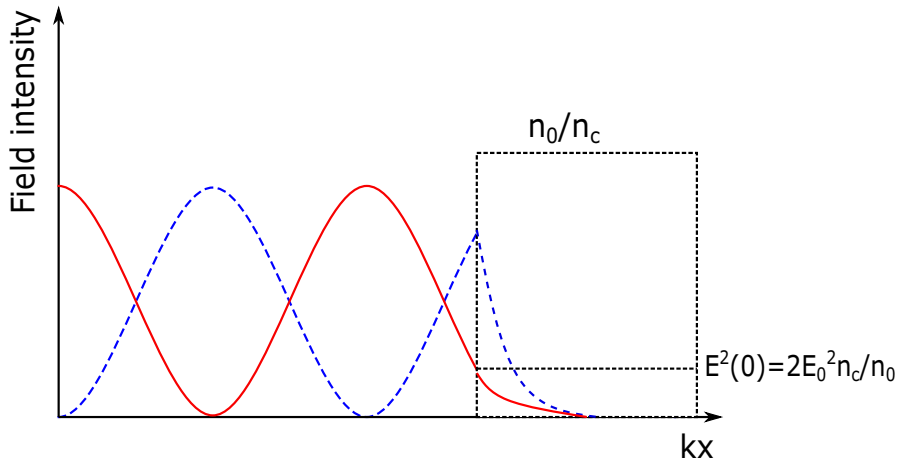

Figure 3.3: Field intensity of electromagnetic fields penetrating into a plasma skin-layer. The red line denotes the square of the electric field E_z^2 and the blue dashed line represents the magnetic field B_y^2 (adapted from [1]).

Now electron-ion collisions are taken into account implying that the plasma behaves like a metal surface with finite conductivity. The Fresnel equations can then be written as [39]

$$R_s = \left|\frac{\sin(\theta-\theta_t)}{\sin(\theta+\theta_t)}\right|^2 \qquad \text{for s-polarized light} \tag{3.2.18}$$

$$R_p = \left|\frac{\tan(\theta-\theta_t)}{\tan(\theta+\theta_t)}\right|^2 \qquad \text{for p-polarized light} \tag{3.2.19}$$

with θ the incident angle and θ_t the complex angle of the transmitted light

$$\theta_t = \sin^{-1}\left(\frac{\sin\theta}{n}\right), \tag{3.2.20}$$

with the refractive index $n = \sqrt{\epsilon}$. To calculate the absorption coefficient we split the dielectric constant and the refractive index into their real and imaginary parts $\epsilon = \epsilon_r + i\epsilon_i$ and $n = n_r + in_i$ [39, 40], which yields

$$\epsilon_r = 1 - \frac{\tilde{\omega}_p^2}{1+\nu^2} = n_r^2 - n_i^2, \tag{3.2.21}$$

$$\epsilon_i = \frac{\nu\tilde{\omega}_p^2}{1+\nu^2} = 2n_r n_i. \tag{3.2.22}$$

Here, it is $\tilde{\omega}_p = \frac{\omega_p}{\omega}$ and $\nu = \frac{\nu_{ei}}{\omega}$. With these assumptions the Fresnel equations simplify to

$$R_s = R_p = \left|\frac{1-n}{1+n}\right|^2 \tag{3.2.23}$$

and we result in the absorption function

$$\eta = 1 - R_s = \frac{4n_r}{(1+n_r)^2 + n_i^2}. \tag{3.2.24}$$

The calculation reduces in determining n_r and n_i. By assuming highly overdense plasma ($\tilde{\omega}_p^2 \gg 1$) we distinguish between light ($\nu \ll 1$) and heavy ($\nu > 1$) damping. For both cases we calculate Eq. (3.2.21) and Eq. (3.2.22) resulting in the absorption coefficient for the normal skin effect (NSE) [41, 42]

$$\eta_{\text{nse}} = \begin{cases} \frac{2\nu_{ei}}{\omega_p} & \nu_{ei} \ll \omega_0 \\ \frac{2\omega_0}{\omega_p}\sqrt{\frac{\nu_{ei}}{\omega_0}} & \nu_{ei} > \omega_0. \end{cases} \tag{3.2.25}$$

It is evident that the electric field in the overdense plasma decays exponentially

$$E(x) = E(0)\exp\left(-\frac{x}{\delta_s}\right) \tag{3.2.26}$$

with the electric field at the plasma-vacuum boundary $E(0)$ and the effective collisional

skin-depth δ_s

$$\delta_s = \frac{c}{\omega_p}\sqrt{|1+i\nu|}. \tag{3.2.27}$$

Theoretically, Eq. (3.2.25) can be used to retrieve information about the transport properties of high density plasmas. However, analytically this is an almost impossible challenge. Numerically, one can calculate the absorption or reflectivity experimentally and compare these to common models such as [43–48].

3.2.3 Heating and thermal conduction

It is obvious that absorption of laser energy and thermal heating of the target material are correlated and should be taken into account simultaneously [41]. However, we first concentrate on thermal heating without any absorption effects. We consider the propagation of a non-linear heat-wave into a cold, conducting, semi-infinite medium with a continuous heat source at one boundary that can be treated by the energy transport equation for a collisional plasma

$$\frac{\partial \varepsilon}{\partial t} + \boldsymbol{\nabla}\cdot(\boldsymbol{q}+\boldsymbol{\Phi_a}) = 0 \tag{3.2.28}$$

with the energy density ε, the heat flow $\boldsymbol{q}$ and the absorbed laser flux $\Phi_a = \eta_a \Phi_L$.
The most common model is the model of volume heating. Assuming that the penetration depth of the heatwave l_h during the pulse duration is smaller than the skin depth l_s we can neglect the thermal transport and get

$$\frac{\mathrm{d}T_e}{\mathrm{d}t} \approx \frac{\Phi_a}{n_{\mathrm{free}} l_s}. \tag{3.2.29}$$

Substituting $\varepsilon = \frac{3}{2} n_{\mathrm{free}} k_B T_e$ yields

$$\frac{\mathrm{d}}{\mathrm{d}t}\left(k_B T_e\right) \approx 4\frac{\Phi_a}{\mathrm{Wcm^{-2}}}\left(\frac{n_{\mathrm{free}}}{\mathrm{cm^{-3}}}\right)^{-1}\left(\frac{l_s}{\mathrm{cm}}\right)^{-1}\mathrm{keV\,fs^{-1}} \tag{3.2.30}$$

resulting in an initial heating rate at the plasma surface of $\sim 1\,\mathrm{keV\,fs^{-1}}$ for a laser intensity of $10^{15}\,\mathrm{Wcm^{-2}}$. Because of the hugh temperature gradient after a few femtoseconds the heat is transported into the cold target material. For an ideal plasma, the heat flow can be written as [49, 50]

$$q(x) = -\kappa_e \frac{\partial T_e}{\partial x} \tag{3.2.31}$$

with κ_e the Spitzer thermal conductivity. By assuming just one spatial dimension we can determine the diffusion equation for T_e

$$\frac{3}{2} n_{\text{free}} k_B \frac{\partial T_e}{\partial t} = \frac{\partial}{\partial x}\left(\kappa_e \frac{\partial T_e}{\partial x}\right) + \frac{\partial \Phi_L}{\partial x}. \tag{3.2.32}$$

Eq. (3.2.32) has a well-known self-similar solution [51]. By solving this equation one finds that the shape of the heatwave stays constant during the penetration of the target although the surface temperature is increasing. We illustrate this in Fig. 3.4 displaying the electron temperature T_e as a function of the depth x for different time steps.

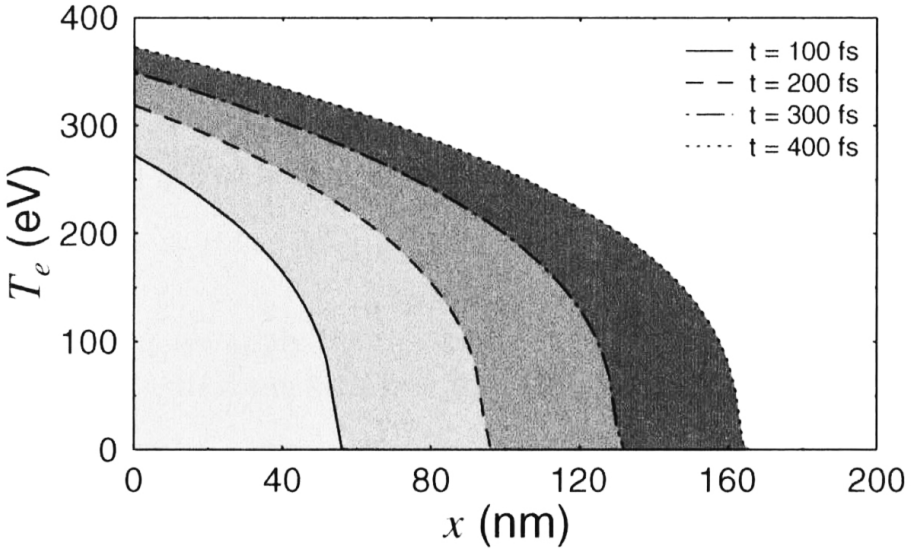

Figure 3.4: Nonlinear heatwave propagating into a solid density plasma at different time steps (taken from [1]).

For determining the self-similar solution we substitute the variables to dimensionless parameters $\tau = t/t_0$, $\xi = x/(v_0 t_0)$ and $\Theta = T_e/(m v_0^2)$ with t_0 and v_0 being time and velocity constants [52].
We plug these substitutions into Eq. (3.2.32) and end up in

$$\frac{\partial \Theta}{\partial \tau} = \frac{\partial}{\partial \xi}\left(\Theta^{\frac{5}{2}} \frac{\partial \Theta}{\partial \xi}\right) \tag{3.2.33}$$

with the boundary condition that at the edge of the target the heat flow into the plasma is equal to the laser flux at that position

$$\Theta^{5/2} \frac{\partial \Theta}{\partial \xi}\bigg|_{\xi=0} = -1. \tag{3.2.34}$$

By choosing $\zeta = \xi/\tau^{\alpha}$ we find that Eq. (3.2.33) reduces to a nonlinear ordinary differential

equation

$$\frac{\mathrm{d}}{\mathrm{d}\zeta}\left(\Psi^{5/2}\frac{\partial\Psi}{\partial\zeta}\right)-\frac{2\Psi}{9}+\frac{7\zeta}{9}\frac{\partial\Psi}{\partial\zeta}=0 \tag{3.2.35}$$

with the boundary condition to be

$$\Psi^{5/2}\frac{\partial\Psi}{\partial\zeta}\bigg|_{\zeta=0}=-1. \tag{3.2.36}$$

This differential equation is not analytically solvable but can be determined with numerical methods as shown in [1]. We end up with a surface temperature of

$$T_e(0)=250\left(\frac{n_{\mathrm{free}}}{10^{23}\,\mathrm{cm}^{-3}}\right)^{-2/9}Z^{2/9}\left(\frac{I_a}{10^{15}\,\mathrm{Wcm}^{-2}}\right)^{4/9}\left(\frac{t}{100\,\mathrm{fs}}\right)^{2/9}\mathrm{eV} \tag{3.2.37}$$

depending on the free electron density n_{free}, the ion charge Z, the absorbed laser intensity I_a and the time t. However, this model overestimates the temperature since absorption effects are not taken into account. By including collisional absorption we obtain a surface temperature of [52]

$$T_e(0)=119\left(\frac{n_{\mathrm{free}}}{10^{23}\,\mathrm{cm}^{-3}}\right)^{1/12}Z^{1/12}\left(\frac{I_a}{10^{15}\,\mathrm{Wcm}^{-2}}\right)^{1/3}\left(\frac{t}{100\,\mathrm{fs}}\right)^{1/6}\mathrm{eV}. \tag{3.2.38}$$

Fig. 3.5 illustrates the electron temperature at the plasma surface as a function of time for the model without absorption (see Eq. (3.2.37)) and with absorption effects (see Eq. (3.2.38)). Here, we assumed $n_{\mathrm{free}}=1\times10^{23}\,\mathrm{cm}^{-3}$, $Z=2$ and $I_a=1\times10^{15}\,\mathrm{Wcm}^{-2}$ and found a significant difference in the electron temperature for times $>100\,\mathrm{fs}$.

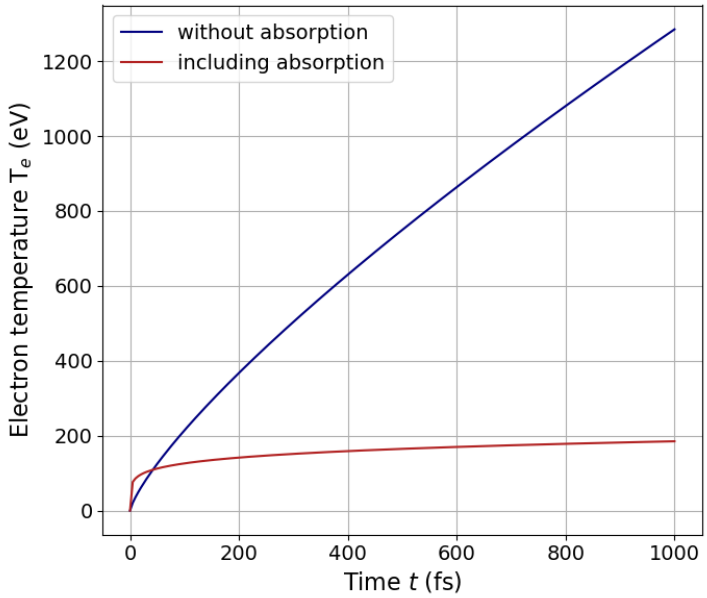

Figure 3.5: Electron temperature at the plasma surface as a function of time comparing two different models with $n_{\text{free}} = 1 \times 10^{23}\,\text{cm}^{-3}$, $Z = 2$ and $I_a = 1 \times 10^{15}\,\text{W/cm}^2$.

3.2.4 Hydrodynamics

The theory of hydrodynamics is based on the two-fluid plasma model which consists of continuity, momentum and energy equations for electrons and ions solved in [32, 33, 53]. For a quasi-neutral plasma ($n_{\text{free}} = Zn_i$) the mass and momentum transport is dominated by the ions resulting in an average fluid density ρ and velocity $\boldsymbol{u}$

$$\rho \equiv n_i\, M + n_{\text{free}}\, m \approx n_i\, M \tag{3.2.39}$$

$$\boldsymbol{u} \equiv \frac{1}{\rho}(n_i\, M\, \boldsymbol{u_i} + n_{\text{free}}\, m\, \boldsymbol{u_e}) \approx \boldsymbol{u_i} \tag{3.2.40}$$

with the ion mass M and the electron mass m. These approximations allow us to reduce the problem to a single-fluid one, but usually both energy equations are required to treat the temperature difference between electrons and ions. Based on these equations we find four essential equations for the laser-plasma hydro code given by [54]

$$\frac{\partial \rho}{\partial t} + \boldsymbol{\nabla} \cdot (\rho \boldsymbol{u}) = 0 \tag{3.2.41}$$

$$\frac{\partial \rho \boldsymbol{u}}{\partial t} + \boldsymbol{\nabla} \cdot (\rho \boldsymbol{u}\boldsymbol{u}) + \boldsymbol{\nabla} P - \boldsymbol{f_p} = 0 \tag{3.2.42}$$

$$\frac{\partial \varepsilon_e}{\partial t} + \boldsymbol{\nabla} \cdot \left[\boldsymbol{u}\,(\varepsilon_e + P_e) - \kappa_e \boldsymbol{\nabla} T_e - \frac{\boldsymbol{Q_{ei}}}{\gamma_e - 1} - \boldsymbol{\Phi_a}\right] = 0 \tag{3.2.43}$$

$$\frac{\partial \varepsilon_i}{\partial t} + \boldsymbol{\nabla} \cdot \left[\boldsymbol{u}\,(\varepsilon_i + P_i) - \kappa_i \boldsymbol{\nabla} T_i + \frac{\boldsymbol{Q_{ei}}}{\gamma_i - 1}\right] = 0. \tag{3.2.44}$$

$\varepsilon_{e,i}$ denotes the energy density of electrons and ions and is defined by the sum of internal and kinetic fluid energies

$$\varepsilon_{e,i} = \frac{P_{e,i}}{\gamma_{e,i} - 1} + \frac{1}{2}\rho u^2 \tag{3.2.45}$$

with the number of degrees of freedom for the electrons or ions $\gamma_{e,i}$. The electron-ion equipartition rate Q_{ei} is defined as [55]

$$Q_{ei} = \frac{2m}{M} \frac{n_{\text{free}} k_B (T_e - T_i)}{\tau_{ei}} \tag{3.2.46}$$

where $\tau_{ei} = \nu_{ei}^{-1}$ describes the electron-ion collision time. κ_e and κ_i denote the thermal conductivities [55], Φ_a is the absorption term and $\boldsymbol{f_p}$ represents the ponderomotive force give by

$$\boldsymbol{f_p} = -\frac{\omega_p^2}{16\pi\omega^2} \boldsymbol{\nabla} E_L^2. \tag{3.2.47}$$

Note that the ponderomotive force acts only on the electrons. To determine the pressures and temperatures of the fluid, a so called equation of states is applied. This is connected via the ideal gas law $P_\alpha = k_B\, n_\alpha\, T_\alpha$ for low densities or via the Thomas-Fermi model at high densities [56].

The five effects described in this chapter form the basis of many models used in short pulse laser plasma interaction. Unfortunately, this is not analytically solvable leading to rather complex and time consuming numerical simulations. This thesis shall help to benchmark and improve the existing models and simulations.

Chapter 4

Experimental setup

In this chapter, the experimental realizations are shown and explained. In section 4.1, we explain the main principles of Free-Electron Lasers, followed by a short description of high-intensity near-infrared lasers in section 4.2. We performed the experiment at the SACLA FEL facility in Japan as shown in section 4.3. Detailed information about the realization of the experiment can be found in section 4.4. The production of the multilayer samples is presented in section 4.5 and the characterization of these multilayer samples is shown in section 4.6.

4.1 Free-Electron Lasers

With the advent of X-ray radiation from X-ray tubes discovered by Wilhelm Conrad Röntgen in 1895 a complete new scientific field (e.g. physics, chemistry and medicine) emerged [57]. In 1947, the first synchrotron light was observed with several orders of magnitude higher photon energies and intensities as illustrated in Fig. 4.1 [58]. The principles of X-ray production have been further developed during the last decades so that the first XUV Free-Electron Laser (FLASH) was built in Hamburg in 2005 [59]. 4 years later, the first hard X-ray FEL facility (LCLS) has been established in Stanford [60].
For the experiment shown in this thesis, it is required to have femtosecond to picosecond single shot time resolution, nanometer spatial resolution and surface sensitivity which is only provided by X-ray Free-Electron Lasers (XFELS).
In the following, we discuss the basic principles of Free-Electron Lasers. Electrons generated by an electron gun optimized for low emittance are accelerated in a linear accelerator (LINAC) close to the speed of light $v \approx c$ and electron pulses are shortened by bunch compression schemes. The accelerated electrons are entering the undulator consisting of magnets with alternating polarity (Fig. 4.2) which produce a sinusoidal magnetic field

$$\boldsymbol{B}(z) = B_0 \cos\left(\frac{2\pi}{\lambda_u} z\right) \hat{\boldsymbol{y}} \tag{4.1.1}$$

with B_0 the maximum intensity of the magnetic field and λ_u the undulator period length [61].

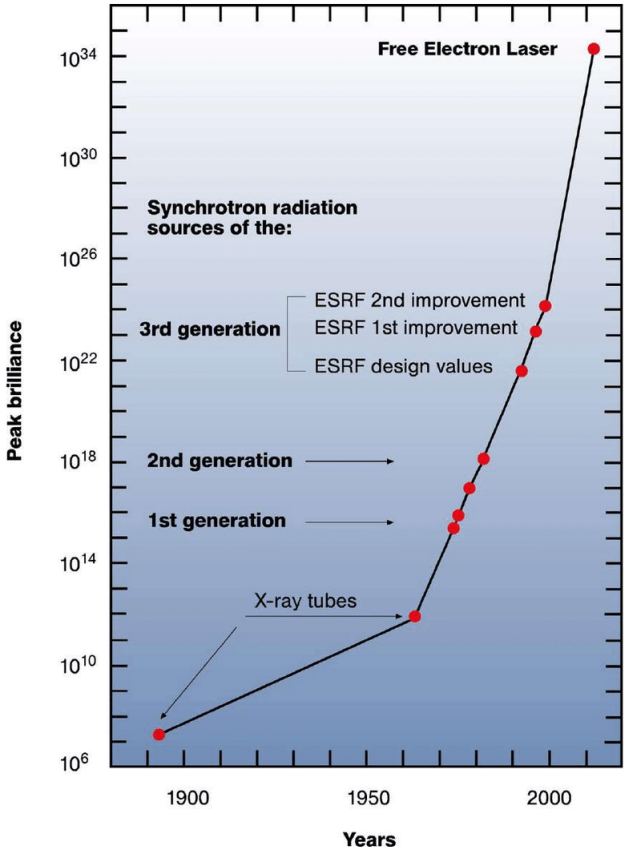

Figure 4.1: Evolution of the peak brilliance over the last 150 years. The Free-Electron Laser has a peak brilliance that is orders of magnitude higher compared to a synchrotron (taken from [62]).

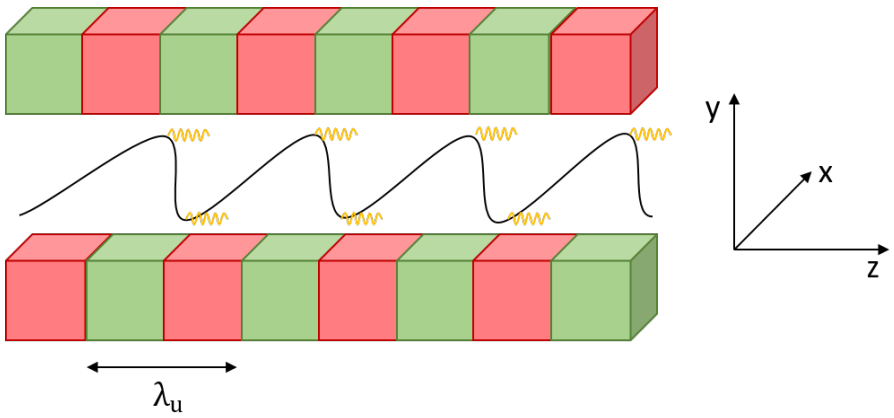

Figure 4.2: Sketch of an undulator with undulator period λ_u. Electrons travel a sinusoidal trajectory forced by the periodic magnetic arrays (adapted from [61]).

The electrons travelling through the magnetic field are affected by the Lorentz force $\boldsymbol{F_L} = e\boldsymbol{v} \times \boldsymbol{B}$ meaning that the electrons gain a momentum in x-direction

$$\frac{\mathrm{d}p_x}{\mathrm{d}t} = -e\frac{\mathrm{d}z}{\mathrm{d}t}B_0 \cos\left(\frac{2\pi}{\lambda_u}z\right). \tag{4.1.2}$$

Integrating Eq. (4.1.2) yields the transverse velocity

$$v_x = -\frac{Kc}{\gamma}\sin\left(\frac{2\pi}{\lambda_u}z\right) \tag{4.1.3}$$

with the non-dimensional undulator parameter K [61]

$$K = \frac{e\,B_0\,\lambda_u}{2\pi\,m_e\,c} = 0.934\,\mathrm{B_0[T]}\,\lambda_\mathrm{u}\mathrm{[cm]}. \tag{4.1.4}$$

Assuming that the emitted photons in the undulator are interfering constructively we can determine the resonant photon wavelength λ_{ph} to

$$\lambda_{ph} = \frac{\lambda_u}{2\gamma^2}\left(1 + \frac{K^2}{2}\right). \tag{4.1.5}$$

Since the electron longitudinal velocity u is slightly smaller than the speed of light c, the electrons and the electromagnetic wave have a small space shift Δs of

$$\Delta s = \frac{\lambda_u}{2}\left(1 - \frac{u}{c}\right). \tag{4.1.6}$$

Since the electrons transfer energy to the wave their longitudinal velocity decreases from u to $(u - \Delta u)$ so that they are less favourable to transfer energy to the wave [63]. When the velocity difference Δu increases, we will reach the point where the electrons do not transfer energy to the wave anymore, but the wave gives energy to the electrons. That process continues until u has increased to its initial conditions. That leads to a periodic density modulation of the electron bunch that has the same period as the radiation field. This process is called microbunching [63]. A schemtatic overview is shown in Fig. 4.3. If the undulator is long enough the electrons radiate coherently and amplify the radiation field leading to increased microbunching. That results in an exponential growth of the radiation power P scaling with the number of electrons $P \sim N_e^2$ (Fig. 4.4). This implies a high peak power of the XFEL more than several tens of gigawatts [64]. When the microbunches are equal to the repulsion forces the radiation power saturates.
Microbunching and the subsequent amplification of the emitted radiation is called Self-Amplified Spontaneous Emission (SASE) and is the key working principle of Free-Electron Lasers [63]. SASE emerges from shot noise in the electron beam and produces an X-ray spectrum containing sharp peaks that vary in intensity, position and photon energy from

shot to shot. Fig. 4.5 illustrates an example of three individual shots (colored) and the average over 100 shots (black).

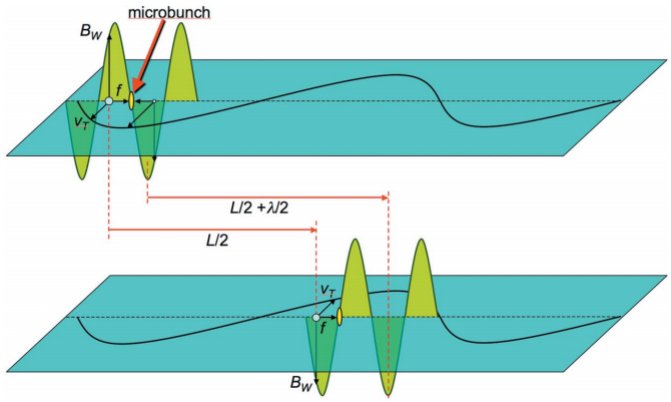

Figure 4.3: Microbunching is forced by the speed difference $u < c$. Top: The magnetic field B_W and the electron transverse velocity v_T create a longitudinal Lorentz force f that pushes the electrons to the same position. Bottom: While the electron travels one-half undulator period the wave is travelling additional one-half wavelength following that both, the electron transverse velocity v_T and the magnetic field B_W are reversed. The Lorentz force f acts on the same directions and microbunching continues (taken from [63]).

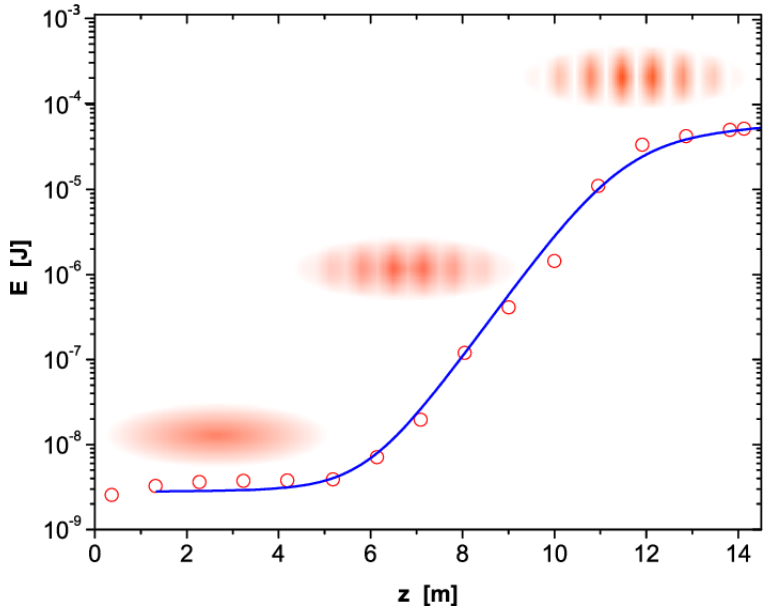

Figure 4.4: Energy increase as a function of undulator distance. The orange patterns illustrate the electron beam microbunching (taken from [65]).

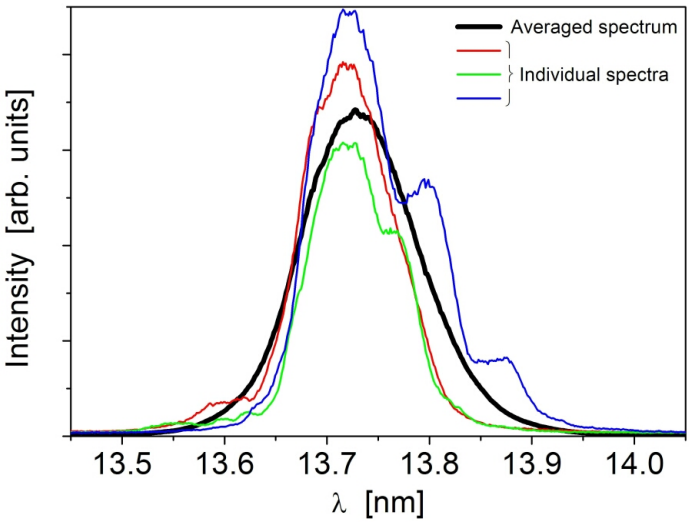

Figure 4.5: Individual SASE FEL pulses at an average wavelength of 13.73 nm. The single-shot spectra show two to three peaks which fluctuate in size, position and height from shot to shot. The average spectrum of 100 FEL pulses is wider than the individual spikes (taken from [66]).

4.2 High-intensity near-infrared laser

The focused intensity of high intensity lasers has increased rapidly during the last 60 years. With the development of chirped-pulse amplification in the 1980s the lasers were even able to accelerate electrons to relativistic velocities (Fig. 4.6).

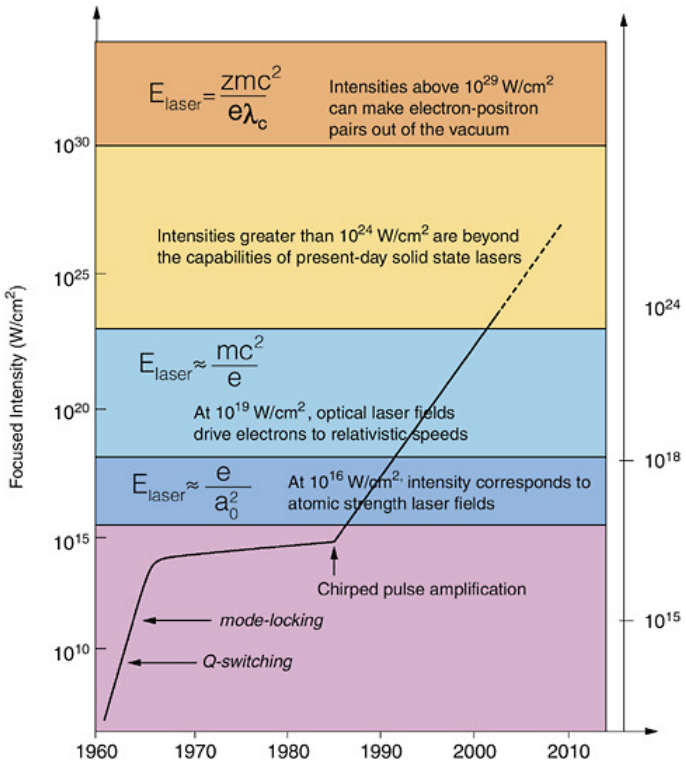

Figure 4.6: Focused intensity of a high-intensity laser during the last 60 years (taken from [67]).

At SACLA, we used a Ti:sapphire (Ti:S) laser with chirped pulse amplification system (CPA) and mode-locked oscillator (see Fig. 4.7). A synchronized optical laser is the key technology for time-resolved pump-probe experiments.

In a free-running laser, phases of equally spaced longitudinal modes with frequency spacing Δ are a set of random numbers meaning that an infinitive series of identical bursts of incoherent light are produced spaced by a time of $t = 2\pi/\Delta$ [69]. For the locked-mode oscillator all modes are forced into equal phases following that they add constructively to a very intense and short burst of light (see Fig. 4.8).
The electric field of this pulse can be written as

$$E(t) = \mathcal{E}(t) \cdot e^{i\Gamma(t)} = \mathcal{E}(t) \cdot e^{i\varphi(t)} \cdot e^{i\omega_0 t} \tag{4.2.1}$$

with $\varphi(t)$ the time dependent phase, $\mathcal{E}(t)$ the field envelope and ω_0 the central frequency

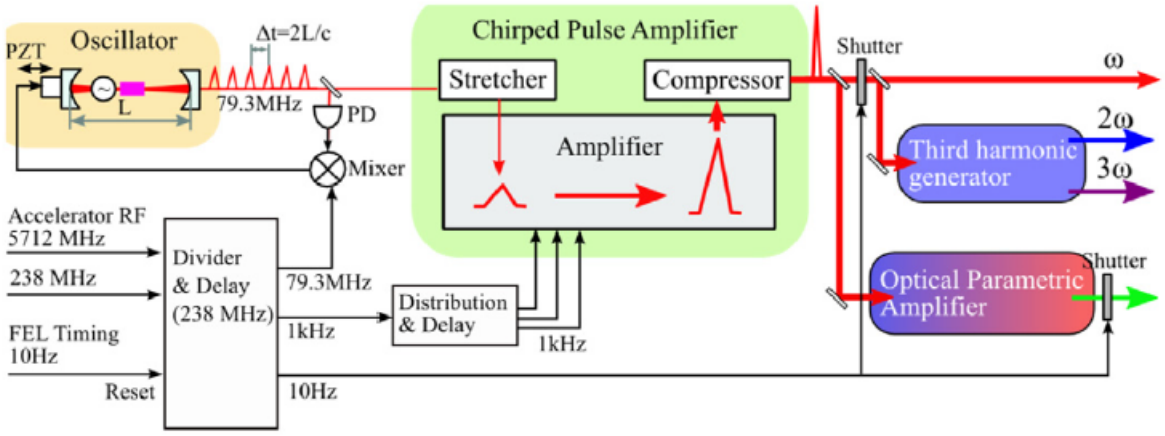

Figure 4.7: Setup of synchronized Ti:sapphire laser (Fig. taken from [68]).

of the pulse. The time dependent carrier frequency $\omega(t)$ is the derivative of the phase factor $\Gamma(t)$ and can be written as

$$\omega(t) = \omega_0 + \frac{\mathrm{d}}{\mathrm{d}t}\varphi(t). \tag{4.2.2}$$

If $\mathrm{d}\varphi/\mathrm{d}t$ varies with time, the frequency is called to be „chirped“. In the laser cavity, the pulses propagate to different media as air or glass following that the pulses get chirped. To circumvent these longer pulses, special mirrors (chirp mirrors) can be applied to shorten the pulses.

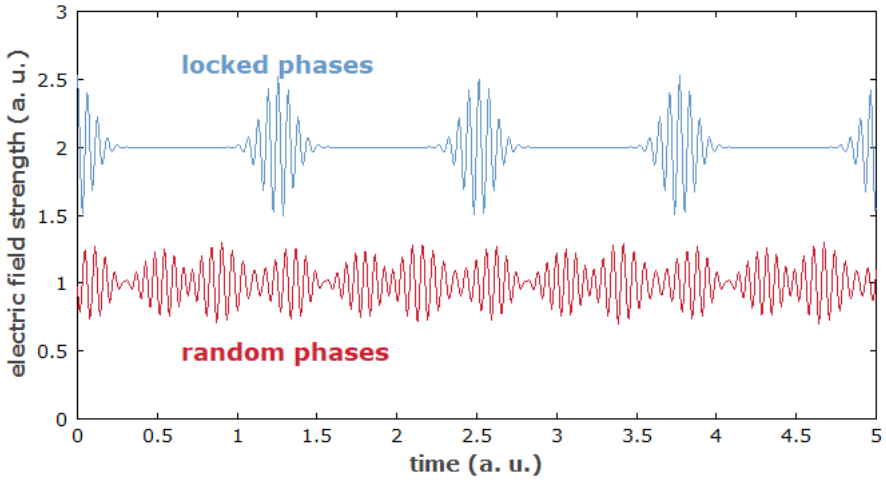

Figure 4.8: Illustration of mode-locking. The red curve shows the electric field for random phases and the blue curve presents the mode-locked phases (Fig. taken from [70]).

Fig. 4.9 illustrates the setup of a Ti:sapphire oscillator where a laser pump is focused into a Ti:S crystal. Due to several mirrors and lenses it gets focused and reaches the chirp mirror in the end which is a combination of different layers with high and low refractive indices resulting in a wavelength dependent penetration depth (see Fig. 4.10) in order to compress the bunch.

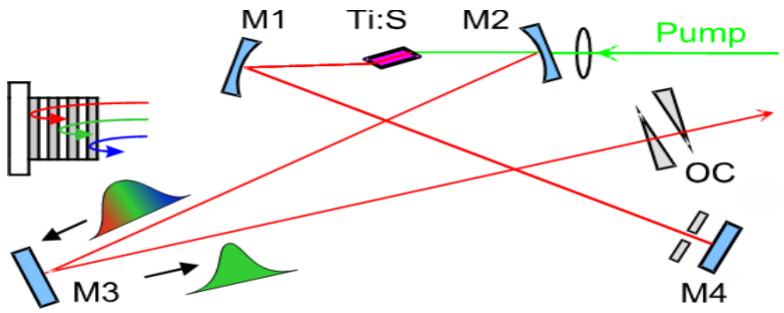

Figure 4.9: Schematic setup of a femtosecond Ti:sapphire laser (Fig. taken from [69]).

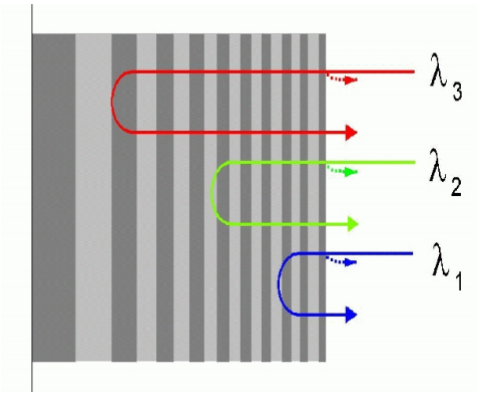

Figure 4.10: Illustration of chirp mirror. Due to materials with different refractive index the penetration depth is wavelength dependent (Fig. taken from [69]).

4.3 SACLA FEL facility

The XDS experiment has been performed at the HEDS station of the **S**Pring-8 **A**ngstrom **C**ompact free-electron **LA**ser (SACLA) facility located in Japan [64]. Fig. 4.11 illustrates a schematic setup of the SACLA XFEL. A graphite heater is heated up and injects the electrons into the linear accelerator (LINAC). This accelerator building has a length of 400 m and consists of C-band accelerators to bring the electrons up to a maximum energy of $E_{\max} = 8.5\,\text{GeV}$. After 400 m the electrons reach the undulator building with a length of 240 m. SACLA is the first compact XFEL facility in the world that uses the technology of in-vacuum undulators that allow just a small gap between the magnetic arrays (1.5 mm) in order to produce a higher magnetic field compared to conventional undulators. By investigating Eq. (4.1.5) one finds that a shorter undulator period L implies a shorter-wavelength radiation λ. It follows by using the in-vacuum undulators a reduced beam energy γ produced in the linear accelerator (accelerator length 400 m [71]) yields the same short-wavelength radiation as using the standard undulator technique (e.g. European XFEL accelerator length 1.7 km [72]). The accelerator parameters of SACLA can be found in Table 4.1. Fig. 4.12 shows the SACLA facility area with the XFEL on the top left and the SPring-8 Synchrotron at the top right. Fig. 4.13 illustrates the three beamlines and their experimental stations of SACLA.

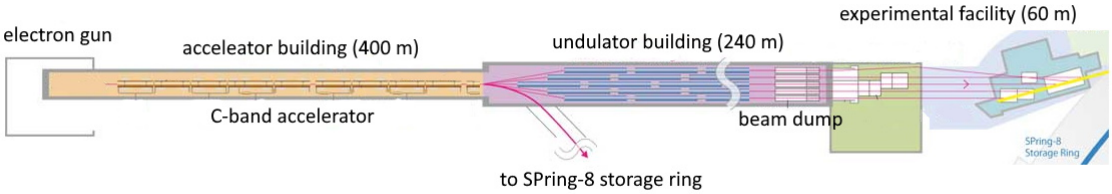

Figure 4.11: Schematic setup of SACLA XFEL (Fig. adapted from [71]).

maximum electron energy $E_{\max}$	8.5 GeV
minimal wavelength $\lambda_{\min}$	0.08 nm
pulses per second	60
total facility length	700 m

Table 4.1: Accelerator parameters of SACLA [71, 72].

Figure 4.12: SPring-8 facility with synchrotron and FEL (Fig. taken from [73]).

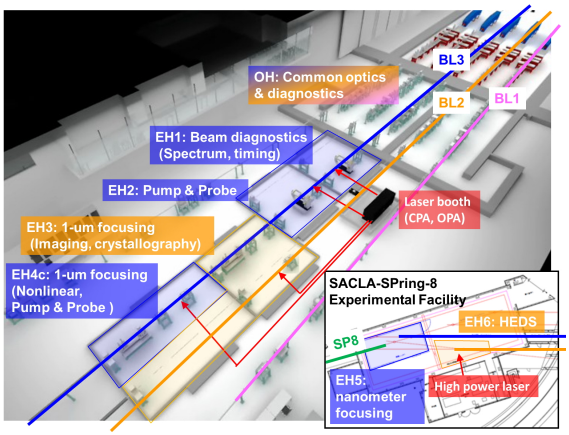

Figure 4.13: Overview over beamlines at SACLA (Fig. taken from [73]).

4.4 Experimental details

In this thesis datasets of two experiments are shown and analyzed. For both experiments we used the same experimental setup but with partially different experimental parameters, e.g. laser energy. In this section the details of the first experiment are described while the parameters of the second experiment are listed in Table 4.2.

Fig. 4.14 shows a photo of the experimental chamber where the setup is built in. On the right the detector is located. Fig. 4.15 illustrates the setup in the chamber.

The experimental setup is depicted in Fig. 4.16. We employed X-ray pulses of photon energy 8.81 keV, pulse intensities of ∼100 µJ and pulse duration 7 fs. The scattered signal is recorded on a 2D area detector **m**ulti-**p**ort **c**harge-**c**oupled **d**evice (MPCCD) which was designed for the SACLA XFEL light source with a frame rate of 30 Hz, 1024×512 pixels with a pixel size of 50 µm, and placed at a distance of 1.27 m from the sample and shielded by a 50 µm thick Al foil to reduce plasma-induced background.The sample is irradiated by an near-infrared (NIR) laser with $\lambda = 800$ nm wavelength, 40 fs FWHM pulse duration, ∼0.07 J energy impinging on the sample surface at 17° incident angle from the surface normal. In order to match with the X-ray footprint on the sample (4 µm FWHM for 0.64° grazing incidence yields 360 µm on sample), the laser beam has been defocused to a diameter of 600 µm yielding an average laser intensity of about 4×10^{14} W/cm^2. The non-collinear geometry between X-ray beam and NIR laser in combination with a large X-ray footprint leads to a temporal resolution of about 1.2 ps as illustrated in Fig. 4.17.

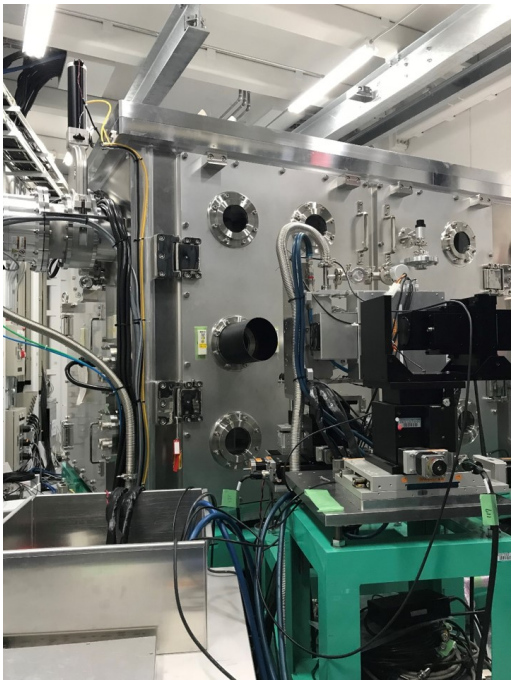

Figure 4.14: Photo from experimental chamber. In the front right is the MPCCD detector.

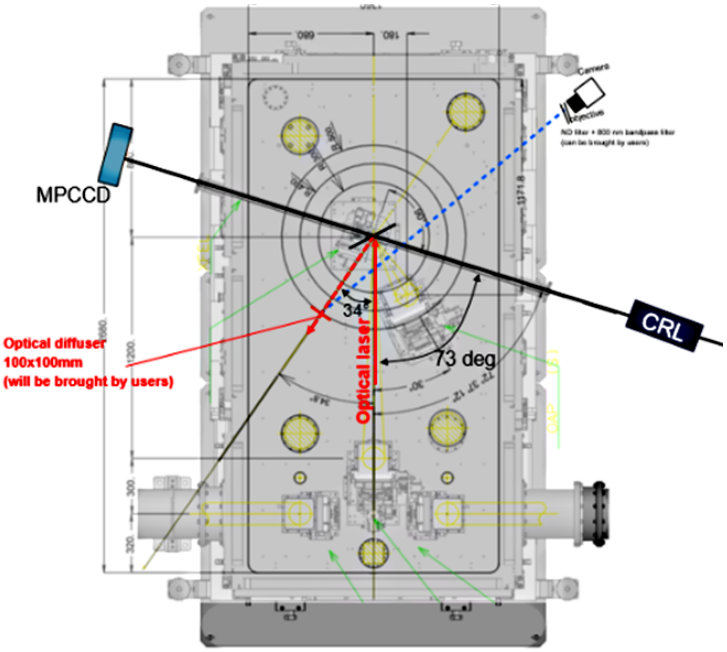

Figure 4.15: Illustration of experimental setup in the chamber (adapted from [74]).

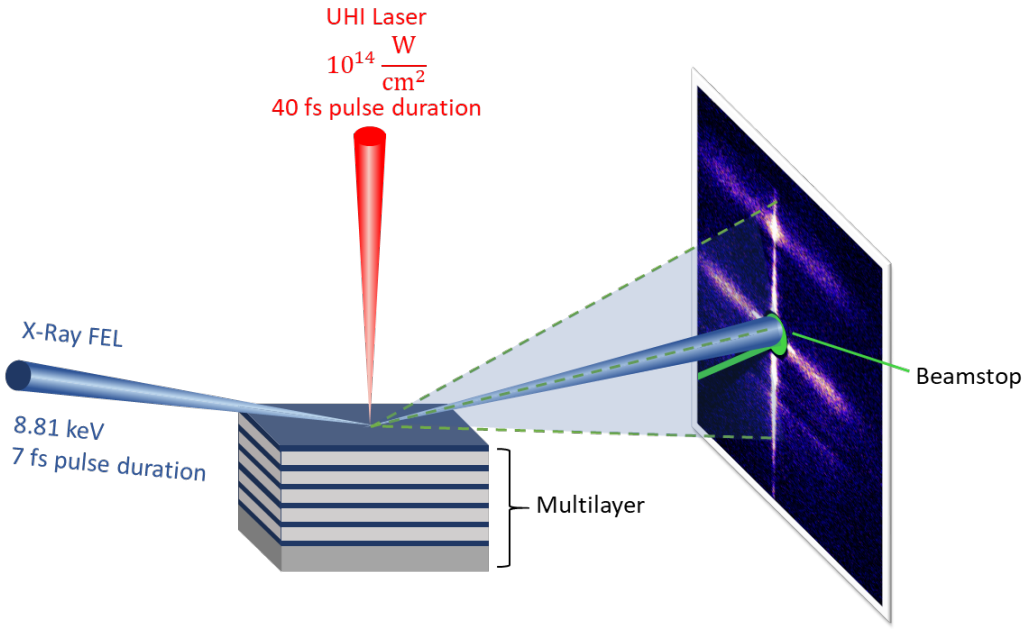

Figure 4.16: Schematics of the experimental setup of the grazing incidence X-ray diffuse scattering (XDS) experiment for investigating the surface dynamics of a solid-density plasma.

The multilayer (ML) samples consist of five repeats of Ta and Cu_3N grown onto a 700 µm thick silicon wafer carrying a Ta seed layer on a 100 nm thick layer of thermal silicon oxide yielding a ML structure of [Ta 4.3 nm / Cu_3N 11.5 nm]$_5$ Ta(4.3 nm) SiO_2(100 nm) Si. The wafers have been laser-cut into hundreds of small samples of size $4 \times 7\,\mathrm{mm}^2$ and mounted on plates shown in Fig. 4.18. These plates have been fixed on a rotation wheel (Fig. 4.19) and each pre-aligned by means of an X-ray reflectivity scan using the attenuated SACLA X-ray beam. For the XDS experiment we fixed the incident angle to 0.64° corresponding to the intense ML Bragg peak at $Q = 0.99\,\mathrm{nm}^{-1}$. Thanks to the high pulse intensities provided by the XFEL, we could successfully record single pulse XDS patterns covering a Q-range up to $1.4\,\mathrm{nm}^{-1}$. The strong specular signal at the exit angle 0.64° is blocked by a beamstop.

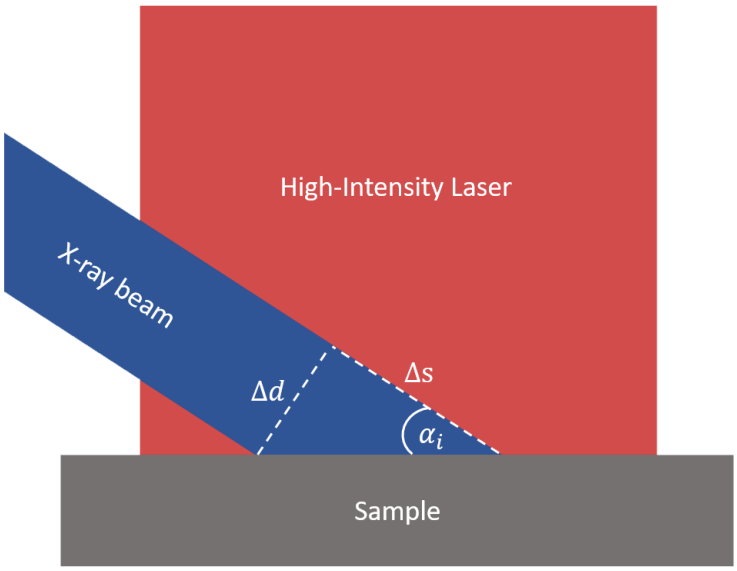

Figure 4.17: Time resolution in the experiment as a result of the non-collinear geometry of laser and X-ray and the X-ray footprint.

	Experiment 1	Experiment 2
Laser intensity	$4 \times 10^{14}\,\mathrm{W/cm^2} - 4 \times 10^{15}\,\mathrm{W/cm^2}$	$8 \times 10^{14}\,\mathrm{W/cm^2} - 8 \times 10^{15}\,\mathrm{W/cm^2}$
Incident angle	0.64°	0.75°
Incident Q_z-vector	$0.99\,\mathrm{nm}^{-1}$	$1.16\,\mathrm{nm}^{-1}$
Q_z-range	up to $1.4\,\mathrm{nm}^{-1}$	up to $2.6\,\mathrm{nm}^{-1}$
Sample-detector distance	1.277 m	1.243 m
Number of pixels	1024×512	2200×600

Table 4.2: Experimental parameters of both experiments.

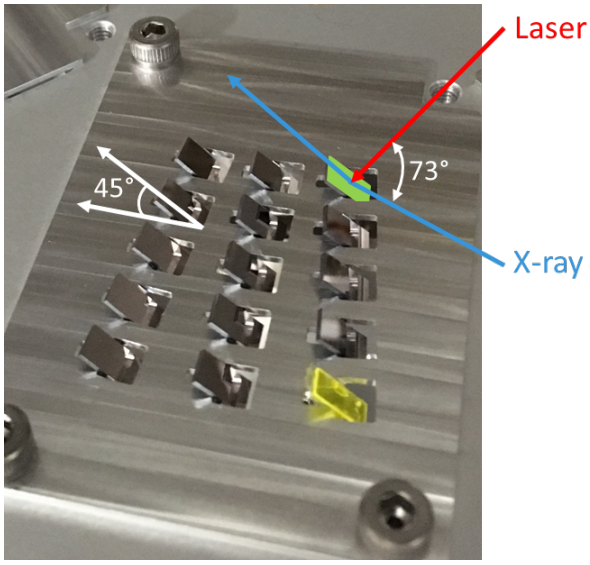

Figure 4.18: The multilayer samples were mounted on these plates with an angle of 45° compared to the surface.

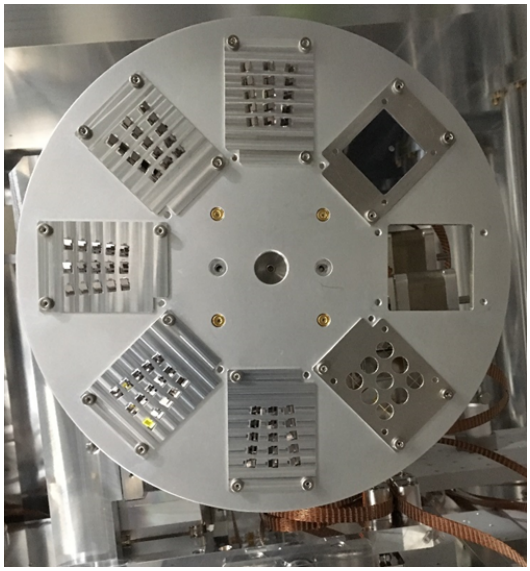

Figure 4.19: The plates were fixed on a rotation wheel.

4.5 Production of multilayer samples

The multilayer samples have been produced at the University of Mainz by the group of Prof. Kläui using the technique of DC magnetron sputtering.
Magnetron sputtering is a type of Physical Vapor Deposition (PVD) that is able to transfer a target material onto a substrate and to form thin films by high energetic particles (i.e. ionized gas atoms) hitting the solid target and breaking the corresponding atoms [75] as shown in Fig. 4.20. For magnetron sputtering, the target material is already present as a metal, oxide or alloy and is positioned on a magnetic system producing a toroidal magnetic field at the target surface. The target and substrate are inserted into a high vacuum and a so-called „sputter agent“, that is usually Argon gas, is added. Additionally, an electric potential is generated accelerating the more and more ionized Argon atoms in the target direction. If the kinetic energy of the atoms is large enough, they can break free single target atoms and scatter them into the argon plasma. The free atoms travel perpendicular from the target and reach the substrate. Because of the high vacuum the collision probability between Argon ions and target atoms is decreased achieving sufficient impact and diffusion rates. The scattered atoms reach the substrate rather slowly meaning that the already sputtered atoms have time to diffuse, rearrange and form homogeneous layers.

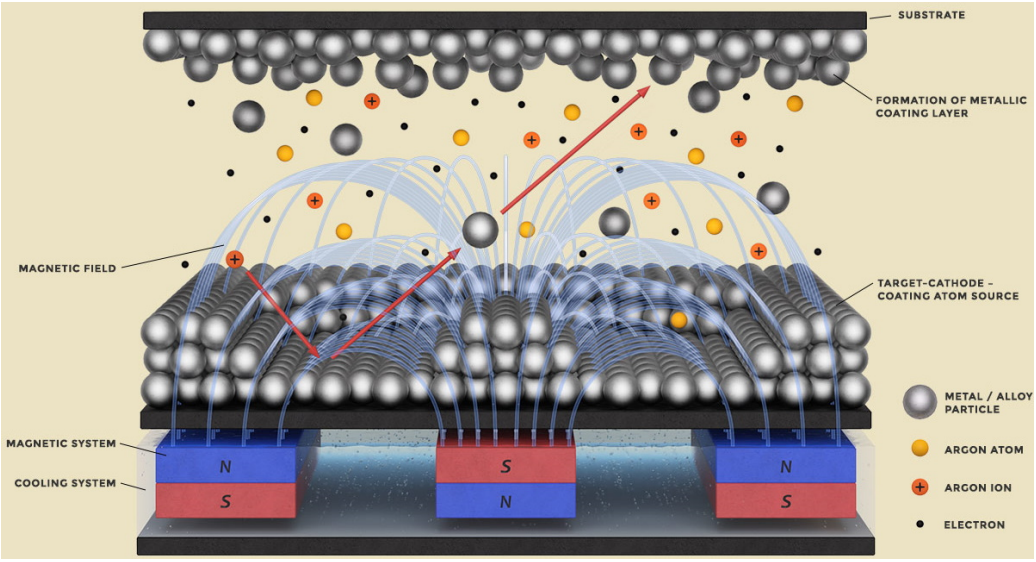

Figure 4.20: Schematic setup of DC magnetron sputtering (adapted from [76]).

The deposition of thin films is a complicated process and can cause defects as vacancies or islands implying that the thin film can differ significantly. To reduce these surface defects an initial seed layer is employed that is known to grow well on the substrate and also allows a homogeneous growth of layer material. By using the technique of magnetron sputtering several multilayers have been grown on a 700 µm thick silicon wafer.

4.6 Sample characterization

We performed X-ray reflectivity (XRR) experiments (see Fig. 4.21) at the synchrotron DELTA in Dortmund to characterize the sample properties of the individual layers such as dispersion δ, absorption β and rms roughness σ.

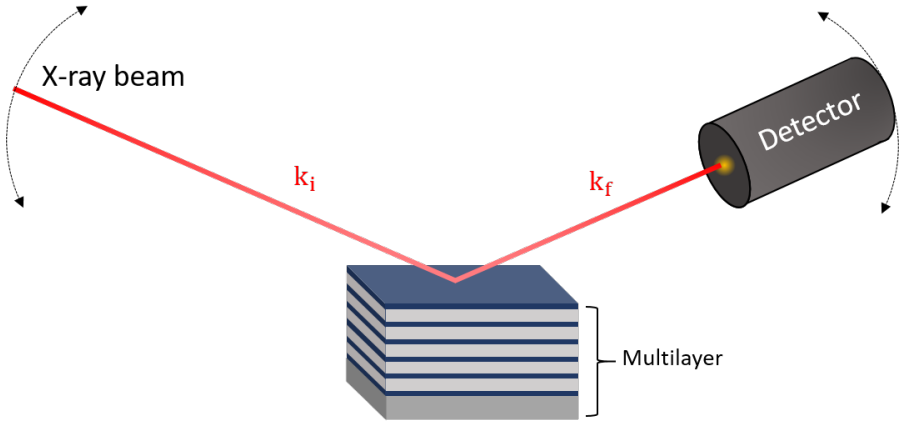

Figure 4.21: Schematic setup of the X-ray reflectivity experiment. X-ray beam and detector are located at the same angular position and move simultaneously to record the scattered intensity.

Modelling the data yields the dispersion profile - note that the dispersion is related to X-ray wavelength $\lambda_{\text{X-ray}}$ and electron density ρ_e via

$$\rho_e = \frac{2\pi\delta}{r_e \lambda_{\text{X-ray}}^2} \tag{4.6.1}$$

and $r_e = 2.817 \cdot 10^{-15}$ m the classical electron radius. To be precise, that is only true for frequencies much larger than the resonance frequencies $\omega \gg \omega_j$ (see Eq. (2.1.3), (2.1.4) and (2.1.5)). Otherwise the dispersion correction term f_1 has to be taken into account illustrated in Fig. 4.22 for Ta as a function of the photon energy. The black dashed line indicates the energy used in the experiment (8.81 keV) showing that we are below three absorption edges (L_I, L_{II}, L_{III}). However, we still use the approximation in Eq. (4.6.1) because we are interested in the electron density difference, or *effective* electron density. Additionally, we measured the reflectivity scans with different photon energies and for reasons of comparison we use electron densities.
The inset in Fig. 4.23 displays the relevant Q-range for the XDS setup representing the characteristic Bragg peak at $Q = 1.35\,\text{nm}^{-1}$ and the four fringes on the left. The specular peak is orders of magnitude more intense than the remaining XDS signal. For the characterization for sample 1 we employed a photon energy of 13 keV and recorded the scattered intensity for $\alpha_i = \alpha_f$ meaning that the X-ray source and the detector have to be moved simultaneously. We took a shot for every angle position between 0.03° and 1.5° in steps

of 0.001°. The PILATUS3 R 100K-A was placed 0.966 m from the sample.
For the sample characterization of sample 2 and 3 we used the X-ray reflectometer in Dortmund employing an photon energy of 8.048 keV. We recorded an angular range between 0.005° and 4°. We transfer the angular range into Q-space via

$$Q_z = \frac{4\pi}{\lambda} \sin \alpha_i \tag{4.6.2}$$

and plot the reflectivity signal as a function of Q_z. Fig. 4.25 and 4.27 show the corresponding reflectivity signal and the insets present the relevant Q-range for the XDS experiment, respectively.

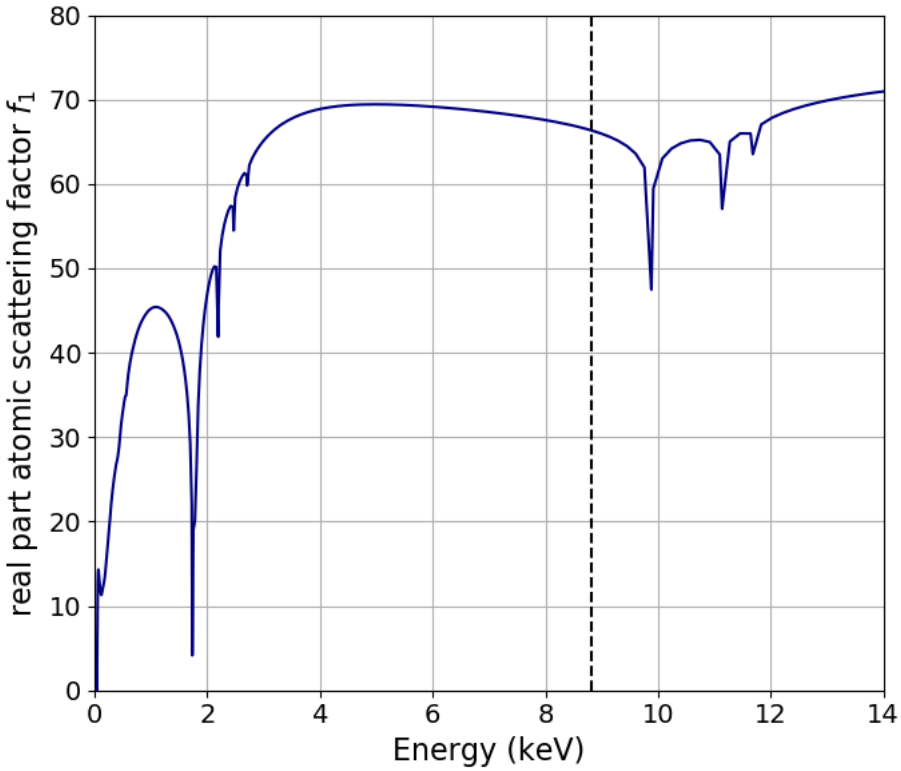

Figure 4.22: f_1 as a function of photon energy for Ta. The black dashed line indicates the photon energy from the XDS experiment (data taken from [77]).

Fig. 4.24, 4.26 and 4.28 illustrate the ML structure obtained from the electron density profiles. Tables 4.3, 4.4 and 4.5 present the modelled parameters for the corresponding samples.

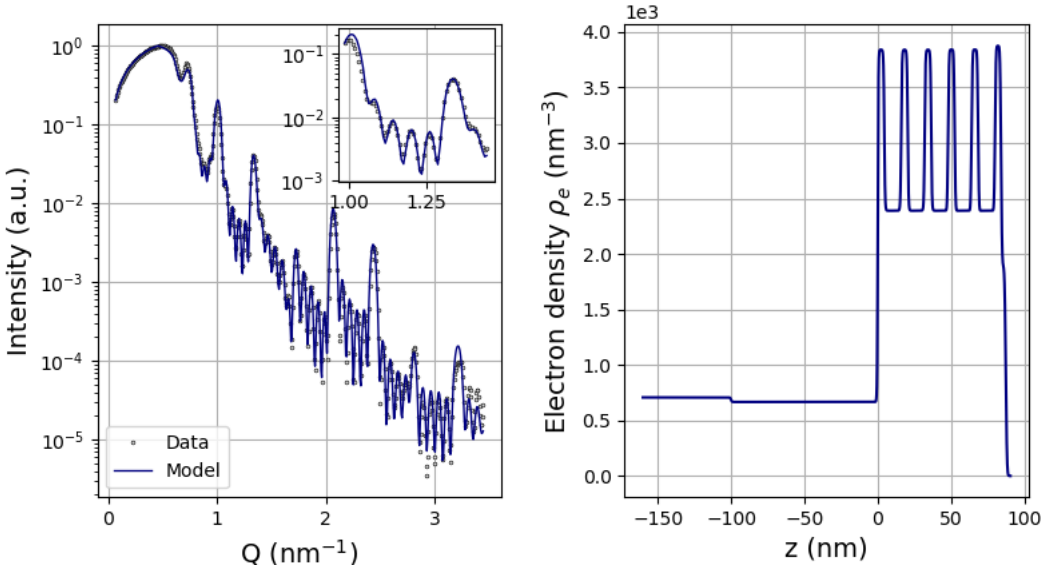

Figure 4.23: left: Reflectivity signal and model as a function of Q_z of sample 1. The inset shows the relevant Q-range for the XDS experiment. right: Electron density profile for modelled signal. The surface is on the right.

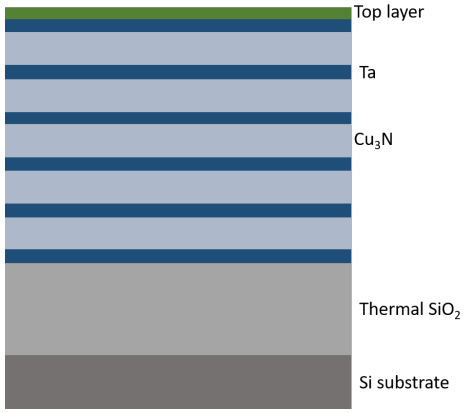

Figure 4.24: Illustration of electron density profile of sample 1.

Sample 1	electron density ρ_e (nm^{-3})	thickness d (nm)	roughness σ (nm)
Top layer	$1.89 \cdot 10^3$	3.2	0.65
Ta	$3.84 \cdot 10^3$	4.5	0.49
Cu_3N	$2.39 \cdot 10^3$	11.5	0.48
SiO_2	$6.66 \cdot 10^2$	100	0.38
Si	$7.06 \cdot 10^2$	$7 \cdot 10^5$	0.54

Table 4.3: Modelled parameters for sample 1.

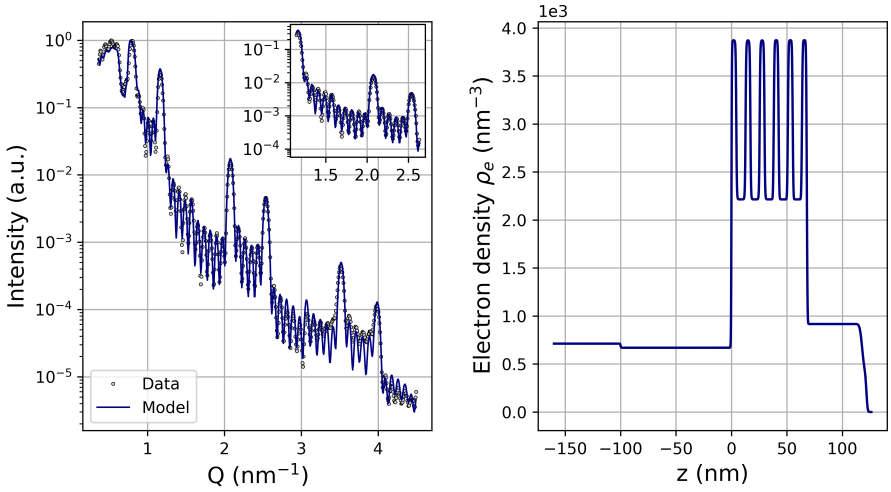

Figure 4.25: left: Reflectivity signal and model as a function of Q_z of sample 2. The inset shows the relevant Q-range for the XDS experiment. right: Electron density profile for modelled signal. The surface is on the right.

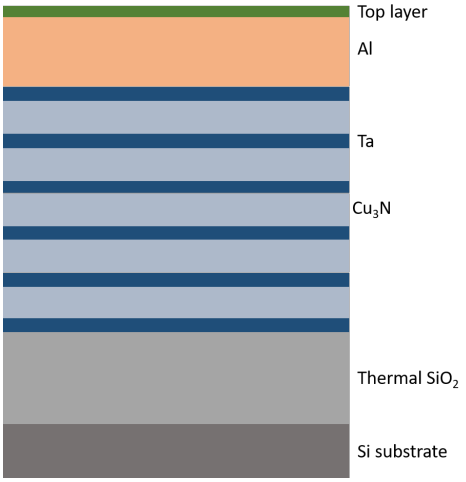

Figure 4.26: Illustration of electron density profile of sample 2.

Sample 2	electron density ρ_e (nm^{-3})	thickness d (nm)	roughness σ (nm)
Top layer	$4.04 \cdot 10^2$	3.8	0.88
Al	$9.16 \cdot 10^2$	50	0.17
Ta	$3.87 \cdot 10^3$	4.3	0.49
Cu_3N	$2.22 \cdot 10^3$	8.4	0.51
SiO_2	$6.70 \cdot 10^2$	100	0.33
Si	$7.12 \cdot 10^2$	$7 \cdot 10^5$	0.40

Table 4.4: Modelled parameters for sample 2.

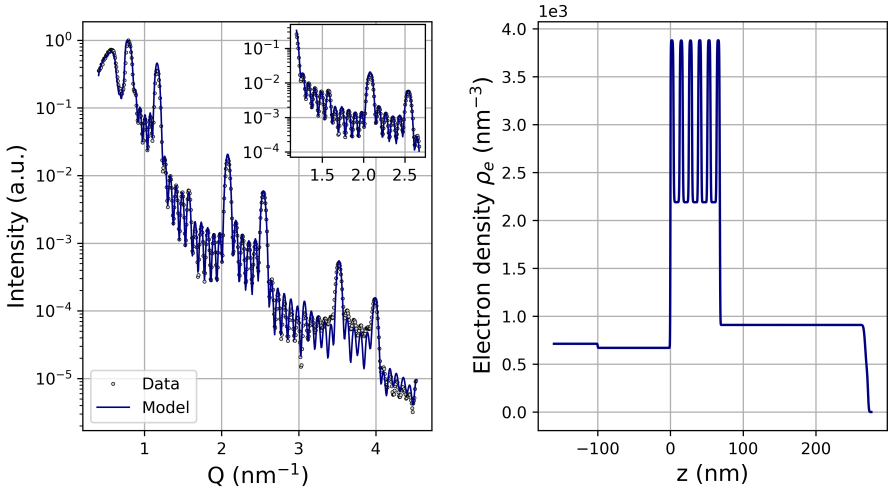

Figure 4.27: left: Reflectivity signal and model as a function of Q_z of sample 3. The inset shows the relevant Q-range for the XDS experiment. right: Electron density profile for modelled signal. The surface is on the right.

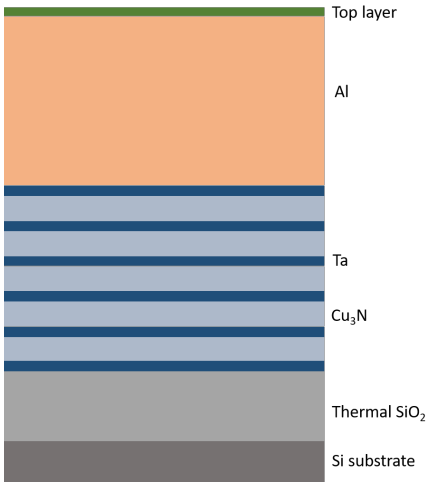

Figure 4.28: Illustration of electron density profile of sample 3.

Sample 3	electron density ρ_e (nm^{-3})	thickness d (nm)	roughness σ (nm)
Top layer	$4.08 \cdot 10^2$	3.7	0.94
Al	$9.09 \cdot 10^2$	200	0.17
Ta	$3.88 \cdot 10^3$	4.3	0.50
Cu_3N	$2.19 \cdot 10^3$	8.4	0.52
SiO_2	$6.70 \cdot 10^2$	100	0.33
Si	$7.12 \cdot 10^2$	$7 \cdot 10^5$	0.40

Table 4.5: Modelled parameters for sample 3.

Chapter 5

Results

In this chapter, we present and discuss the main findings. In section 5.1, we show a detailed analysis of the SACLA 2018 experiment including electron density reconstruction and demonstrations of the uniqueness of model refinements. In section 5.2 a qualitative in-plane analysis of the SACLA 2020 experiment is presented. Additionally, in section 5.3 we investigate the out-of-plane scattering along Q_y and compare different ML samples containing a description of the interface structures.

5.1 SACLA 2018

5.1.1 Data treatment

Fig. 5.1 (left) illustrates a raw detector pattern (MPCCD) with 1024 pixels in z-direction and 512 pixels in y-direction. We observe characteristic vertical lines which arise from the vertical read out direction of the chip. Fig. 5.1 (middle) shows a dark image taken without any X-ray beam. For the background correction we subtract the dark image from the raw data image resulting in the pattern shown in Fig. 5.1 (right).
Fig. 5.2 shows a detector pattern from the cold sample without laser excitation. Regions of interest are colored differently: the blue circle at $Q_z = 0.99\,\mathrm{nm}^{-1}$ and $Q_y = 0\,\mathrm{nm}^{-1}$ is the position of the beamstop blocking the specular signal which is several orders of magnitude more intense than the rest of the signal. The green box between $Q_y = -0.03 - 0.03\,\mathrm{nm}^{-1}$ along Q_z represents the in-plane scattering. Averaging this signal over Q_y and analyzing along Q_z yields information about the electron density profile of the sample. The yellow box between $Q_y = 0.15 - 0.5\,\mathrm{nm}^{-1}$ along Q_z is called the out-of-plane scattering along Q_z and the averaged signal provides additional information about lateral correlations between the different layers. The signal in the red boxes between $Q_z = 0.97 - 1.03\,\mathrm{nm}^{-1}$ and $Q_z = 1.30 - 1.38\,\mathrm{nm}^{-1}$ along Q_y represents the out-of-plane signal along Q_y and yields information about the structure of the interfaces, such as e.g. the hurst parameter.

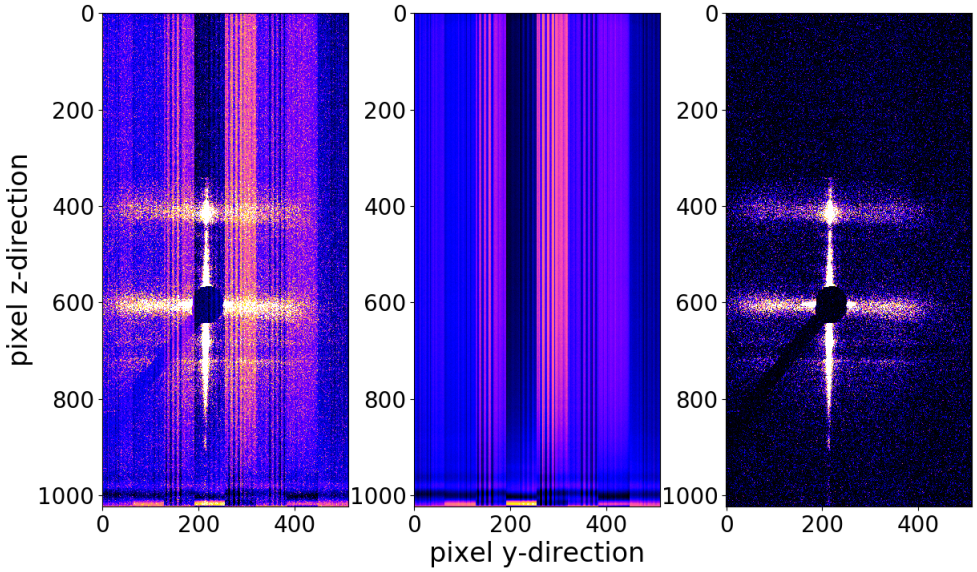

Figure 5.1: left: Typical raw data image. Vertical lines are visible. middle: Dark image. right: Data image after dark-image subtraction.

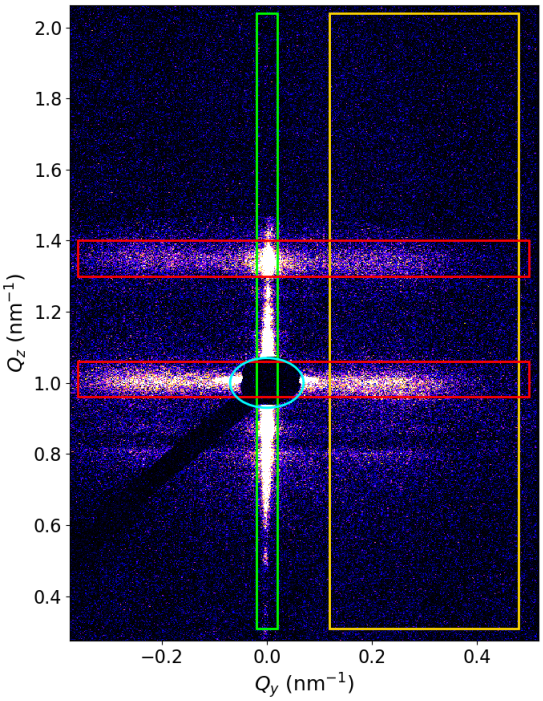

Figure 5.2: Scattering signal from the cold sample without laser excitation. The blue circle indicates the beamstop, the green box represents the in-plane signal, the yellow box shows the out-of-plane signal and the red lineout denotes the diffuse scattering signal.

A summary of the different areas can be found in Table 5.1. Note that the flange at the exit window of the chamber results in a limited Q_z-range up to $1.45\,\mathrm{nm}^{-1}$ on the detector as illustrated in Fig. 5.3.

area	pixel	Q-range
green box	$200 - 230$ in y-direction	$Q_y = -0.03 - 0.03\,\mathrm{nm}^{-1}$
yellow box	$300 - 500$ in y-direction	$Q_y = 0.15 - 0.50\,\mathrm{nm}^{-1}$
red box 1	$590 - 625$ in z-direction	$Q_z = 0.97 - 1.03\,\mathrm{nm}^{-1}$
red box 2	$390 - 435$ in z-direction	$Q_z = 1.30 - 1.38\,\mathrm{nm}^{-1}$

Table 5.1: Overview of different colored areas in Fig. 5.2.

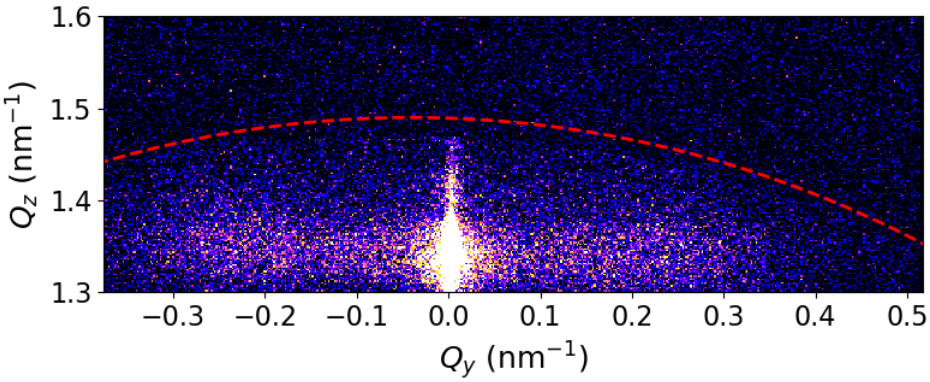

Figure 5.3: Q-range limitation due to the flange at the exit window.

In a next step, we investigate the in-plane signal of various cold samples (green box in Fig. 5.2). Fig. 5.4 represents the signal averaged over $Q_y = -0.03 - 0.03\,\mathrm{nm}^{-1}$ around the specular beam and plotted along the Q_z direction. It is important to note that the diffraction patterns we observe here are representing a cut through reciprocal space along Q =(Q_x, Q_y, Q_z). The specular condition for which $\alpha_i = \alpha_f$ is located at (0, 0, Q_z) and is blocked by the beamstop. The vertical lineout thus represents a path along Q =(Q_x, 0, Q_z) and contains information about the z-direction (density profile) and about vertical correlations along the x-direction simultaneously.
For visualization the lineouts in Fig. 5.4 are vertically shifted. Between 0.7 and $0.9\,\mathrm{nm}^{-1}$ two Yoneda peaks are visible associated with dynamical diffraction effects located at positions where the exit angles α_f are equal to the critical angles of Cu_3N and Ta, respectively. The peak at $Q_z = 0.8\,\mathrm{nm}^{-1}$ represents the Cu_3N peak while the peak at $Q_z = 0.87\,\mathrm{nm}^{-1}$ is assigned to Ta. These peaks arise from the evanescent X-ray wave travelling parallel to

the surface with the values of the exit angles being sensitive to the electron density of the topmost layers.
Between 1.1 and 1.3 nm^{-1} we see three Kiessig fringes which are a fingerprint of the number of repeats of the double layer structure. By comparing the different preshots taken from identical samples we note small fluctuations from shot to shot originating from the SASE fluctuations. At $Q_z = 1.33\,\mathrm{nm}^{-1}$ we find the characteristic Bragg peak that represents the typical thickness of the Ta/Cu_3N double layer (the Bragg peak at $0.99\,\mathrm{nm}^{-1}$ is blocked because this specular peak is too intense for the detector).

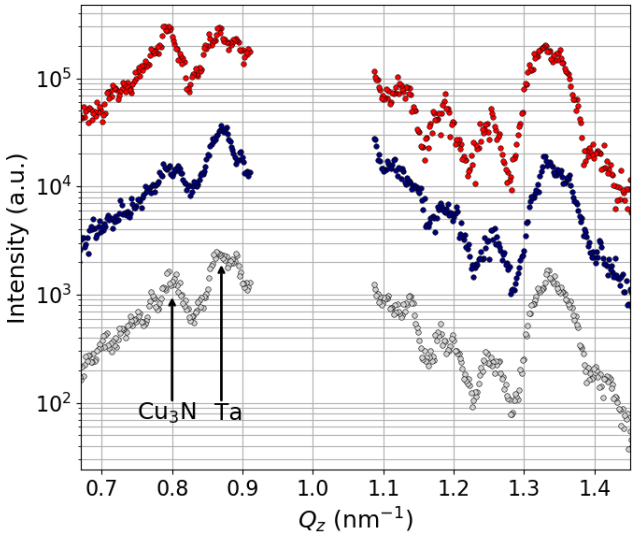

Figure 5.4: In-plane profiles along Q_z of different cold samples. left: Yoneda peaks for Cu_3N and Ta. right: Scattering peaks from layer composition.

Comparing a preshot and the corresponding mainshot upon laser irradiation yields important information about changes inside the sample. 3.5 ps after laser excitation we detect significant differences in the scattering patterns (Fig. 5.5). The presence of the ML Bragg peak at $Q_z = 1.33\,\mathrm{nm}^{-1}$ indicates that the typical length scale of 15.8 nm of the ML double layers still exists. However, the previously clearly visible fringes in-between the Bragg peaks are now washed out considerably indicating that the high periodicity of the cold ML sample is lost to a large extent. Interestingly, we observe the appearance of a new Yoneda peak at $Q_z = 0.73\,\mathrm{nm}^{-1}$ upon pumping, indicative of a region of reduced electron density at the sample surface. An additional new shoulder also appears upon pumping at $1.17\,\mathrm{nm}^{-1}$ indicating that a new layer structure is arising.

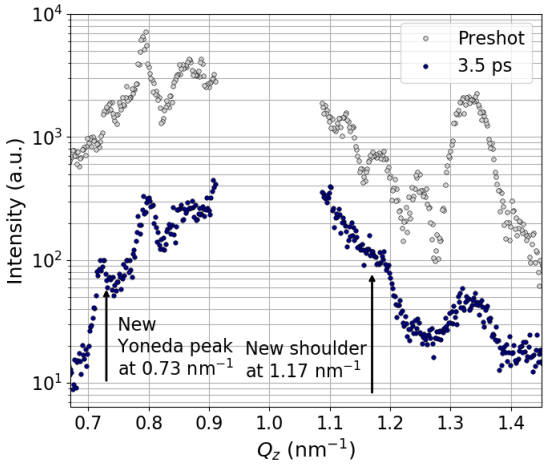

Figure 5.5: In-plane profiles of the cold sample (grey) and 3.5 ps after laser excitation (blue) with spatially averaged laser intensity of $4 \times 10^{14}\,\mathrm{W/cm^2}$.

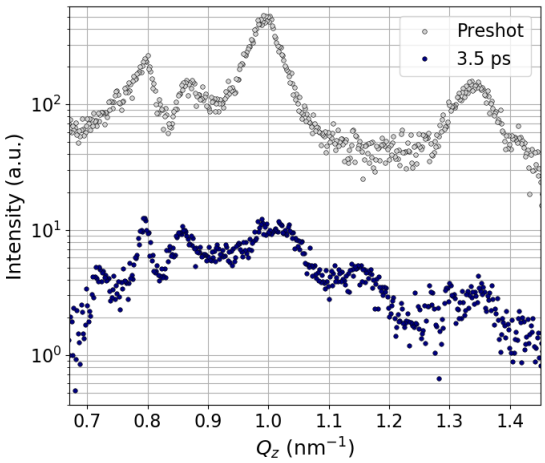

Figure 5.6: Out-of-plane profiles of the cold sample (grey) and 3.5 ps after laser excitation (blue) with spatially averaged laser intensity of $4 \times 10^{14}\,\mathrm{W/cm^2}$.

Fig. 5.6 shows the lineouts from the off-specular signal containing also scattering contributions from out-of plane components of the ML structure. We observe considerable weaker signals from both ML Bragg peaks with the fringes in-between barely visible beyond the detector noise.

5.1.2 Simulation with BornAgain

In this thesis the simulations are performed with BornAgain which is an open-source software for the simulation and modelling of XDS experiments developed by the Scientific Computing Group of the Jülich Centre for Neutron Science (JCNS) [78]. The simulated XDS patterns are based on the DWBA theory and are well suited for multilayer samples as every layer can be adjusted separately with different characteristic properties described in the following. The functions of BornAgain can be accessed via a Graphical User Interface but this has a limited functionality compared to Python scripts. For this reason we used BornAgain with the help of Python scripts. An example is shown in the appendix in chapter 8.1.

In BornAgain we distinguish between „general“ experimental parameters and sample parameters which can be modified for every single layer. Table 5.2 shows the experimental parameters we used for the simulation of the ML sample of our experiment such as the detector area, the position of the specular beam, the X-ray wavelength, incident angle, beam intensity and background. Table 5.3 presents the sample parameters including dispersion, absorption, thickness, roughness, hurst parameter and lateral correlation length. Furthermore, we define one single value for the cross correlation length of the ML sample.

Experimental parameters	
pixel size	50 µm
pixel y-direction	512
distance in y-direction	25.6 mm
pixel z-direction	1024
distance in z-direction	51.2 mm
sample detector distance	1277 mm
y-position of specular beam	10.75 mm
z-position of specular beam	20.65 mm
wavelength	0.140 73 nm
incident angle	0.64°
azimuthal angle	0.0°
beam intensity	varying
constant background	varying

Table 5.2: Experimental parameters used for the XDS simulation with BornAgain.

Sample parameters	
dispersion δ	varying
absorption β	varying
thickness d	varying
rms roughness σ	varying
hurst parameter h	varying
lateral correlation length ξ_L	30 nm
cross correlation length ξ_{cc}	300 nm

Table 5.3: Sample parameters used for the XDS simulation with BornAgain.

Using the experimental parameters from Table 5.2 and the sample parameters, as extracted from the reflectivity measurement, we obtain an 2D simulation pattern shown in Fig. 5.7.

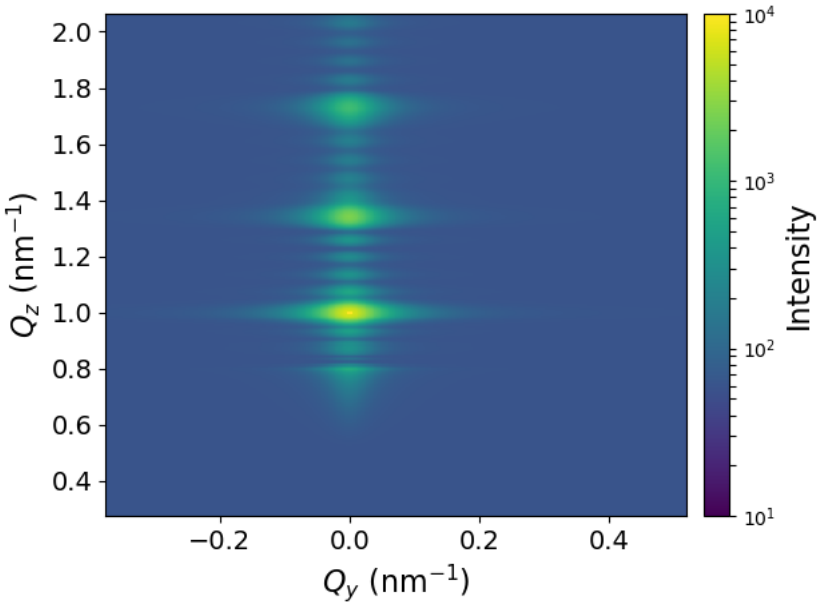

Figure 5.7: Simulated scattering pattern with BornAgain for the cold ML sample.

Taking only the Q_y-cut of 30 pixels around the specular beam as done for the experimental data we result in Fig. 5.8.

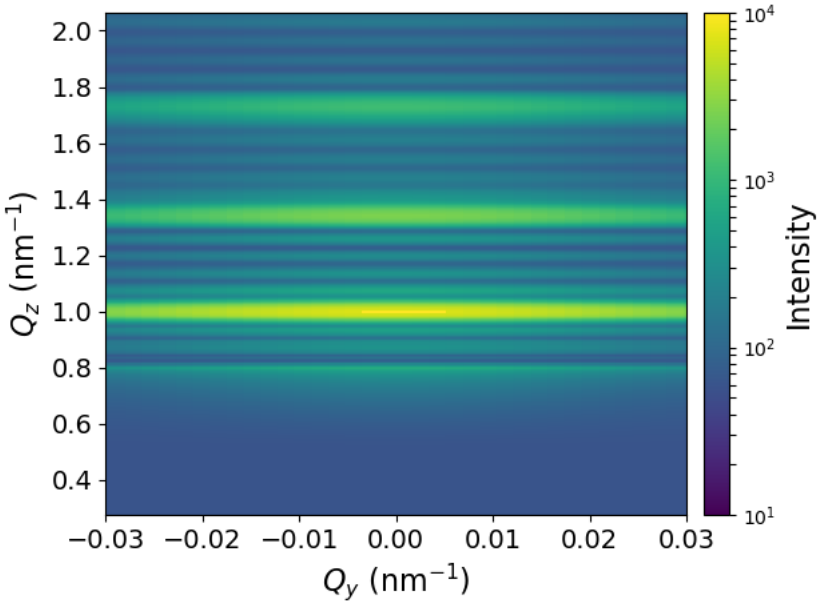

Figure 5.8: Simulated scattering pattern with BornAgain for the cold ML sample for the in-plane region.

Averaging over Q_y results in the in-plane signal as presented in Fig. 5.9. It is obvious that the simulated signal does not fit well to the data. Instead there is an underlying background signal related to a parasitic scattering signal from the beamstop.

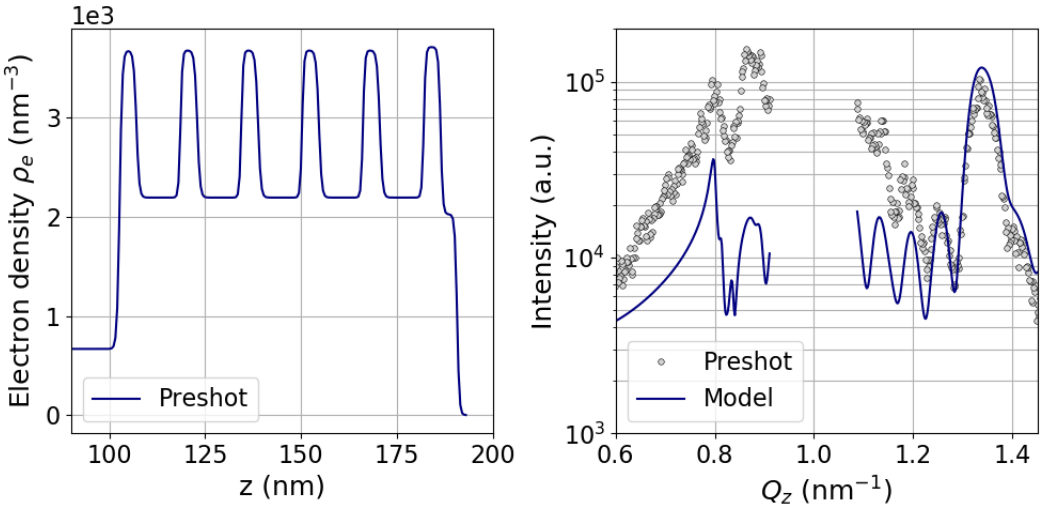

Figure 5.9: left: Electron density profile from a cold sample with parameters extracted from sample characterization. right: Grey points denote the experimental data, the blue solid line displays the simulated in-plane scattering signal according to the electron density profile.

The tails of this parasitic scattering have been modelled via $(Q_z - Q_0)^{-x}$ with x denoting an adjustable parameter with slightly different magnitudes for Q_z values above or below the specular position. Taking this background into account the solid line represents the resulting XDS model based on the density profile of the cold sample as obtained from the XRR characterization (see Fig. 5.10).

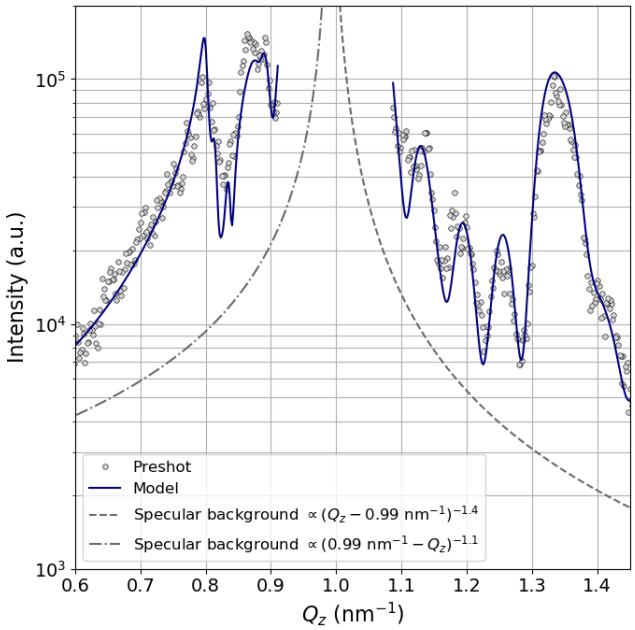

Figure 5.10: Grey points: XDS data from a preshot. The grey dotted line represents the model accounting for parasitic scattering tails from the beamstop used to block the highly intense specular signal at $Q_z = 0.99\,\mathrm{nm}^{-1}$. The blue solid line shows the model based on the density profile including the background.

In a next step, we demonstrate that the modelled tails fit also for two other preshots as shown in Fig. 5.11. Here, we only adjusted the beam intensity and the constant background value.

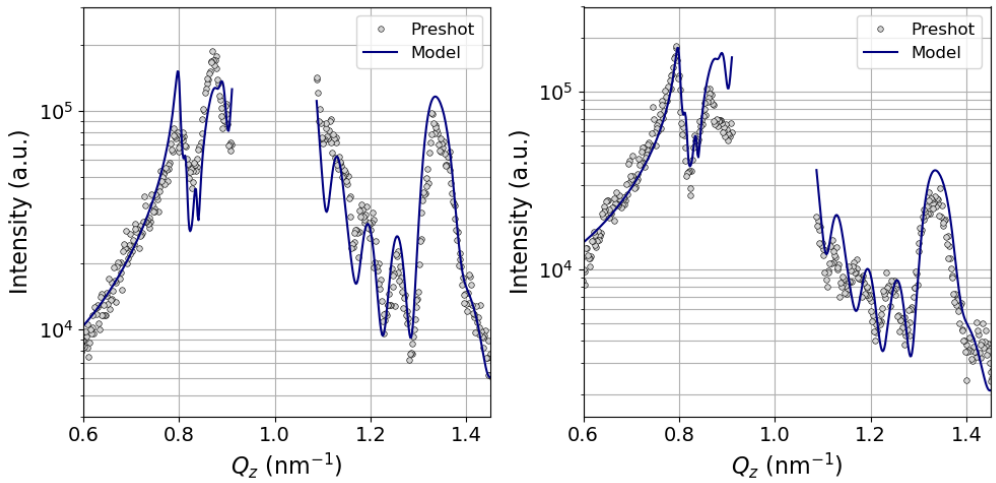

Figure 5.11: The grey points display the in-plane scattering data from two preshots and the blue solid line represents the simulated signal including the parasitic scattering background with adjusted beam intensity and constant background value.

5.1.3 In-plane scattering

Now, we discuss the features and changes we observed from the XDS data taken at various delay times (see Fig. 5.12). For 0.5 ps, we detect the two Yoneda peaks at $Q_z = 0.8\,\mathrm{nm}^{-1}$ and $Q_z = 0.87\,\mathrm{nm}^{-1}$ and on the right hand side the three Kiessig fringes and the ML Bragg peak at $Q_z = 1.33\,\mathrm{nm}^{-1}$. At 1.0 ps delay the underlying slope of the signal changed and with that also the relative height of the Kiessig fringes compared to the ML Bragg peak. 1.5 ps after laser irradiation we observe that the Ta Yoneda peak starts to decay while the Cu_3N peak remains constant. At $t = 2.0$ ps the ML Bragg peak is shifting to larger Q_z values. Furthermore, the Ta Yoneda peak vanished and the Cu_3N peak increases sharply. At 2.5 ps after laser irradiation we observe a reduced number of Kiessig fringes combined with a slightly shifted ML Bragg peak. At the left hand side the Cu_3N Yoneda peak appears more broadened and also slightly shifted to larger Q_z values. For 3.0 ps delay the ML Bragg peak starts to decay and the position of the remaining fringes is shifting to smaller Q_z values. At the Yoneda side, we observe a new peak arising at $Q_z = 0.73\,\mathrm{nm}^{-1}$ related to a reduced electron density in the surface region. This new peak appears more clearly at $t = 3.5$ ps and $t = 4.0$ ps. Besides that, the Kiessig fringes on the right hand side disappeared and the ML Bragg peak is continuously decreasing in intensity. At the time delay of $t = 5.0$ ps we find small features on the left hand side including a small Yoneda peak at the Cu_3N position ($Q_z = 0.8\,\mathrm{nm}^{-1}$). On the right hand side there is only a leftover from the ML Bragg peak. At the latest time delay of $t = 6.0$ ps we observe a clear Yoneda peak at $Q_z = 0.8\,\mathrm{nm}^{-1}$ and a broadened ML Bragg peak that may be splitted at $Q_z = 1.3\,\mathrm{nm}^{-1}$.

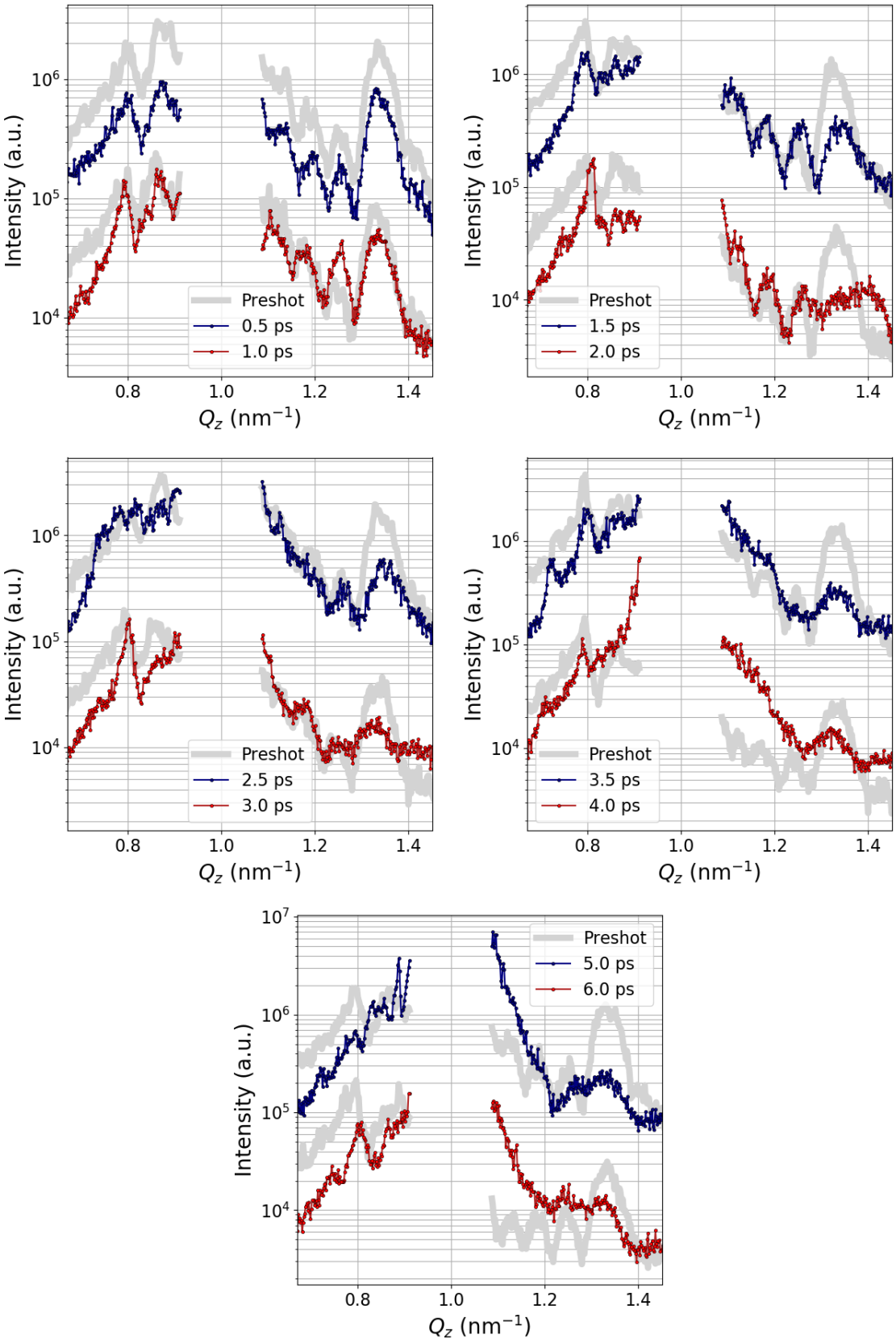

Figure 5.12: In-plane signal for various time delays. Blue and red lines denote the mainshots, respectively and the grey lines represent the corresponding preshot.

For a more quantitative analysis, we model now the in-plane XDS data using BornAgain. Here, we want to emphasize that the process of modelling the XDS data is not a straight forward task. Instead, it is a rather complex and time consuming process because we have to combine the logical temporal evolution with a mathematical process including the minimization of χ^2. As an counter example, Fig. 5.13 shows a simulated scattering signal and electron density profile where BornAgain modelled all possible layer parameters with a large parameter range. For the very short time delay of $t = 0.5\,\mathrm{ps}$ this kind of electron density profile is obviously not correct since the intermixing of all the layers cannot have taken place at this early stage.

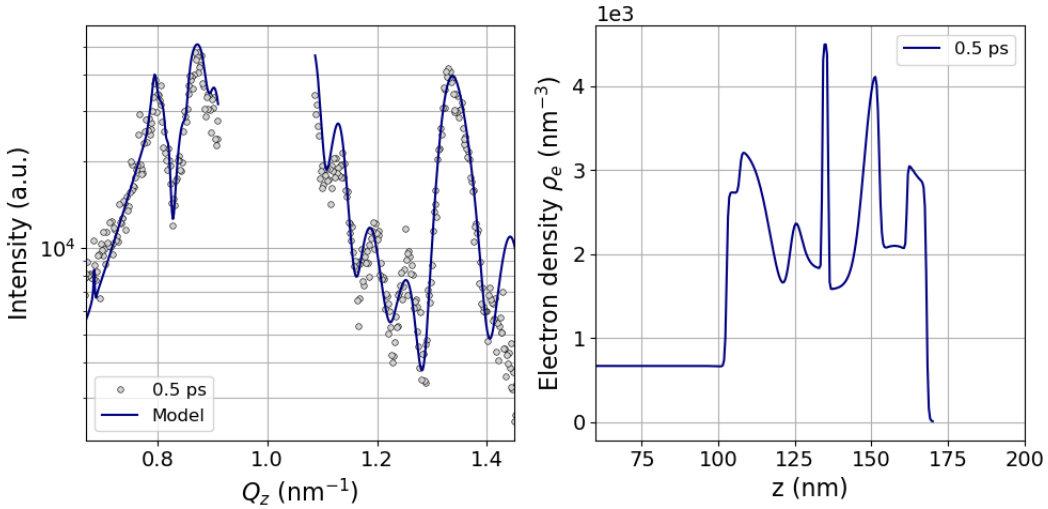

Figure 5.13: Problem of non-uniqueness: Refined in-plane signal from a cold sample with a huge parameter range.

Therefore, it is important to consider the following restrictions for the modelling process:

1.) The laser impinges from the surface (right) following that the ML starts to change the electron density also from the surface.

2.) Parameters such as electron density or layer thickness cannot change orders of magnitude meaning that we have to choose a realistic parameter range for the modelling.

3.) The ML cannot increase in volume meaning that regions with increased electron density need regions with decreased electron density for compensation.

Here only a selection of time delays is shown, the full analysis can be found in the appendix (chapter 8.2).

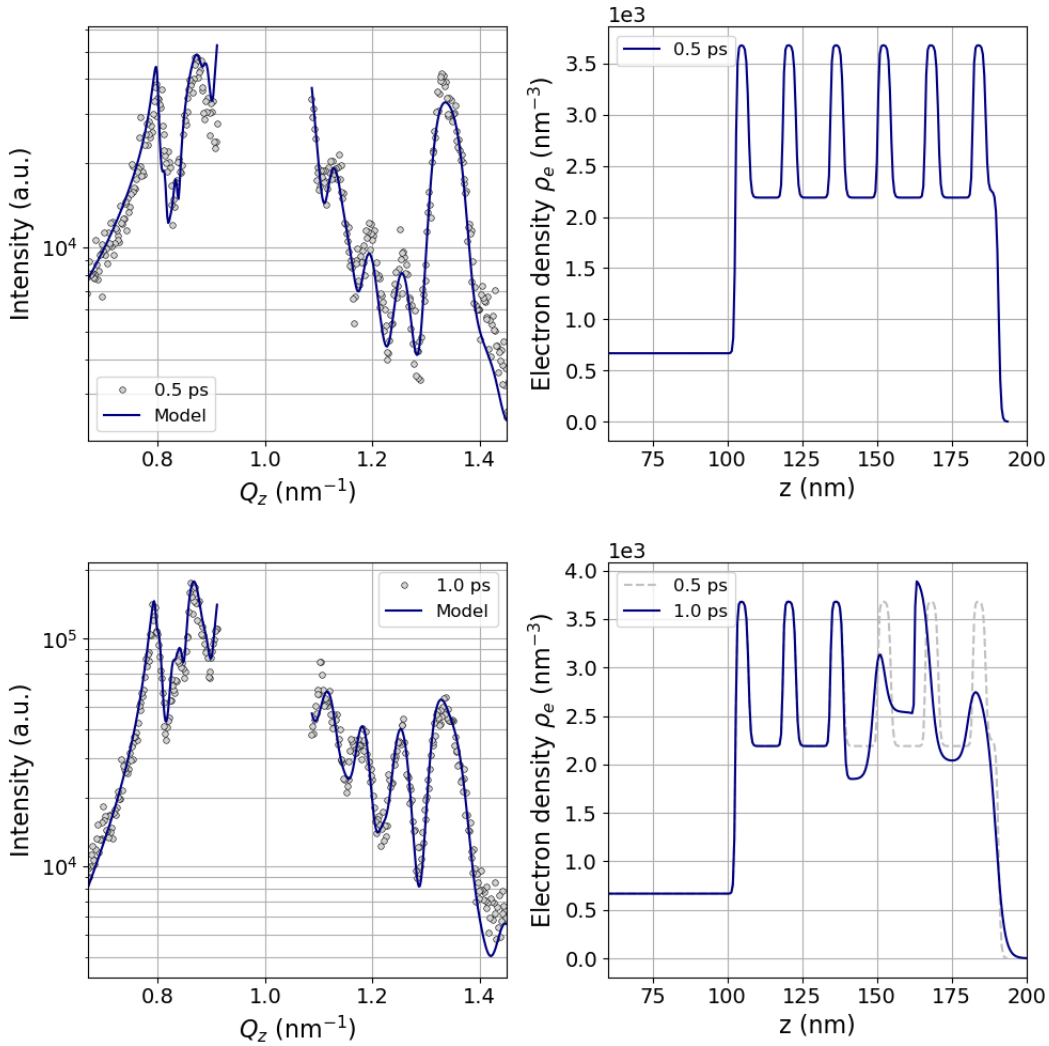

Figure 5.14: top: Refined in-plane signal for $t = 0.5\,\text{ps}$. bottom: Refined in-plane signal for $t = 1.0\,\text{ps}$.

For $t = 0.5\,\text{ps}$ the preshot model fits quite good indicating that no preplasma was created during laser excitation (Fig. 5.14 top). For $t = 1.0\,\text{ps}$, we expect that the ML changes its structure starting from the surface (from the right). Therefore we fixed the deeper layers of the initial parameters and refine only the first 3 double layers. With these assumptions we obtain the simulation model and corresponding electron density model presented in Fig. 5.14 bottom. We observe that the topmost Ta layer is reduced in density, while the second Ta and the Cu_3N layers are being compressed and shifted slightly inwards by the ablation pressure from the first layer. Note that the deeper third double layer already shows a reduced density at this time while the remaining layers are still

intact. This changes at $t = 3.0\,\text{ps}$ when intermixing and compression continues and the high density material is now mostly located at regions previously hosting the low density Cu_3N layers (Fig. 5.15 top). The ablation front also successively moved inwards with now the topmost 30 nm of material ablated. Finally, at $t = 5.0\,\text{ps}$ the previously sharp ML Bragg peak reduces in intensity and also broadens considerably as shown in Fig. 5.15 bottom. However, we can still identify Yoneda peaks indicating the presence of higher electron density layer than the Si substrate.

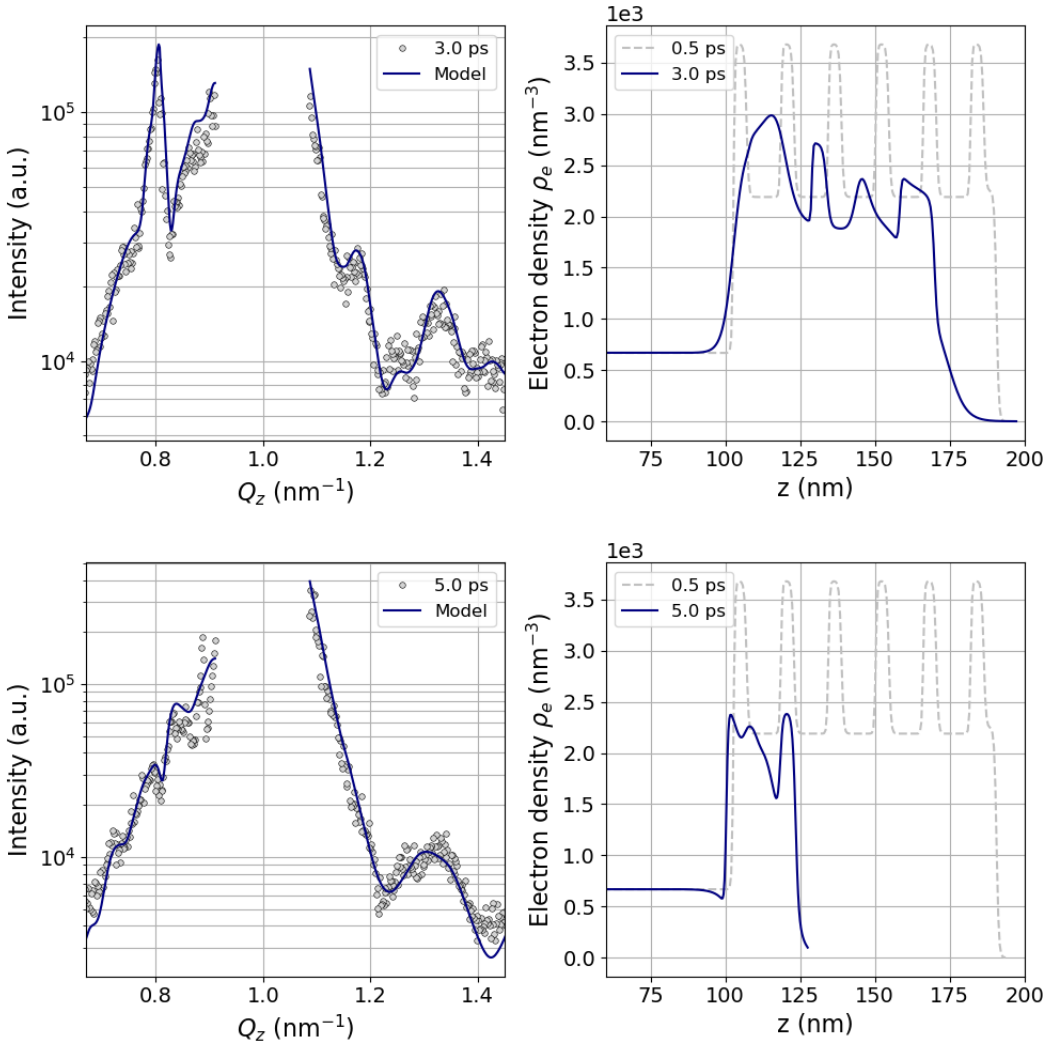

Figure 5.15: top: Refined in-plane signal for $t = 3.0\,\text{ps}$. bottom: Refined in-plane signal for $t = 5.0\,\text{ps}$.

Now, we compare the resulting electron density profiles extracted from the modelled XDS data shown in Fig. 5.16. For reasons of comparison we labelled the double layers $1 - 5$ starting from the ML surface. After $t = 1.0\,\text{ps}$, we find that the topmost and third Ta/Cu_3N layers are reduced in density compared to the initial ML, while the 2nd Ta and

the Cu_3N layers being compressed and shifted slightly inwards by the ablation pressure from the first layer. The remaining layers are still intact. Based on the maximum depth of density modulation of 40 nm at 1 ps delay we can estimate a value for the thermal diffusion velocity of $v = 4 \times 10^4\,\mathrm{m\,s^{-1}}$.
1.5 ps after laser excitation the first Ta layer disappeared while the 2nd Ta layer is still compressed but thinner compared to 1.0 ps. The third Ta layer has further decreased in density. Furthermore, the first three Cu_3N layer display an increased density.
At $t = 2.0$ ps the topmost layer is fully ablated while the rest of the ML starts to show intermixing of the Ta and Cu_3N layers with the heatwave reaching the substrate. However, the Ta layers can still be recognized and are located at their original positions.
This changes at 2.5 ps when intermixing and compression continues and the high density material is now mostly located at regions previously hosting the low density Cu_3N layers, only the last Ta layer is located at its original position. The ablation front also successively moved inwards. After 3.0 ps also the last Ta layer has intermixed with the Cu_3N layers and the substrate.
At $t = 3.5$ ps we find a new sharp peak at the ML surface located at $z \approx 140$ nm supported also by the appearance of a new Yoneda peak at $Q_z = 0.73\,\mathrm{nm^{-1}}$ (see Fig. 5.12). Upon temporal evolution at $t = 4.0$ ps the sample thickness is further reduced by 40 nm and the ML structure shows only a few density oscillation reminiscent of the previously ordered ML structure. Finally, at $t = 5.0$ and 6.0 ps the previously sharp ML Bragg peak reduces in intensity and also broadens considerably. The resulting density profile shows a film thickness of 30 nm with some smaller density oscillations still existing.

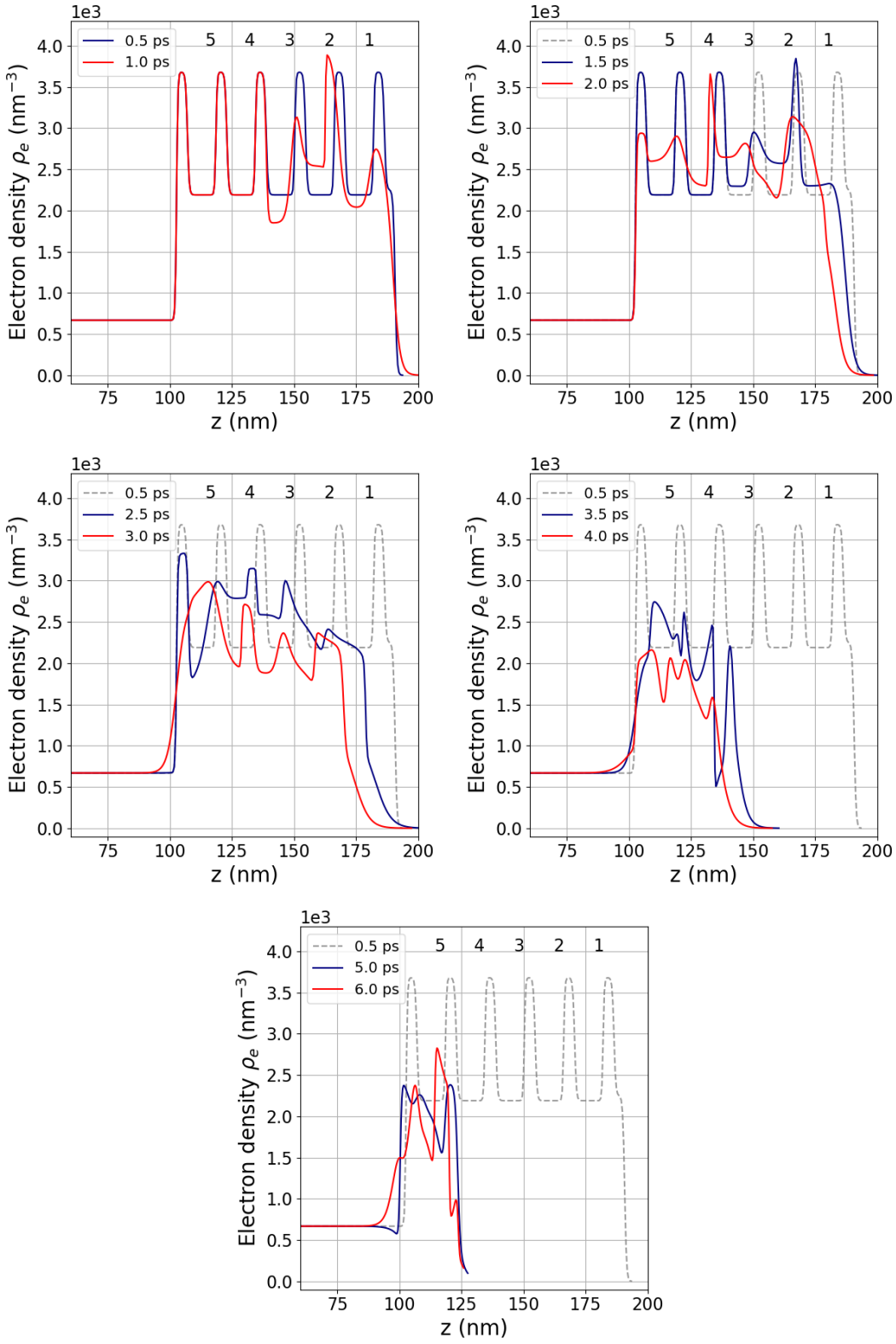

Figure 5.16: Time evolution of corresponding density profiles of modelled XDS simulations.

Having described the time dependence of the density profiles we now extract several parameters from the profiles. We start with the difference ($\Delta\rho_e$) in densities between two consecutive delay times as shown in Fig. 5.17 for selected time intervals. At early times (blue line at 1 ps) we observe the start of ablation into the vacuum visible as a reduction of density at the front surface. Deeper inside the ML structure the difference shows sharp transitions from reduced to enhanced densities which we attribute to the compression of the ML generating sharp differences between new and old interface positions. The sharp features also indicate that intermixing of the layers does not play a role at early times. In contrast, at 2.5 ps the differences are rounded much more consistent with starting of intermixing between the layers while at the surface the ablation continues as visible by the negative values of $\Delta\rho_e$. At 3.5 ps we observe a strong onset of ablation with almost 30 nm of material ablating within 0.5 ps.

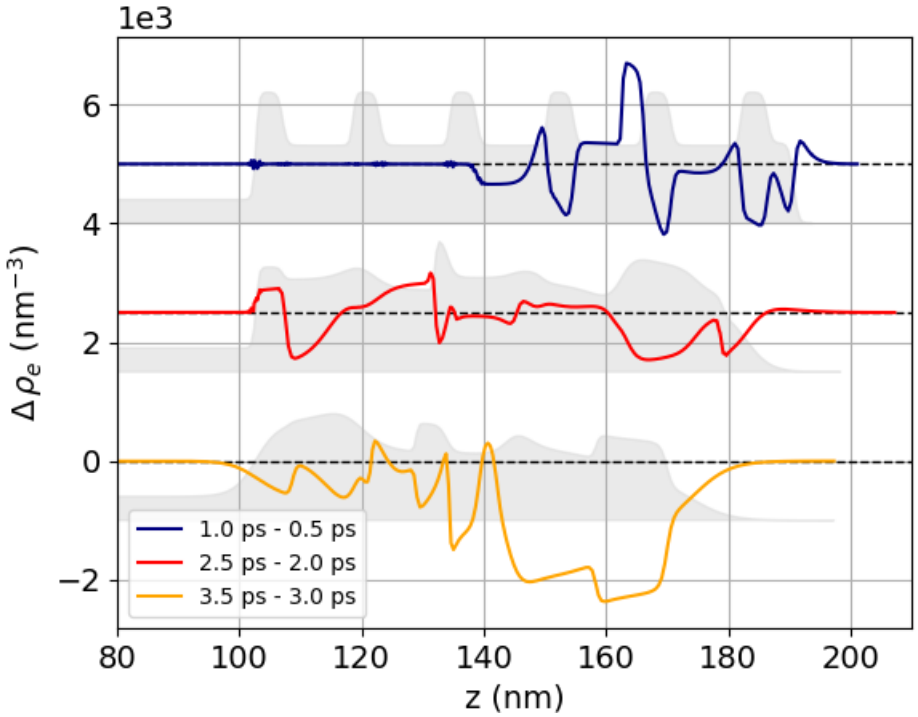

Figure 5.17: Depth resolved differences in electron density $\Delta\rho$. The blue line represents the differences between 1.0 and 0.5 ps, the red line displays the differences between 2.5 and 2.0 ps and the yellow line shows the differences between 3.5 and 3.0 ps. The grey shadows indicate the electron density profiles at $t = 0.5$, 2.0 and 3.0 ps, respectively.

Additionally, we investigate the surface position as a function of time delay as illustrated in Fig. 5.18. We define the surface as the position where $\rho_e = 2.0 \times 10^3\,\mathrm{nm}^{-3}$ and find that up to 2.5 ps the ablation velocity is rather slow, namely $0.6 \times 10^4\,\mathrm{m\,s}^{-1}$, and accelerating between 2.5 and 5 ps to a velocity of $2.4 \times 10^4\,\mathrm{m\,s}^{-1}$ resulting in a strong surface ablation of roughly 55 nm. After 5 ps the surface ablation velocity is decreasing again to $0.4 \times 10^4\,\mathrm{m\,s}^{-1}$ indicating that the dynamics are slowing down ending with a 30 nm thick film.

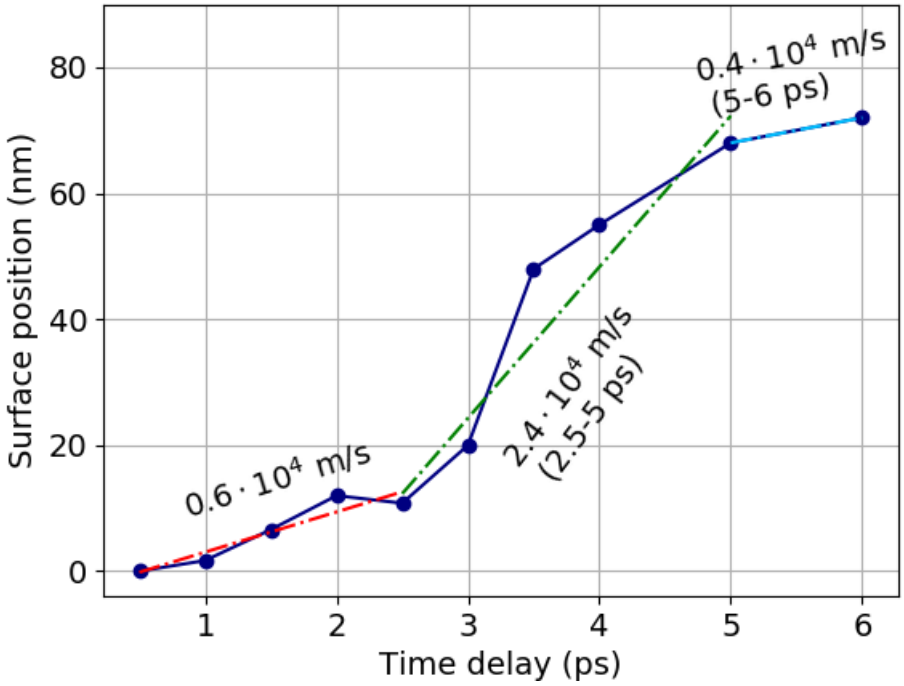

Figure 5.18: Surface position as a function of time delay. The surface position is defined as $\rho_e = 2.0 \times 10^3\,\mathrm{nm}^{-3}$. The colored dashed lines denote the surface ablation velocity for different time intervals.

5.1.4 Uniqueness of model refinement

A known problem of reconstructing electron density profiles from XDS data is the appearance of non-unique solutions since the in-plane signal is connected to the electron density basically via the absolute square of the Fourier transform. By determining the absolute square of the Fourier transform the phase information gets lost and for that reason we cannot exclude the existence of other density profiles providing different local minima in parameter space. However, we show here a method to minimize these problems by simultaneous data refinement of in-plane and out-of-plane scattering signals.
The in-plane signal represents an average of a region of 30 pixels centered around the position of $Q_y = 0\,\mathrm{nm}^{-1}$. The out-of-plane signal is an average of the scattering signal within the interval $Q_y = 0.15\,\mathrm{nm}^{-1}$ to $0.5\,\mathrm{nm}^{-1}$ (see Fig. 5.19).

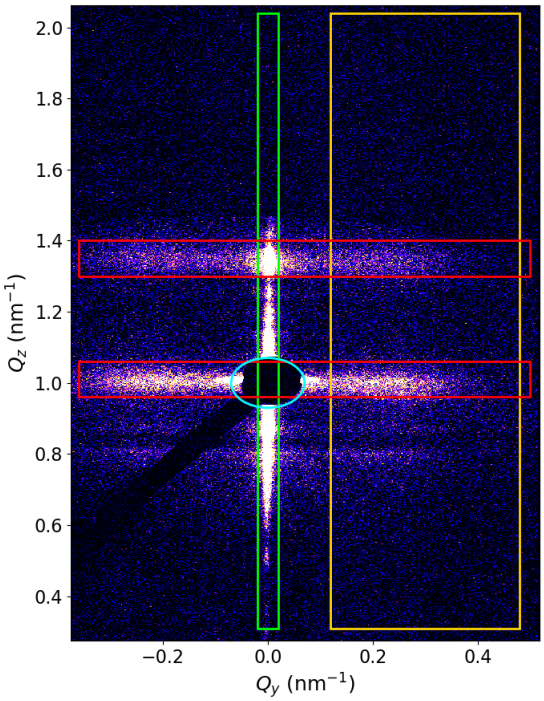

Figure 5.19: Scattering signal from the cold sample without laser excitation. The blue circle indicates the beamstop, the green box represents the in-plane signal, the yellow box shows the out-of-plane signal and the red lineout denotes the diffuse scattering signal.

Here we investigate in detail the aspects of uniqueness of the refinement results for $t = 2.0$ (appendix chapter 8.4) and 3.5 ps. Fig. 5.20 displays the in-plane signal as a function of the corresponding vertical wave vector transfer Q_z and two fits according to the models displays in Fig. 5.20 (right). While both modelled X-ray signals look similar to a certain extent we find a clear difference in the corresponding χ^2 values favouring the blue density profile. Further evidence for this can now be obtained by inspecting the corresponding out-of-plane scattering signal.

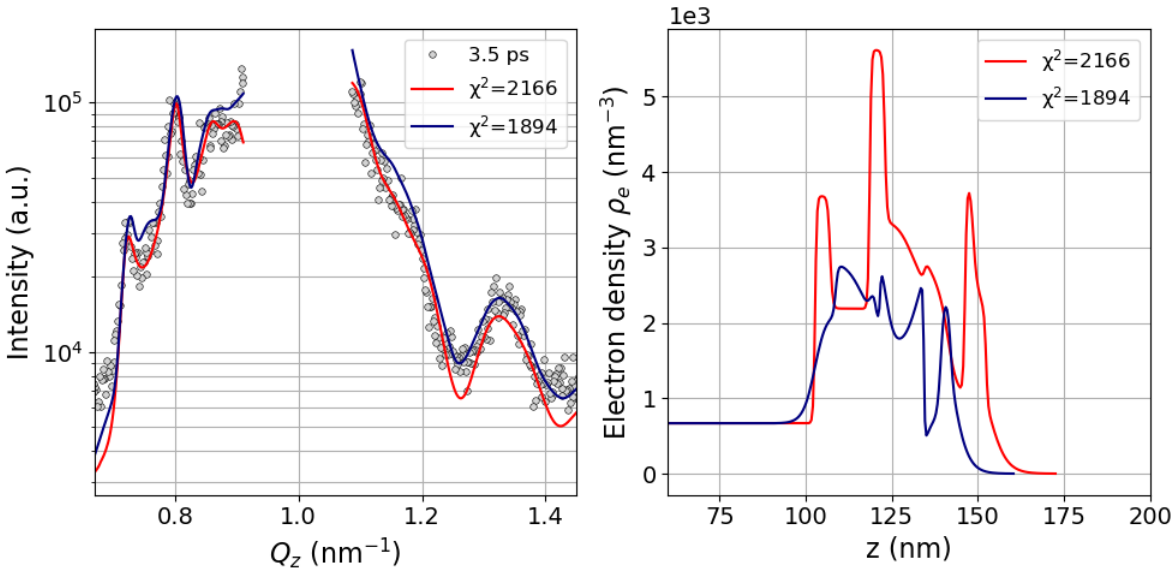

Figure 5.20: Two fits for the in-plane signal with $t = 3.5\,\text{ps}$ time delay. Both X-ray signals look similar while showing very different density profiles.

In terms of scattering, the out-of-plane signal does not only depend on the density profile but also on roughness and correlations between the layers. These correlations are modelled in the program BornAgain with the following statistical description of the height-height correlation function for the j$^{\text{th}}$ interface with height contour $U_j(x, y)$

$$< U_j(x,y)\, U_j(x',y') >= \sigma^2 \exp\left[-\left(\frac{\tau}{\xi_{Lj}}\right)^{2h}\right] \tag{5.1.1}$$

with

$$\tau = \sqrt{(x-x')^2 + (y-y')^2}. \tag{5.1.2}$$

We observed that the Q_z-dependence of the out-of-plane signal is not very sensitive to the absolute value of the lateral correlation lengths ξ_L, although it is quite sensitive to differences in the correlation lengths between different layers in the following way: correlation lengths $\xi_L > 30\,\text{nm}$ switch the scattering contribution of the corresponding layer „on“, while a small value of $\xi_L = 1\,\text{nm}$ switches the contribution to the out-of-plane signal „off“. Upon pumping we find that the in-plane correlation lengths decrease starting from the top layers. In contrast to this, we find that the vertical correlation length $\xi_\perp$ needs to be kept at a value on the order of the ML thickness.
Fig. 5.21 and 5.22 display the out-of-plane scattering signal for both density profiles (Fig. 5.20 (right)) with the corresponding correlation lengths ξ_L from top to bottom displayed

in the subcaptions (layer 1 is the topmost layer and layer 14 the layer closest to the substrate).

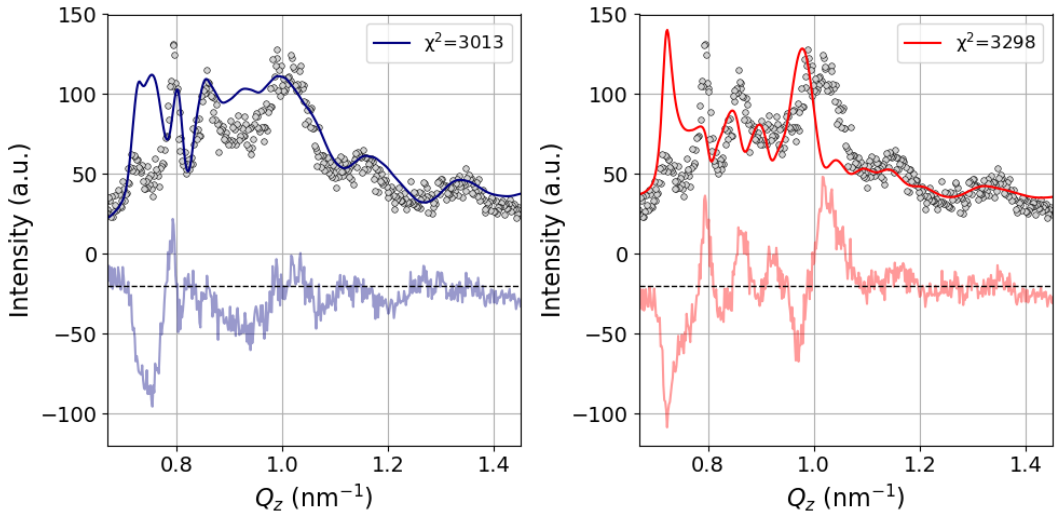

(a) Layer $1-14$: $\xi_L = 30\,\text{nm}$

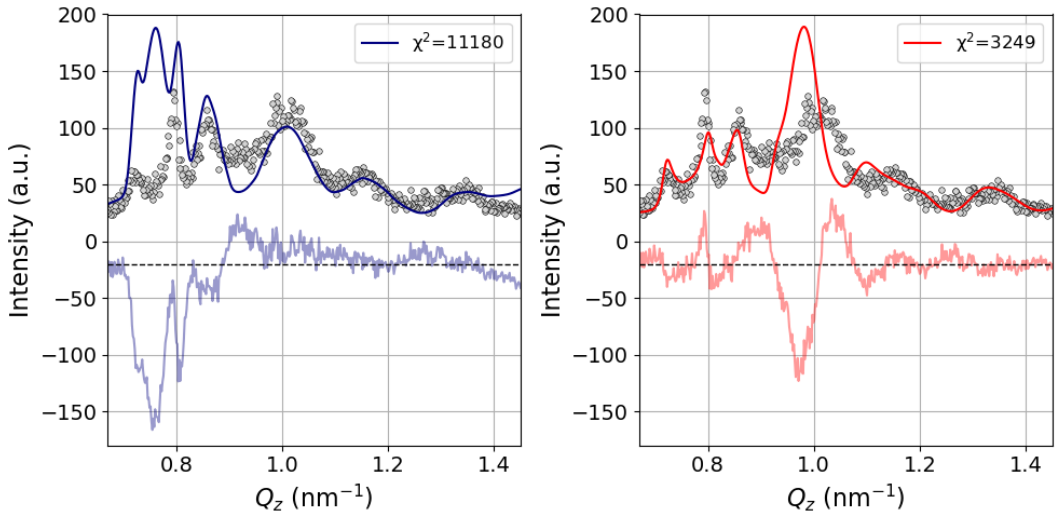

(b) Layer $1-3$: $\xi_L = 1\,\text{nm}$; Layer $4-14$: $\xi_L = 30\,\text{nm}$

Figure 5.21: Out-of-plane signal along Q_z based on the electron density profile in Fig. 5.20 (right). The grey points denote the XDS data, the blue and red lines indicate the simulated out-of-plane signal and the light blue and red lines display the differences between simulation and data. The blue colored figure (left) corresponds to the blue electron density profile and the red colored figure to the red profile, respectively. (a) displays the out-of-plane signal with a lateral correlation length $\xi_L = 30\,\text{nm}$ for all layers. (b) shows the out-of-plane signal with a decreased lateral correlation length $\xi_L = 1\,\text{nm}$ for the first three layers.

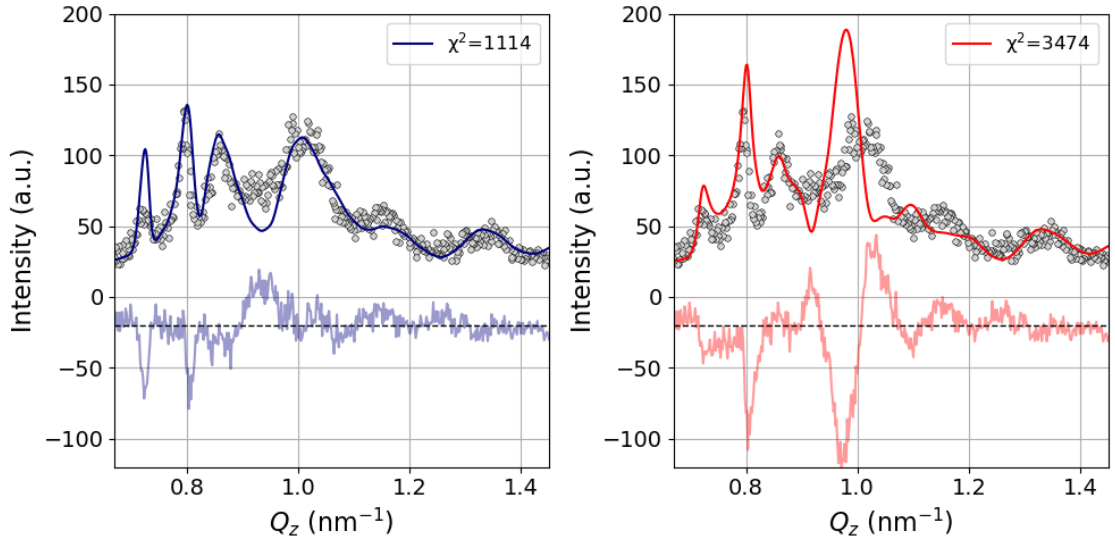

(a) Layer $1-10$: $\xi_L = 1\,\text{nm}$; Layer $11-14$: $\xi_L = 30\,\text{nm}$

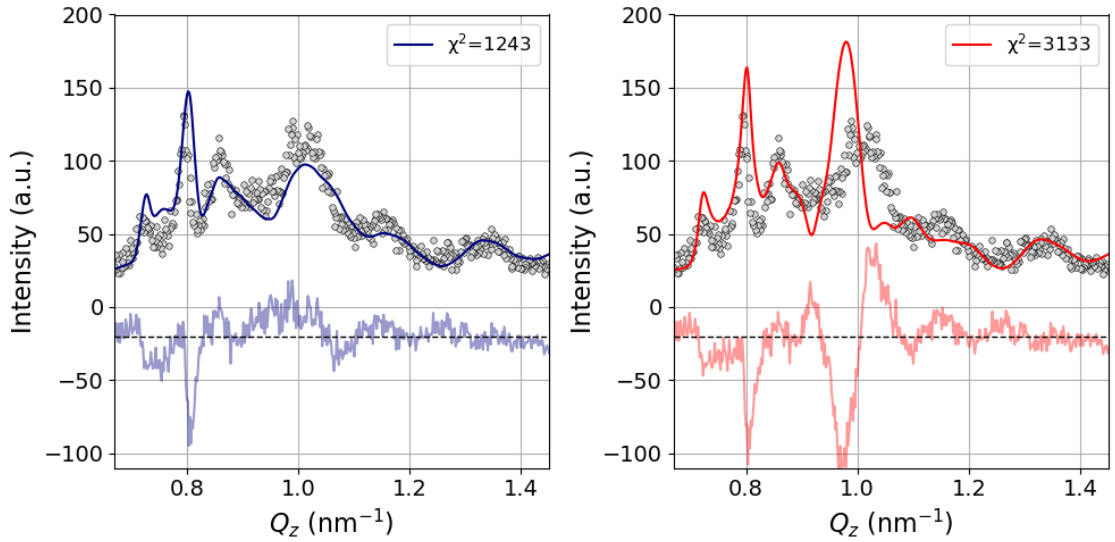

(b) Layer $1-12$: $\xi_L = 1\,\text{nm}$; Layer $13-14$: $\xi_L = 30\,\text{nm}$

Figure 5.22: Out-of-plane signal along Q_z based on the electron density profile in Fig. 5.20 (right). The grey points denote the XDS data, the blue and red lines indicate the simulated out-of-plane signal and the light blue and red lines display the differences between simulation and data. The blue colored figure (left) corresponds to the blue electron density profile and the red colored figure to the red profile, respectively. (a) displays the out-of-plane signal with a lateral correlation length $\xi_L = 1\,\text{nm}$ for layer $1-10$ and $\xi_L = 30\,\text{nm}$ for layer $11-14$. (b) shows the out-of-plane signal with a decreased lateral correlation length $\xi_L = 1\,\text{nm}$ for layer $1-12$.

We present the resulting χ^2 for all cases in Table 5.4 and find that the blue dispersion profile fits the out-of-plane signal significantly better than the red dispersion profile. This is also apparent from an inspection of the difference traces (light blue and red lines). Thus a simultaneous inspection of in-plane and out-of-the plane scattering components helps considerably to narrow down the search for density profiles. We note, however, that ultimately an extension of the available Q-space would be beneficial.

3.5 ps	$\xi_L = 1$ nm	$\xi_L = 30$ nm	χ^2 blue profile	χ^2 red profile
1	-	layer $1-14$	3013	3298
2	layer $1-3$	layer $4-14$	11180	3249
3	**layer $1-10$**	**layer $11-14$**	**1114**	**3474**
4	layer $1-12$	layer $13-14$	1243	3133

Table 5.4: Overview of the different combinations of lateral correlation length ξ_L and resulting χ^2 values from Fig. 5.21 and 5.22.

For judging and demonstrating the sensitivity of the out-of-plane scattering signal for changes in the dispersion profile we systematically reduced the dispersion profile at $t = 3.5$ ps layer by layer starting from the top (see Fig. 5.23 and 5.24). It becomes evident that the dispersion profile has a pronounced influence on the out-of-plane scattering signal as well.

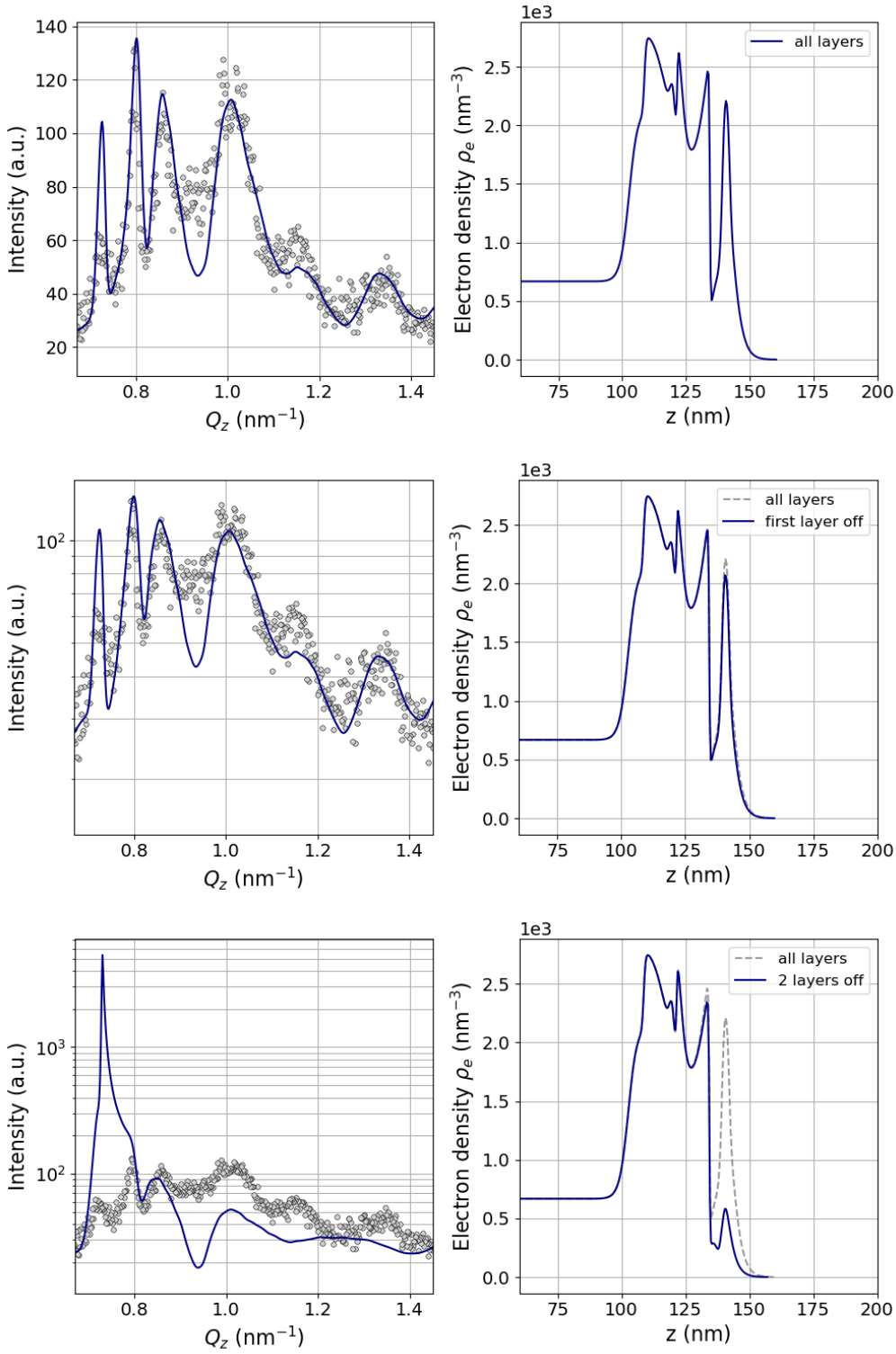

Figure 5.23: Out-of-plane signal along Q_z with systematically reduced number of surface layers from the density profile.

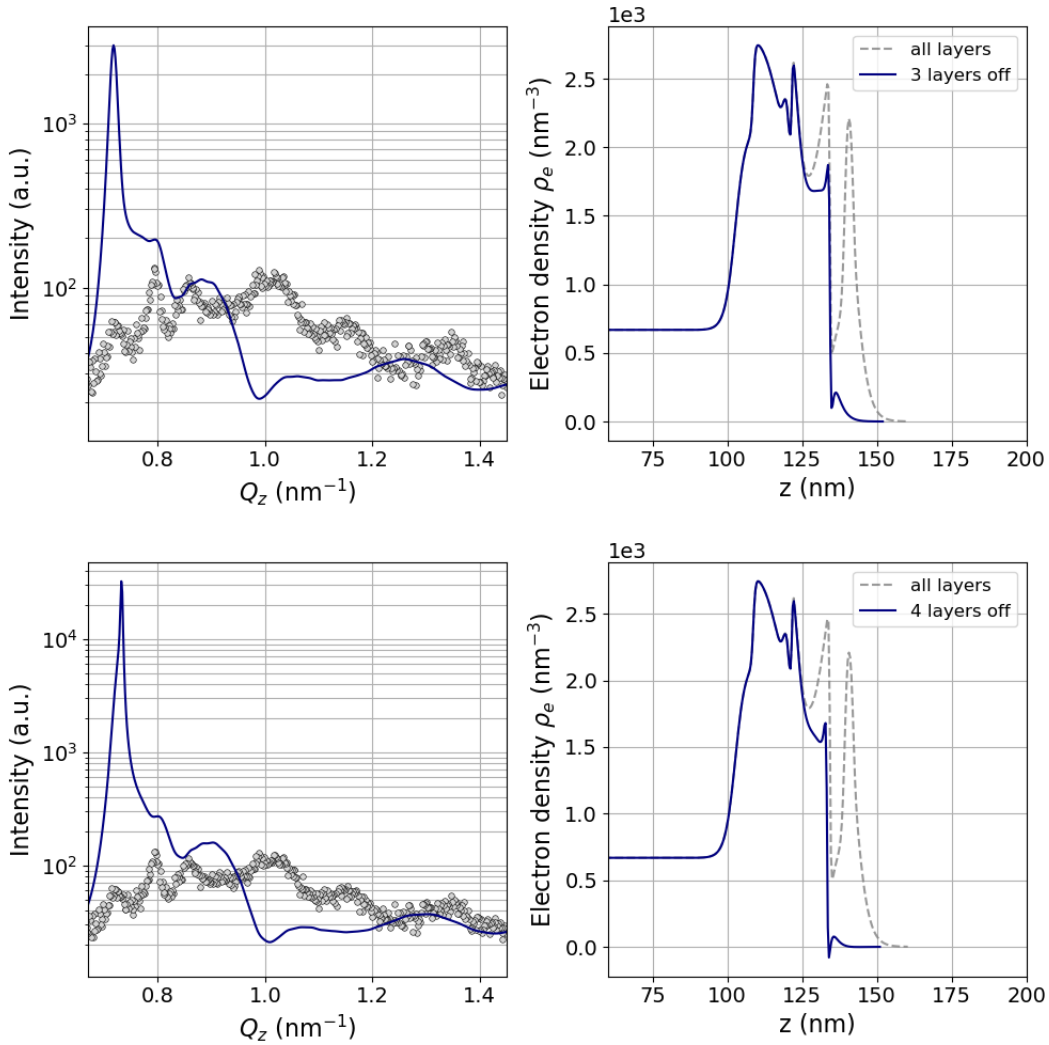

Figure 5.24: Out-of-plane signal along Q_z with systematically reduced number of surface layers from the density profile.

5.1.5 Time dependence of out-of-plane scattering

Fig. 5.25 displays the out-of-plane scattering data including refinement with varied lateral correlation lengths ξ_L. For $t = 0.5\,\mathrm{ps}$, we detect the two Yoneda peaks at $Q_z = 0.8\,\mathrm{nm}^{-1}$ and $0.87\,\mathrm{nm}^{-1}$, the central Bragg peak at $Q_z = 0.99\,\mathrm{nm}^{-1}$ and the next Bragg peak at $Q_z = 1.33\,\mathrm{nm}^{-1}$. The small fringes observed in the in-plane signal are only barely visible since the intensity is orders of magnitude smaller compared to the in-plane signal. We extract from the in-plane scattering at this early time of $t = 0.5\,\mathrm{ps}$ a lateral correlation length of all layers to be $\xi_L = 30\,\mathrm{nm}$.

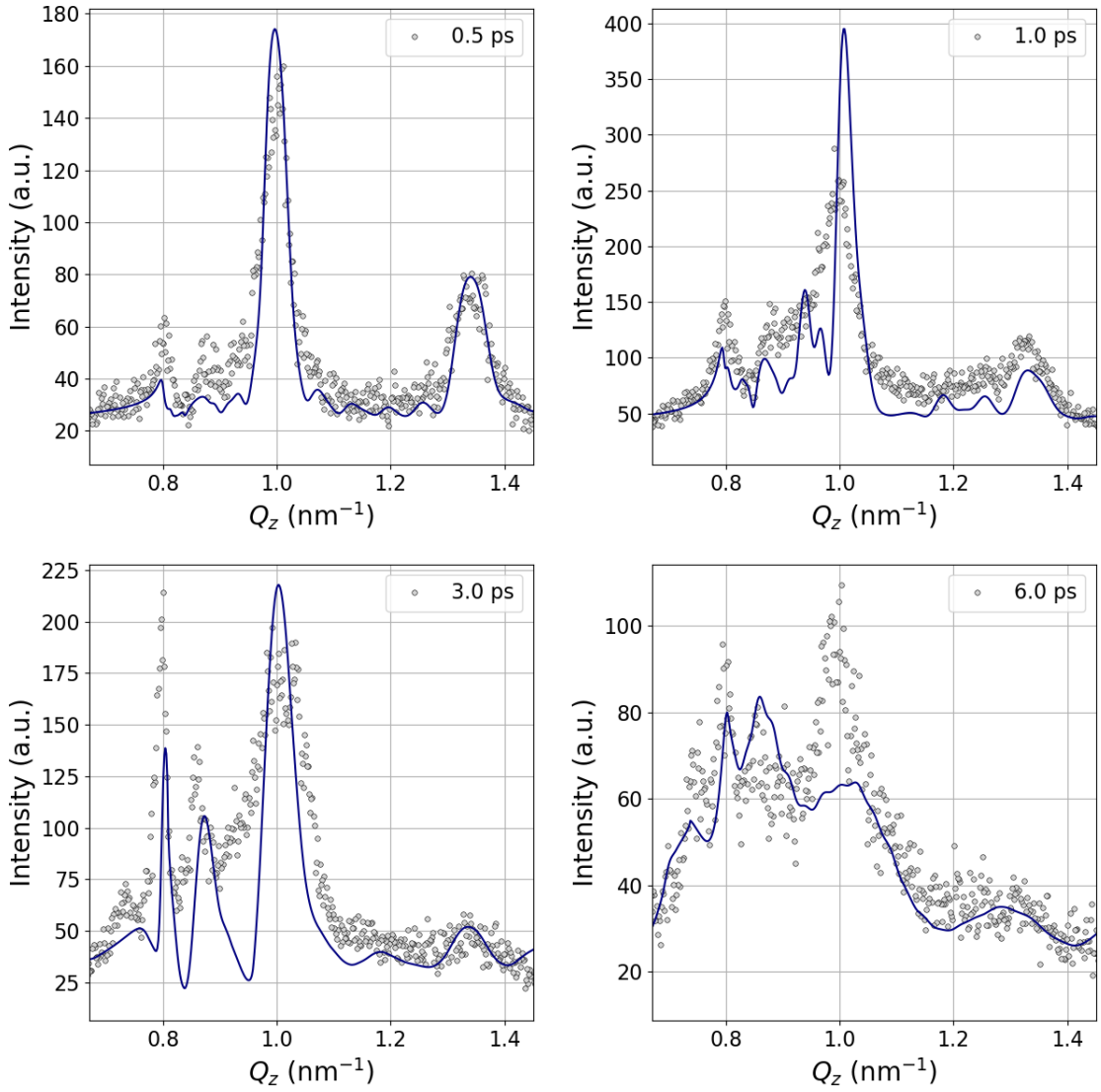

Figure 5.25: Refined out-of-plane signals along Q_z for various time delays.

Refining the experimental data for $t = 1.0\,\text{ps}$ we use the extracted electron density model and adjust the lateral correlation length ξ_L of the first 3 layers to $\xi_L = 1\,\text{nm}$ while the correlation length of the deeper layers remains constant. At $t = 3.0\,\text{ps}$ the out-of-plane signal is structurally changing as the Bragg peak at $Q_z = 1.33\,\text{nm}^{-1}$ is mostly vanished. The Yoneda peaks appear now as really sharp and intensive peaks. Additionally, we find a new signal appearing from a new Yoneda peak at $Q_z = 0.7\,\text{nm}^{-1}$. With the model from the in-plane scattering we adjust the lateral correlation length ξ_L of layer $1-4$ to $1\,\text{nm}$ in order to fit these sharp Yoneda peaks.
For the large delay time of $t = 6.0\,\text{ps}$ there is no clear structure for $Q_z > 0.99\,\text{nm}^{-1}$ anymore which leads to the assumption that almost all layers have a reduced lateral correlation length. Taking the model from the in-plane scattering we decrease ξ_L to $1\,\text{nm}$ for layer $1-12$ following that just the thermal SiO_2 and the Si substrate have the initial lateral correlation length of $\xi_L = 30\,\text{nm}$. An overview of ξ_L is listed in Table 5.5.
A reduced lateral correlation length ξ_L implies here that the interfaces get more rough upon laser excitation. We notice that the interfaces change their structure starting from surface for the early delay times ($1.0\,\text{ps}$) to the deeper layers for the large delay times such as $6.0\,\text{ps}$.

delay	$\xi_L = 1\,\text{nm}$	$\xi_L = 30\,\text{nm}$
$0.5\,\text{ps}$	–	Layer $1-14$
$1.0\,\text{ps}$	Layer $1-3$	Layer $4-14$
$3.0\,\text{ps}$	Layer $1-4$	Layer $5-14$
$6.0\,\text{ps}$	Layer $1-12$	Layer $13-14$

Table 5.5: Lateral correlation lengths ξ_L used for the out-of-plane refinement along Q_z for various time delays.

5.1.6 Intermediate intensity

Fig. 5.26 and 5.27 display the in-plane signal and the density profiles for average laser intensity of $I_L = 4 \times 10^{15}\,\mathrm{W/cm^2}$. Note that a negative delay time means that the X-ray beam arrives the ML sample **before** the laser irradiation.
At $t = -1.0\,\mathrm{ps}$ all the features discussed in section 5.1.3 are visible including the Yoneda peaks, the small fringes and the Bragg peak. To model the in-plane data we used the density profile from the cold sample demonstrating that 1 ps before laser irradiation the sample structure did not change. 0.5 ps before laser irradiation we detect significant changes in the Yoneda peaks since the peak at $Q_z = 0.87\,\mathrm{nm^{-1}}$ is strongly reduced. Additionally, the fringes between $Q_z = 1.1 - 1.3\,\mathrm{nm^{-1}}$ start to vanish meaning that already before the temporal peak of the laser pulse arrives, the ML structure is affected by the rising edge of the laser pulse. Modelling the XDS data we result in an electron density profile shown in Fig. 5.26 bottom right.

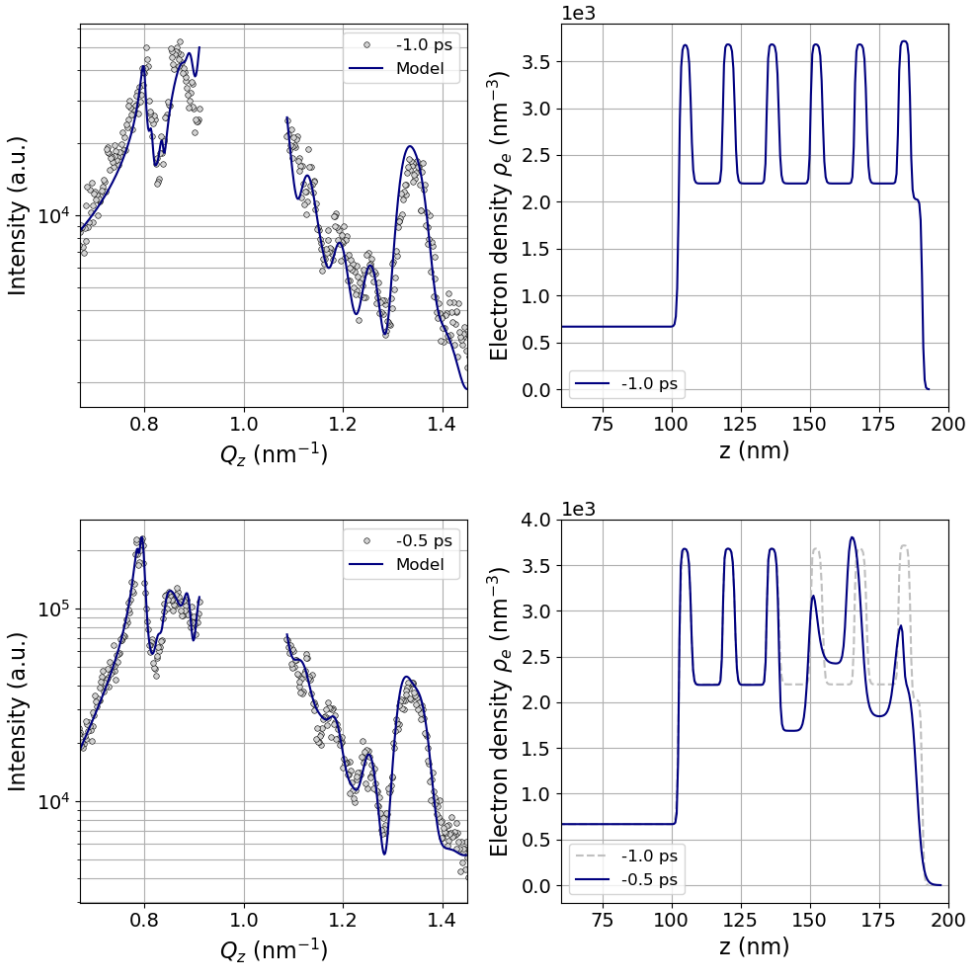

Figure 5.26: In-plane signals with higher laser intensity $I_L = 4 \times 10^{15}\,\mathrm{W/cm^2}$ for $t = -1.0\,\mathrm{ps}$ (top) and $t = -0.5\,\mathrm{ps}$ (bottom).

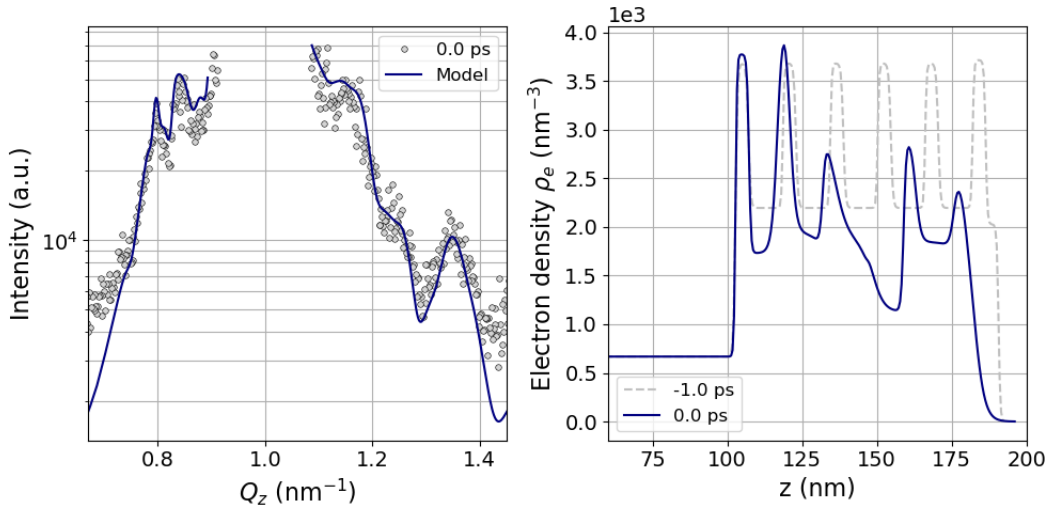

Figure 5.27: In-plane signals with higher laser intensity $I_L = 4 \times 10^{15}\,\mathrm{W/cm^2}$ for $t = 0.0\,\mathrm{ps}$.

Interestingly, at $t = 0.0\,\mathrm{ps}$ the in-plane signal has structurally changed, e.g. the Yoneda peaks are strongly reduced and the fringes are not visible anymore. The Bragg peak is decreased as well.

Investigating the resulting electron density profiles (Fig. 5.28) we find even before the main laser pulse arrives at the sample, the ML structure is strongly changing affected by the rising edge of the laser pulse. While at $t = -1.0\,\mathrm{ps}$ the model for the cold sample fits well, at $t = -0.5\,\mathrm{ps}$ the density of the first and 3rd double layer is reduced while the 2nd double layer is compressed showing that a compression wave already travelled through the first 60 nm of the ML sample. For $t = -0.4\,\mathrm{ps}$ we find a rather similar structure, the ML has just increased in roughness. At $t = -0.3\,\mathrm{ps}$ the surface appears rather smooth since the clear layer structure is not visible anymore. Instead the 5th Ta layer is strongly compressed while the 3rd and 4th Cu_3N layers are reduced in density. At $t = -0.15$ and $0.0\,\mathrm{ps}$ the electron density is reduced the first 75 nm starting from the top. Only the 2 deepest Ta layers are slightly compressed. As a result we find that the higher laser intensity of $I_L = 4 \times 10^{15}\,\mathrm{W/cm^2}$ causes much faster dynamics inside the sample since already at $t = 0.0\,\mathrm{ps}$, indicating the laser peak arrives the sample, the structure has strongly changed while for the lower laser intensity of $I_L = 4 \times 10^{14}\,\mathrm{W/cm^2}$ 0.5 ps after the laser pulse we cannot detect any changes in the sample structure. The full in-plane analysis for the intermediate intensity of $I_L = 4 \times 10^{15}\,\mathrm{W/cm^2}$ can be found in chapter 8.3.

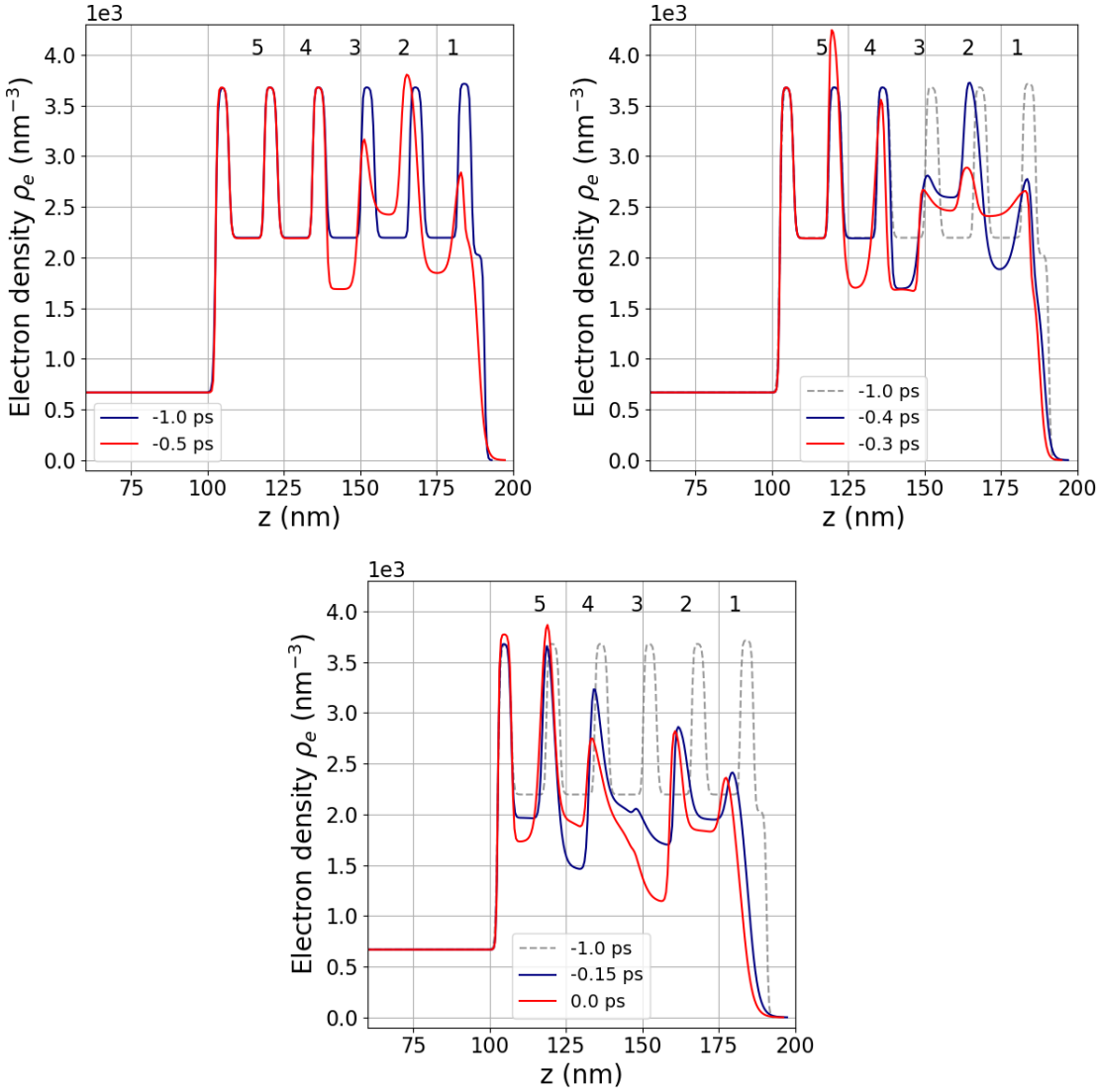

Figure 5.28: Time evolution of corresponding density profiles of modelled XDS simulations showing the effect of the rising edge of the laser.

5.2 SACLA 2020

From the SACLA 2018 data we were able to reconstruct the electron density profiles. However, due to the limited Q_z-space available a precise determination of the density profiles was quite difficult. Therefore, we performed a second experiment with a larger Q_z-space up to $Q_z = 2.6\,\mathrm{nm}^{-1}$ as displayed in Fig. 5.29 showing the in-plane signal of an unperturbed ML sample with 200 nm Aluminium top layer. The large number of Kiessig fringes and Bragg peaks allows a more accurate reconstruction of the electron density profiles. Furthermore, we modified our samples with a 200 nm Aluminium top layer to obtain access to larger delay times $> 6\,\mathrm{ps}$ than in the first experiment.

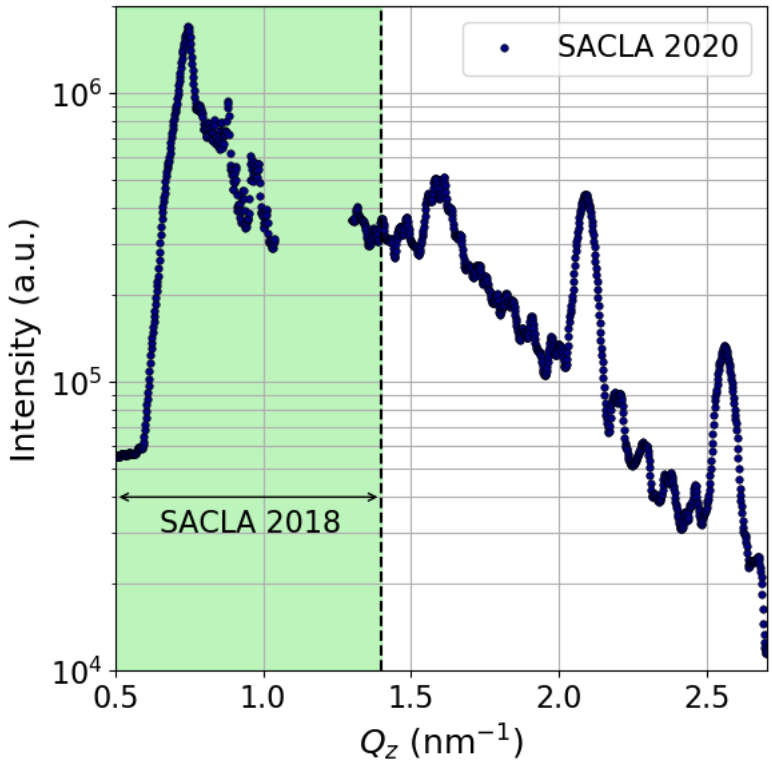

Figure 5.29: In-plane signal along Q_z as a comparison between the first and the second experiment at SACLA. While during the first experiment the Q_z space was limited to $1.45\,\mathrm{nm}^{-1}$, in the second experiment it was extended to $Q_z = 2.6\,\mathrm{nm}^{-1}$.

5.2.1 Data treatment

Fig. 5.30 (left) displays a raw detector pattern with 2200 pixels in z-direction and 600 pixels in y-direction. We note that the detector pattern is horizontally split at pixels $\approx 1120 - 1130$ indicating that the detector consists of two different chips. Furthermore, we observe characteristic vertical lines which arise from the vertical read out direction of the chip. Fig. 5.30 (middle) illustrates a dark image taken without any X-ray beam. For the background correction we subtract the dark image from the raw data image resulting in the pattern shown in Fig. 5.30 (right).

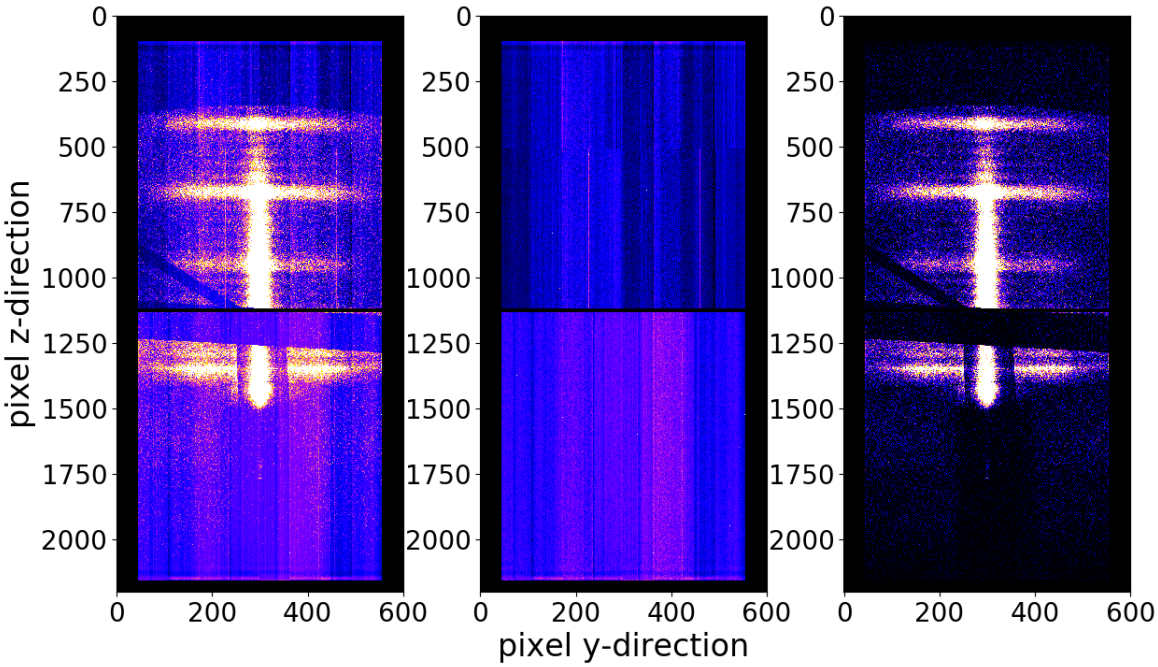

Figure 5.30: left: Typical raw data image. Vertical lines are visible. middle: Dark image. right: Data image after dark-image subtraction.

Fig. 5.31 represents a detector pattern from the cold sample without laser excitation. Regions of interest are colored differently: the blue box at $Q_z = 1.1 - 1.3\,\mathrm{nm}^{-1}$ along Q_y is the position of the beamstop blocking the specular signal which is several orders of magnitude more intense than the rest of the signal. The green box between $Q_y = -0.02 - 0.02\,\mathrm{nm}^{-1}$ along Q_z represents the in-plane scattering. Averaging this signal over Q_y and analyzing along Q_z yields the electron density profile of the sample. The signal in the red boxes between $Q_z = 0.82 - 0.91\,\mathrm{nm}^{-1}$, $Q_z = 1.55 - 1.63\,\mathrm{nm}^{-1}$, $Q_z = 2.05 - 2.12\,\mathrm{nm}^{-1}$ and $Q_z = 2.51 - 2.59\,\mathrm{nm}^{-1}$ along Q_y represents the out-of-plane scattering along Q_y and yields information about the structure of the interfaces, such as e.g. the hurst parameter. A summary of the different areas can be found in Table 5.6.

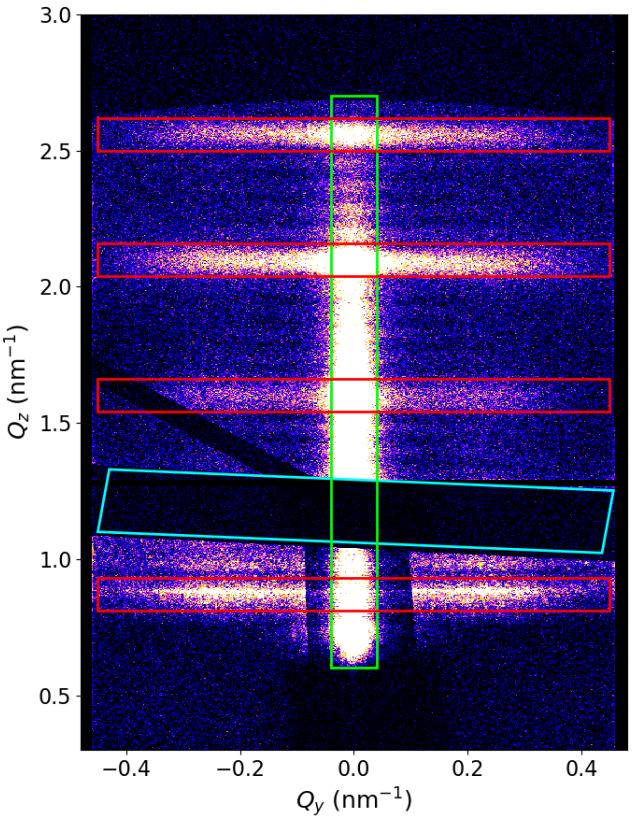

Figure 5.31: Scattering signal from the cold sample without laser excitation. The blue box indicates the beamstop. The green box represents the in-plane signal and the red lineouts denote the out-of-plane scattering signal along Q_y.

area	pixel	Q-range
green box	$290 - 310$ in y-direction	$Q_y = -0.02 - 0.02\,\mathrm{nm}^{-1}$
red box 1	$1330 - 1380$ in z-direction	$Q_z = 0.82 - 0.91\,\mathrm{nm}^{-1}$
red box 2	$932 - 975$ in z-direction	$Q_z = 1.55 - 1.63\,\mathrm{nm}^{-1}$
red box 3	$660 - 700$ in z-direction	$Q_z = 2.05 - 2.12\,\mathrm{nm}^{-1}$
red box 4	$394 - 440$ in z-direction	$Q_z = 2.51 - 2.59\,\mathrm{nm}^{-1}$

Table 5.6: Overview of different colored areas in Fig. 5.31.

5.2.2 In-plane scattering

Now, we investigate the in-plane signal of equal cold samples (green box in Fig. 5.31). Fig. 5.32 (left) displays the signal averages over $Q_y = -0.02 - 0.02\,\mathrm{nm}^{-1}$ around the specular beam plotted along the Q_z direction. For visualization the lineouts are vertically shifted. At $Q_z = 0.75\,\mathrm{nm}^{-1}$ we recognize the Yoneda peak located at the position where the exit angle α_f is equal to the critical angle α_c of Al. Between $Q_z = 0.75 - 1.0\,\mathrm{nm}^{-1}$ the signal appears rather noisy coming from the fact that the 200 nm thick Al layer causes fast oscillations in the scattering signal on the order of $\Delta Q_z \approx 0.03\,\mathrm{nm}^{-1}$ (see Fig. 5.32 (right)). For $Q_z > 1.3\,\mathrm{nm}^{-1}$ the Kiessig fringes and the Bragg peaks are visible. Compared to the first experiment shown in section 5.1 now three Bragg peaks are visible instead of one, thus we are more sensitive to smaller perturbations in the density profiles now. We observe again the substructure in the Kiessig fringes caused by the 200 nm Al top layer. By comparing the different preshots taken from equal samples we note small fluctuations from shot to shot originated from the SASE fluctuations.

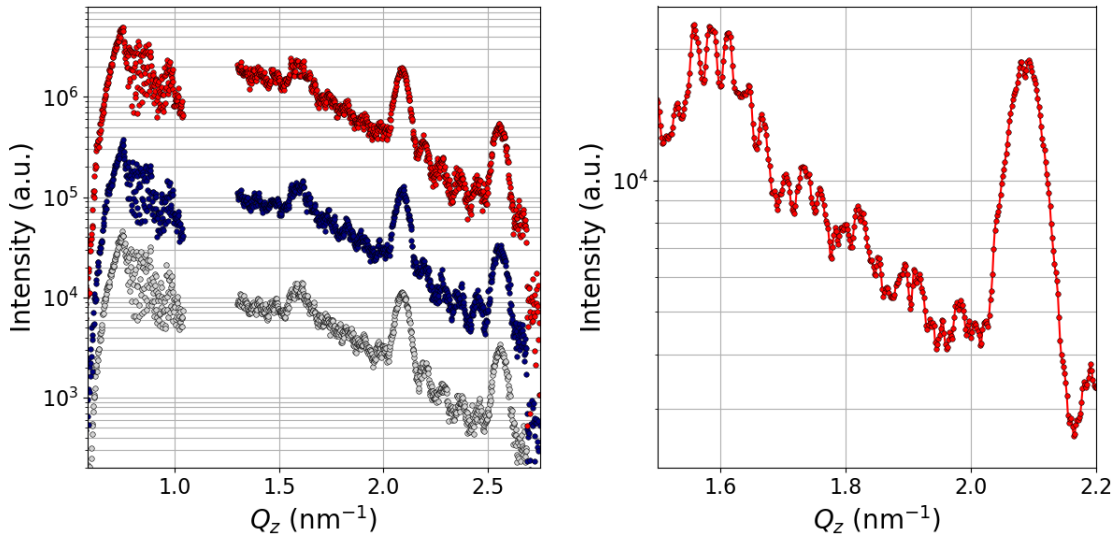

Figure 5.32: left: In-plane profiles along Q_z of different cold samples. right: Zoom into $Q_z = 1.5 - 2.2\,\mathrm{nm}^{-1}$ showing the substructure produced by the 200 nm Al layer. For a better visualization the in-plane signal is modified by a 1-D convolution filter.

We refine the in-plane signal again with BornAgain to extract detailed information about the electron density profiles. Fig. 5.33 displays the electron density profile and the corresponding in-plane signal created with BornAgain using the parameters we extracted from the sample characterization with X-ray reflectivity scans. We notice that the peak positions match, but the underlying slope is slightly different due to the parasitic scattering from the beamstop. For this reason we adjust the slope of the simulated data multiplying the simulated in-plane signal for $Q_z < 1.16\,\mathrm{nm}^{-1}$ with $(1.16 - Q_z)^{1.5}$ and the region for

$Q_z > 1.16\,\mathrm{nm}^{-1}$ with $(Q_z - 1.16)^{-0.1}$ as shown in Fig. 5.34.

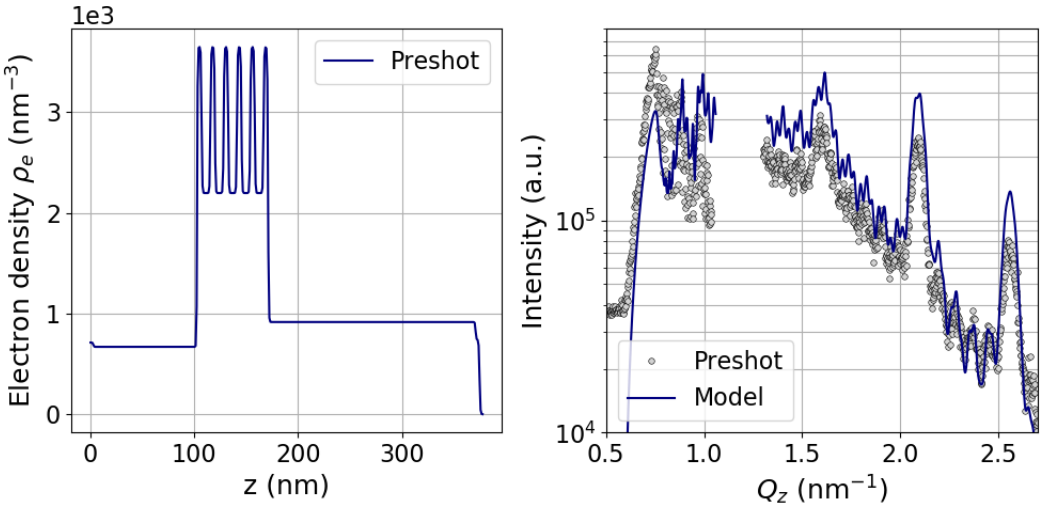

Figure 5.33: BornAgain simulation using the parameters obtained from the sample characterization.

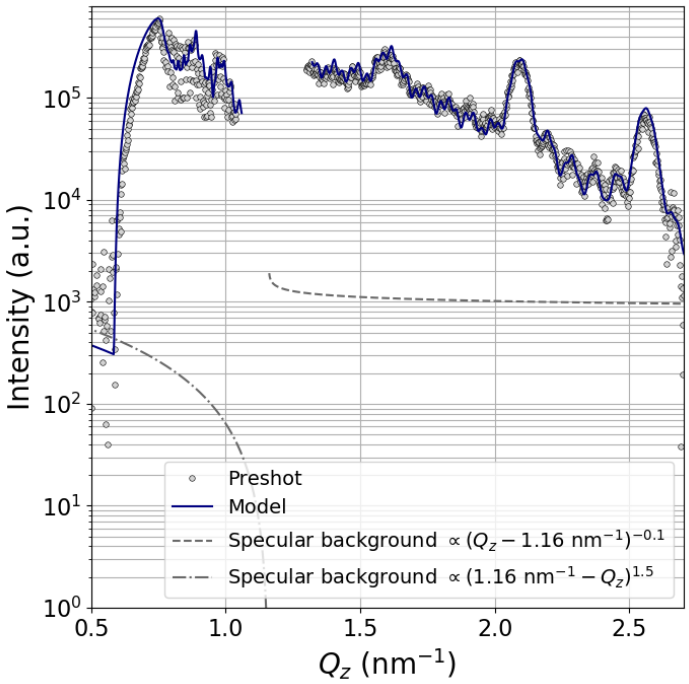

Figure 5.34: Grey points: XDS data from a preshot. The grey dotted line represents the model accounting for parasitic scattering tails from the beamstop used to block the highly intense specular signal at $Q_z = 1.16\,\mathrm{nm}^{-1}$. The blue solid line shows the model based on the density profile including the background.

Fig. 5.35 displays the region of interest of the in-plane signal demonstrating that the

model including the adjusted background is in agreement with the experimental data.

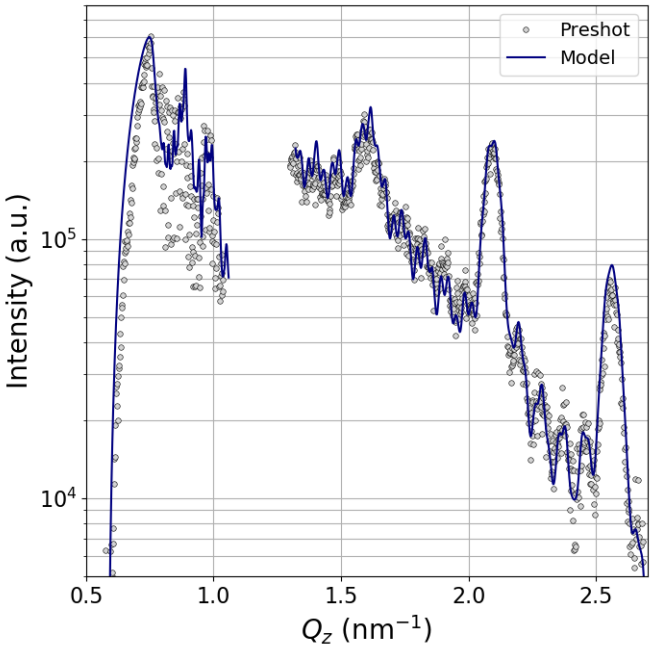

Figure 5.35: Detail of the in-plane scattering data including the BornAgain model.

Now, we investigate the in-plane signals after laser excitation for different delay times between laser and X-ray. In Fig. 5.36 we plot the intensity as a function of Q_z for the mainshot (blue and red) and their corresponding preshots (grey). At $t = 0$ ps we detect no significant changes between pre- and mainshot indicating that the the layers are still unperturbed. Starting from $t = 1.0$ ps we observe that the underlying slope of the signal has changed and with that the relative height of the Kiessig fringes compared to the ML Bragg peak. For $t = 3.0$ and 5.0 ps the substructure of the Kiessig fringes appears much weaker meaning that the 200 nm Al top layer starts to vanish. At $t = 7.0$ ps the Yoneda peak at $Q_z = 0.75\,\mathrm{nm}^{-1}$ decreases significantly indicating the vanishing Al layer. From $t = 9.0$ ps on the Bragg peak at $Q_z = 2.1\,\mathrm{nm}^{-1}$ is shifting to higher Q_z values and starts to intermix with the next Kiessig fringe while the other Kiessig fringes are still visible. At $t = 10$ ps distinct changes in the characteristic peak structure are visible showing that the Bragg peaks are further shifting to higher Q_z values and also the Kiessig fringes start to vanish. At $t = 11$ ps the Bragg peak at $Q_z = 1.6\,\mathrm{nm}^{-1}$ is decreased considerably and is intermixing with the Kiessig fringes indicating that the ML double layer thickness is decreasing and the periodic layer structure is vanishing. At $t = 12$ and 13 ps the Kiessig fringes are gone and the Bragg peaks are further decreasing while there is a new peak arising at $Q_z = 1.7\,\mathrm{nm}^{-1}$ pointing towards the formation of a new substructure. Although the ML structure is mostly gone, we still see a (weak) feature of the Al Yoneda peak implying that there must be a leftover of the Al top layer. At the very large delay times

of $t = 14$ and 15 ps we notice that the new peak at $Q_z = 1.7\,\mathrm{nm}^{-1}$ is increasing while the other Bragg peaks still decaying. Even after 15 ps we observe traces of the Al Yoneda peak.

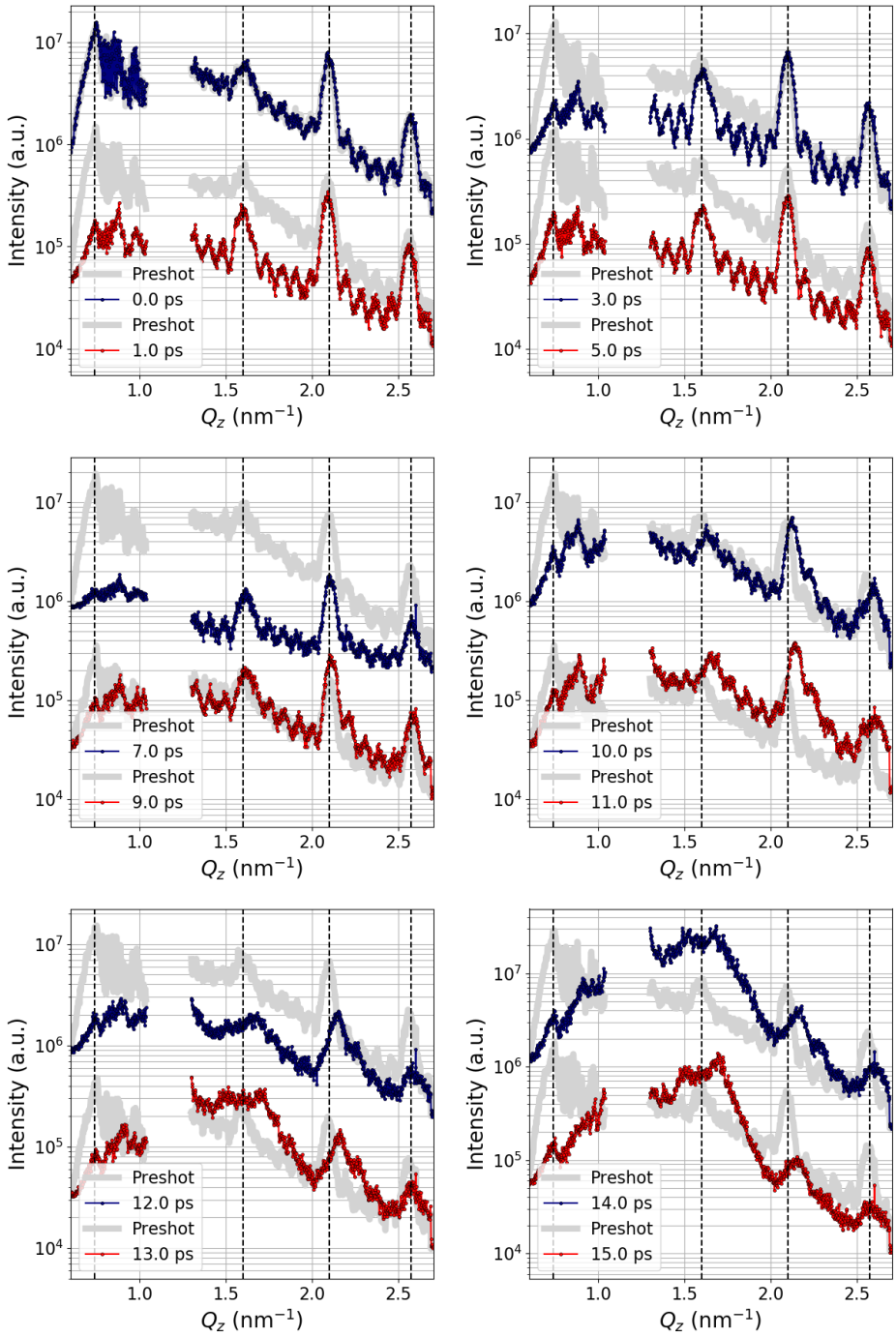

Figure 5.36: In-plane signal as a function of Q_z for various time delays. The blue and red lines display several mainshots and the grey lines the corresponding preshot. The vertical dashed lines indicate the initial Q_z positions of the Yoneda peak and the Bragg peaks.

We investigated identical ML samples with higher laser intensity of $I_L = 8 \times 10^{15}\,\mathrm{W/cm^2}$ and analyse now the influence of higher laser intensity on the in-plane scattering signal as illustrated in Fig. 5.37 comparing the mainshots taken at the same delay time with both laser intensities. Here, the blue curve represents the in-plane signal taken with laser intensity $I_L = 8 \times 10^{14}\,\mathrm{W/cm^2}$, while the red curve is the signal taken with 10 times higher laser intensity $I_L = 8 \times 10^{15}\,\mathrm{W/cm^2}$. The vertical dashed lines indicate the initial peak positions of Yoneda and Bragg peaks. At $t = 0.0\,\mathrm{ps}$ we observe no significant changes between both intensities, only the underlying slope differs. For $t = 3.0\,\mathrm{ps}$ we notice that the Bragg peak at $Q_z = 1.6\,\mathrm{nm^{-1}}$ is decaying for the high intensity signal. Furthermore, the Kiessig fringes for the high intensity case between $Q_z = 1.7 - 1.9\,\mathrm{nm^{-1}}$ are weaker and more noisy compared to the low intensity case. After $t = 5.0\,\mathrm{ps}$ we detect significant changes in the high intensity case. The Bragg peak at $Q_z = 1.6\,\mathrm{nm^{-1}}$ is not visible anymore and also the Kiessig fringes are much weaker compared to the low intensity signal. However, the peak positions of the Yoneda and Bragg peaks remain constant. For $t = 7.0\,\mathrm{ps}$, in the high intensity case the Kiessig fringes are completely gone. The Bragg peaks at $Q_z = 2.1$ and $2.6\,\mathrm{nm^{-1}}$ are weaker but still at the initial Q_z position. Additionally, a new peak is arising at $Q_z = 1.5\,\mathrm{nm^{-1}}$. The signal for the low intensity case shows at this time delay only minor changes in the Kiessig fringes, while the Bragg peaks do not show structural changes. By comparing the in-plane signal with both laser intensities we observe that the higher laser intensity causes changes in the in-plane scattering signal at earlier delay times compared to the low laser intensity. That is because a higher laser intensity produces higher temperatures in the ML sample and thus, the dynamics (heatwave, electrons, ions) are faster. However, the most important difference between both laser intensities is a different temporal evolution. While in the low intensity case first the Bragg peaks are shifting before the Kiessig fringes vanish, the high intensity signal indicates first the decaying Kiessig fringes and the shifting Bragg peaks afterwards.

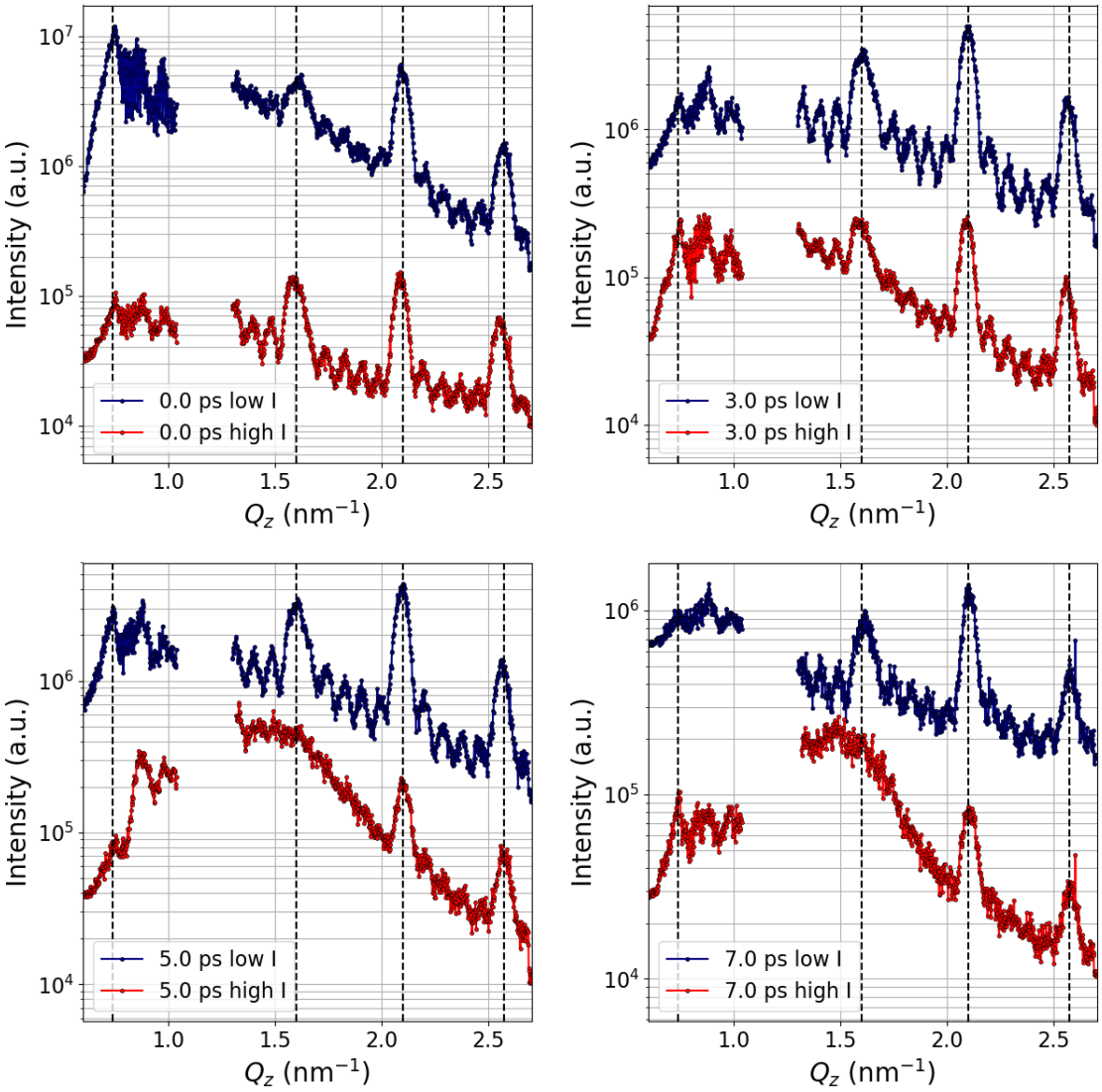

Figure 5.37: In-plane signal along Q_z comparing two laser intensities of $8 \times 10^{14}\,\mathrm{W/cm^2}$ and $8 \times 10^{15}\,\mathrm{W/cm^2}$ for the same time delay, respectively. Blue indicates the low laser intensity and red corresponds to the high laser intensity. The vertical dashed lines indicate the initial Q_z positions of the Yoneda peak and the Bragg peaks.

Fig. 5.38 illustrates the signal at that time delay where the Bragg peaks start to shift to higher Q_z values (11.0 ps for the low intensity case and 7.25 ps for the high intensity case). For the low intensity case we can clearly recognize the Kiessig fringes while they are not visible anymore in the high intensity case meaning that the ML sample after high intensity laser excitation changes first the single layers „isolated“ and only afterwards the double layer thickness while the low intensity laser excitation causes stronger intermixing between the layers resulting in faster changes of the double layer thickness and thus a shift of the Bragg peak.

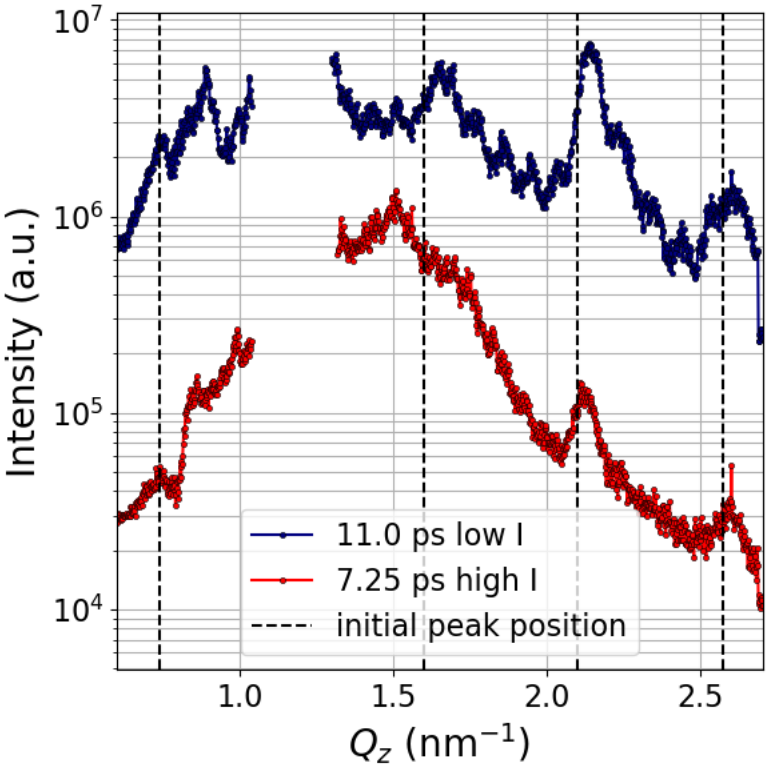

Figure 5.38: In-plane signal along Q_z comparing two laser intensities of $8 \times 10^{14}\,\mathrm{W/cm^2}$ and $8 \times 10^{15}\,\mathrm{W/cm^2}$ for that time where the Bragg peaks start to shift to higher Q_z values. Blue indicates the low laser intensity and red corresponds to the high laser intensity. The vertical dashed lines indicate the initial Q_z positions of the Yoneda peak and the Bragg peaks.

Although the large Q_z-space has many advantages such as the possibility of a very detailed reconstruction of the electron density profiles, the complexity of the data increases considerably and with it the time needed to reconstruct these profiles since the scattering intensity is distributed over two orders of magnitude. At this point we reach our limits to analyze the data „by hand“. In the future, we plan to use machine learning techniques for the density reconstruction, but that is beyond the scope of this thesis.

5.3 Out-of-plane scattering along Q_y

In this chapter we discuss the details of the time dependence of interfacial properties such as lateral correlation lengths, interface roughness and hurst parameter.

5.3.1 ML sample without Aluminium

Fig. 5.39 displays a detector pattern from a cold ML sample without Aluminium. The red boxes along Q_y denote the out-of-plane signal which we investigate in this chapter.

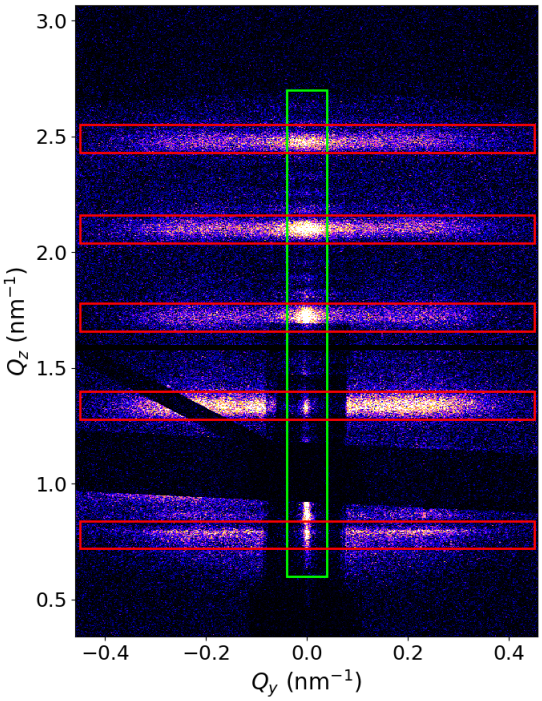

Figure 5.39: Detector pattern from a cold sample without Aluminium. The green box denotes the in-plane signal and the red boxes represent the out-of-plane scattering signal along Q_y at different ML Bragg peaks.

We first discuss the influence of the different interfacial properties on the scattering signal. In Fig. 5.40 we plot the profile of the red box at $Q_z = 1.7\,\mathrm{nm}^{-1}$ along Q_y for different time delays. The red points indicate the preshot and the blue points denote the signal after laser excitation. We observe that the cutoff-value Q_c connected to the lateral correlation length ξ_L at $Q_c = 0.3\,\mathrm{nm}^{-1}$ is not changing upon pumping. For $Q_y > Q_c$, we notice that the slope of the diffuse scattering power law decreases upon pumping.
We first discuss the determination of the lateral correlation length ξ_L. Simulating the out-of-plane scattering signal with BornAgain yields $\xi_L \approx 3\,\mathrm{nm}$ in agreement with grain sizes from sputtered ML films [79]. However, we note here an inconsistency in the BornAgain program as choosing a lateral correlation length of 3 nm leads to unrealistically

large distortions of the whole in-plane signal. We attribute this behaviour to a numerical instability upon integration of the experimental functions involved. This inconsistency could not been removed during this thesis making the determination of the absolute value of the lateral correlation length difficult. It will thus be between 3 and 30 nm.

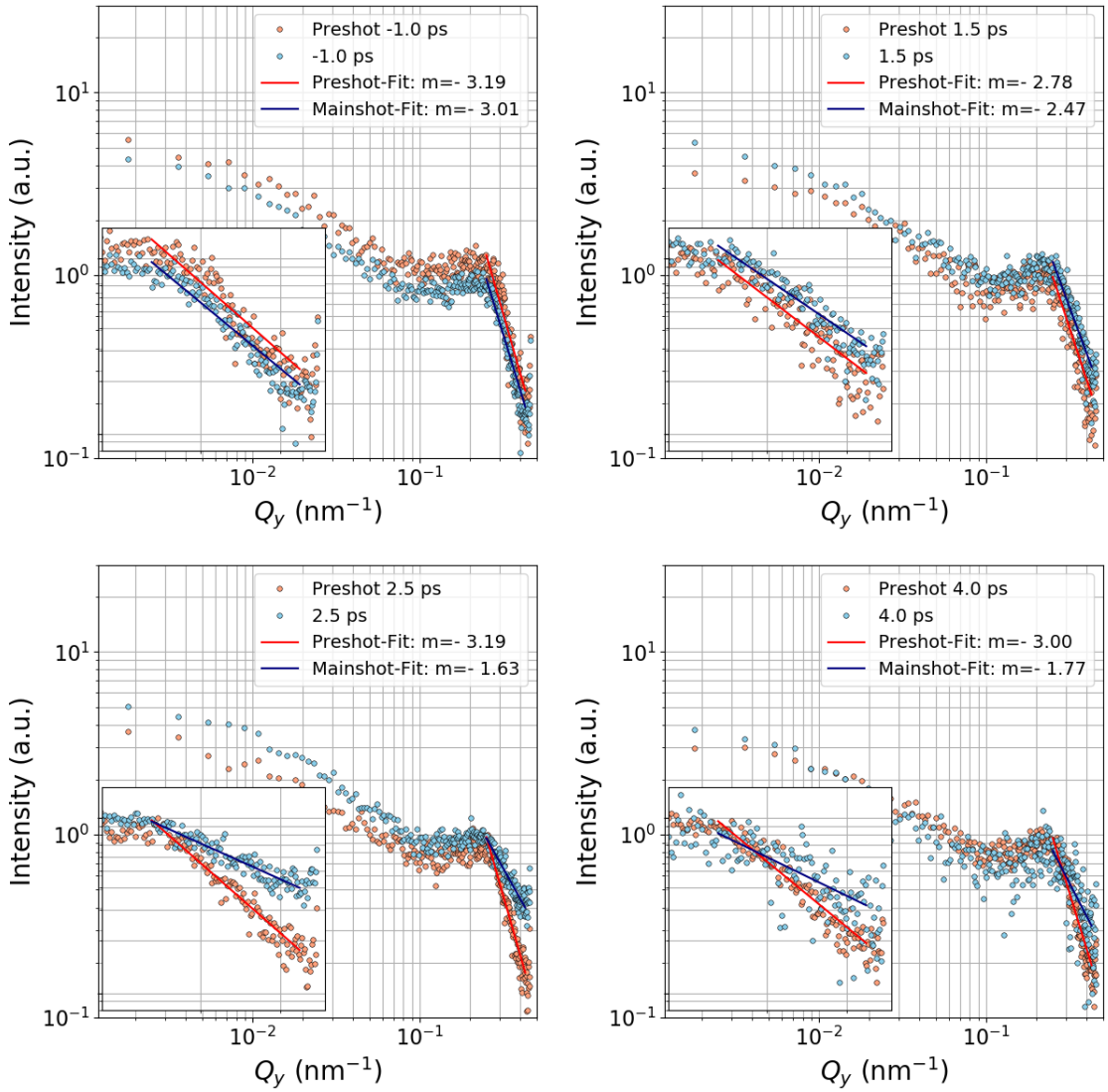

Figure 5.40: Out-of-plane signal along Q_y from ML sample for different time delays. The red points indicate the preshot, the blue points represent the mainshot. The solid lines represent a fit with a power law $\propto Q_y^m$.

Discussion of roughness and hurst parameter

We investigate now the effects of the laser excitation on both roughness and hurst parameters. We can extract changes of roughness and hurst parameter by investigating the slope of the power law in Q_y direction. Fig. 5.40 shows that the fall-off of the power-law

tail decreases upon laser excitation. Modelling this power-law with $y = a \cdot Q_y^m$ yields the corresponding slope m.

Fig. 5.41 and 5.42 show the resulting exponent m as a function of delay time for all 5 streaks (Q_z = 0.79, 1.33, 1.73, 2.10 and 2.47 nm^{-1}). The red points denote the preshot exponents and the red dashed line the corresponding average. The blue points represent the mainshot exponents showing a step-like increase followed by a constant behaviour afterwards. The blue dashed line is a guide to the eyes. Furthermore, we note that the preshot exponents increase with increasing Q_z as visualized in Fig. 5.43.

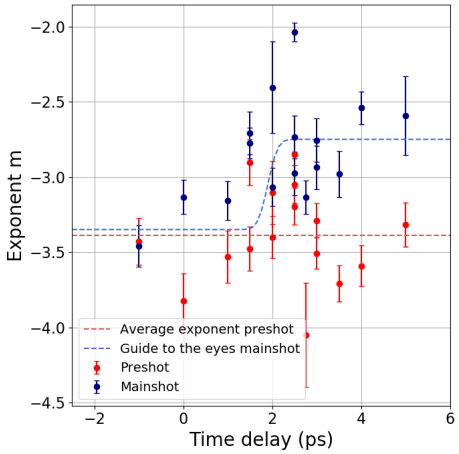

(a) Exponent m as a function of time delay for $Q_z = 0.79\,\mathrm{nm}^{-1}$.

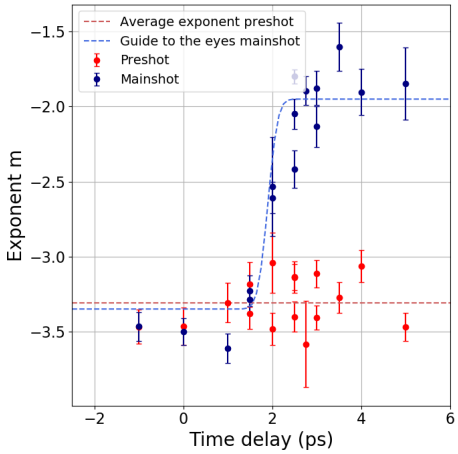

(b) Exponent m as a function of time delay for $Q_z = 1.33\,\mathrm{nm}^{-1}$.

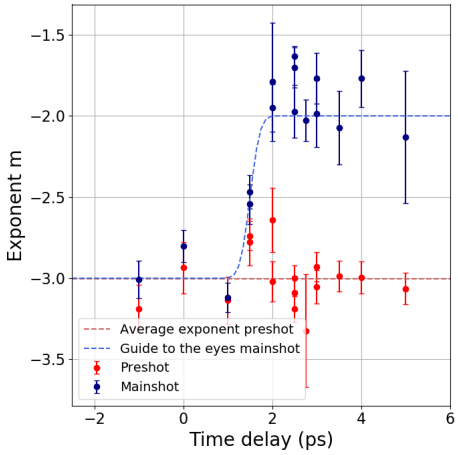

(c) Exponent m as a function of time delay for $Q_z = 1.73\,\mathrm{nm}^{-1}$.

Figure 5.41: Modelled exponent m as a function of time delay for the ML sample without Aluminium for different Q_z values.

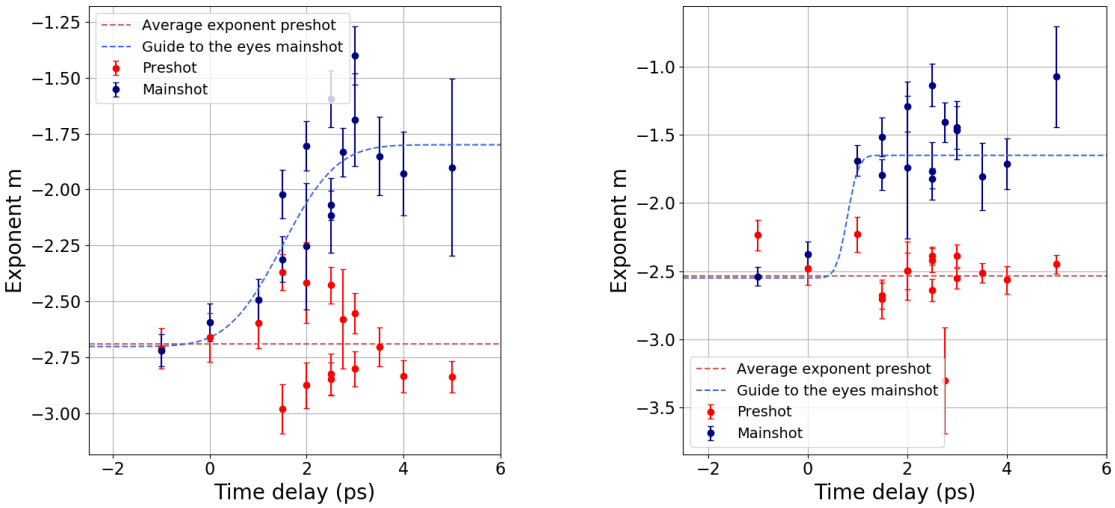

(a) Exponent m as a function of time delay for $Q_z = 2.10\,\mathrm{nm}^{-1}$.

(b) Exponent m as a function of time delay for $Q_z = 2.47\,\mathrm{nm}^{-1}$.

Figure 5.42: Modelled exponent m as a function of time delay for the ML sample without Aluminium for different Q_z values.

In Fig. 5.43 we plot the mean preshot exponent as a function of Q_z (red points). We define average exponents for pre- and mainshot by averaging m before and after the step like increase, respectively. We notice that the exponents at $Q_z = 0.79$ and $1.33\,\mathrm{nm}^{-1}$ are similar ($m = -3.4$) and increase continuously for the larger Q_z values up to $m = -2.5$.

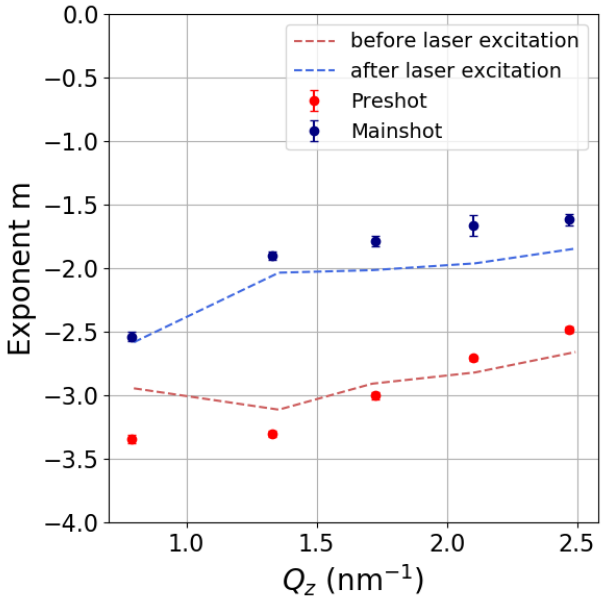

Figure 5.43: Averaged exponents of the power law tail Q_y^m for pre- and mainshot. The dashed lines are the results based on parameters of Table 5.7.

For the averaged mainshot exponent only the exponents after the increase are taken into account and illustrated with blue points. Also the mainshot exponents are continuously increasing from values of $m = -2.5$ up to $m = -1.6$. To connect these exponents with layer roughness and hurst parameter we performed BornAgain simulations based on the preshot model and refined these to match the experimental data.
Applying the parameters listed in Table 5.7 yields the dashed lines in Fig. 5.43, showing a good agreement with the data. We observe that the overall roughness increases upon laser excitation and that the hurst parameter h decreases. A lower hurst parameter is an indication for a more jagged surface configuration after laser excitation.

Parameter	Preshot	Mainshot
beam intensity I	5×10^{17}	5×10^{17}
background b	1×10^{-1}	1×10^{-1}
hurst parameter h	0.6	0.1
roughness factor r	first 2 layers 4 others 2	6
lateral correlation length ξ_L (nm)	30	30

Table 5.7: Simulation parameters from the dashed lines in Fig. 5.43 for pre- and mainshot.

5.3.2 ML samples with Aluminium

In a next step, we investigate the ML samples with Aluminium top layer and perform the same analysis as before (shown in the appendix chapters 8.5, 8.6 and 8.7). Fig. 5.44 displays the average exponent m as a function of Q_z for the ML sample with 50 nm Aluminium top layer. We notice that both exponents at $Q_z = 0.87\,\mathrm{nm}^{-1}$ are identical (-2.5) while the exponents at larger Q_z values show a difference of ~ 1. We find that the hurst parameter cannot change significantly since a change of the hurst parameter would result in a shift of **all** exponents, but the exponent at $Q_z = 0.87\,\mathrm{nm}^{-1}$ remains constant.

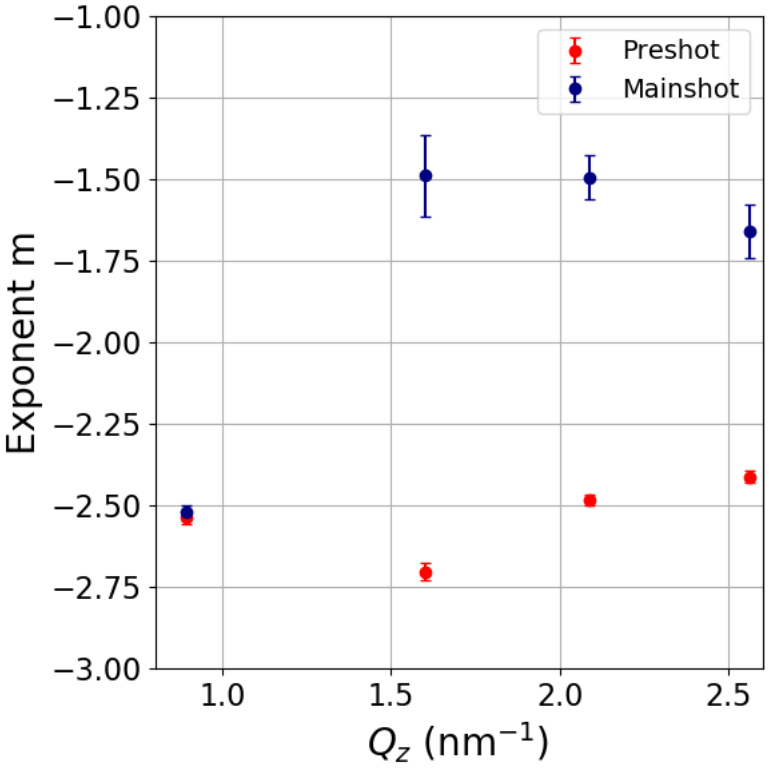

Figure 5.44: Averaged exponents for pre- and mainshot and refined simulations for the ML sample with 50 nm Aluminium toplayer.

In a last step, we analyze the ML sample with 200 nm Aluminium toplayer. In our experiment, we measured this sample with two laser intensities of $I_L = 8 \times 10^{14}\,\mathrm{W/cm^2}$ and $8 \times 10^{15}\,\mathrm{W/cm^2}$. The red points in Fig. 5.45 denote the preshot average exponent, the blue points represent the mainshot exponents irradiated with the higher laser intensity of $I_L = 8 \times 10^{15}\,\mathrm{W/cm^2}$ while the green points show the mainshot exponents irradiated with the previous laser intensity of $I_L = 8 \times 10^{14}\,\mathrm{W/cm^2}$.

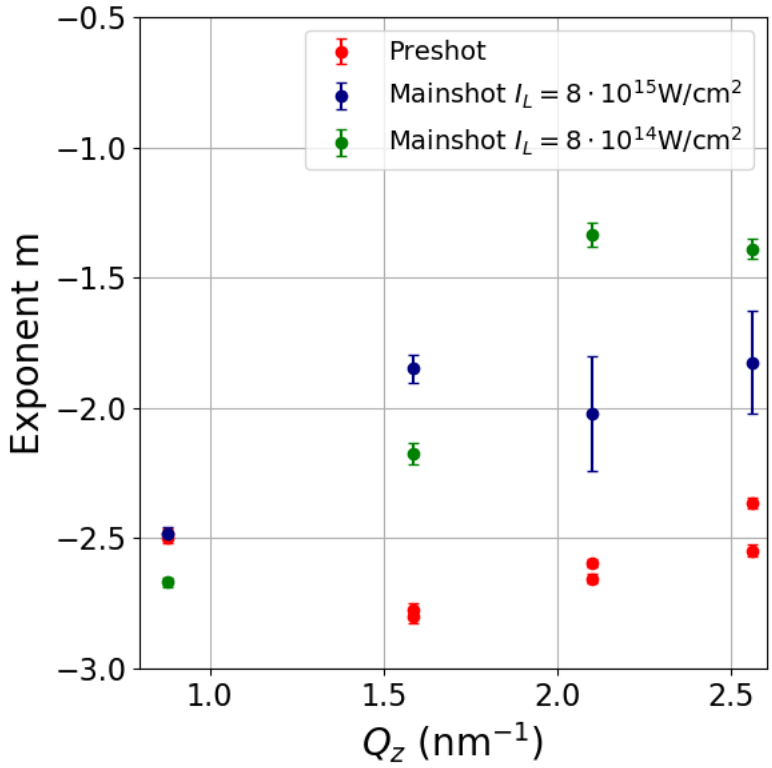

Figure 5.45: Averaged exponents for pre- and mainshot and refined simulations for the ML sample with 200 nm Aluminium toplayer.

We observe again that the exponents at $Q_z = 0.87\,\mathrm{nm}^{-1}$ remain constant and only the exponents at larger Q_z values change. Furthermore, the exponents with larger laser intensity seem to increase not as much compared to the exponents with lower laser intensity. As before, the hurst parameter cannot change significantly since the exponent at $Q_z = 0.87\,\mathrm{nm}^{-1}$ does not change. Since the exponents of the higher laser intensity are less changing compared to the low laser intensity, most probably the changes of the roughness factor for the high laser intensity are smaller meaning that with higher laser intensity less intermixing between the layers is occurring but instead the layers are compressed „isolated“.
In conclusion, we note that for the ML sample without Aluminium the hurst parameter and the roughness change upon laser excitation. By using Aluminium as a toplayer the hurst parameter seems to remain constant and only the roughness is increasing meaning that the ML sample with Aluminium layer is changing its structure in a different way compared to the sample without Aluminium.

5.3.3 Rise time

Now we investigate the temporal evolution of the mainshots upon pumping. We plot the exponents as a function of time delay for all samples for $Q_z = 2.5 - 2.6\,\mathrm{nm}^{-1}$ in Fig. 5.46.

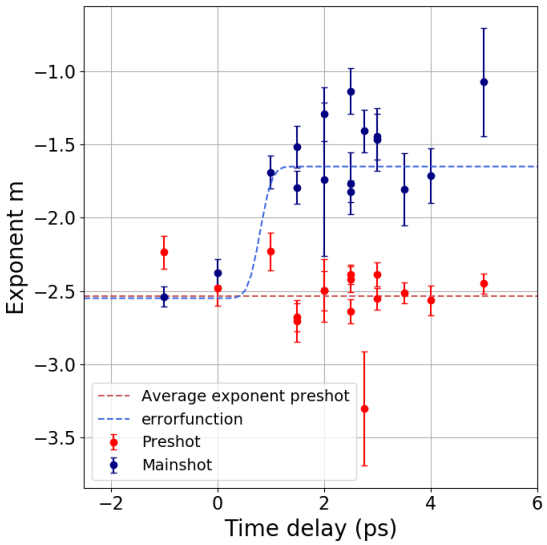

(a) Exponent m as a function of time delay for the ML sample without Aluminium.

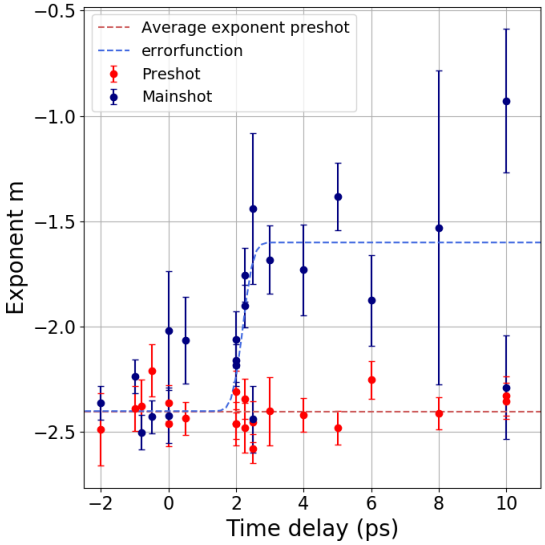

(b) Exponent m as a function of time delay for the ML sample with 50 nm Aluminium toplayer.

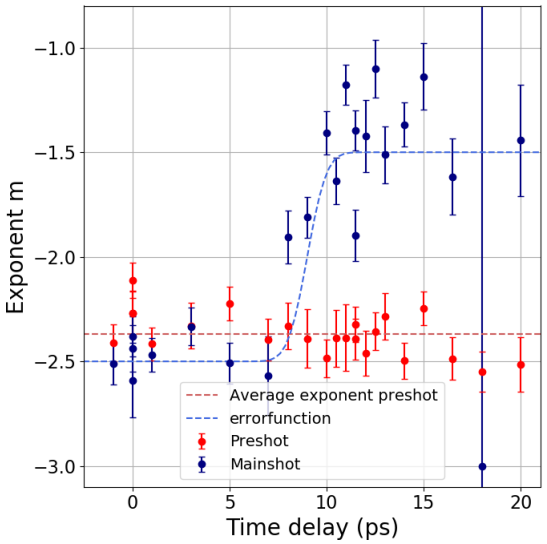

(c) Exponent m as a function of time delay for the ML sample with 200 nm Aluminium toplayer.

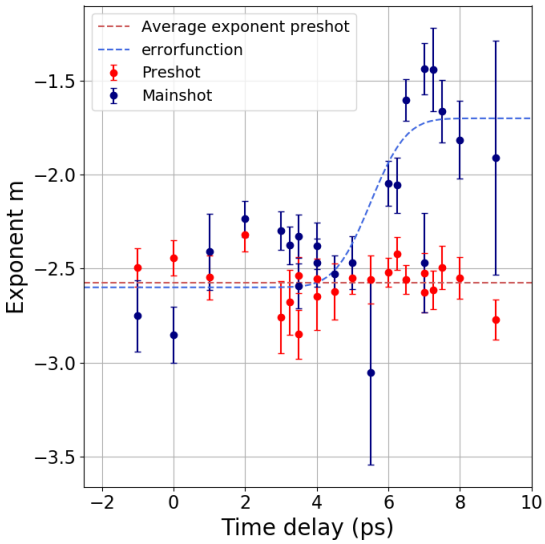

(d) Exponent m as a function of time delay for the ML sample with 200 nm Aluminium toplayer upon higher laser intensity.

Figure 5.46: Exponent m as a function of time delay at $Q_z = 2.5 - 2.6\,\mathrm{nm}^{-1}$ for all samples.

The increase of the mainshot exponents can be modelled with an errorfunction (blue dashed lines)

$$m(t) = m_0 \cdot \mathrm{erf}\left(\frac{t - t_0}{\Delta t}\right), \tag{5.3.1}$$

m_0 denotes the exponent before pumping, t_0 indicates the time until the increase begins and Δt represents the duration of increase, called rise time.
First, we plot the time t_0 when the increase begins as a function of the Aluminium thickness and find an exponential increase as displayed in Fig. 5.47 indicating that the heatwave travels a longer way to reach the ML sample because of the Aluminium layer. With higher laser intensity of $I_L = 8 \times 10^{15}\,\mathrm{W/cm^2}$ the increase of exponents occurs 4 ps earlier meaning that the heatwave velocity gets faster by a factor of 5/3 with increasing laser intensity.

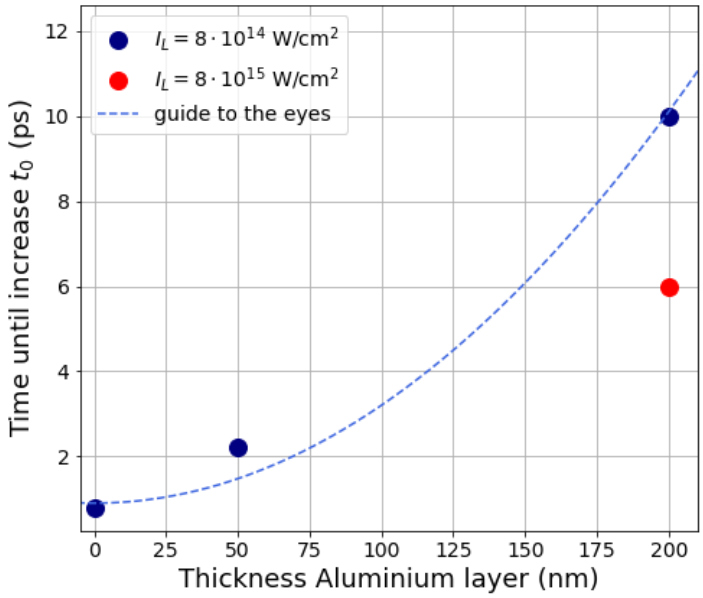

Figure 5.47: Time until the mainshot exponents increase as a function of Aluminium thickness.

Finally, we investigate the rise time shown in Fig. 5.48. We find again a quadratic increase as a function of Aluminium layer thickness. We interpret this as a temporal broadening of the heatwave upon travelling through the Aluminium layer. After 200 nm the rise time increases to about 1.2 ps significantly larger than for the sample without Aluminium. We speculate about an efficient dispersion of the electronic heatwave upon propagation through the solid material.

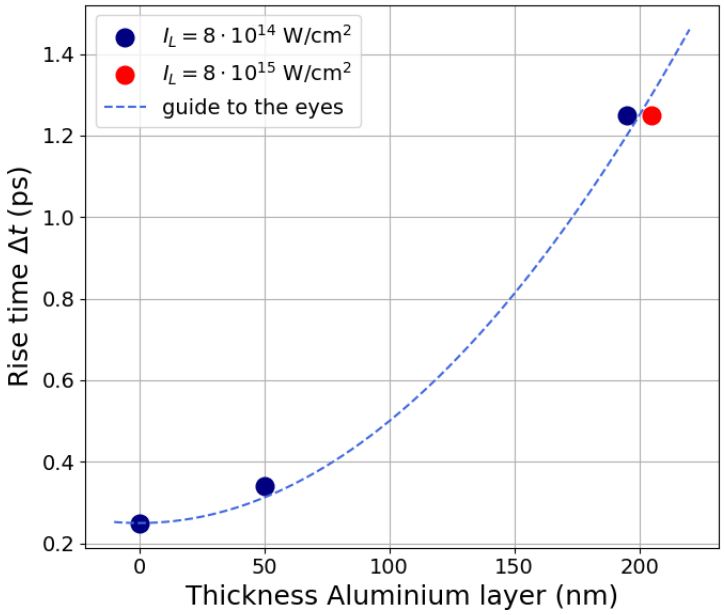

Figure 5.48: Rise time as a function of Aluminium thickness.

In summary, we showed a detailed analysis of the SACLA 2018 beamtime including in-plane, out-of-plane and uniqueness analysis in section 5.1 followed by a qualitative in-plane analysis from the SACLA 2020 beamtime in section 5.2. In section 5.3 we investigated the out-of-plane signal along Q_y from the SACLA 2020 beamtime. In the following chapter 6 we will discuss the major results and explain them with the background of plasma dynamics.

Chapter 6

Discussion

Here, we discuss the major findings and explain them with the help of of plasma dynamics. We start with the SACLA 2018 beamtime in section 6.1. Subsequently, in section 6.2 we explain the results from the in-plane signal analysis and in the last section in 6.3 we investigate the influence of Aluminium thickness with the help of the out-of-plane signal along Q_y.

6.1 SACLA 2018

In this section, we discuss the three major findings from reconstructing the electron density profiles.

1.) **Surface ablation**: Between $0.5 - 2.0\,\mathrm{ps}$ the surface ablation slowly starts with a velocity of $0.6 \times 10^4\,\mathrm{m\,s^{-1}}$ and is then significantly increasing between $2.5 - 5.0\,\mathrm{ps}$ to $2.4 \times 10^4\,\mathrm{m\,s^{-1}}$. $5.0\,\mathrm{ps}$ after laser excitation the surface ablation is slowing down again to $0.4 \times 10^4\,\mathrm{m\,s^{-1}}$.

2.) **Density modulations**: At $0.5\,\mathrm{ps}$ the ML sample appears unperturbed while at $1.0\,\mathrm{ps}$ the first $40\,\mathrm{nm}$ are modulated corresponding to a modulation velocity of $v = 4 \times 10^4\,\mathrm{m\,s^{-1}}$. After $2.0\,\mathrm{ps}$ all layers changed compared to the initial electron density leading to the same velocity of $v = 4 \times 10^4\,\mathrm{m\,s^{-1}}$. $3.5\,\mathrm{ps}$ after laser excitation the layer structure is not visible anymore until we end up with a $30\,\mathrm{nm}$ thick film with some smaller density oscillations at $6.0\,\mathrm{ps}$.

3.) **Intermixing between adjacent layers**: The layers are not compressed or expanded separately but show clear intermixing between adjacent ones. This effect is starting at $2.0\,\mathrm{ps}$ for the first 3 double layers and continues at $3.0\,\mathrm{ps}$ for the whole multilayer.

We note that the scattering cross-section for non-resonant scattering is largest for the electrons bound to the ions, so with hard X-rays in the energy range of $8 - 9\,\mathrm{keV}$ we are only sensitive to the ions.

We start with the surface ablation after laser excitation illustrated in Fig. 5.18. The laser energy is deposited primarily to free electrons via inverse Bremsstrahlung (intraband absorption) because of the high collision frequency. The average energy per electron in the initial plasma can be estimated as follows: Assuming a laser absorption rate $\eta = 0.2$ for our laser intensity of $I_L = 4 \times 10^{14}\,\mathrm{W/cm^2}$, quasi-normal incidence (73°) [80] and neglecting the energy loss by ionization, the average electron temperature within the skin layer at the end of the laser pulse can be expressed as

$$T_e = \frac{\eta I_L \tau_L}{\delta_s C_e}. \tag{6.1.1}$$

$\delta_s = 16\,\mathrm{nm}$ denotes the collisionless skin depth of cold Ta^{2+} and $C_e = 1.5 k_B n_{\mathrm{free}}$ is the electron heat capacity for an ideal gas with $n_{\mathrm{free}}(Ta^{2+}) = 1.11 \times 10^{23}\,/\mathrm{cm^3}$ (and $n_{\mathrm{free}}(Cu^{1+}) = 8.56 \times 10^{22}\,/\mathrm{cm^3}$) leading to $T_e \sim 90\,\mathrm{eV}$ which we assume to be the maximum threshold. Here, the thermal conduction and ionization during laser excitation are neglected. Note that around the Fermi temperature, the heat capacity approaches $C_e \to k_B n_{\mathrm{free}}$ using an interpolation between solid and plasma behavior [80]. The real heat capacity is rather complex [81], implying that estimating a temperature from simulations with high precision is a challenging task. Hydro-simulations (performed by Mohammadreza Banjafar in the framework of his PhD [82]) predict an initial temperature after the laser pulse ($t \sim 100\,\mathrm{fs}$) of $15 - 20\,\mathrm{eV}$ [82] close to the Fermi temperature ($T_F = 8.4\,\mathrm{eV}$ for Ta^{2+} and $7\,\mathrm{eV}$ for Cu^{1+}).

The collision frequency $\nu_e = \nu_{ee} + \nu_{ei}$ is one of the most important physical quantities for density dynamics because the moving electrons transfer energy to the ions. The ion-ion collisions are negligible compared to ν_{ei} and ν_{ee} since their velocity is much slower than the electron velocity. The precise value of ν_e under HED states is often unknown, and interpolation formulas between metal-like solids ($\nu_e \propto T$) and ideal gas plasmas ($\nu_e \propto T^{-1.5}$) are used [83] as shown in Fig. 6.1.

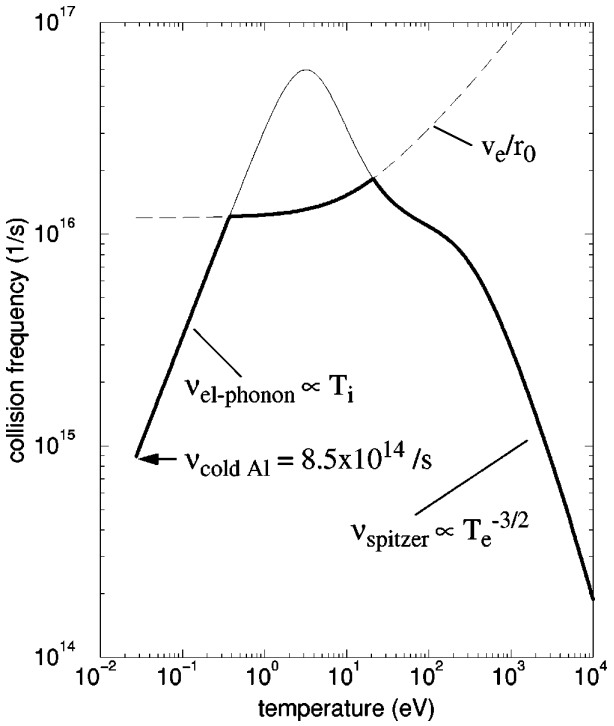

Figure 6.1: Collision frequency of solid Al as a function of the temperature $T_e = T_i$ represented by the thick solid line. The thin solid line is the result of the interpolation, the dashed line the upper limit of the collision frequency given by the requirement that the electron mean free path is larger than the ion sphere r_0 (taken from [83]).

The collision frequency reaches its maximum value around the Fermi temperature T_F, with a value close to the plasma frequency

$$\omega_{pe} = 56.4\sqrt{n_{\text{free}}}, \tag{6.1.2}$$

which is 1.9×10^{16} rad/s for cold Ta^{2+} and 1.6×10^{16} rad/s for Cu^{1+}. The velocity of individual electrons around or below T_F in a metal is

$$v_F = \frac{\hbar}{m_e}\left(3\pi^2 n_{\text{free}}\right)^{1/3}, \tag{6.1.3}$$

which is 1.7×10^6 and $1.6 \times 10^6\,\mathrm{m\,s^{-1}}$ for cold Ta^{2+} and Cu^{1+}, respectively. At $T_e > T_F$, the thermal electron velocity $v_{th} = \sqrt{k_B T_e/m_e}$ also needs to be taken into account, which leads to the electron velocity of

$$v_e = \sqrt{v_F^2 + 3v_{th}^2}. \tag{6.1.4}$$

The thermal electron velocity v_{th} can be determined with the energy of electrons under

an oscillating electric field

$$E_{osc} = \frac{e^2 E_L^2}{4 m_e \omega_L^2} = 9.3 \times 10^{-14}\, \mathrm{I_L[W/cm^2]}\, \lambda_\mathrm{L}^2[(\mu\mathrm{m})^2] \approx 24\,\mathrm{eV}. \tag{6.1.5}$$

From this we obtain electron velocities of $v_e = 3.9 \times 10^6\,\mathrm{m\,s^{-1}}$ for Ta and Cu leading to an electron mean free path of $l_\mathrm{mfp} = \frac{v_e}{\omega_{pe}} \sim 0.2\,\mathrm{nm} \leq \delta_s$, much less than the skin depth. Under this condition, a ballistic transport of electrons is inefficient allowing to use the diffusion approximation for the electron heat transfer. In addition, due to $l_\mathrm{mfp} \leq T_e/\nabla T_e$, flux-limited heat transport is not important [84].
Another effect of surface dynamics upon laser excitation are ion-density modulations with sound velocity driven by pressure relaxation. Using the ideal gas equation of state (EOS), we express the sound velocity as

$$C_s = \left(\frac{\gamma_e\, Z^*\, k_B\, T_e + \gamma_i\, k_B\, T_i}{m_i} \right)^{0.5}, \tag{6.1.6}$$

where γ_e and γ_i are adiabatic indices of electrons and ions, respectively and $m_i = 181\,\mathrm{u}$ and $63\,\mathrm{u}$ is the ion mass for Ta and Cu, respectively. From the ideal gas EOS we obtain $\gamma = 1 + 2/n$ with n being the motional degree of freedom. In most of the cases, $\gamma_e = 1$ and $\gamma_i = 3$ can be used. Assuming $T_e = 20\,\mathrm{eV}$, $T_i = 10\,\mathrm{eV}$ and $Z^* = 5$ we calculate a sound velocity of $C_{s_{Ta}} = 8.3 \times 10^3\,\mathrm{m\,s^{-1}}$ and $C_{s_{Cu}} = 1.4 \times 10^4\,\mathrm{m\,s^{-1}}$ much slower than what we observe in our experiment. This leads us to the conclusion that the dominant energy transport is driven by the heatwave expressed by the two-temperature energy conservation equations

$$C_e \frac{\partial T_e}{\partial t} = -\boldsymbol{\nabla} \boldsymbol{q} - \gamma(T_e - T_i) + Q(z,t) \tag{6.1.7}$$

$$C_i \frac{\partial T_i}{\partial t} = \gamma(T_e - T_i) \tag{6.1.8}$$

where C_e, C_i are, respectively, the heat capacity of electrons and ions, $\boldsymbol{q} = \kappa \boldsymbol{\nabla} T_e$ is the Spitzer-Härm heat flow with $\kappa(\nu)$ being the heat conductivity, and $Q(z,t) = \nabla I_{abs}$ is the laser energy deposition rate with the absorbed laser intensity I_{abs}. The energy transfer rate from electrons to ions is expressed by $\gamma = C_i \tau_i^{-1}$ with

$$\tau_i = \frac{m_i}{2 m_e \nu_{ei}} \tag{6.1.9}$$

the characteristic time for ion heating, where m_e and m_i are electron and ion mass, leading to $\tau_i \sim 8.5\,\mathrm{ps}$ and $3.5\,\mathrm{ps}$ for Ta^{2+} and Cu^{1+} at $\nu_{ei} \sim \omega_{pe}$, respectively. The hydrodynamic simulation including laser absorption indicates a heatwave propagation speed of $\sim 6 \times 10^4\,\mathrm{m\,s^{-1}}$ [82] in agreement with the density perturbation velocity observed in the experiment. The density perturbation is therefore triggered by an increased electron

pressure driven by the electron temperature.
On the surface, we observe that the ablation starts slowly at the beginning and is accelerated at $\sim 3\,\mathrm{ps}$. We attribute this temporal behaviour to the finite ion heating time τ_i. It is well known that the surface ablation can be separated into multiple phases [85]. The electrostatic ablation within the skin layer under non-equilibrium condition takes place immediately when the electron temperature exceeds the sum of the work function E_{esc} (7.6 eV for Ta and 4.7 eV for Cu) and the atomic binding energy E_b (4.2 eV for Ta and 3.5 eV for Cu). The maximum energy of ablated ions is then

$$E_i = k_B T_e - E_{esc} - E_b, \tag{6.1.10}$$

which is $\sim 8.2\,\mathrm{eV}$ for Ta and $\sim 11.8\,\mathrm{eV}$ for Cu. One can see that the electron temperature of $T_e = E_{esc} + E_b$ is the threshold for ion ablation here. Note that the maximum electron temperature at the ablation threshold for metals is approximately twice the binding energy E_b [85]. A more efficient mass ablation starts when the ions obtain enough energy from electrons via collisions to overcome their binding energy themselves. The onset of the mass ablation therefore manifests the electron-to-ion energy transfer time. In the hydrodynamic simulation, it takes 1.5 – 3 ps for ions to overcome the binding energy [82] in good agreement with the time scales observed in the experiment. The ablation speed eventually decreases at later times due to both the lower temperature in deeper parts of the ML and adiabatic cooling. The surface recession velocity observed in our experiment ($2.4 \times 10^4\,\mathrm{m\,s^{-1}}$) is slightly faster than the sound velocity predicted from the temperature inferred by the simulation: $C_s \leq 1.5 \times 10^4\,\mathrm{m\,s^{-1}}$ for $T_e \leq 15\,\mathrm{eV}$ [82]. The experimentally observed velocity would require $T_e \geq 50\,\mathrm{eV}$, highlighting the difficulty of precise estimation of the temperature by simulations in our experimental regime.
The simple energy conservation equation indicates a maximum possible temperature of about 90 eV. For material removal, the energy density should exceed $n_i E_{bond}$, which are $3.7 \times 10^4\,\mathrm{J/cm^3}$ for Ta and $4.2 \times 10^4\,\mathrm{J/cm^3}$ for Cu at solid density. Assuming 20% laser absorption [80] and a homogeneous distribution of energy along the 83.3 nm total ML thickness, yields $\sim 5 \times 10^5\,\mathrm{J/cm^3}$. This is sufficient to remove the whole ML sample as indeed observed in the experiment.

The density modulations illustrated in Fig. 5.16 imply a modulation velocity of $4 \times 10^4\,\mathrm{m\,s^{-1}}$ also indicating that the dynamics are driven by the heatwave instead of the slower sound velocity of $\leq 1.4 \times 10^4\,\mathrm{m\,s^{-1}}$.
The detailed density evolution of the ML sample does not agree with the simulation; the Ta layers withstand much longer in the simulation compared to the experiment [82]. The intermixing we observe is pointing towards the importance of ion velocities a few ps after laser excitation. Indeed we can estimate that for $T_i = 5\,\mathrm{eV}$ velocities of Ta $\sim 1.6\,\mathrm{nm\,ps^{-1}}$

and Cu $\sim 5\,\mathrm{nm\,ps^{-1}}$ should be reached. Our experiment reveals that the layer structure changes significantly after $2-3\,\mathrm{ps}$. Given the thickness of the layers of 4.38 nm (Ta) and 11 nm (Cu) we estimate that the corresponding velocities are on the order of 2.2 and $5.5\,\mathrm{nm\,ps^{-1}}$ which is in good agreement with the anticipated values explained above.
For the higher laser intensity of $I_L = 4 \times 10^{15}\,\mathrm{W/cm^2}$ we found that the density modulations are starting even before nominal time zero $t = 0\,\mathrm{ps}$, the origin of that is still under discussion. A possible explanation for these early dynamics is that the absorption increases immediately when the laser pulse reaches the sample and ionizes the atoms. An increased absorption implies then that the penetration depth of the X-rays into the sample decreases indicating that the scattering signal has less features. However, this phenomenon should appear immediately and then slowly decrease but the in-plane signal shows continuous changes which originate most probably from real changes in the sample structure. If these changes are originating from the increased absorption, this would be also visible in the signal from the SACLA 2020 experiment. However, the in-plane signal from SACLA 2020 shows no indication of an increased absorption. Instead we attribute the early dynamics to the increased electron temperature discussed in detail in the next section.

In summary, we have shown that the heat conduction is the dominant energy transport here because of the high velocities we observe from the experiment. We compared our experimentally retrieved results with simulations [82] indicating a good agreement. Only the density modulations do not fit to the simulations emphasizing again how important these results are to improve and benchmark existing simulation models.

6.2 SACLA 2020

For the SACLA 2020 experiment, we implemented three major changes. First, we increased the maximum Q_z-range from $1.45\,\mathrm{nm}^{-1}$ to $2.6\,\mathrm{nm}^{-1}$. Second, we increased the laser intensity from $I_L = 4 \times 10^{14}\,\mathrm{W/cm^2}$ to $8 \times 10^{14}\,\mathrm{W/cm^2}$ and $8 \times 10^{15}\,\mathrm{W/cm^2}$ and third, we modified the multilayer samples with an 200 nm thick Aluminium layer on top.
This section is focusing on a qualitative comparison of the in-plane signal between both laser intensities. We observe two significant differences:

1.) **Time scales**: The density modulations occur earlier for the higher laser intensity. Employing a laser intensity of $8 \times 10^{15}\,\mathrm{W/cm^2}$ we observe structural changes after $\sim 5.0\,\mathrm{ps}$ while for a laser intensity of $8 \times 10^{14}\,\mathrm{W/cm^2}$ the first structural changes are occurring after $\sim 9.0\,\mathrm{ps}$ (Fig 5.36 and 5.37).

2.) **Temporal evolution**: For the lower intensity of $I_L = 8 \times 10^{14}\,\mathrm{W/cm^2}$ first the Bragg peaks are shifting to higher Q_z-values and afterwards the Kiessig fringes are vanishing attributed to stronger intermixing while for the high intensity of $I_L = 8 \times 10^{15}\,\mathrm{W/cm^2}$ these effects are occurring vice versa (Fig. 5.37 and 5.38).

As in the previous section, we first determine the average electron temperature within the skin layer at the end of the laser pulse by

$$T_e = \frac{\eta I_L \tau_L}{\delta_s C_e}. \tag{6.2.1}$$

Because of the 200 nm thick Aluminium top layer, we determine the values here for Aluminium with $n_{\mathrm{free}}(\mathrm{Al}) = 1.8 \times 10^{23}\,/\mathrm{cm}^3$. With a collisionless skin depth of $\delta_s = 12\,\mathrm{nm}$ we calculate electron temperatures assumed as the maximum threshold of $\sim 130\,\mathrm{eV}$ for the low laser intensity of $I_L = 8 \times 10^{14}\,\mathrm{W/cm^2}$ and $\sim 1300\,\mathrm{eV}$ for the high laser intensity of $I_L = 8 \times 10^{15}\,\mathrm{W/cm^2}$.
The electron energy in an oscillating field is

$$E_{osc} = \frac{e^2 E_L^2}{4 m_e \omega_L^2} = 9.3 \times 10^{-14}\,\mathrm{I_L[W/cm^2]}\,\lambda_\mathrm{L}^2[(\mu\mathrm{m})^2]. \tag{6.2.2}$$

Inserting both laser intensities yields $E_{osc} \approx 48\,\mathrm{eV}$ for the low intensity and $E_{osc} \approx 480\,\mathrm{eV}$ for the high intensity. We assume that the low intensity case can still be approximated with the effects around the Fermi temperature as discussed in the previous section while the high intensity case is clearly not on the order of the Fermi temperature but a factor of 10 higher.
We calculate an electron velocity via

$$v_e = \sqrt{v_F^2 + 3 v_{th}^2} \tag{6.2.3}$$

to $\sim 5.4 \times 10^6\,\mathrm{m\,s^{-1}}$ for the low intensity leading to a mean free path of $\sim 0.3\,\mathrm{nm}$ using $\nu_e \sim \omega_{pe}$. For the high intensity case the electron velocity is $\sim 16 \times 10^6\,\mathrm{m\,s^{-1}}$ following that the approximation $\nu_e \sim \omega_{pe}$ is not valid anymore. Instead it is $\nu_e \propto T^{-1.5}$ meaning that the collision frequency is smaller than the plasma frequency resulting in a mean free path $> 0.9\,\mathrm{nm}$.
For the laser intensity of $I_L = 8 \times 10^{14}\,\mathrm{W/cm^2}$ we attribute the main contribution to the mass ablation due to electron-ion collision because of the relatively low electron temperature as already discussed in the previous section. However, the higher laser intensity of $I_L = 8 \times 10^{15}\,\mathrm{W/cm^2}$ implies a 10 times higher electron temperature leading to the assumption that the maximum energy of ablated ions

$$E_i = k_B T_e - E_{esc} - E_b \tag{6.2.4}$$

is the main contribution here on the order of several hundred eV. Note that for a precise determination for intensities well over the ablation threshold Eq. (6.2.4) needs to be modified by including energy losses for the ion heating and for electron ionization and emission [42]. However, for a qualitative estimation we keep to Eq. (6.2.4). With this, first the different time scales (9 ps for low intensity and 5 ps for high intensity) of density modulations can be explained. For the high intensity the maximum energy of ablated ions is several orders of magnitude larger than the ablation threshold meaning that the ablation of ions is starting immediately while the mass ablation process starts only later when the electrons transferred enough energy to the ions due to collisions (a few ps).
On the other hand that could also describe the different temporal evolution of the in-plane signal for both laser intensities since there are just different processes contributing.

In conclusion, we measured ML samples with Aluminium top layer using different laser intensities. We found that the dynamics produced with the higher intensity are driven by the increased electron temperature while the dynamics originated from the lower intensity occur mainly because of the energy transfer from electron-ion collisions. For a more quantitative analysis a reconstruction of density profiles by machine learning techniques is required. This, however, is beyond the scope of this thesis.

6.3 Out-of-plane scattering along Q_y

In this section, the main results from the out-of-plane scattering along Q_y are discussed:

1.) **Layer parameters before and after laser excitation without Aluminium**: While the lateral correlation length ξ_L does not change upon laser excitation, the layer roughness is increasing from a roughness factor $r = 2$ to $r = 6$ and the hurst parameter is decreasing from $h = 0.6$ to $h = 0.1$ (Fig. 5.43).

2.) **Layer parameters before and after laser excitation with Aluminium**: With an Aluminium layer on top of the ML sample we observed that the hurst parameter is not changing significantly. Instead the overall roughness is increasing (Fig. 5.44 and 5.45).

3.) **Time scales depending on Aluminium thickness**: Depending on the Aluminium layer we could extract the time t_0 when the layer parameters start to change ranging from $t_0 = 2$ to $t_0 = 10\,\mathrm{ps}$. Additionally, the rise time Δt also depends on the Aluminium thickness increasing from 0.25 ps (0 nm Al) to 1.25 ps (200 nm Al) (Fig. 5.47 and 5.48).

In section 6.1 we explained that the materials experience different electronic pressures and upon thermalization the ions therefore start to intermix with adjacent layers for compensation. This intermixing implies that the layers significantly increase in layer roughness with a reduced hurst parameter.
The origin of the different behaviour of the hurst parameter with and without Al layer is not yet completely clear. But it points towards different processes active for interface mixing depending on Al layer thickness.
We explain the increase of t_0 depending on the Aluminium layer thickness with the time the heatwave needs to penetrate the Aluminium layer for causing density modulations. The dependence is clearly not linear but exponential and we calculate a velocity of $\sim 2.5 \times 10^4\,\mathrm{m\,s^{-1}}$ to penetrate the 50 nm thick Aluminium layer and $\sim 2.0 \times 10^4\,\mathrm{m\,s^{-1}}$ for the 200 nm thick Aluminium layer. By increasing the laser intensity we determine a velocity of $\sim 3.3 \times 10^4\,\mathrm{m\,s^{-1}}$ which is 65% faster. We find also here that the dynamics must be driven by thermal conduction since the sound velocity is much slower.
Finally, we attribute the increasing rise time with increasing Al layer thickness to a significant temporal broadening of the electronic heatwave when passing through the Al layer. Indeed one may expect that the electronic temperature gradient inside the Al plays an important role here in broadening of the heatwave. Again, further simulations are needed to understand and explain this observation quantitatively.

In conclusion, we have shown the feasibility of extracting information about the layer

parameters from the out-of-plane signal along Q_y. The outcome is in good agreement with the result from the in-plane scattering, namely that the dynamics are driven by the heatwave and for laser intensity below $1 \times 10^{15}\,\mathrm{W/cm^2}$ the mass ablation due to electron-ion collisions is the main contribution while for the higher laser intensity the electrostatic ablation is more prominent. Last, we could identify the influence of the Aluminium top layer on the velocity and shape of the heatwave.

Chapter 7

Conclusion and outlook

We studied for the first time surface dynamics of solids upon high-intensity laser irradiation by grazing-incidence X-ray diffuse scattering; in particular, aiming for new insights into dynamically changing density profiles with nanometer spatial and picosecond time resolution. The experiments have been performed at the Free-Electron Laser SPring-8 Angstrom Compact free electron LAser (SACLA) in Japan. Multilayer samples have been excited with a high-intensity laser of intensities from 4×10^{14} to $8 \times 10^{15}\,\mathrm{W/cm^2}$ and pulse duration of $\tau_L = 40\,\mathrm{fs}$. The single pulse X-ray probing has been achieved by using 7 fs XFEL pulses of hard X-rays at 8.81 keV photon energy.

The resulting 2D scattering images have been analyzed with the program BornAgain including background modelling because of parasitic scattering from the beamstop. From the in-plane scattering signal detailed electron density profiles have been reconstructed. We addressed the generic problem of non-unique solutions in reflectivity experiments by also investigating the out-of plane signal along Q_z. Taking the lateral correlation length ξ_L into account helped us to reduce the number of possible solutions to the density profile. We found that after 2 ps all layers are perturbed resulting in a perturbation velocity of $4 \times 10^4\,\mathrm{m\,s^{-1}}$. After 5 ps only a small layer of 30 nm is left while the rest of the material is evaporated into vacuum.

The slow start of ablation is attributed to a finite ion heating time (few picoseconds). After 2 ps we observed dynamics driven by the heatwave with an ablation velocity of $2.4 \times 10^4\,\mathrm{m\,s^{-1}}$. Compression waves can be excluded since they are driven by the sound velocity ($C_s \leq 1.5 \times 10^4\,\mathrm{m\,s^{-1}}$) much slower than the dynamics we observe. For later times the dynamics are decreasing again because of the lower temperature in the deeper layers due to the short laser pulse duration. We compared our experimentally retrieved results with simulations [82] indicating a good agreement. Only the density modulations do not fit to the simulations again emphasizing how important these results are to improve and benchmark existing simulation models.

In the SACLA 2020 experiment, the Q_z-range has been increased up to $Q_z = 2.6\,\mathrm{nm^{-1}}$

to further minimize the problem of multiple solutions. The ML samples have been modified with Aluminium top layers of different thicknesses resulting in a much more detailed scattering pattern, that is on the other hand more complicated to analyze. In the framework of this thesis we demonstrated the refinement of a preshot without laser excitation and performed a qualitative in-plane analysis. The dynamics produced with the higher intensity are driven by electrostatic ablation while the dynamics originated from the lower intensity occur mainly because of the energy transfer from electron-ion collisions. For a more quantitative analysis a reconstruction of density profiles by machine learning techniques is required, however, this is not part of this thesis.

By investigating the out-of-pane signal along Q_y, we have shown the feasibility of extracting information about the surface configuration such as correlation lengths and hurst parameters. The outcome is in good agreement with the result from the in-plane scattering, namely that the dynamics are driven by the heatwave and for laser intensity below $10^{15}\,\mathrm{W/cm^2}$ the mass ablation due to electron-ion collisions is the main contribution while for the higher laser intensity the electrostatic ablation is more prominent. Last, the influence of the Aluminium top layer on the velocity and shape of the heatwave has been identified.

Before these new methods have been developed, the reconstruction of the exact plasma profile during laser excitation was not feasible and prevented from controlling the dynamics for applications and from performing plasma simulations with correct initial conditions. Our new technique will play an important role towards long-awaited quantitative benchmark and improvement of various models and simulation codes.

These results can be useful for all applications that rely on transient dynamics of high-density states: material processing, isochoric heating, laser dynamic compression and relativistic laser matter interaction.

In the future, we want to employ smaller X-ray beam sizes or a co-linear geometry between high-intensity laser and X-ray beam resulting in a temporal resolution on the order of the X-ray pulse duration, only a few femtoseconds. Furthermore, it is absolutely required to implement computational methods such as machine learning for electron density reconstruction, especially with the larger Q_z-range.

More general, only the recent advent of Free-Electron Lasers allows us to study these nanoscale dynamics with femtosecond time resolution. Up to now, this was not possible because of missing techniques. Bringing together X-ray scattering techniques and high energy density science opens a complete new field in understanding the fundamental processes in laser-plasma interaction. In the framework of this thesis, we developed important new methods that will support the fundamental understanding of plasma surface dynamics.

Chapter 8

Appendix

8.1 BornAgain code

```
material_1 = ba.HomogeneousMaterial("Air", 0.0, 0.0)
material_2 = ba.HomogeneousMaterial("TaO", 1.8e-05, 3.3e-7)
material_3 = ba.HomogeneousMaterial("Ta1", 3.3e-05, 2.34e-06)
material_4 = ba.HomogeneousMaterial("Cu3N1", 1.95e-05, 3.65e-07)
material_5 = ba.HomogeneousMaterial("Ta2", 3.27e-05, 2.34e-06)
material_6 = ba.HomogeneousMaterial("Cu3N2", 1.95e-05, 3.65e-07)
material_7 = ba.HomogeneousMaterial("Ta3", 3.27e-05, 2.34e-06)
material_8 = ba.HomogeneousMaterial("Cu3N3", 1.95e-05, 3.65e-07)
material_9 = ba.HomogeneousMaterial("Ta4", 3.27e-05, 2.34e-06)
material_10 = ba.HomogeneousMaterial("Cu3N4", 1.95e-05, 3.65e-07)
material_11 = ba.HomogeneousMaterial("Ta5", 3.27e-05, 2.34e-06)
material_12 = ba.HomogeneousMaterial("Cu3N5", 1.95e-05, 3.65e-07)
material_13 = ba.HomogeneousMaterial("Ta6", 3.27e-05, 2.34e-06)
material_14 = ba.HomogeneousMaterial("SiO2", 5.93e-06, 7.42e-08)
material_15 = ba.HomogeneousMaterial("Substrate", 6.31e-06, 1.21e-07)
```

Figure 8.1: BornAgain code defining dispersion and absorption coefficients for all materials.

```
# Defining Layers
layer_1=ba.Layer(material_1)
layer_2 = ba.Layer(material_2, 4.29)
layer_3 = ba.Layer(material_3,4.38)
layer_4 = ba.Layer(material_4, 11.49)
layer_5 = ba.Layer(material_5, 4.38)
layer_6 = ba.Layer(material_6, 11.49)
layer_7 = ba.Layer(material_7, 4.38)
layer_8 = ba.Layer(material_8, 11.49)
layer_9 = ba.Layer(material_9, 4.38)
layer_10 = ba.Layer(material_10, 11.49)
layer_11 = ba.Layer(material_11, 4.38)
layer_12 = ba.Layer(material_12, 11.49)
layer_13 = ba.Layer(material_13, 4.38)
layer_14 = ba.Layer(material_14, 100)
layer_15 = ba.Layer(material_15)
```

Figure 8.2: BornAgain code setting an individual layer thickness for every layer.

```
# Defining Roughness Parameters
layerRoughness_1 = ba.LayerRoughness(0.46,0.6,30.0*nm)
layerRoughness_2 = ba.LayerRoughness(0.46, 0.6, 30.0*nm)
layerRoughness_3 = ba.LayerRoughness(0.39, 0.6, 30.0*nm)
layerRoughness_4 = ba.LayerRoughness(0.57, 0.6, 30.0*nm)
layerRoughness_5 = ba.LayerRoughness(0.39, 0.6, 30.0*nm)
layerRoughness_6 = ba.LayerRoughness(0.57, 0.6, 30.0*nm)
layerRoughness_7 = ba.LayerRoughness(0.39, 0.6, 30.0*nm)
layerRoughness_8 = ba.LayerRoughness(0.57, 0.6, 30.0*nm)
layerRoughness_9 = ba.LayerRoughness(0.39, 0.6, 30.0*nm)
layerRoughness_10 = ba.LayerRoughness(0.57, 0.6, 30.0*nm)
layerRoughness_11 = ba.LayerRoughness(0.39, 0.6, 30.0*nm)
layerRoughness_12 = ba.LayerRoughness(0.57, 0.6, 30.0*nm)
layerRoughness_13 = ba.LayerRoughness(0.54, 0.6, 30.0*nm)
layerRoughness_14 = ba.LayerRoughness(0.54, 0.6, 30.0*nm)
```

Figure 8.3: BornAgain code defining a roughness, hurst parameter and lateral correlation length for every layer.

```
def get_sample():
    material_1
    material_2
    ...

    layer_1
    layer_2
    ...

    layerRoughness_1
    layerRoughness_2
    ...

    multiLayer_1 = ba.MultiLayer()
    multiLayer_1.setCrossCorrLength(2000)
    multiLayer_1.addLayer(layer_1)
    multiLayer_1.addLayerWithTopRoughness(layer_2, layerRoughness_1)
    multiLayer_1.addLayerWithTopRoughness(layer_3, layerRoughness_2)
    ...



    return multiLayer_1
```

Figure 8.4: BornAgain code connecting every layer thickness to material and roughness, hurst parameter and lateral correlation length. Additionally, the cross correlation length is defined.

```
def get_simulation():
    simulation = ba.GISASSimulation()

    detector = ba.RectangularDetector(30, 1.5, 1024, 51.2)
    detector.setPerpendicularToReflectedBeam(1277.0, 0.75, 20.65)
    simulation.setDetector(detector)

    simulation.setDetectorResolutionFunction(ba.ResolutionFunction2DGaussian(0.02, 0.02))
    simulation.setBeamParameters(0.14073*nm, 0.64*deg, 0.0*deg)
    simulation.setBeamIntensity(1e+13)
    simulation.getOptions().setUseAvgMaterials(True)
    simulation.getOptions().setIncludeSpecular(False)
    background = ba.ConstantBackground(6e+01)
    simulation.setBackground(background)
    return simulation
```

Figure 8.5: BornAgain code creating a simulation. The detector properties and setup parameters are defined.

```
def run_simulation():
    sample = get_sample()
    simulation = get_simulation()
    simulation.setSample(sample)
    simulation.runSimulation()

    return simulation.result()
```

Figure 8.6: BornAgain code for running the simulation.

8.2 In-plane modelling low intensity

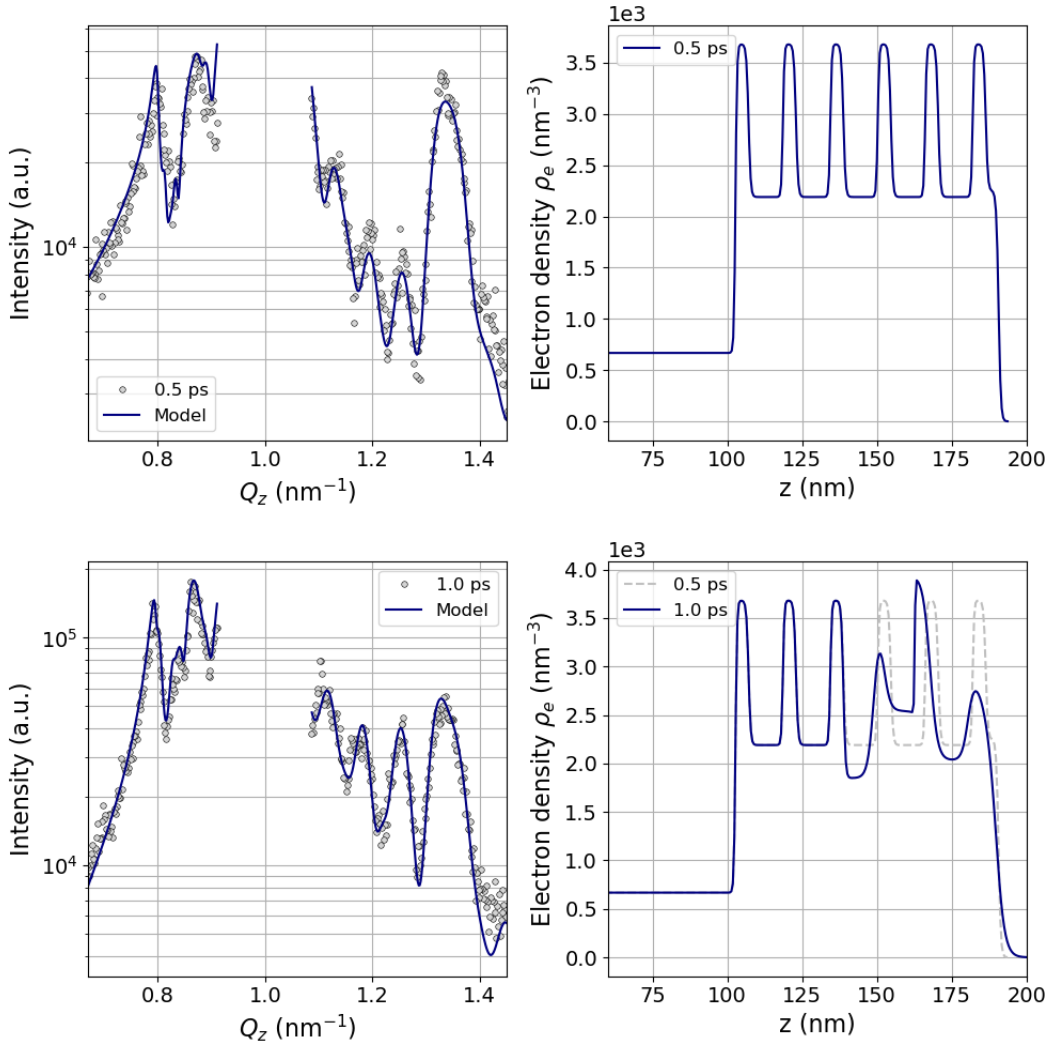

Figure 8.7: Top left: In-plane signal along Q_z for $t = 0.5\,\text{ps}$ and refinement. Top right: Reconstructed electron density profile for 0.5 ps. Bottom left: In-plane signal along Q_z for $t = 1.0\,\text{ps}$ and refinement. Bottom right: Reconstructed electron density profile for 1.0 ps.

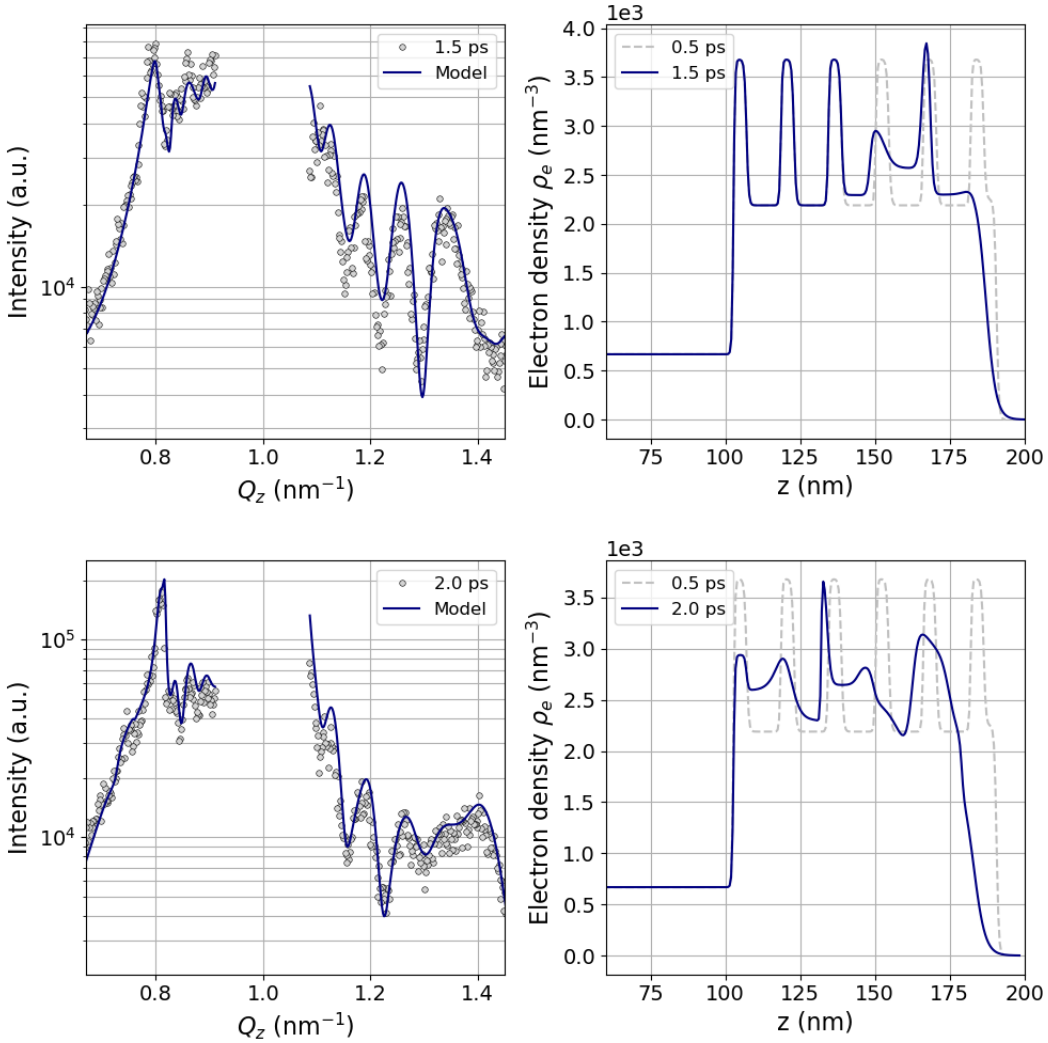

Figure 8.8: Top left: In-plane signal along Q_z for $t = 1.5\,\text{ps}$ and refinement. Top right: Reconstructed electron density profile for 1.5 ps. Bottom left: In-plane signal along Q_z for $t = 2.0\,\text{ps}$ and refinement. Bottom right: Reconstructed electron density profile for 2.0 ps.

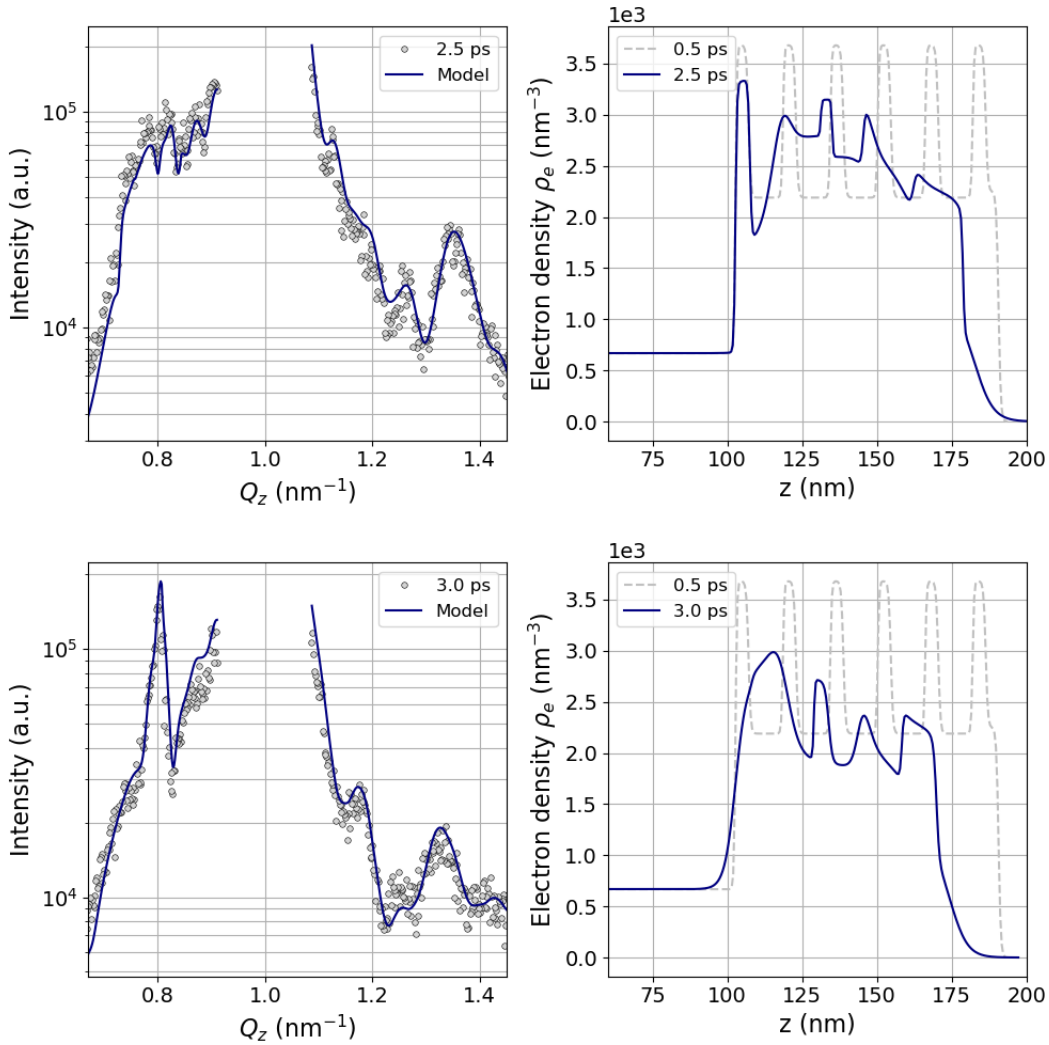

Figure 8.9: Top left: In-plane signal along Q_z for $t = 2.5\,\text{ps}$ and refinement. Top right: Reconstructed electron density profile for 2.5 ps. Bottom left: In-plane signal along Q_z for $t = 3.0\,\text{ps}$ and refinement. Bottom right: Reconstructed electron density profile for 3.0 ps.

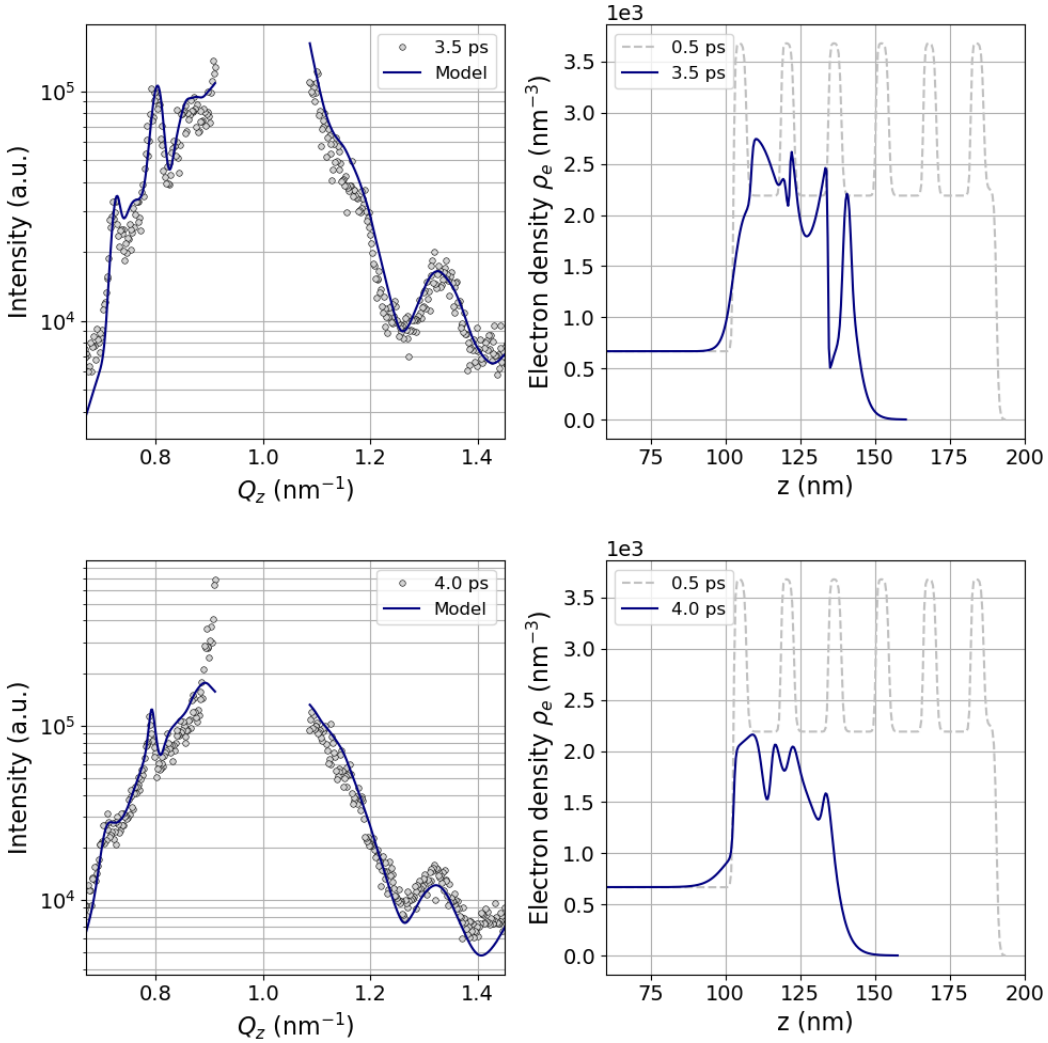

Figure 8.10: Top left: In-plane signal along Q_z for $t = 3.5\,\text{ps}$ and refinement. Top right: Reconstructed electron density profile for 3.5 ps. Bottom left: In-plane signal along Q_z for $t = 4.0\,\text{ps}$ and refinement. Bottom right: Reconstructed electron density profile for 4.0 ps.

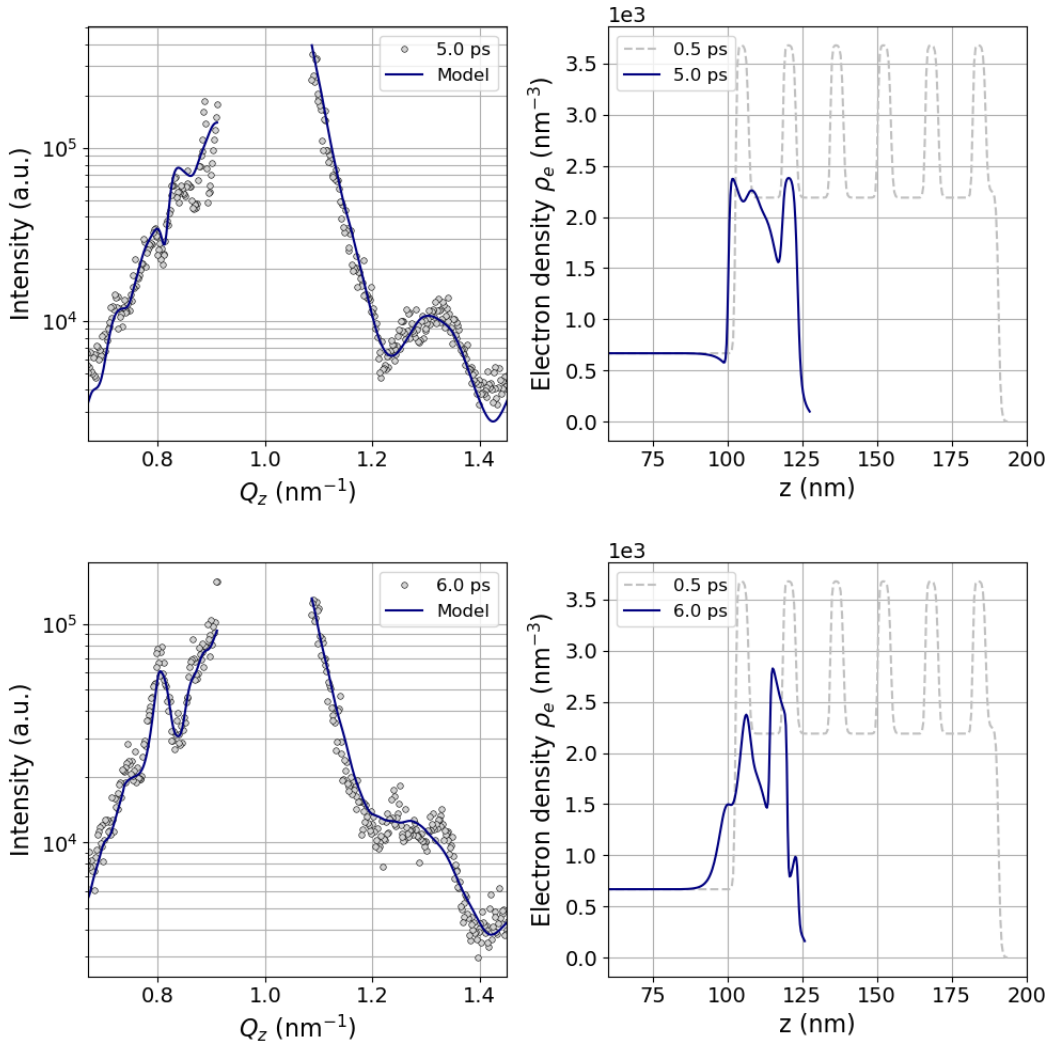

Figure 8.11: Top left: In-plane signal along Q_z for $t = 5.0\,\text{ps}$ and refinement. Top right: Reconstructed electron density profile for 5.0 ps. Bottom left: In-plane signal along Q_z for $t = 6.0\,\text{ps}$ and refinement. Bottom right: Reconstructed electron density profile for 6.0 ps.

8.3 In-plane modelling intermediate intensity

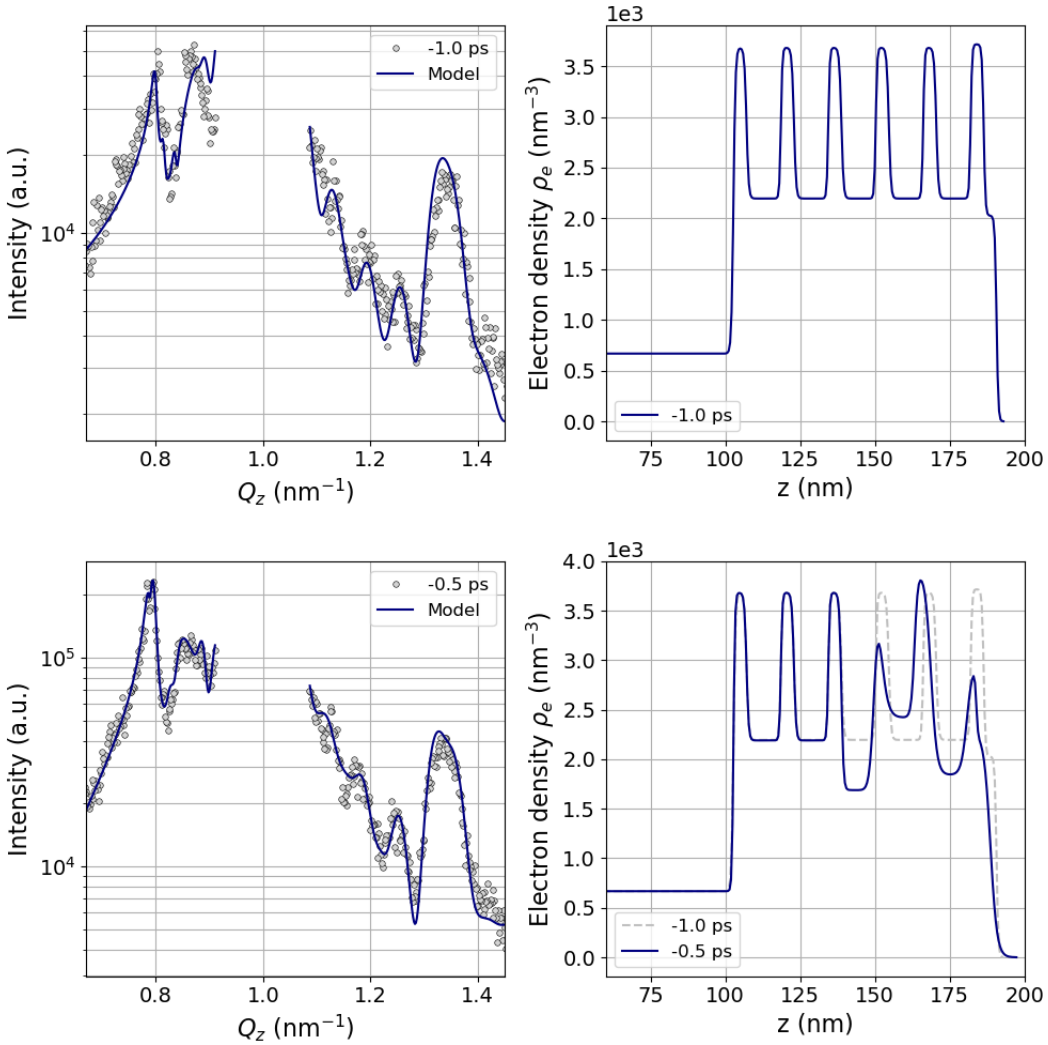

Figure 8.12: Top left: In-plane signal along Q_z for $t = -1.0\,\text{ps}$ and refinement. Top right: Reconstructed electron density profile for $-1.0\,\text{ps}$. Bottom left: In-plane signal along Q_z for $t = -0.5\,\text{ps}$ and refinement. Bottom right: Reconstructed electron density profile for $-0.5\,\text{ps}$.

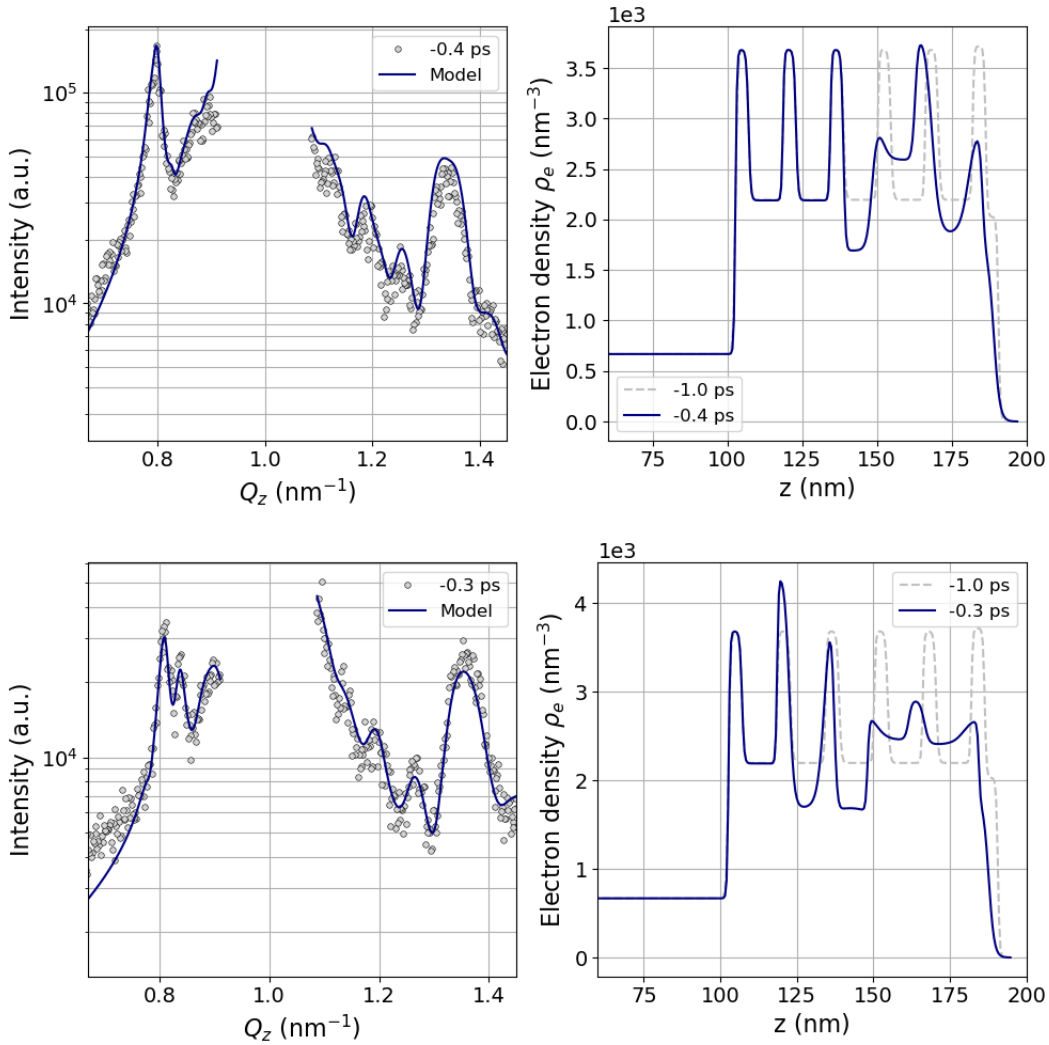

Figure 8.13: Top left: In-plane signal along Q_z for $t = -0.4\,\text{ps}$ and refinement. Top right: Reconstructed electron density profile for $-0.4\,\text{ps}$. Bottom left: In-plane signal along Q_z for $t = -0.3\,\text{ps}$ and refinement. Bottom right: Reconstructed electron density profile for $-0.3\,\text{ps}$.

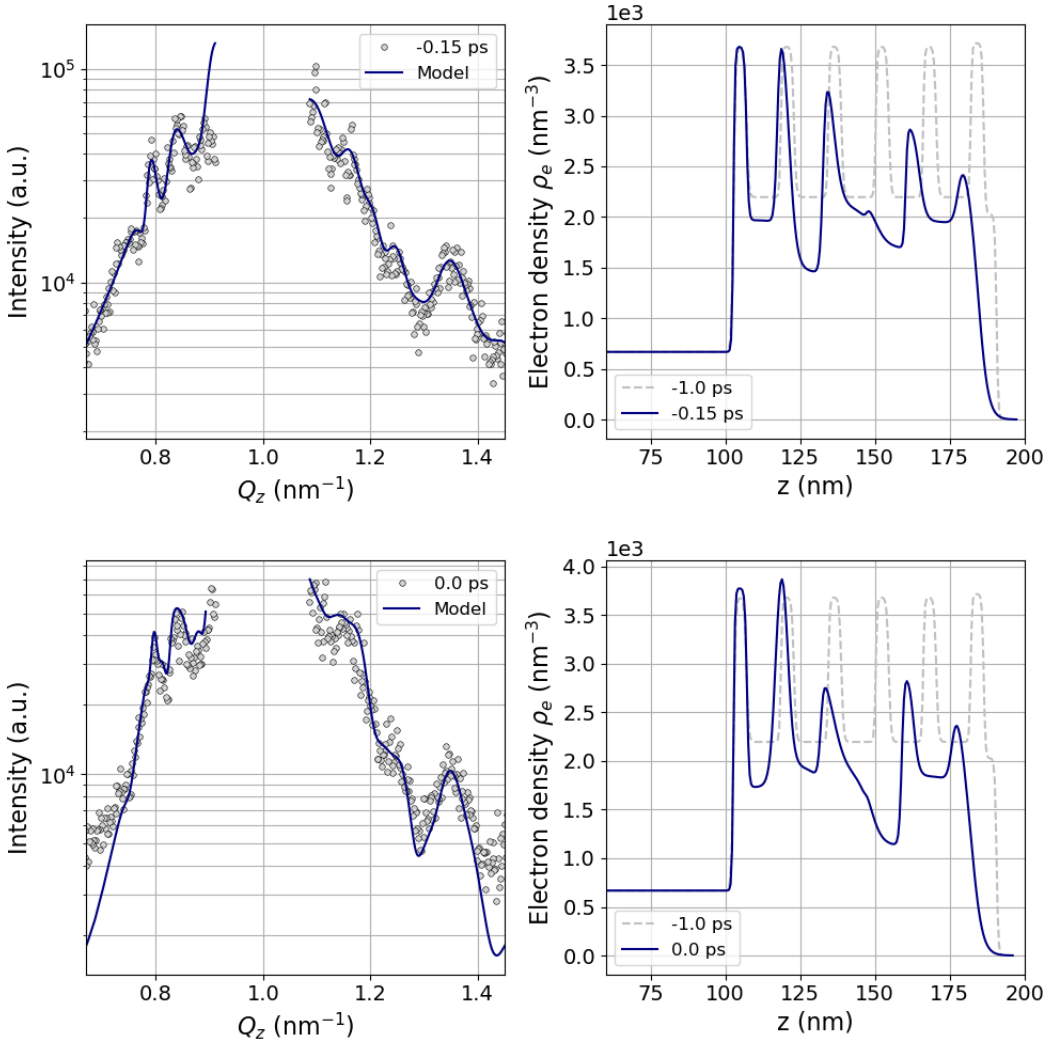

Figure 8.14: Top left: In-plane signal along Q_z for $t = -0.15\,\text{ps}$ and refinement. Top right: Reconstructed electron density profile for $-0.15\,\text{ps}$. Bottom left: In-plane signal along Q_z for $t = 0.0\,\text{ps}$ and refinement. Bottom right: Reconstructed electron density profile for $0.0\,\text{ps}$.

8.4 Uniqueness analysis for 2.0 ps

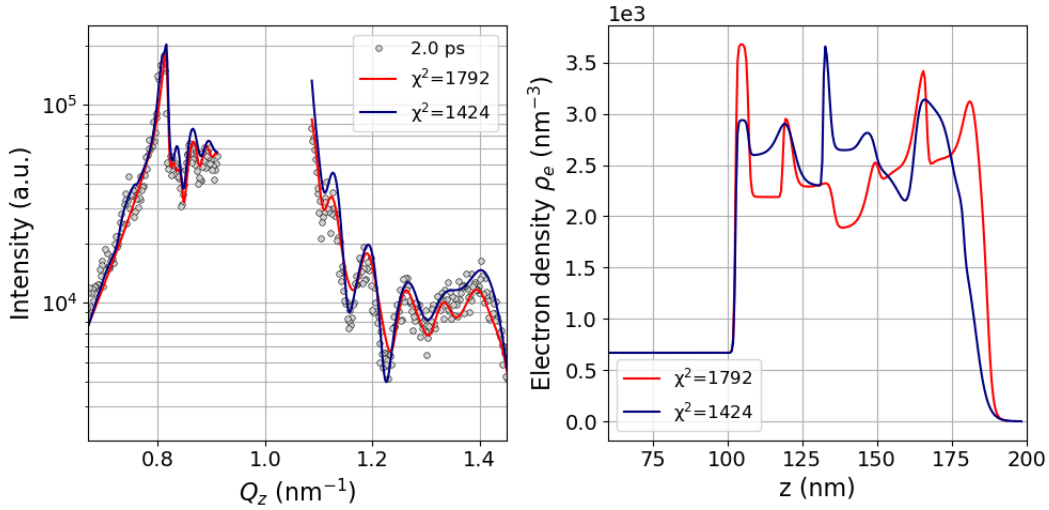

Figure 8.15: Two fits for the in-plane signal with $t = 2.0\,\text{ps}$ time delay. Both X-ray signals look similar while showing very different density profiles.

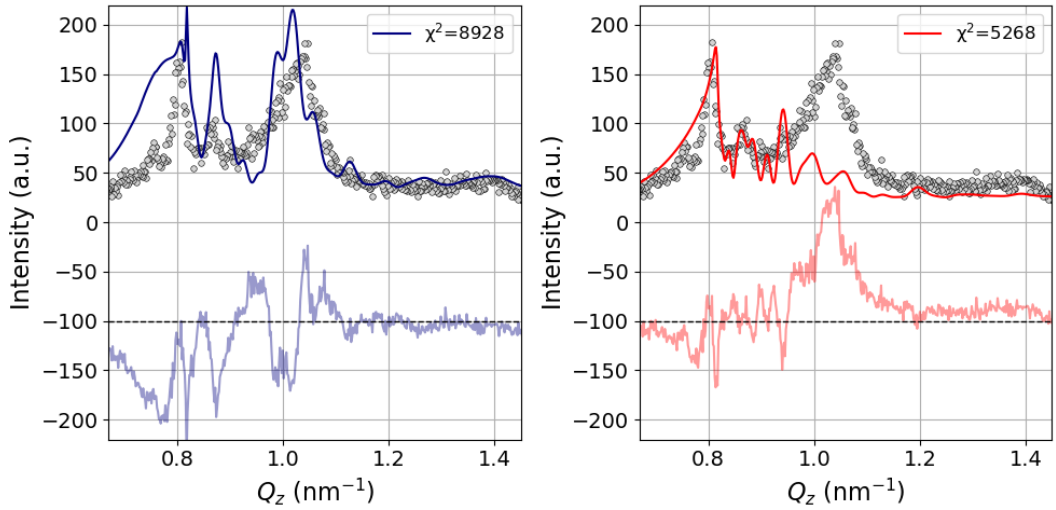

(a) Layer 1 – 14: $\xi_L = 30\,\text{nm}$

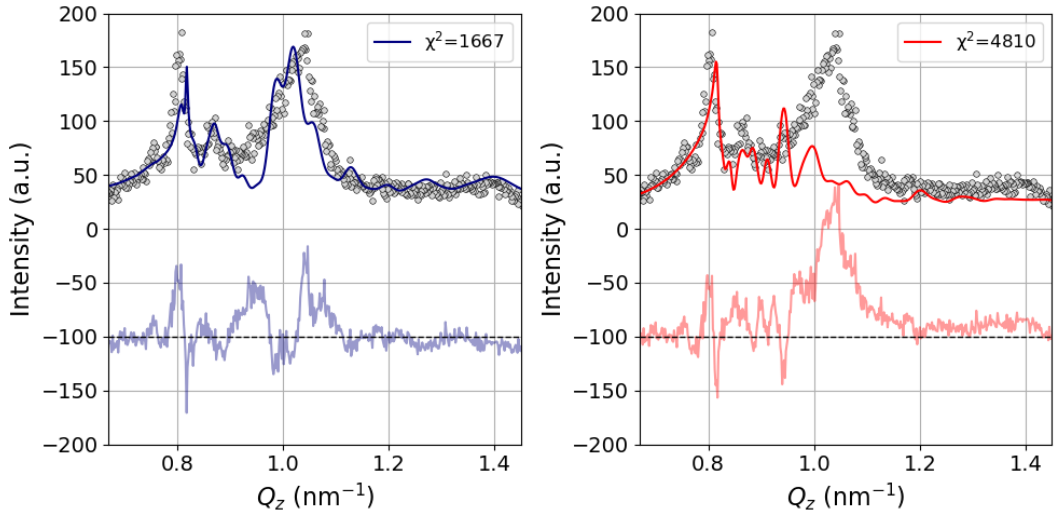

(b) Layer 1: $\xi_L = 1\,\text{nm}$; Layer 2 – 14: $\xi_L = 30\,\text{nm}$

Figure 8.16: Out-of-plane signal along Q_z based on the electron density profile in Fig. 8.15(right). The grey points denote the XDS data, the blue and red lines indicate the simulated out-of-plane signal and the light blue and red lines display the differences between simulation and data. The blue colored figure (left) corresponds to the blue electron density profile and the red colored figure to the red profile, respectively. (a) displays the out-of-plane signal with a lateral correlation length $\xi_L = 30\,\text{nm}$ for all layers. (b) shows the out-of-plane signal with a decreased lateral correlation length $\xi_L = 1\,\text{nm}$ for the first layer.

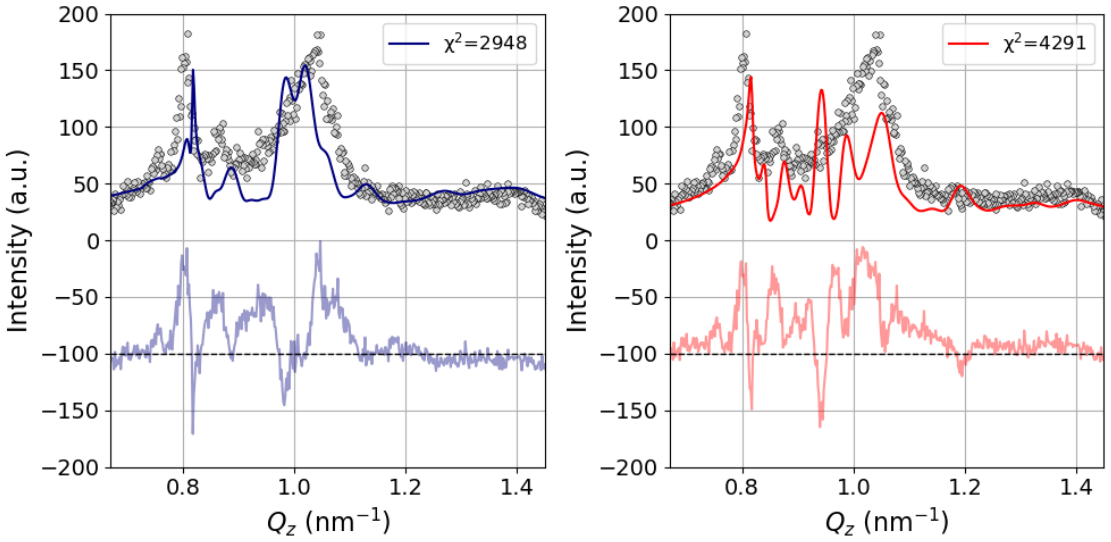

(a) Layer $1-6$: $\xi_L = 1\,\text{nm}$; Layer $7-14$: $\xi_L = 30\,\text{nm}$

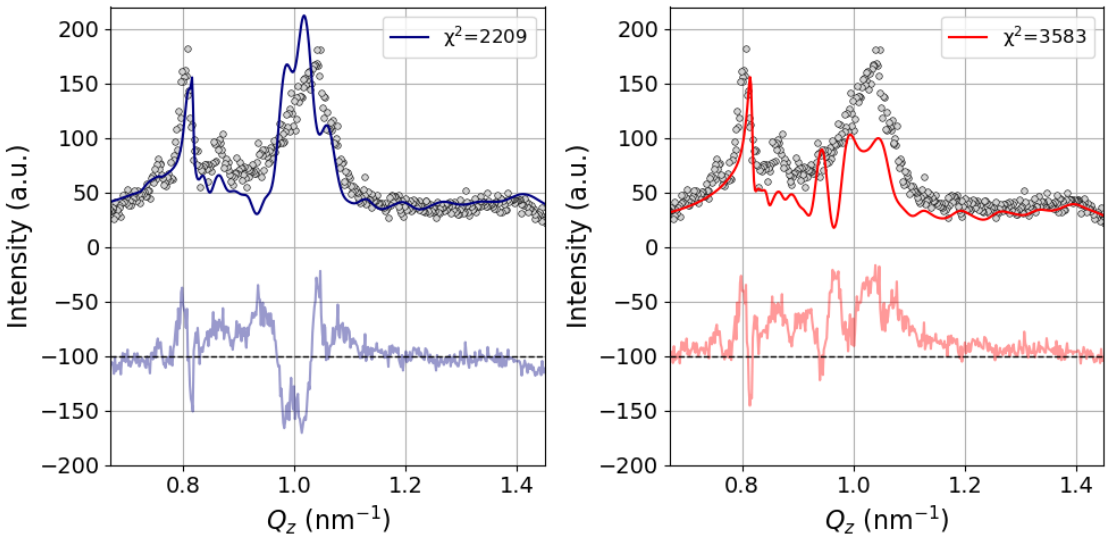

(b) Layer $1-12$: $\xi_L = 1\,\text{nm}$; Layer $13-14$: $\xi_L = 30\,\text{nm}$

Figure 8.17: Out-of-plane signal along Q_z based on the electron density profile in Fig. 8.15(right). The grey points denote the XDS data, the blue and red lines indicate the simulated out-of-plane signal and the light blue and red lines display the differences between simulation and data. The blue colored figure (left) corresponds to the blue electron density profile and the red colored figure to the red profile, respectively. (a) displays the out-of-plane signal with a lateral correlation length $\xi_L = 1\,\text{nm}$ for layer $1-6$ and $\xi_L = 30\,\text{nm}$ for layer $7-14$. (b) shows the out-of-plane signal with a decreased lateral correlation length $\xi_L = 1\,\text{nm}$ for layer $1-12$.

2.0 ps	$\xi_L = 1\,\text{nm}$	$\xi_L = 30\,\text{nm}$	χ^2 blue profile	χ^2 red profile
1	-	layer $1-14$	8928	5268
2	**layer 1**	**layer $2-14$**	**1667**	**4810**
3	layer $1-6$	layer $7-14$	2948	4291
4	layer $1-12$	layer $13-14$	2209	3583

Table 8.1: Overview of the different combinations of lateral correlation length ξ_L and resulting χ^2 values from Fig. 8.16 and 8.17.

8.5 Diffuse scattering with 50 nm Aluminium

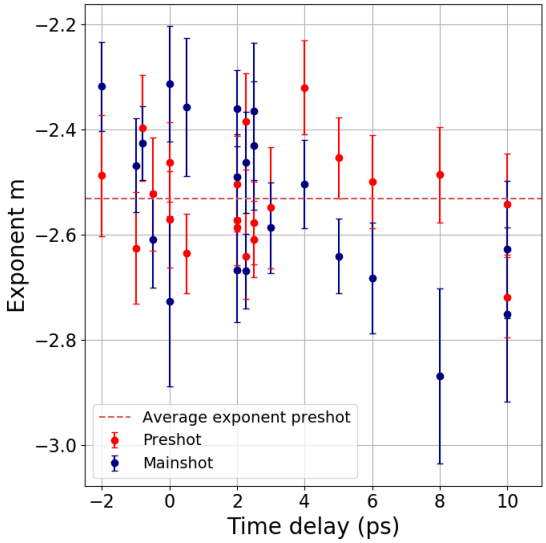

(a) Exponent m as a function of time delay for $Q_z = 0.79\,\mathrm{nm}^{-1}$.

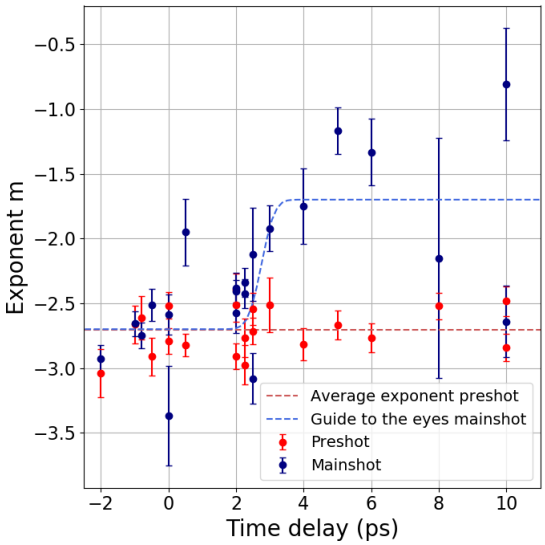

(b) Exponent m as a function of time delay for $Q_z = 1.33\,\mathrm{nm}^{-1}$.

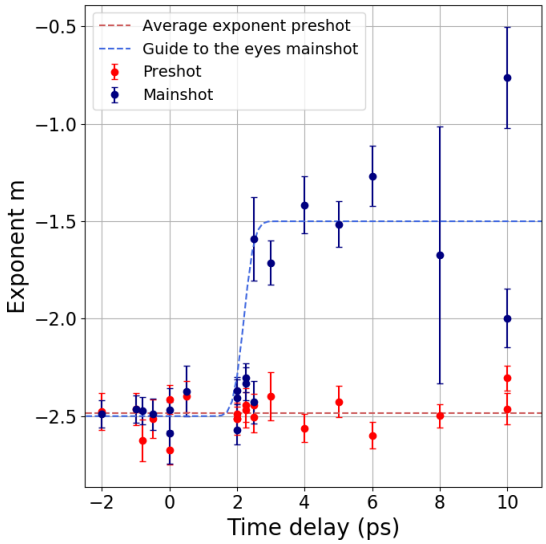

(c) Exponent m as a function of time delay for $Q_z = 1.73\,\mathrm{nm}^{-1}$.

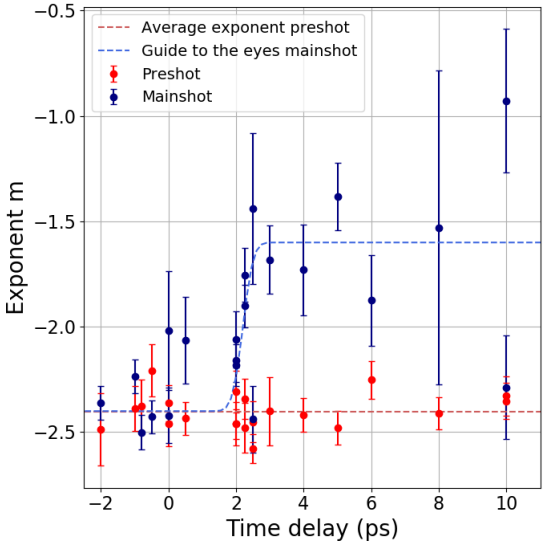

(d) Exponent m as a function of time delay for $Q_z = 2.10\,\mathrm{nm}^{-1}$.

Figure 8.18: Modelled exponent m as a function of time delay for the ML sample with 50 nm thick Aluminium for different Q_z values.

8.6 Diffuse scattering with 200 nm Aluminium low intensity

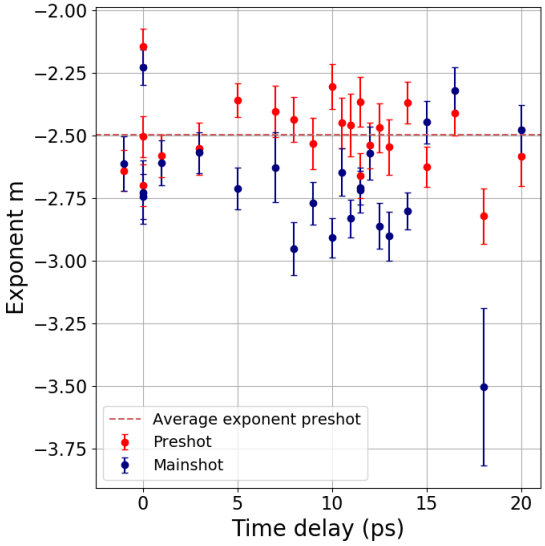

(a) Exponent m as a function of time delay for $Q_z = 0.79\,\mathrm{nm}^{-1}$.

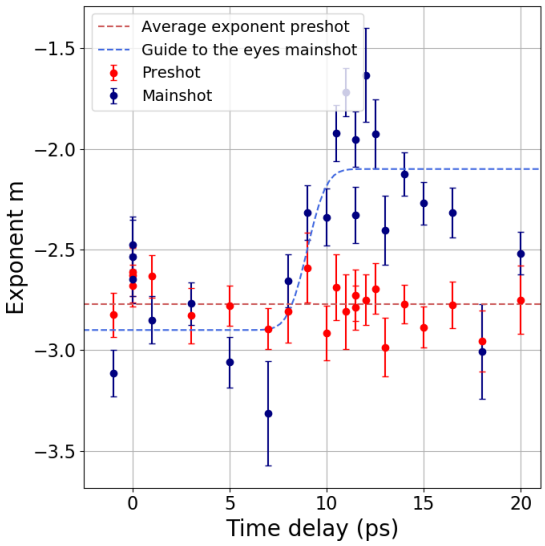

(b) Exponent m as a function of time delay for $Q_z = 1.33\,\mathrm{nm}^{-1}$.

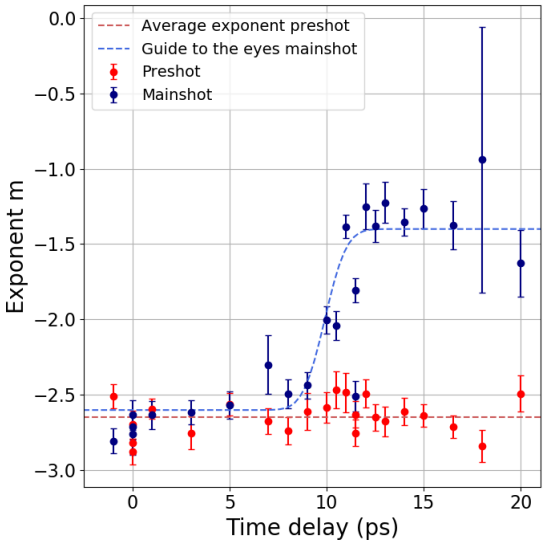

(c) Exponent m as a function of time delay for $Q_z = 1.73\,\mathrm{nm}^{-1}$.

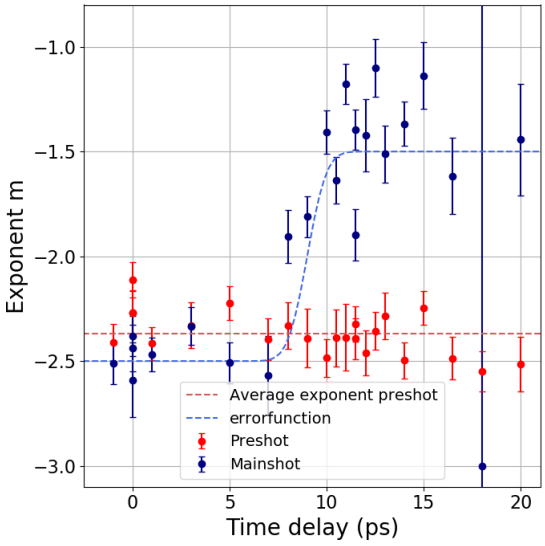

(d) Exponent m as a function of time delay for $Q_z = 2.10\,\mathrm{nm}^{-1}$.

Figure 8.19: Modelled exponent m as a function of time delay for the ML sample with 200 nm thick Aluminium investigated with the lower laser intensity for different Q_z values.

8.7 Diffuse scattering with 200 nm Aluminium high intensity

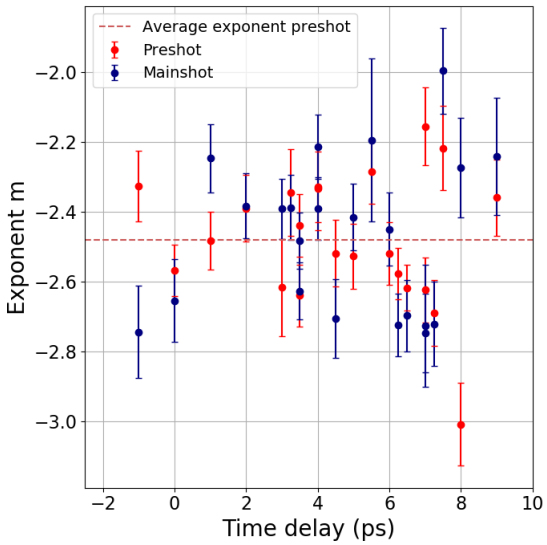

(a) Exponent m as a function of time delay for $Q_z = 0.79\,\mathrm{nm}^{-1}$.

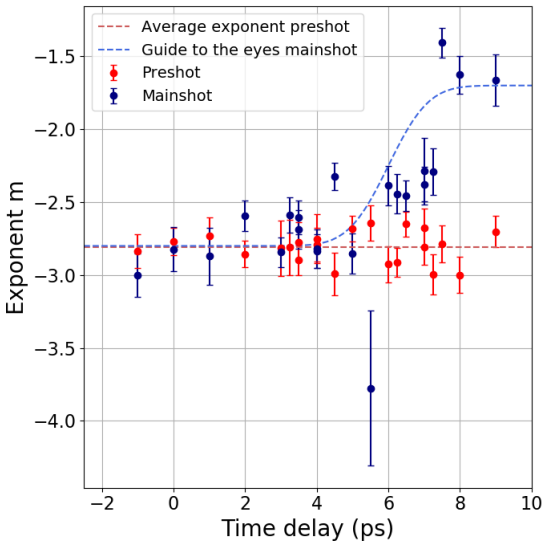

(b) Exponent m as a function of time delay for $Q_z = 1.33\,\mathrm{nm}^{-1}$.

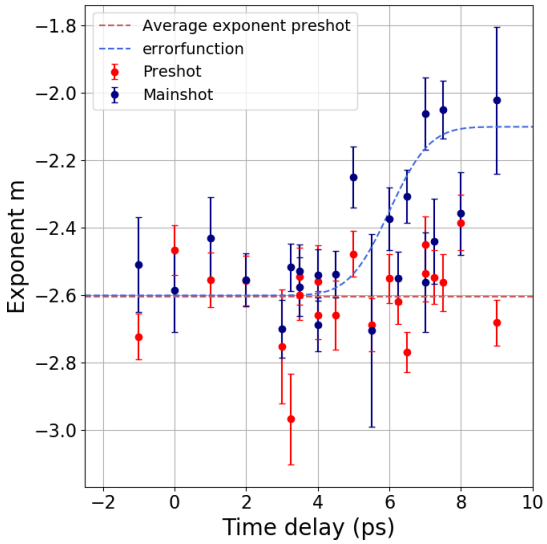

(c) Exponent m as a function of time delay for $Q_z = 1.73\,\mathrm{nm}^{-1}$.

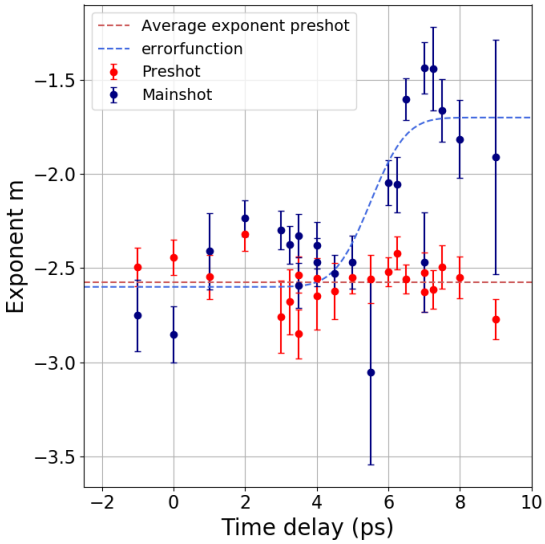

(d) Exponent m as a function of time delay for $Q_z = 2.10\,\mathrm{nm}^{-1}$.

Figure 8.20: Modelled exponent m as a function of time delay for the ML sample with 200 nm thick Aluminium investigated with the higher laser intensity for different Q_z values.

Bibliography

[1] P. Gibbon, *Short Pulse Laser Interactions with Matter*. London: Imperial College Press, 2005.

[2] B. A. Remington, R. P. Drake, H. Takabe, and D. Arnett, "A review of astrophysics experiments on intense lasers," *Physics of Plasmas*, vol. 7, no. 5, pp. 1641–1652, 2000.

[3] C. Thaury and F. Quéré, "High-order harmonic and attosecond pulse generation on plasma mirrors: basic mechanisms," *Journal of Physics B: Atomic, Molecular and Optical Physics*, vol. 43, p. 213001, oct 2010.

[4] A. Macchi, M. Borghesi, and M. Passoni, "Ion acceleration by superintense laser-plasma interaction," *Rev. Mod. Phys.*, vol. 85, pp. 751–793, May 2013.

[5] L. Chopineau, A. Leblanc, G. Blaclard, A. Denoeud, M. Thévenet, J.-L. Vay, G. Bonnaud, P. Martin, H. Vincenti, and F. Quéré, "Identification of coupling mechanisms between ultraintense laser light and dense plasmas," *Phys. Rev. X*, vol. 9, p. 011050, Mar 2019.

[6] A. Lévy, T. Ceccotti, P. D'Oliveira, F. Réau, M. Perdrix, F. Quéré, P. Monot, M. Bougeard, H. Lagadec, P. Martin, J.-P. Geindre, and P. Audebert, "Double plasma mirror for ultrahigh temporal contrast ultraintense laser pulses," *Opt. Lett.*, vol. 32, pp. 310–312, Feb 2007.

[7] M. Nakatsutsumi, A. Kon, S. Buffechoux, P. Audebert, J. Fuchs, and R. Kodama, "Fast focusing of short-pulse lasers by innovative plasma optics toward extreme intensity," *Opt. Lett.*, vol. 35, pp. 2314–2316, Jul 2010.

[8] S. Weber, S. Bechet, S. Borneis, L. Brabec, M. Bučka, E. Chacon-Golcher, M. Ciappina, M. DeMarco, A. Fajstavr, K. Falk, E.-R. Garcia, J. Grosz, Y.-J. Gu, J.-C. Hernandez, M. Holec, P. Janečka, M. Jantač, M. Jirka, H. Kadlecova, D. Khikhlukha, O. Klimo, G. Korn, D. Kramer, D. Kumar, T. Lastovička, P. Lutoslawski, L. Morejon, V. Olšovcová, M. Rajdl, O. Renner, B. Rus, S. Singh, M. Šmid, M. Sokol, R. Versaci, R. Vrána, M. Vranic, J. Vyskočil, A. Wolf, and Q. Yu, "P3: An installation for high-energy density plasma physics and ultra-high intensity laser–matter interaction

at eli-beamlines," *Matter and Radiation at Extremes*, vol. 2, no. 4, pp. 149 – 176, 2017.

[9] H. Vincenti, S. Monchocé, S. Kahaly, G. Bonnaud, P. Martin, and F. Quere, "Optical properties of relativistic plasma mirrors (open access)," *Nature Communications*, vol. 5, p. 3403, 03 2014.

[10] J. P. Geindre, P. Audebert, A. Rousse, F. Falliès, J. C. Gauthier, A. Mysyrowicz, A. D. Santos, G. Hamoniaux, and A. Antonetti, "Frequency-domain interferometer for measuring the phase and amplitude of a femtosecond pulse probing a laser-produced plasma," *Opt. Lett.*, vol. 19, pp. 1997–1999, Dec 1994.

[11] Z. Chen, M. Mo, L. Soulard, V. Recoules, P. Hering, Y. Y. Tsui, S. H. Glenzer, and A. Ng, "Interatomic potential in the nonequilibrium warm dense matter regime," *Phys. Rev. Lett.*, vol. 121, p. 075002, Aug 2018.

[12] T. Kluge, M. Rödel, J. Metzkes-Ng, A. Pelka, A. L. Garcia, I. Prencipe, M. Rehwald, M. Nakatsutsumi, E. E. McBride, T. Schönherr, M. Garten, N. J. Hartley, M. Zacharias, J. Grenzer, A. Erbe, Y. M. Georgiev, E. Galtier, I. Nam, H. J. Lee, S. Glenzer, M. Bussmann, C. Gutt, K. Zeil, C. Rödel, U. Hübner, U. Schramm, and T. E. Cowan, "Observation of ultrafast solid-density plasma dynamics using femtosecond x-ray pulses from a free-electron laser," *Phys. Rev. X*, vol. 8, p. 031068, Sep 2018.

[13] T. Kluge, M. Bussmann, H.-K. Chung, C. Gutt, L. G. Huang, M. Zacharias, U. Schramm, and T. E. Cowan, "Nanoscale femtosecond imaging of transient hot solid density plasmas with elemental and charge state sensitivity using resonant coherent diffraction," *Physics of Plasmas*, vol. 23, no. 3, p. 033103, 2016.

[14] T. Kluge, C. Gutt, L. G. Huang, J. Metzkes, U. Schramm, M. Bussmann, and T. E. Cowan, "Using x-ray free-electron lasers for probing of complex interaction dynamics of ultra-intense lasers with solid matter," *Physics of Plasmas*, vol. 21, no. 3, p. 033110, 2014.

[15] T. Kluge, C. Rödel, M. Rödel, A. Pelka, E. E. McBride, L. B. Fletcher, M. Harmand, A. Krygier, A. Higginbotham, M. Bussmann, E. Galtier, E. Gamboa, A. L. Garcia, M. Garten, S. H. Glenzer, E. Granados, C. Gutt, H. J. Lee, B. Nagler, W. Schumaker, F. Tavella, M. Zacharias, U. Schramm, and T. E. Cowan, "Nanometer-scale characterization of laser-driven compression, shocks, and phase transitions, by x-ray scattering using free electron lasers," *Physics of Plasmas*, vol. 10, no. 24, p. 102709, 2017.

[16] A. Hexemer and P. Müller-Buschbaum, "Advanced grazing-incidence techniques for modern soft-matter materials analysis," *IUCrJ*, vol. 2, pp. 106–125, Jan 2015.

[17] V. Holý, J. Kuběna, I. Ohlídal, K. Lischka, and W. Plotz, "X-ray reflection from rough layered systems," *Phys. Rev. B*, vol. 47, pp. 15896–15903, Jun 1993.

[18] V. H. U. Pietsch and T. Baumbach, *High-Resolution X-Ray Scattering*. Springer, 2004.

[19] M. Tolan, *X-Ray Scattering from Soft-Matter Thin Films*. Berlin-Heidelberg: Springer-Verlag, 1999.

[20] "Material:silicon." `http://gisaxs.com/index.php/Material:Silicon`. (accessed: 18.06.2020).

[21] Z. Jiang, "Theory of gisaxs." `https://docplayer.net/44132960-Theory-of-gisaxs-zhang-jiang-advanced-photon-source-argonne-national-laboratory-aca-gisaxs-workshop.html`. (accessed: 18.06.2020).

[22] L. G. Parratt, "Surface studies of solids by total reflection of x-rays," *Phys. Rev.*, vol. 95, pp. 359–369, Jul 1954.

[23] J.-P. Schlomka, M. Tolan, L. Schwalowsky, O. H. Seeck, J. Stettner, and W. Press, "X-ray diffraction from si/ge layers: Diffuse scattering in the region of total external reflection," *Phys. Rev. B*, vol. 51, pp. 2311–2321, Jan 1995.

[24] S. K. Sinha, E. B. Sirota, S. Garoff, and H. B. Stanley, "X-ray and neutron scattering from rough surfaces," *Phys. Rev. B*, vol. 38, pp. 2297–2311, Aug 1988.

[25] J. R. Levine, J. B. Cohen, Y. W. Chung, and P. Georgopoulos, "Grazing-incidence small-angle X-ray scattering: new tool for studying thin film growth," *Journal of Applied Crystallography*, vol. 22, pp. 528–532, Dec 1989.

[26] A. Meyer, "Gisaxs grazing incidence small-angle x-ray scattering." `http://gisaxs.de/theory.html`. (accessed: 09.12.2019).

[27] J. N. Bardsley, B. M. Penetrante, and M. H. Mittleman, "Relativistic dynamics of electrons in intense laser fields," *Phys. Rev. A*, vol. 40, pp. 3823–3835, Oct 1989.

[28] I. H. Hutchinson, *Principles of Plasma Diagnostics*. Cambridge: Cambridge University Press, 1987.

[29] J. Edwards and S. J. Rose, "Ionization time scales in hot dense plasma," *Journal of Physics B: Atomic, Molecular and Optical Physics*, vol. 26, pp. L523–L527, aug 1993.

[30] R. P. J. Town, A. R. Bell, and S. J. Rose, "Fokker-planck calculations with ionization dynamics of short-pulse laser-solid interactions," *Phys. Rev. Lett.*, vol. 74, pp. 924–927, Feb 1995.

[31] A. Djaoui, "Time-dependent hydrogenic ionization model for non-lte mixtures," *Journal of Quantitative Spectroscopy and Radiative Transfer*, vol. 62, no. 3, pp. 303 – 320, 1999.

[32] W. L. Kruer and K. Estabrook, "J $\times b$ heating by very intense laser light," *The Physics of Fluids*, vol. 28, no. 1, pp. 430–432, 1985.

[33] R. Dendy, *Plasma Physics: An Introductory Course*. Cambridge: Cambridge University Press, 1993.

[34] S. Steinke, "Entwicklung eines doppel-plasmaspiegels zur erzeugung hochenergetischer ionen mit ultra-dünnen targets." `https://refubium.fu-berlin.de/bitstream/handle/fub188/16482/diplom/_%20steinke.pdf?sequence=1`. (accessed: 28.07.2020).

[35] H. M. Milchberg and R. R. Freeman, "Light absorption in ultrashort scale length plasmas," *J. Opt. Soc. Am. B*, vol. 6, pp. 1351–1355, Jul 1989.

[36] J. . Kieffer, J. . Matte, S. Belair, M. Chaker, P. Audebert, H. Pepin, P. Maine, D. Strickland, P. Bado, and G. Mourou, "Absorption of an ultrashort laser pulse in very steep plasma density gradients," *IEEE Journal of Quantum Electronics*, vol. 25, pp. 2639–2647, Dec 1989.

[37] R. Fedosejevs, R. Ottmann, R. Sigel, G. Kühnle, S. Szatmári, and F. P. Schäfer, "Absorption of subpicosecond ultraviolet laser pulses in high-density plasma," *Applied Physics B*, vol. 50, pp. 79–99, Feb 1990.

[38] S. C. Rae and K. Burnett, "Reflectivity of steep-gradient plasmas in intense subpicosecond laser pulses," *Phys. Rev. A*, vol. 44, pp. 3835–3840, Sep 1991.

[39] M. Born and E. Wolf, *Principles of Optics*. Oxford: Pergamon Press, 6th ed., 1980.

[40] R. P. Godwin, "Fresnel absorption, resonance absorption, and x rays in laser-produced plasmas," *Appl. Opt.*, vol. 33, pp. 1063–1069, Feb 1994.

[41] R. More, Z. . Zinamon, K. Warren, R. . Falcone, and M. Murnane, "Heating of solids with ultra-short laser pulses," *Journal de Physique Colloques*, vol. 49, no. C7, pp. 43–51, 1988.

[42] E. G. Gamaly, "Ultrashort powerful laser matter interaction: Physical problems, models, and computations," *Laser and Particle Beams*, vol. 12, p. 185, Jan 1994.

[43] S. Pfalzner and P. Gibbon, "Direct calculation of inverse-bremsstrahlung absorption in strongly coupled, nonlinearly driven laser plasmas," *Phys. Rev. E*, vol. 57, pp. 4698–4705, Apr 1998.

[44] T. Millat, A. Selchow, A. Wierling, H. Reinholz, R. Redmer, and G. R. pke, "Dynamic collision frequency for a two-component plasma," *Journal of Physics A: Mathematical and General*, vol. 36, pp. 6259–6264, may 2003.

[45] M. Schlanges, T. Bornath, D. Kremp, and P. Hilse, "Quantum kinetic approach to transport processes in dense laser plasmas," *Contributions to Plasma Physics*, vol. 43, no. 5-6, pp. 360–362, 2003.

[46] R. L. Shepherd, D. R. Kania, and L. A. Jones, "Measurement of the resistivity in a partially degenerate, strongly coupled plasma," *Phys. Rev. Lett.*, vol. 61, pp. 1278–1281, Sep 1988.

[47] W. Theobald, R. Häßner, R. Kingham, R. Sauerbrey, R. Fehr, D. O. Gericke, M. Schlanges, W.-D. Kraeft, and K. Ishikawa, "Electron densities, temperatures, and the dielectric function of femtosecond-laser-produced plasmas," *Phys. Rev. E*, vol. 59, pp. 3544–3553, Mar 1999.

[48] D. Riley, I. Weaver, D. McSherry, M. Dunne, D. Neely, M. Notley, and E. Nardi, "Direct observation of strong coupling in a dense plasma," *Phys. Rev. E*, vol. 66, p. 046408, Oct 2002.

[49] L. Spitzer and R. Härm, "Transport phenomena in a completely ionized gas," *Phys. Rev.*, vol. 89, pp. 977–981, Mar 1953.

[50] L. Spitzer Jr., *Physics of Fully Ionized Gases.* New York: John Wiley, 1962.

[51] Y. B. Zel'dovich and Y. P. Raizer, *Physics of Shock Waves and High-Temperature Phenomena.* New York: Academic Press, 1966.

[52] W. Rozmus and V. T. Tikhonchuk, "Skin effect and interaction of short laser pulses with dense plasmas," *Phys. Rev. A*, vol. 42, pp. 7401–7412, Dec 1990.

[53] N. A. Krall and A. W. Trivelpiece, *Priciples of Plasma Physics.* New York: McGraw-Hill, 1986.

[54] D. Nicholas, "The development of fluid codes for the laser compression of plasma," *RL-82-083*, 1982.

[55] J. D. Huba, *NRL Plasma Formulary.* Washingten DC: Naval Research Laboratory, 1994.

[56] S. Pfalzner, "Statistical description of ionization potentials in dense plasmas," *Applied Physics B*, vol. 53, pp. 203–206, Oct 1991.

[57] W. C. Röntgen, "Ueber eine neue art von strahlen," *Annalen der Physik*, vol. 300, no. 1, pp. 12–17, 1898.

[58] Synchrotron, "Synchrotron light." https://www.iop.org/publications/iop/2011/page_47511.html#gref. (accessed: 22.07.2020).

[59] DESY, "Free-electron laser flash." https://flash.desy.de/. (accessed: 22.07.2020).

[60] LCLS, "Lcls overview." https://lcls.slac.stanford.edu/overview. (accessed: 22.07.2020).

[61] Z. Huang and K.-J. Kim, "Review of x-ray free-electron laser theory," *Phys. Rev. ST Accel. Beams*, vol. 10, p. 034801, Mar 2007.

[62] DESY, "Desy photon science." https://www.desy.de/. (accessed: 22.07.2020).

[63] G. Margaritondo and P. Rebernik Ribic, "A simplified description of X-ray free-electron lasers," *Journal of Synchrotron Radiation*, vol. 18, pp. 101–108, Mar 2011.

[64] M. Yabashi, H. Tanaka, and T. Ishikawa, "Overview of the SACLA facility," *Journal of Synchrotron Radiation*, vol. 22, pp. 477–484, May 2015.

[65] D. P. Science, "High-gain fel by microbunching." https://photon-science.desy.de/facilities/flash/the_free_electron_laser/how_it_works/high_gain_fel/index_eng.html. (accessed: 21.07.2020).

[66] D. P. Science, "Sase: Self-amplified spontaneous emission." https://photon-science.desy.de/facilities/flash/the_free_electron_laser/how_it_works/sase_self_amplified_spontaneous_emission/index_eng.html. (accessed: 16.08.2020).

[67] N. R. Council, *Controlling the Quantum World: The Science of Atoms, Molecules, and Photons*. Washington DC: The National Academies Press, 2007.

[68] K. Tono, T. Togashi, Y. Inubushi, T. Sato, T. Katayama, K. Ogawa, H. Ohashi, H. Kimura, S. Takahashi, K. Takeshita, H. Tomizawa, S. Goto, T. Ishikawa, and M. Yabashi, "Beamline, experimental stations and photon beam diagnostics for the hard x-ray free electron laser of SACLA," *New Journal of Physics*, vol. 15, p. 083035, aug 2013.

[69] "Femtosecond ti:sapphire laser." https://www.atto.physik.uni-muenchen.de/download/praktikum/femtosec__laser.pdf. (accessed: 19.03.2020).

[70] "Rp photonics." https://www.rp-photonics.com/mode_locking.html. (accessed: 19.03.2020).

[71] "Sacla technology." http://xfel.riken.jp/eng/sacla/index02.html. (accessed: 27.03.2020).

[72] "European xfel." https://www.xfel.eu/. (accessed: 27.03.2020).

[73] "Spring-8 / linear accelerator." http://www.spring8.or.jp/en/about_us/whats_sp8/facilities/accelerators/linac/. (accessed: 13.01.2020).

[74] T. Yabuuchi, A. Kon, Y. Inubushi, T. Togahi, K. Sueda, T. Itoga, K. Nakajima, H. Habara, R. Kodama, H. Tomizawa, and M. Yabashi, "An experimental platform using high-power, high-intensity optical lasers with the hard X-ray free-electron laser at SACLA," *Journal of Synchrotron Radiation*, vol. 26, pp. 585–594, Mar 2019.

[75] K. S. (Editor), *Handbook of Thin Film Deposition*. Elsevier, 3rd ed., 2012.

[76] Farotex, "A brief explanation of how magnetron sputtering works." https://farotex.com/technology.html. (accessed: 23.07.2020).

[77] S. Steinke, "The atomic scattering factor files." https://henke.lbl.gov/optical_constants/sf/ta.nff. (accessed: 11.08.2020).

[78] G. Pospelov, W. Van Herck, J. Burle, J. M. Carmona Loaiza, C. Durniak, J. M. Fisher, M. Ganeva, D. Yurov, and J. Wuttke, "*BornAgain*: software for simulating and fitting grazing-incidence small-angle scattering," *Journal of Applied Crystallography*, vol. 53, pp. 262–276, Feb 2020.

[79] X. Zhang, X.-H. Song, and D.-L. Zhang, "Thickness dependence of grain size and surface roughness for dc magnetron sputtered au films," *Chinese Physics B - CHIN PHYS B*, vol. 19, 08 2010.

[80] D. Fisher, M. Fraenkel, Z. Henis, E. Moshe, and S. Eliezer, "Interband and intraband (drude) contributions to femtosecond laser absorption in aluminum," *Phys. Rev. E*, vol. 65, p. 016409, Dec 2001.

[81] K. P. Driver, F. Soubiran, and B. Militzer, "Path integral monte carlo simulations of warm dense aluminum," *Phys. Rev. E*, vol. 97, p. 063207, Jun 2018.

[82] M. Banjafar, *in progress*. PhD thesis, TU Dresden, 2021.

[83] K. Eidmann, J. Meyer-ter Vehn, T. Schlegel, and S. Hüller, "Hydrodynamic simulation of subpicosecond laser interaction with solid-density matter," *Phys. Rev. E*, vol. 62, pp. 1202–1214, Jul 2000.

[84] S. C. Chae, N. Lee, Y. Horibe, M. Tanimura, S. Mori, B. Gao, S. Carr, and S.-W. Cheong, "Direct observation of the proliferation of ferroelectric loop domains and vortex-antivortex pairs," *Phys. Rev. Lett.*, vol. 108, p. 167603, Apr 2012.

[85] E. Gamaly, "The physics of ultra-short laser interaction with solids at non-relativistic intensities," *Physics Reports*, vol. 508, no. 4, pp. 91 – 243, 2011.

Chapter 9

Acknowledgements

First of all, I want to thank my supervisor **Christian Gutt**:

I thank you for letting me work on such a new and exciting topic which also involved lots of risk. Thank you for your support, the constructive discussions and your endless patience. Thank you for giving me the opportunity to travel once to the USA and twice to Japan to get to know the world's best research facilities. I like to think back to the trips, it was not only a great experience scientifically, I also enjoyed the Matcha ice cream, our trip through Tokyo or complaining about my jetlag. Thank you for always challenging and supporting me in every way and believing in me even though I've told you many times I can't.

Second, I want to thank my second reviewer **Ulf Zastrau**:

Thank you for accepting to be my second reviewer and spending time for reading and evaluating my thesis.

The next one is **Motoaki Nakatsutsumi**:

Thank you so much for letting me participate in your experiments that you perfectly organized. Thank you for your confidence in letting me analyze the data. Thank you for the many constructive meetings that brought plasma physics much closer to me. Thanks for always letting me bug you with my plasma questions.

I also want to thank **Thomas Kluge**:

Thanks for the great discussions with you and for pointing out the problems in my analysis so that I could improve and complete it. Thank you for inviting me to the HZDR and thank you for letting me participate in your beamtime at SLAC.

Furthermore, I want to thank **Mohammadreza Banjafar**:

Thanks for letting me work with you and thanks for producing all the simulations for me. I am looking forward to our future projects.

To my master student **Frederic Schon**:

I can't tell you enough times how much I enjoyed working with you. You have made a very important contribution to the success of this work and this would certainly not have been possible so fast without you.

Additionally, I want to thank **Michael Paulus**:

I thank you that I was always allowed to come to the TU Dortmund for measuring all reflectivity scans with you.

Very important, thanks to all the **collaborators from beamtimes (Proposal No. 2018B8049 and 2019B8076)**:

Many thanks for the support of all collaborators during the beamtimes, without you this would not have been possible at all. I would like to emphasize in particular **Thomas Preston**, **Mikako Makita** and the beamline scientist from SACLA **Toshinori Yabuuchi**.

I also want to thank **Gerhard Jakob**:

Thank you for producing the multilayer samples for us at the university of Mainz.

To my office mates **Hendrik Rahmann**, **Clémentine Lovato** and **Sonja Timmermann**:

I thank you for repairing me after each low and encouraging me that heights will come again. I also thank you for the constant distraction from work and the fun in the office. Most of all, I thank you for being friends.

To **Mario Reiser**:

I thank you for your constant mental support. It was so good to talk to someone who was facing the same ups and downs. Thank you for being my friend.

Many thanks to the other (and also former) group members **Mohammad Akhundzadeh**, **Ahmed Al-Masoodi**, **Dmitriy Kzensov**, **Anna-Lena Becker**, **Kevin Lopata** and **Jan Verwohlt**:

I really appreciate to work together with you at beamtimes or here at university and I always enjoy to spend time with you on christmas parties, summer parties,...

Not to be forgotten are **Kai Mehlich**, **Paulus Aleksa** and **Dina Wilks**:

Thanks for the constant distraction from work. Thanks for great movie nights, sports events like the Siegerländer Firmenlauf, bowling nights and ice breaks.

Thanks to **Mahmoud Al-Humaidi**:

Thank you for the endless number of coffee breaks and always listening to my problems.

Also thanks to **Carsten Busse**:

Thanks for the funny carpool and discussing the gossip.

To my **parents**:

Thanks for your constant support throughout my studies and during my PhD. Without you this would not have been possible at all.

To **Magnus**:

Thank you for your endless support over the last years. Thank you for enduring my ups and downs. Thank you for letting me always talk about my research and accepting that this is high priority.

Erklärung

Ich erkläre hiermit an Eides statt, dass ich die vorliegende Arbeit ohne unzulässige Hilfe Dritter und ohne Benutzung anderer, nicht angegebener Hilfsmittel angefertigt habe. Die aus anderen Quellen direkt oder indirekt übernommenen Daten und Konzepte sind unter Angabe der Quelle gekennzeichnet.
Die Arbeit wurde bisher weder im In- noch im Ausland in gleicher oder ähnlicher Form einer anderen Prüfungsbehörde vorgelegt.
Es wurden keine Dienste eines Promotionsvermittlungsinstituts oder einer ähnlichen Organisation in Anspruch genommen.

Zu den vorgeschlagenen Mitgliedern der Promotionskommission bestehen keine verwandtschaftlichen Beziehungen, keine Verwandtschaft ersten Grades, Ehe, Lebenspartnerschaft oder eheähnliche Gemeinschaft.

Siegen, den 26. August 2020

.....

Lisa Randolph